UNCLASSIFIED

AD NUMBER: AD0857654
LIMITATION CHANGES
TO: Approved for public release; distribution is unlimited.
FROM: Distribution authorized to US Government Agencies only; Export Control; 1 Jun 1969. Other requests shall be referred to Air Force Materials Laboratory, Wright-Patterson AFB, OH 45433.
AUTHORITY
AFML ltr dtd 12 Jan 1972

THIS PAGE IS UNCLASSIFIED

AFML TR-69-106
PART I

AD857654

A STUDY OF PLATE-SLAP TECHNOLOGY

PART I. A CRITICAL EVALUATION OF PLATE-SLAP TECHNOLOGY

H. M. BERKOWITZ, Ph.D.
L. J. COHEN, Ph.D.

McDonnell Douglas Astronautics Company

TECHNICAL REPORT No AFML-TR-69-106, PART I

JUNE 1969

This document is subject to special export controls and each transmittal to foreign governments or foreign nationals may be made only with prior approval of the Metals and Ceramics Division (MAM), Air Force Materials Laboratory, Wright-Patterson Air Force Base, Ohio 45433.

AIR FORCE MATERIALS LABORATORY
AIR FORCE SYSTEMS COMMAND
WRIGHT-PATTERSON AIR FORCE BASE, OHIO

186

NOTICE

When Government drawings, specifications, or other data are used for any purpose other than in connection with a definitely related Government procurement operation, the United States Government thereby incurs no responsibility nor any obligation whatsoever; and the fact that the Government may have formulated, furnished, or in any way supplied the said drawings, specifications, or other data, is not to be regarded by implication or otherwise as in any manner licensing the holder or any other person or corporation, or conveying any rights or permission to manufacture, use, or sell any patented invention that may in any way be related thereto.

This document is subject to special export controls and each transmittal to foreign governments or foreign nationals may be made only with prior approval of the Metals and Ceramics Division (MAM), Air Force Materials Laboratory, Wright-Patterson Air Force Base, Ohio 45433.

The distribution of this report is limited because the protection of technical know-how relating to technology restricted by U. S. Export Control Act.

Copies of this report should not be returned unless return is required by security considerations, contractual obligations, or notice on a specific document.

400 - August 1969 - CO455 - 87-1942

FINAL REPORT
A STUDY OF PLATE-SLAP TECHNOLOGY
Part I, A Critical Evaluation of Plate-Slap Technology

H. M. Berkowitz, Ph.D.
L. J. Cohen, Ph.D.

This document is subject to special export controls and each transmittal to foreign governments or foreign nationals may be made only with prior approval of the Metals and Ceramics Division (MAM), Air Force Materials Laboratory. Wright-Patterson Air Force Base, Ohio 45433.

BLANK PAGE

FOREWORD

This is the first of three parts of the final technical report that describes work conducted under USAF Contract No. F33615-68-C-1414. The three parts are identified as follows:

Part I. A Critical Evaluation of Plate-Slap Technology, AFML-TR-69-106, PART I (DAC 63180).

Part II. The Nuances of Plate-Slap Testing of Composite Materials, AFML-TR-69-106, PART II (DAC 62444).

Part III. The Mechanical Response of Composite Materials to Stress-Pulse Loading, AFML-TR-69-106, PART III (DAC 62445).

This report was prepared by the Nuclear Effects Section of the Structural Research Branch, Advance Structures and Mechanical Department, McDonnell Douglas Astronautics Company - Western Division (MDAC-WD), Santa Monica, California. Dr. H. M. Berkowitz served as principal investigator. The contract was initiated under Project No. 7351, "Metallic Materials," Task No. 735106, "Behavior of Metals." The work was monitored by the Metals and Ceramics Division, Air Force Materials Laboratory, Air Force Systems Command, with Dr. T. Nicholas, MAMD, as project scientist.

The authors of this report are deeply indebted to Messrs. J. A. Garretson and S. A. Schechter for their assistance in performing computer analyses and data reduction during the study, and to Messrs. D. C. MacKallor and J. F. Young of MDAC-WD and Mr. J. J. Dick of Stanford Research Institute for acquiring the plate-slap data. The valuable suggestions and critiques made by Drs. J. F. Garibotti and R. J. Reck of MDAC-WD and by Dr. T. Nicholas of the AFML are also gratefully acknowledged.

This report covers work conducted from April 1968 to April 1969. The manuscript of this report was released by the authors May 1969 for publication.

This technical report has been reviewed and is approved.

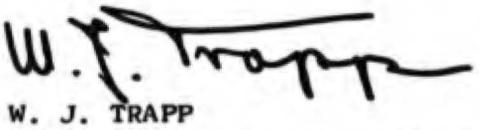

W. J. TRAPP
Chief, Strength and Dynamics Branch
Metals and Ceramics Division
Air Force Materials Laboratory

ABSTRACT

This report presents the motivation, philosophy, technical approach, and results of the part of "A Study of Plate-Slap Technology" entitled "A Critical Evaluation of Plate-Slap Technology." Under this study, state-of-the-art practices of plate-slap technology pertinent to characterization and design use of anisotropic, composite materials for re-entry vehicle thermal-protection systems have been documented and evaluated. The program plan, results, and conclusions are summarized herein. Basic characterization data, high stress-amplitude constitutive data obtained by gas-gun testing, and short load-duration failure data obtained by exploding-foil testing are all presented for the study material, a quartz-cloth reinforced-phenolic. Methods of data reduction are described. The results of the proof-testing that was conducted to provide a check on the validity of the design use of the data are presented, and the overall technology is evaluated. In addition, the other two parts of this final report are summarized; these are "The Nuances of Plate-Slap Testing of Composite Materials," AFML-TR-69-106, PART II and "The Mechanical Response of Composite Materials to Stress-Pulse Loading," AFML-TR-69-106, PART III.

This abstract is subject to special export controls and each transmittal to foreign governments or foreign nationals may be made only with prior approval of the Metals and Ceramics Division (MAM), Air Force Materials Laboratory, Wright-Patterson Air Force Base, Ohio 45433.

BLANK PAGE

CONTENTS

Section		Page
I	INTRODUCTION AND SUMMARY	1
	1. Purpose	1
	2. Definition of Plate-Slap Testing	1
	3. Summary of Results	2
II	PROGRAM PLAN AND TECHNICAL APPROACH	7
	1. Program Plan	7
	2. Study Philosophy	9
	3. Summary of Technical Approach	11
III	SPECIMEN PREPARATION AND CHARACTERIZATION	17
	1. Fabrication and Machining	17
	2. Pretest Characterization of Specimens	19
IV	GAS-GUN TESTING	27
	1. Motivation	27
	2. SRI Test Data Report	28
	3. Experimental Results	28
V	EXPLODING-FOIL TESTING	33
	1. Introduction	33
	2. Pretest Examination	33
	3. Fracture Threshold Testing at the MDAC-WD Facility	33
VI	EXAMINATION OF EXPLODING-FOIL TEST SPECIMENS	39
	1. Macroscopic and Preliminary Microscopic Examination of Specimens	39
	2. High Magnification Microscopic Examination of Specimens	43
VII	DETERMINATION OF DY AMIC STRESS-STRAIN CURVES FROM THE SRI GAS-GUN DATA	47
	1. Introduction	47
	2. Basic Considerations of the Mechanics and Thermodynamics of High-Amplitude Stress-Wave Propagation	48

Section		Page
	3. Determination of the Constitutive Relations from the Gas-Gun Data	60
VIII	DETERMINATION OF A FAILURE CRITERION	69
	1. Introduction	69
	2. Material Strength Theories for Wave Propagation	70
	3. Reduction and Analysis of the Failure Data	78
IX	PROOF-TESTING	83
	1. Design of the Proof-Tests	83
	2. Pre-Test Analysis of the Proof-Test Configuration	84
	3. Proof-Testing at the MDAC-WD Exploding-Foil Facility	84
	4. Pre- and Post-Test Characterization of Specimens	86
	5. Post-Test Microscopic Examination of Proof-Test Specimens	87
X	CONCLUSIONS AND RECOMMENDATIONS	89
	1. An Evaluation of Plate-Slap Technology	89
	2. Recommendations	92
	REFERENCES	97

ILLUSTRATIONS

Figures		Page
1	Idealization of Plate-Impact Configuration	103
2	Trim of Block	103
3	Blanks from Block Remaining After Trim	104
4	Blanks from Panel	104
5	Specimens from Panel HMB-2	105
6	Specimens from Panel HMB-3	106
7	Specimens from Blanks 7, 8, 9, 10	106
8	Specimens from Blanks 1, 2, 3, 4, 5, 6	107
9	Dimensions of Specimens 1, 2, 3, 4, 5, 6	107
10	Dimensions of Specimens 7, 8, 9, 10, 29, 30, 31, 32	108
11	Dimensions of Specimens 11 and 12 (from Blanks 11 and 12)	108
12	Dimensions of Specimens 13 through 28	109
13	Dimensions of Specimens 33 through 66	109
14	Thickness Machining of Surfaces of Quartz-Phenolic Blanks for Specimens P1 – P6	110
15	Cutting of Quartz-Phenolic Specimens P1 through P6 from Machined Blank	110
16	Thickness Machining of Surfaces of 6061-T6 Aluminum Blank	111
17	Cutting of Aluminum Back Up Blocks from Machined Blank	111
18	Specimen No. 44 Parallel to Direction of Reinforcement–25X	112
19	Specimen No. 46 Parallel to Direction of Reinforcement–25X	112
20	Specimen No. 51 Perpendicular to Direction of Reinforcement–25X	113
21	Specimen No. 51 Parallel to Direction of Reinforcement–25X	113
22	Specimen No. 51 Parallel to Direction of Reinforcement–75X	114
23	Specimen No. 63 Perpendicular to Direction of Reinforcement–6X	114
24	Specimen No. 63 Perpendicular to Direction of Reinforcement–25X	115
25	Specimen No. 63 Parallel to Direction of Reinforcement–6X	115
26	Specimen No. 63 Parallel to Direction of Reinforcement–25X	116
27	Test Setup for Measurement of Sinusoidal Wave Velocity in Materials	116
28	Stress-Time Profile, Shot 13594: Hugoniot Shot on Zero-Degree Quartz-Phenolic	117
29	Stress-Time Profile, Shot 13605: Hugoniot Shot on Zero-Degree Quartz-Phenolic	118
30	Stress-Time Profile, Shot 13603: Hugoniot Shot on 90-Degree Quartz-Phenolic	119
31	Stress-Time Profile, Shot 13606: Hugoniot Shot on 90-Degree Quartz-Phenolic	120

Figure		Page
32	Stress-Time Profile, Shot 13604: Hugoniot Shot on 90-Degree Quartz-Phenolic	121
33	Stress-Time Profile, Shot 13592: Attenuation Shot on 90-Degree Quartz-Phenolic	122
34	Stress-Time Profile, Shot 13595: Attenuation Shot on Zero-Degree Quartz-Phenolic	123
35	Schematic of MDAC-WD Exploding-Foil Facility	124
36	Schematic of MDAC-WD Exploding-Foil Facility Power Supply	124
37	Single-Plate Exploding-Foil Assembly	125
38	Double-Plate Exploding-Foil Assembly	125
39	Exploding-Foil Target Holder	126
40	Target Catcher	127
41	Exploded View of Target Catcher	128
42	Identation of Quartz-Phenolic Target Against Foam Catcher	128
43	Framing Camera Record of Flyer Target Impact	129
44	Streak Camera Record for Determination of Flyer Velocity	130
45	MDAC-WD Exploding-Foil Facility	131
46	Post-Test Damage Produced by 5-Mil Flyer Impacting at 0.98 mm/μsec. Specimen No. 15, Edge	132
47	Post-Test Internal Damage Produced by 5-mil Flyer Impacting at 0.98 mm/μsec. Specimen No. 15 – 10X	132
48	Post-Test Damage Produced by 5-Mil Flyer Impacting at 1.11 mm/μsec. Specimen No. 18	133
49	Post-Test Damage Produced by 14.7-Mil Flyer Impacting at 0.75 mm/μsec. Specimen No. 14, Edge – 4X	133
50	Post-Test Damage Produced by 14.7-Mil Flyer Impacting at 0.59 mm/μsec. Specimen No. 26	134
51	Post-Test Inspection of Condition Produced by 5-Mil Flyer Impacting at 1.11 mm/μsec. Specimen No. 18, Front Face – 4X	134
52	Post-Test Inspection of Condition Produced by 14.7-Mil Flyer Impacting at 0.57 mm/μsec. Specimen No. 22, Front Face – 4X	135
53	Post-Test Inspection of Condition Produced by 5-Mil Flyer Impacting at 0.98 mm/μsec. Specimen No. 19, Back Face – 4X	135
54	Post-Test Damage Produced by 5-Mil Flyer Impacting at 1.11 mm/μsec. Specimen No. 18, Delaminated Plane–4X	136
55	Post-Test Photomicrograph of Section Through Specimen No. 13-10X (5-Mil Flyer at 0.966 mm/μsec)	136
56	Post-Test Photomicrograph of Section Through Specimen No. 19-10X (5-Mil Flyer at 0.98 mm/μsec)	137
57	Post-Test Photomicrograph Specimen No. 22-10X Unpolished Section	137
58	Specimen No. 24, Impacted at 0.61 mm/μsec with 5-Mil Flyer, 100X Magnification	138
59	Specimen No. 23, Impacted at 0.66 mm/μsec with 5-Mil Flyer, 100X Magnification	138
60	Specimen No. 25, Impacted at 0.77 mm/μsec with 5-Mil Flyer, 65X Magnification	139

Figure		Page
61	Specimen No. 27, Impacted at 0.39 mm/μsec with 14.7-Mil Flyer, 50X Magnification	139
62	Specimen No. 21, Impacted at 0.41 mm/μsec with 14.7-Mil Flyer, 30X Magnification	140
63	Control Specimen at 75X Magnification, Showing Microcracks	140
64	Hugoniot Impedance Match Solution	141
65	Quartz-Phenolic Hugoniot Curves Calculated by SRI	141
66	Hugoniot Shock Velocity Versus Particle Velocity	142
67	Dynamic Stress-Strain Curve from Low-Velocity Shot (No. 13594), Zero-Degree Orientation	143
68	Dynamic Stress-Strain Curve from High-Velocity Shot (No. 13605), Zero-Degree Orientation	143
69	Dynamic Stress-Strain Curve from Low-Velocity Shot (No. 13603), 90-Degree Orientation	144
70	Dynamic Stress-Strain Curve from Intermediate Velocity Shot (No. 13606), 90-Degree Orientation	144
71	Dynamic Stress-Strain Curve from Highest Velocity Shot (No. 13604), 90-Degree Orientation	145
72	Quartz-Phenolic Hugoniot Stress Versus Condensation	145
73	Quartz-Phenolic Hugoniot Data	146
74	History of Stress at Quartz-Phenolic/Quartz Interface, Attenuation Shot, Zero-Degree Orientation	147
75	Stress Profile at 2.0003 μsec, Attenuation Shot, Zero-Degree Orientation	148
76	History of Stress at Mylar/Quartz-Phenolic Interface, Attenuation Shot, Zero-Degree Orientation	149
77	History of Stress at Quartz-Phenolic/Quartz Interface, Attenuation Shot, 90-Degree Orientation	150
78	Stress Profile at 1.5007 μsec; Attenuation Shot, 90-Degree Orientation	151
79	History of Stress at Mylar/Quartz-Phenolic Interface, Attenuation Shot, 90-Degree Orientation	152
80	Spall Data for Lucite. Like-on-Like Impact. Slapper to Target Thickness Ratio = 1:4	153
81	Stress Wave Pulse Shapes	153
82	Time-Dependent Strength of Solids	154
83	Time-Dependent Fracture Stress of Several Materials at Room Temperature	155
84	Time-Dependent Failure of Epoxy Resin-Constant Strain Rate (Epon 815/Versamide 140 (1:1 Mix))	155
85	Stress vs Strain Rate – SC1008 Phenolic	156
86	Yield Stress of 3-Phase Composite vs Strain Rate	156
87	Time-Dependent Fracture Strength of Aluminum Annealed at: a) 290°C; b) 420°C; c) 550°C	157
88	5-Mil Mylar Impactor on 250-Mil Quartz-Phenolic Target at 0.960 mm/μsec	158
89	14.7-Mil Mylar Impactor on 250-Mil Quartz-Phenolic Target at 0.56 mm/μsec	159
90	60-Mil Quartz-Phenolic Impactor on 125-Mil Quartz-Phenolic Target at 0.473 mm/μsec	160

Figure		Page
91	125-Mil Quartz-Phenolic Impactor on 225-Mil Quartz-Phenolic Target at 0.473 mm/μsec	160
92	5-Mil Mylar Impactor on 250-Mil Quartz-Phenolic Target at 0.600 and 0.650 mm/μsec	161
93	14.7-Mil Mylar Impactor on 250-Mil Quartz-Phenolic Target at 0.390 mm/μsec	161
94	60-Mil Quartz-Phenolic Impactor on 125-Mil Quartz-Phenolic Target at 0.213 mm/μsec	162
95	125-Mil Quartz-Phenolic Impactor on 225-Mil Quartz-Phenolic Target at 0.213 mm/μsec	162
96	Estimated Delamination Thresholds Zero-Degree Shingle-Angle Quartz-Phenolic	163
97	Visual Delamination Threshold Zero-Degree Shingle-Angle Quartz-Phenolic	163
98	Microscopic Delamination Threshold Zero-Degree Shingle-Angle Quartz-Phenolic	164
99	Proof-Test Configuration	164
100	Post-Test Photographs (2X) of the Front Faces of the Specimens	165
101	Post-Test Photographs (2X) of the Edges of the Specimens	166
102	Delamination of Visually Damaged Specimen Contrasted to Microscopically Damaged Specimen	167
103	Microscopically Damaged Specimens Showing Meandering Delaminations/Microcracks at 100X	168
104	Contrast of Front Face Microscopic Delamination at High- and Low-Velocity Impacts (100X Magnification)	169
105	Contrast of Conditon of Mid-Plane Regions of Specimens at High- and Low-Velocity Impacts (100X Magnification)	170
106	Contrast of Condition of Specimens Near Rear Face Following High- and Low-Velocity Impacts (100X Magnification)	171
107	Dense Microcracking Exhibited by Specimen P2 at 65X Magnification	172
108	Acoustic Velocity Degradation Versus Impact Velocity	172

TABLES

Table		Page
I	Cure Cycle Used for Block	18
II	Cure Cycle Used for Panel	18
III	Post-Cure Cycle Used for Specimen Blanks	19
IV	Comporite Density and Porosity; Burnout Test	22
V	Summary of Composite Density and Porosity; Burnout Test	23
VI	Summary of Composite Density and Porosity; Aminco Porosimeter	23
VII	Summary of Longitudinal Acoustic-Velocity Measurements for Quartz-Phenolic	25
VIII	Summary of Longitudinal Wave-Velocities	26
IX	Hugoniot and Attenuation Data Obtained at SRI for the Quartz-Phenolic	31
X	Summary of Photomicrographic Examination of Visually Undamaged Quartz-Phenolic Failure-Threshold Specimens	37
XI	Summary of Post-Test Microscopic Examination of Quartz Phenolic Failure-Threshold Specimens	40
XII	Sonic-Velocity Measurements Through 2D Quartz-Phenolic Specimens Before and After Plate-Slap Tests	44
XIII	Constitutive Parameters for the Study Materials	66
XIV	Summary of Dynamic Fracture Criteria	71
XV	Assumed Impact Conditions Producing Failure Threshold Data Points	79
XVI	Failure Parameters Selected as Representing Visual Threshold Points	80
XVII	Failure Parameters Selected as Representing Microscopic Threshold Points	81
XVIII	Visual Post-Test Examination of Proof-Test Specimens	85
XIX	Pre- and Post-Test Characteristics of the Proof-Test Specimens	86

BLANK PAGE

SECTION I

INTRODUCTION AND SUMMARY

1. PURPOSE

This final report documents the results of "A Study of Plate-Slap Technology" conducted under a contract with the United States Air Force. The study evaluated the validity of plate-slap technology applied to materials providing thermal protection to re-entry vehicles. The investigation of current practices of plate-slap technology was both analytical and experimental, and these practices were evaluated with respect to their use in analyzing and designing thermal-protection materials. Quartz-phenolic, a typical material of this type, was characterized to determine a constitutive model and failure criterion. Failure of a proof-test configuration was successfully predicted.

At the beginning of this investigation, plate-slap testing in its various forms was considered a valid technique for investigating phenomena or for obtaining material-property data, which, in conjunction with an analytical technique, could conceptually be used to predict stress-wave propagation and failure. However, the technology associated with plate-slap testing as applied to thermal-protection materials had not previously received critical evaluation. It was not really certain whether the current technology was valid for design use when applied to re-entry-vehicle materials, many of which are anisotropic composites. Thus, a study to evaluate plate-slap technology critically was necessary to ensure that adequate design practices exist and to direct proper development of materials.

2. DEFINITION OF PLATE-SLAP TESTING

For purposes of this study, plate-slap testing is considered to be any test technique that involves impacting at high velocities a flyer plate of one material against a target of the same or other material. The flyer can be a well characterized material, instrument, or the specimen under study. It can be launched by sudden expansion of a gas, sudden vaporization of a metal foil, detonation of a high explosive, impact by another flyer, electromagnetic repulsion, or any other conceivable means for achieving a high-flyer velocity. It can be flown unsupported or saboted. The target may be a plate specimen of the material under study or some experimental instrument. Flyer velocities can be determined by pin closures, by various optical techniques, or by indirect calibration methods.

The mathematical model for all standard plate-slap testing assumes that a unidirectional, plane wave-front is produced by normal impact of a plane flyer upon a plane target, with no lateral variation in load or response.

This model represents impact of one laterally semi-infinite medium upon another, as shown in Figure 1. If impact is truly planar, the central regions of laterally finite flyers and targets do behave, during early-response times, as if the items are semi-infinite. At later times, the lateral boundary effects produce complicated responses of the flyer and target-plate structures. The time for this to occur in cases of true planar impact depends upon the lateral dimensions, thicknesses, and physical properties of the material.

The analytical technique most often used to reduce plate-slap data and subsequently apply it in design involves a one-dimensional numerical computer code capable of predicting wave propagation and failure (References 1, 2). The reduced data are often used in designing vehicles for a variety of situations, which encompass several decades of temperature, pressure-pulse duration, and pressure-pulse magnitude.

A complete critical evaluation of plate-slap technology should consider all the various thermochemical, thermomechanical, and thermophysical effects that can be produced by the environments the vehicle may encounter. However, this present initial study is limited to considerations of only the thermomechanical and/or thermophysical effects of the laboratory environments produced by the plate-slap tests.

3. SUMMARY OF RESULTS

Current plate-slap technology can be used to produce an engineering design that will behave as predicted, provided the design analyst recognizes all aspects of the technology and their ramifications. He must possess a reasonably sophisticated knowledge of test technique, material-response characteristics, material-behavioral models, and material-environmental interactions. This report supplies adequate information on testing and characterization to permit design of a structure that can survive plate-slap environments, if sufficient test data are acquired for the materials.

a. Effects of Test Technique

Part II of this report (Reference 3) is devoted entirely to a discussion of the nuances of plate-slap techniques. The types of tests needed to obtain good data have been considered. These nuances of test techniques have been accounted for in the experimental part of this study.

(1) Choice of Propulsion Method

Thick-and thin-flyer plates launched by gas gun are commonly used to obtain data with which to establish constitutives models of materials. It was concluded that exploding-foil testing primarily should be employed to obtain failure data for composite materials. The exploding-foil technique can launch thin flyers at higher impact velocities than the gas gun, and is much less expensive. However, it is easier to get constitutive data for composites by using the gas gun with a quartz transducer, manganin wire, or similar electrical instrumentation, than by using these or optical instrumentation with the exploding-foil technique. Therefore, the gas-gun was selected to obtain constitutive data for this study, and the exploding foil was selected to get failure data.

(2) Closure Times

Simultaneity of impact of flyer on target (closure-time) can critically affect data obtained. Simultaneity can be better controlled and more accurately measured by using the gas gun. Gas-gun flyer closures were less than 50 nanoseconds, but exploding-foil flyer closures ranged from 50 to 350 nanoseconds.

To obtain data generally applicable after reduction to all stress-wave analyses, closure times should be less than 10% of loading-pulse duration. However, this criterion apparently need not be met if it is known that the same variability in loading time that exists for the data also will exist for cases to which the reduced data are subsequently applied. In this study, this criterion was not satisfied by the thin-flyer data, but this did not affect subsequent engineering results. The tests to obtain basic data and the subsequent tests to verify technology (proof tests) had the same type of closures.

(3) Operational Conditions

All testing was conducted in a vacuum. Tests in air produce an air-cushion effect that can cause the velocities of thin flyers producing target failure to be almost twice those necessary to produce failure in vacuum.

Exploding-foil flyers must have sufficient free flight (free run) before impact, so that steady-state conditions exist at impact. Free runs of 6 to 17 mm in vacuum were used and considered sufficient.

(4) Conditions of Target Support and Recovery

To obtain accurate stress-wave failure data, the targets must be supported at impact and their motion stopped after impact, without introducing significant secondary stress-wave or structural damage. This was accomplished by wrapping the targets in Teflon tape and supporting them laterally by steel blocks. They were caught in low-density foam after impact.

(5) Determination of Flyer Velocity and Closure Times

In gas-gun tests, flyer velocity and simultaneity of impact can be measured by pin closures or optical techniques. For exploding-foil tests, optical techniques are most often used to measure these quantities. Framing cameras commonly used in making such optical measurements have a minimum interframe time of 500 nanoseconds. It therefore was concluded that streak cameras should be used to measure velocities in those plate-slap tests where free runs are small, instead of framing cameras. Simultaneity can be estimated from framing pictures. However, the values so obtained are usually poor because of picture quality and the projected view of the flyer. As a result of these conclusions, pin closures were employed in the gas-gun tests under this study, and both streak and framing cameras were simultaneously used in the exploding-foil tests.

b. Damage Induced by Plate-Slap

Failure testing was conducted with specimens oriented with the planes of lamination normal to the direction of flyer motion (i.e., parallel to the flyer face). Upon microscopic examination, many of the impacted specimens exhibited delaminations induced by stress waves. The phenolic resin of all specimens exhibited microcracks that were parallel to the direction of flyer motion. The cause of these cracks is unknown; they could represent either stress-wave damage or late-time structural damage. Plate-slap damage is not always visually observable on a specimen before destructive examination, even though extensive damage may exist internally. Often, sectioning of apparently undamaged specimens revealed large, visually observable delaminations. Connected delaminations, which extended across the entire lateral dimension of the loaded region, could be found by microscopic examination of many of the other specimens. These existed even in specimens impacted at about 2/3 of the velocities defining the thresholds at which visual damage of unsectioned specimens could first be observed.

Damage itself is not a specific term. The effect of any degree of microcracking or delamination on the usefulness of a structure after it has experienced the stress-wave environment, has not been established in the literature.

c. Phenomenology of Composites

Composites exhibit all the behavioral aspects of other materials. In addition, their heterogeneity and anisotropy produce dispersive wave fronts. Because of anisotropy, stress waves propagating in different directions through the same material can also have different propagation velocities, wave amplitudes, pulse attenuation, and pulse profiles, even though the same load is applied to excite the wave in each direction. Anisotropy can also lead to shear waves propagating along with the compressive-stress waves excited by surface-pressure loads, which does not occur for isotropic materials. These anisotropic phenomena were shown analytically, by using the low-stress-amplitude elastic-wave theory (Reference 4). It is expected that they all also occur for high-stress loadings.

(1) Constitutive Modeling

Hugoniot and pulse-attenuation data were obtained to illustrate that the aforementioned differences in wave propagation in different directions in an anisotropic material did occur for high-amplitude waves. To reduce such data to adequate constitutive models, this study has shown the need to properly account for thermodynamic state variables and thermodynamic dissipative variables. This was done in establishing the model for the orthotropic study material in each of its two principal directions. The two resulting models are those characteristic of rate-independent, nonlinear elastic, linearly work-hardening plastic materials, and they differ from each other, which again reflects the anisotropy of the material.

The theoretical framework for each of these models was that for an isotropic material, because analytical theory and methodology do not presently exist for obtaining physically proper constitutive models from data on the propagation of high-amplitude stress waves through anisotropic composites. The means of using such proper models in analyses (e.g., computer codes) obviously also does not exist. Similar remarks can be made concerning accounting for the dispersion effects caused by the heterogeneity of composites. Also, the rate effects found in certain isotropic monoconstituent materials, as well as in certain composite materials, cannot be accounted for adequately within the current technology.

(2) Material Variations

Hugoniot states achieved in this study and compared to others for quartz-phenolics (found in the literature) have shown that they all differ. This reflects the difference in quartz-phenolic materials, caused by differing volume fractions of constituents, fabrication techniques, and direction of wave propagation. Thus, all materials called quartz-phenolic are not identical, and the constitutive models used in any analyses should reflect the specific material considered, as well as its particular anisotropy.

d. Dynamic Fracture Theories

This study has also documented fundamental aspects of dynamic fracture theories pertinent to wave propagation. Use of a failure criterion based on rate-process considerations has been recommended. This recommendation was based on the physical foundation of such a theory, plus the success the authors have had in applying it to another material, 6061-T6 aluminum. The raw data on plate-slap failure were reduced by analysis of the constitutive models, and the reduced data were fitted to this failure criterion.

The failure criterion used expresses failures in terms of two basic wave-propagation parameters: the peak stress and total impulse of the tensile stress-wave pulse that caused failure. The quasi-empirical nature of the criterion also reflects pulse-profile effects. Two failure levels were defined: the visual threshold, and a microscopic threshold represented as the lower limit of connected delaminations. This microscopic threshold was an arbitrary choice of a damage level representing failure.

e. Proof-Testing

To demonstrate the validity of plate-slap technology as applied under this study, a proof-test configuration was designed. The constitutive model and failure criterion developed were then used to predict the visual and microscopic failure levels of the proof-test configuration. Plate-slap tests were conducted and the experimental results agreed reasonably well with the pretest predictions.

Success of the proof-test resulted from procedures that involved use of all aspects of plate-slap technology: testing, data reduction, computer-code analyses, constitutive modeling, development of a failure criterion, etc. This success lead to the conclusion that the technology is adequate.

f. Limitations of the Technology

(1) Application of Material Models from This Study

Testing was limited. The reader is therefore cautioned to use constitutive and failure models developed under this study only to predict the response to plate-slap environments of a material similar to the study material, and only for the purpose of preliminary engineering design. The nuances of acquiring good data and reducing them to good models for other applications have been pointed out under this study. However, the analyst must recognize the degree each aspect affects the desired accuracy of the analytical results he is seeking. For example, this study used data for nominally 100-nanosecond pulses, for which the criterion stated earlier requires 10-nanosecond closure times. However, actual closures were between 50 to 350 nanoseconds. It was felt that this was not serious for subsequent prediction of the response to similar pulses with similar closure times: the individual models may be questionable, but their combined use in an engineering preliminary design should not have reflected this uncertainty.

The quartz-transducer traces used to establish the constitutive models exhibited some anomalies attributed to transducer breakdown. This also raises doubt as to the general validity of these models other than for use as engineering models, as applied in this study. More plate-slap data about the study material are required to check the conclusion that this material definitely does not exhibit rate effects, and to obtain more accurate and thus generally applicable engineering models.

(2) Testing for Engineering Models for Other Materials

To obtain preliminary design data about any other material for engineering applications, more plate-slap tests should be conducted than were in this study. The quantities of constitutive and failure data obtained for any one principal axis of the study material could not alone establish with certainty the validity of the one-dimensional engineering models developed, even for preliminary design; proof tests subsequently had to be conducted.

(3) Testing for Complete Constitutive Characterization

To achieve the goals of this study, a few plate-slap tests were conducted along two principal axes of an anisotropic composite material. Considerably greater quantities of plate-slap test data will be required to completely and adequately characterize any anisotropic composite material with three-dimensional constitutive models and three-dimensional failure criteria, instead of the simple one-dimensional engineering models described previously. Much more study of composite materials is needed.

Only the nature of some of the problems such characterization will entail have been identified. Future studies will have to establish the proper three-dimensional constitutive models and failure criteria representing such materials, and the proper test schemes and test quantities needed to determine the physical parameters of these models, for use in stress-wave environments.

SECTION II

PROGRAM PLAN AND TECHNICAL APPROACH

1. PROGRAM PLAN

The following specific work tasks have been performed. A subcontractor, Stanford Research Institute (SRI), has assisted in part of the testing, as indicated under Task 4.

TASK 1: Definition of the State of the Art

(a) The present state of the art of plate-slap technology has been defined as to testing techniques, data reduction techniques, material constitutive equations, material-failure criteria, and analytical techniques.

(b) The interrelationship among these areas as applied to re-entry vehicle design and analysis methodology has been described.

TASK 2: Fabrication and Machining

Procurement of raw materials and fabrication and machining of all quartz-phenolic specimens required for characterization testing and plate-slap testing has been accomplished at MDAC-WD.

TASK 3: Material Characterization

(a) Previous pertinent material property data on the quartz-cloth reinforced-phenolic test material available in the literature have been collated.

(b) The following material property testing for characterization and quality control has been performed:

(1) Acoustic velocity tests: acoustic velocity measurements were made to determine the longitudinal wave velocities of the material along each of the 3 principal axes of the material.

(2) Physical Property Tests: density, porosity, weight fractions of resin and reinforcement, and volume fractions of resin, reinforcement, and pores have been determined.

(3) Photomicrographs: Photomicrographs have been made of typical specimens prior to plate-slap testing in the MDAC-WD exploding-foil facility. Photomicrographs have been made at various levels of magnification of specimens after plate-slap testing in the MDAC-WD exploding-foil facility.

TASK 4: Equation-of-State Measurements and Pulse-Attenuation Tests at SRI

SRI, under subcontract to MDAC-WD, has conducted flyer-plate impact tests on quartz-phenolic targets instrumented with quartz transducers, as follows:

(a) Equation-of-state-type data has been determined using thick flyers. Shots were made parallel to and transverse to the direction of reinforcement.

(b) A pulse-attenuation test has been conducted, using a 5-mil Mylar* flyer for each principal direction (parallel and transverse).

TASK 5: Plate-Slap Testing at the MDAC-WD Exploding-Foil Facility

MDAC-WD has conducted plate impact tests on uninstrumented target specimens to obtain failure data pertinent to determination of a criterion for predicting failure due to a stress-wave propagation phenomenon. Measurements included flyer velocity at impact. Specimen dimensions were 1-1/4 inches by 1-1/4 inches by 1/4 inches thick. Flyers were made of 5-mil and 14.7-mil Mylar. The failure thresholds were determined for each of these two flyers. Impact in all cases was in the direction of the principal axis transverse to the lay-up planes (0° shingle-angle).

Task 6: Analysis

MDAC-WD has conducted the following analyses:

(a) Determination of Constitutive Equations. A best estimate has been established of the proper constitutive equations to use for predicting unidirectional wave propagation in the direction of each of the principal axes. The equations were based upon data determined in Tasks 3(a), 4(a), and 4(b). Computer code analysis using the PUFF code (References 1, 2) has been conducted as required.

(b) Determination of a Criterion for Predicting Failure Due to Stress-Wave Propagation. A best estimate has been established of the proper failure criterion for use in predicting failure due to stress-wave propagation in the direction of the transverse material principal axis. The criterion was based upon data determined in Tasks 3(a) and 5. The PUFF code was used as required.

*Trade name for polyester film by E. I. duPont de Nemours and Company

In establishing the philosophy for a critical study of plate-slap technology, the question arises, "What basic philosophy is involved in the acceptance of other technologies involving simpler test techniques?" For example, what would be the approach to an analogous problem, a study of the simple tension test? Such a study is conducted every so often by perceptive individuals who recognize some previously unquestioned aspect of the technology of the simple tension test (Reference 5). Despite repeated evaluation, the technology based upon the test survives the scrutiny it receives. The reason for this is that the technology permits design and analysis that lead to structural end-items, which behave according to intent in the design environment. This is the only practical criterion upon which an evaluation can be based. This is also the only practical criterion upon which a critical evaluation of plate-slap technology can be based.

Tension test data is used in a relativistic fashion. First, a theory (mathematical model of physical behavior) is established, encompassing the tension test as one case to which it is applicable. A model of the idealistic tension test is then developed mathematically. A physical approximation to this ideal is then constructed. Testing is next conducted upon a material whose "properties" are to be determined. The data is then reduced in the light of the theory and the mathematical model of the test to provide the properties needed in the theory. The properties are then used with the theory in subsequent analysis conducted for engineering design. The process breaks down only when the structural end-item so designed behaves unpredictably in the design environment.

The relativistic aspect of the above tension test technology is that the data are being interpreted and used within an arbitrarily established framework based upon limited physical experiments. In other words, it is forced into a theory. The theory is usually that which is simplest to apply to adequately describe physical behavior. Sometimes it is recognized that the theory is applicable as an "approximation" but actually is in "error" in the light of an established higher-order theory. At other times the higher-order theory is needed to predict some otherwise unpredictable behavior of an engineering design.

Of course, sometimes it is incorrectly felt that the state of the art theory is inadequate. In these cases, either the test technique or the analytical technique (calculation methodology) is improper. The test technique can fail to perform in close enough approximation to its idealistic behavior. The analytical technique can similarly be too distant an approximation to an "exact" mathematical solution of the theoretical model. Alternatively, errors can pile up in the analysis loop, leading to predictions that do not agree with real world behavior.

Thus, it is necessary to examine the combination of theory, testing technique, and analytical technique from the standpoint of whether together they adequately predict the behavior of the structural end-item designed for a given environment and given response. If the prediction is inadequate, it is then necessary to determine (1) where in the prediction loop the sources of error lie, and (2) what steps must be taken to improve the technology.

The above paragraphs tacitly suggest that the technology of the simple tension test be considered to establish the study philosophy with respect to a more commonly familiar subject area. However, the statements apply to all engineering or scientific technology built around test data that is fit into an empirically developed model of some general aspect of physical behavior. To evaluate plate-slap technology, this study has used as a criterion the answer to the question, "Does the result eventually lead to a design that behaves as predicted--that is, does the technology work?"

3. SUMMARY OF THE TECHNICAL APPROACH

The detailed work tasks established to provide information to evaluate the plate-slap technology were listed in Section II-1. The following paragraphs describe the approach and the technical rationale behind it.

The approach taken was a moderate analytical and experimental effort to establish the validity of re-entry vehicle material test and analysis methodology. The methodology starts by obtaining raw plate-slap data and ends with a proven design. The initial work effort was to first establish the state of the art and the appropriate interrelationship among subtechnologies as applied to the re-entry-vehicle design problem. A typical re-entry-vehicle heatshield material was then characterized as required for use in design and analysis. The material is a quartz-cloth reinforced phenolic. This class of material has received extensive investigation under a variety of government-sponsored programs. Thus, its description in the literature is representative of the best the state of the art has or will have to offer.

MDAC-WD fabricated the material and conducted simple characterization tests to establish the statistics representing reproducibility of its properties from sample to sample, as well as to establish a reference to enable future investigators to fabricate similar materials. The material was layed-up during fabrication by alternating the bias of adjacent cloth layers from 0° to 90°; this constructed an orthotropic material having the same properties in the directions of the two principal axes in the plane of the layup, but different properties along the principal axis normal to this plane. Quartz-transducer-instrumented gas-gun-launched plate-slap tests were then conducted at Stanford Research Institute (SRI) at nominally the same front face impact pressures in the two different principal orientations. Impacts were made in both the direction of the fibers of the cloth (parallel) and the direction normal to the cloth (transverse). Several of the shots in a given principal direction were equation-of-state-type measurements using a thick flyer. One other shot in each orientation was a thin flyer impact, measuring pulse attenuation. The impact pressures were chosen to be low enough to show a possible "unstable shock-wave" structure. If such a structure were truly exhibited by the measurements made during the equation-of-state tests, as was anticipated, it would then consist of an elastic precursor followed by a dispersive plastic wave-front. The attenuation shots served as comparison to the equation-of-state tests to indicate the attenuation occurring because of various effects. Analysis using the PUFF code has been made to predict the attenuation test response, to evaluate the constitutive models, and to identify the sources of attenuation. The shots were made in each of the two distinct material principal directions to exhibit the expected effects of anisotropy.

The transverse principal direction of the material was selected for dynamic failure tests. Stress-wave propagation failure-threshold data were determined in the MDAC-WD exploding-foil facility. Two visual and two microscopic failure-threshold points have been determined: one pair for a 5-mil mylar flyer and another pair for a 14.7-mil mylar flyer. From these data, and data which exist in the literature, MDAC-WD subsequently estimated a failure criterion. When PUFF runs were made to simulate the exploding-foil tests for purposes of data reduction, an attempt was to be made to account for the temperature of the hot mylar flyer; however, it was decided that this sophistication was unwarranted.

MDAC-WD established its best estimate of a limited constitutive model and failure criterion for quartz-phenolic for use in design analysis. Using these models and the PUFF code, an attempt was made to predict the failure of the proof-test configuration previously described in Section II-1. After the proof test was conducted and its results were interpreted, an evaluation was made of the state of the art of plate-slap technology.

The approach described above is exactly that used in the design of a re-entry-vehicle skin. It has been simplified to involve only one material, quartz-phenolic. The steps involved in the usual approach to end-item design are (1) evolve a design and analysis procedure (the state of the art determination), (2) fabricate material, (3) establish material models based on existing data, (4) supplement the data as required, (5) design, (6) proof-test and/or flight-test, and (7) conduct a critical evaluation of the design technology if something goes awry.

Certain decisions were made in establishing the work plan, based upon current practices of plate-slap technology. These represent a priori decisions that were themselves evaluated by the program. The first was that the plate-slap test experimental techniques are adequate if test objectives are kept in mind and close scrutiny is kept concerning test variables. (This covers variables such as flyer conditions at impact, instrumentation of specimens, flight in vacuum versus flight in air, interpretation of instrumentation output, etc.) This decision was made on the basis of experience gained from two studies, the Air Force Weapons Laboratory (AFWL) GAM contract (Reference 6) and a supplemental study conducted under the Space and Missile Systems Organization (SAMSO) RESEP contract (Reference 7).

The pertinent conclusion evolving from those studies is that quartz transducers do measure a representative stress in a composite material even more heterogeneous than that used in this study. Furthermore, the stresses predicted by a computer code performing the same function that PUFF performs for one-dimensional response compare favorably with the experimental results. It was therefore also assumed that the PUFF code would prove adequate for analyses conducted during this study, if used properly with an adequate constitutive model for the anisotropic material.

The versions of PUFF most in use at MDAC-WD are PUFF 66 and PUFF V, as described in References 1 and 2. The main problem arising from use of these programs is availability of equation-of-state data for the materials of

interest. They generally use the Mie-Gruneisen form for the solid phase. The Mie-Gruneisen equation incorporates Rankine-Hugoniot pressure data empirically determined from plate-slap or other shock-wave data. The Hugoniot-type pressure data are not available for most materials. This is because numerous materials are available, many of which do not warrant the time and cost associated with developing a complete equation-of-state. Estimates of the equations-of-state therefore must be made by suitably modifying existing data on similar materials and/or supplementing them with more data, as was done in this study.

The geometric shock-dispersion effects that occur in certain composite materials cannot be predicted at present with the one-dimensional PUFF code. It has been assumed that such effects are insignificant for the material and loading conditions chosen for this study.

Variable yield-strength (work-hardening) models, which suitably describe the behavior of many heat-shield materials, have been built into the MDAC-WD PUFF codes. The variable yield-strength model is available for use when sufficient material behavior data are available. It had been assumed that sufficient data of this kind existed for the quartz-phenolic under study, from existing data supplemented by the testing conducted under this program.

The greatest limitation of the PUFF code is that it has been developed considering an isotropic material model. It is therefore necessary to modify either the designations of property inputs for orthotropic materials, or the code for use with orthotropic materials. For this study, either of these steps was feasible because the wave propagation in the orthotropic medium was always limited to propagation in the direction of a material principal axis. The former approach was used because of its simplicity. However, general anistropic elastic materials are characterized by 21 elastic constants. Solution for unidirectional waves propagating due to forced response to pressures on one surface of a laterally semi-infinite body shows that the response is a superposition of one longitudinal and two shear waves. This is because all three displacement components of any point are coupled in the boundary conditions and excited by the forcing function. If the material is orthotropic, this is, in general, still the case unless propagation takes place along a material principal axis. In that special case, which is the one pertinent to this study, the situation is similar to that for an isotropic material. Only a longitudinal wave is propagated because only the axial displacement component is excited. It is expected that similar effects of respective anisotropy are exhibited at moderate- to high-amplitude "shock" pressures.

On the whole, for general orientations of an orthotropic material and shock-type loadings, PUFF has often been used in the past without questioning the anisotropic nature of the material. It is recognized that this is not proper usage. PUFF is often similarly used in studies without questioning the rate-dependence of the material constitutive properties, which the code cannot now handle. This limitation was recognized but has not been considered in this study. The material has been assumed not to be significantly rate-dependent for the types of loadings considered. This will be discussed further in Section VII.

The PUFF version at MDAC-WD has an option to permit material spall. Unfortunately, a criterion for accurate prediction of spall is open to question. It was assumed that a failure criterion could be evolved for the test material. A rate-dependent criterion was chosen. It has been possible to establish a limited portion of a failure threshold, which is a function of two variables. The current MDAC-WD practice is to use as variables the peak tensile stress and the total tensile impulse contained in the stress-wave tensile pulse producing failure. The criterion was developed in terms of these variables (see Section VIII).

Acoustic velocity tests in the 0.5 to 5.0-MHz range were performed on the test specimens. Longitudinal wave velocities were measured at four frequencies along each of the three principal directions in the orthotropic material, using a through-transmission water-immersion test. It was recognized, as borne out by the acoustic velocity tests, that the quartz-cloth reinforced phenolic is orthotropic. In this report, the acoustic velocity measurements will subsequently be compared to those available in the literature to establish similarities or differences in materials. They also served for quality control. The frequency sweep was not expected to show any frequency dependence, and it did not. Had it displayed such a frequency dependence, this would have indicated a dispersive effect that would have to be accounted for in establishing a constitutive model. A stress-wave pulse can be dispersed and attenuated by a variety of mechanisms. It is necessary to model them properly in a constitutive representation and recognize their occurrence experimentally.

Dispersion due to dissipation of the mechanical energy in a stress-wave pulse can be achieved by conversion to heat energy through material mechanisms such as shock formation or plastic or viscous flow, possibly accompanied by internal mechanical work, as in crushing. Additional "geometric" dispersion of the pulse can be achieved by internal reflections of the stress pulse off reinforcing particles or by interaction between adjacent wave-guiding materials. Similar dispersion can occur as a result of rate-sensitive processes. These spread the pulse spatially within the material by attenuation of peak amplitudes. However, attenuation caused by geometric or rate effects can also be exhibited by shock-wave fronts even for very long pulse widths, without significant dispersion of the fronts. As stated previously, the effects of geometric-dispersion or rate-effects have been assumed to be insignificant in this study.

Because the goals of this contract include documenting and evaluating the state of the art practices of plate-slap technology, two survey-type reports have been written. These originally appeared as Vols. II and III of the 6-month technical management report (Reference 8) and are Parts II and III of this Final Report (References 3, 4).

Part II of this final report considers three plate-slap test techniques used to produce low-to-moderate impact pressures (less than several hundred kilobars) and flyer-plate velocities less than 5 mm/μsec. These techniques are the gas-gun, exploding-foil, and electromagnetic methods of launching flyer plates. Various facilities have been surveyed, and their representative

features are described with respect to 13 categories: (1) method of propulsion, (2) facility characteristics, (3) flyer support conditions, (4) operational conditions, (5) determination of flyer velocity, (6) determination of flyer planarity, (7) determination of simultaneity of impact (closure time), (8) flyer dimensions and special characteristics, (9) flyer free run, (10) target support conditions, (11) target dimensions and special characteristics, (12) instrumentation of target, and (13) target recovery.

The implications of the various aspects of the plate-slap test techniques are subsequently discussed with respect to selecting a facility and obtaining meaningful data for the following four specific test purposes: (1) shock wave studies, (2) dynamic stress-strain relations, (3) thin-pulse attenuation effects, and (4) dynamic-fracture criteria. The multitude of considerations that should be recognized are enumerated. The effects of several of these on the test data obtained are discussed.

Part III of this final report has been written in part to point out the many aspects of mechanical response of composite materials affecting measurements made using the techniques of plate-slap technology. Therefore, only a portion of the report includes new findings. The report is directed toward a large audience of varied backgrounds. For this reason, it begins with such fundamental considerations as motivation for plate-slap testing and a restatement of many of the mechanisms of material response common to homogeneous, isotropic, monoconstituent materials. However, the prime purpose of the report is to familiarize the reader with those aspects of stress-pulse response of heterogeneous, anistropic composite materials which make such response different from that of homogeneous, isotropic materials. It also has been an attempt to identify and tie together previous and current studies pertinent to the state of the art of the stress-wave response of composite materials.

At the same time, such a report obviously cannot be all-inclusive. The current major motivations for any wave-propagation studies of the properties of composite materials is to be able to obtain data and to analyze the environmental response of composites used for aircraft and aerospace vehicles. Thus, the report is specific to wave-propagation of pulses of moderate-to-low stress amplitudes. Understanding of data from such pulses is required to eventually predict the behavior of pulses which either do not produce stress-wave failures of the materials, or which are of magnitudes required to produce only incipient damage, so that adequate structural designs can be evolved.

Part III emphasizes the effects of material anisotropy. It presents a brief historical survey of previous studies of elastic-waves in anisotropic materials, specifically referencing pertinent documents of the last decade as well as those earlier reports and texts which can direct the reader to the work of the preceding century. Basic aspects and concepts of propagation of elastic-waves in anisotropic materials are mathematically developed and illustrated by examples involving the quartz-phenolic material of this study. Extension of the results inferred from the elastic-wave analysis to the high-stres amplitude, anelastic-response regime is briefly discussed. Reference is made to the high-stress amplitude data reported in Section IV of this report and reduced in Section VII.

BLANK PAGE

Section III

SPECIMEN PREPARATION AND CHARACTERIZATION

1. FABRICATION AND MACHINING

The specimen requirements for the present study necessitated that MDAC-WD fabricate two quartz-phenolic laminates from which specimens were machined:

- A press-cured block (0° shingle-angle butter-bar).
- A press-cured board (0° shingle-angle panel).

The first laminate is fabricated by laying up shingles of the quartz-cloth upon each other to construct a relatively thick (high) piece. This is then cut to the desired block dimensions. It then has the appearance of a butter-bar, with plies parallel to the base, i.e., 0° shingle angle. It is subsequently cured in a mold. The second laminate is constructed as a board with shingles laid up parallel to its base (0° shingle angle) until a relatively thin piece height is reached. Both pieces are cured and post-cured under pressure. MDAC-WD utilized its own recommended cure and post-cure cycles to fabricate the quartz-cloth reinforced-phenolic used in this study. Experience had shown that these cycles would produce a relatively void free, structurally sound material.

The fabrication and characterization of the study materials are considered in detail in this section. This is to enable future researchers to duplicate the material as closely as possible should they desire. Of course, the characterization data were required for this study as well, to ensure quality control and to gain a fundamental understanding of the material itself prior to plate-slap testing.

Twelve linear yards of J. P. Stevens Co., 581 quartz-fabric, impregnated with Monsanto Corp. SC1008 phenolic-resin and B-staged, were ordered and procured from American Reinforced Plastics, Inc., (ADLOCK 301 PHQ - 38 inch width). A 0° shingle-angle butter-bar block was made up as an approximately 4-1/2-inch high laminate with base dimensions approximately 3-3/4 inches by 5-3/4 inches. Similarly, the 0° shingle-angle panel was made with lateral dimensions 12 inches by 10 inches and a thickness of about 0.35 inch. In laying up the block and panel, first the warp and then the fill direction of a ply of quartz-cloth alternately coincided with the long axis of the laminate. This was done to construct laminates which had the same material properties in both of the in-plane principal directions. The cure cycles actually used for the block and the panel are listed in Tables I and II.

Table I. Cure Cycle Used for Block

Temperature, T, °F	Pressure, p, psi	Time at T and p, Hours
200	200	1-1/2
250	500	2
300	1000	3
350	1000	6

NOTES: 1. Average gradient to each temperature approximately 45°F/Hour.
2. Block allowed to cool to room temperature in autoclave under 1000 psi pressure.

It was elected to machine and post-cure specimen-blanks prior to final machining of the specimens. This was done to ensure that proper dimensions are achieved for all specimens. Fourteen specimen-blanks were rough-machined from the block and the panel, as indicated in Figures 2 through 4, prior to post-cure of the material. The blanks from the block were identified with numbers 1 through 12, exactly as shown in Figure 3. The blanks from the panel were identified with the designations HMB-2 and HMB-3, exactly as shown in Figure 4. This identification system permits orientation of the blanks, and subsequently the properties of the specimens machined therefrom, with respect to the location in the original block and panel. Excess material from the top and bottom of the block, as well as

Table II. Cure Cycle Used for Panel

Temperature, T, °F	Pressure, p, psi	Time at T and p, Hours
200	50	1/3
250	500	1/3
300	1000	1
325	1000	2
350	1000	2

NOTE: Panel allowed to cool to room temperature in autoclave under 1000 psi pressure.

that from the panel, was saved for future use. The specimen-blanks from this block had dimensions of about 0.30, while those from the panel were about 0.35. They were all given the nominal four day post-cure specified in Table III.

Final machining of the specimens which were used for the plate-slap and characterization tests was done to the dimensions shown in Figures 5 through 13, and identified exactly as shown in these figures.

The proof-test specimens were machined from a nominally 1-1/2-inch wide by 8-3/4-inch long blank remaining after specimens 21 through 28 were machined from panel HMB-3. Figures 14 and 15 depict the dimensions to which these six nominally 1-1/2 by 1-1/2 by 1/4-inch specimens were cut. The specimens were labeled P1 through P6 after machining. The six aluminum back-up blocks used with these proof-test specimens were machined from a stock 6061-T6 aluminum blank to the dimensions shown in Figures 16 and 17.

2. PRETEST CHARACTERIZATION OF SPECIMENS

After specimen machining was completed, typical specimens were characterized by measuring density, fiber and resin weight and volume fractions, porosity, and acoustic velocities, as well as with photomicrographs.

a. Determination of Volume and Weight Fractions and Void Content by Burn-out and Porosimeter

A total of 12 specimens (6 from flat plate, 6 from butter bar) were subjected to a resin burnout test at 1000°F for 1 hour to determine the composite

Table III. Post-Cure Cycle Used for Specimen Blanks

Temperature, T, °F	Time to T, Hours	Time at T, Hours
300	32	16
350	8	16
Ambient	24	--

NOTES: 1. Leeds and Northrup programmed oven used.
2. Temperatures reached at constant gradients.

resin, fiber and void content. The data were reduced using the following relationships (Reference 9):

$$V_f + V_m + V_v = V_c \tag{1}$$

$$C_f = \frac{V_f}{V_c}; \quad C_m = \frac{V_m}{V_c}; \quad C_v = \frac{V_v}{V_c} \tag{2}$$

$$n = \frac{w_f}{w_m} = \frac{\text{Burnout weight of filaments}}{\text{Weight of resin}} = \frac{C_f}{C_m} \cdot \frac{\gamma_f}{\gamma_m} \tag{3}$$

$$b = \frac{\gamma_m}{\gamma_f} \tag{4}$$

where

C = volumetric fraction

γ = density (g/cm^3)

w = weight (grams)

V = volume

c, f, m, v = subscripts which denote, composite, filament, resin and voids, respectively.

By suitable algebraic manipulation, the void content C_v of the three-phase system, i.e., filaments, resin and voids, is determined using the following relationships:

$$C_f = \frac{\gamma_c \cdot n}{\gamma_f(n + 1)} \tag{5}$$

$$C_m = \frac{\gamma_c}{\gamma_m(n + 1)} \tag{6}$$

Table IV. Composite Density and Porosity; Burnout Test

Specimen No.	γ_c g/cm^3	w_m g	w_f g	n	C_f%	C_m%	C_v%	W_f%	W_m%	Specimen from
33	1.665	0.7229	1.1518	1.593	46.49	50.96	2.55	61.44	38.56	Flat Plate
34	1.682	0.7425	1.1720	1.578	46.79	51.78	1.43	61.22	38.78	Flat Plate
35	1.691	0.7273	1.1527	1.584	47.11	51.95	0.94	61.31	38.69	Flat Plate
40	1.678	0.7476	1.1759	1.572	46.60	51.79	1.61	61.13	38.87	Flat Plate
43	1.687	0.7651	1.1454	1.497	45.97	53.62	0.41	59.95	40.00	Flat Plate
45	1.655	0.7401	1.1610	1.568	45.93	51.16	2.91	61.07	38.93	Flat Plate
47	1.714	0.8552	1.4653	1.713	49.19	50.14	0.67	63.15	36.85	Butter Bar
53	1.714	0.8652	1.4500	1.675	48.76	50.86	0.38	62.63	37.37	Butter Bar
55	1.730	0.8313	1.5264	1.836	50.91	48.41	0.68	64.74	35.26	Butter Bar
56	1.707	0.8210	1.4796	1.802	49.90	48.35	1.75	64.31	35.69	Butter Bar
60	1.731	0.8243	1.5243	1.849	51.06	48.23	0.71	64.90	35.10	Butter Bar
64	1.712	0.8723	1.4368	1.644	48.42	51.33	0.25	62.22	37.78	Butter Bar

Table V. Summary of Composite Density and Porosity; Burnout Test

Quantity	Flat Plate	Butter Bar
$\bar{\gamma}_c$ g/cm^3	1.676	1.718
$\bar{C}_f$%	46.45	49.70
$\bar{C}_m$%	51.87	49.55
$\bar{C}_v$%	1.68	0.75
$\bar{W}_f$%	61.02	63.65
$\bar{W}_m$%	38.98	36.35

NOTE: Average values of six specimens denoted by bar over symbol.

Table VI. Summary of Composite Density and Porosity; Aminco Porosimeter

Specimen No.	γ_c g/cm^{3*}	Open Porosity %**	Specimen from
50	1.936	0.57	Butter Bar
57	1.715	1.71	Butter Bar
62	1.712	1.20	Butter Bar
36	1.685	1.03	Flat Plate
41	1.684	1.00	Flat Plate
42	1.658	2.30	Flat Plate

*Apparent density as measured in mercury
**Pore volume of sample. No correction is made for micro-pores less than 0.012 microns. No correction is made for closed pores.

made at higher frequencies (e.g., 1.0, 2.25 and 5.0 MHz) and various locations, to ascertain the presence of inhomogeneities and determine the frequency dependence of the longitudinal wave velocity. A summary of the longitudinal wave velocities of all specimens tested, and the corresponding test frequencies, is given in Tables VII and VIII. Each of the longitudinal wave velocities indicated in Table VII is an average of three readings.

As shown in Table VII, results from longitudinal wave velocity tests on specimens 1 through 10 indicate that there is no difference in nominal warp and fill properties. This test is interpreted as verification that all properties are the same in each of these directions. The material was layed-up with this as the intent, and symmetry considerations lead one to believe it is the case. There is, however, a significant difference between properties for these two longitudinal axes and the transverse axis properties, as exhibited by the fact that the transverse velocity is only about 75% of the longitudinal. Over the decade of frequencies tested, there does not appear to be a significant frequency-dependence of either wave velocity.

Table VII. Summary of Longitudinal Acoustic-Velocity Measurements for Quartz-Phenolic

Specimen from	Direction of Wave Propagation	Specimen No.	Delay Time* (μsec)				Specimen Thickness (in.)	Longitudinal Wave Velocity (cm/μsec)			
			0.5 MHz	1.0 MHz	2.25 MHz	5.0 MHz		0.5 MHz	1.0 MHz	2.25 MHz	5.0 MHz
Butter Bar	Longitudinal[3]	1	1.633	1.627	1.680	1.587	0.2560	0.3982	0.3997	0.3871	0.4097
		2	1.573	1.597	1.637	1.580	0.2543	0.4106	0.4045	0.3946	0.4088
		3	1.573	1.580	1.643	1.543	0.2537	0.4097	0.4079	0.3922	0.4176
		4	1.660	1.660	1.673	1.537	0.2536	0.3880	0.3880	0.3850	0.4191
		5	1.613	1.637	1.697	1.727	0.2548	0.4012	0.3954	0.3814	0.3722
		6	1.627	1.627	1.700	1.693	0.2540	0.3965	0.3965	0.3795	0.3811
		7	1.727	1.680	1.687	1.557	0.2547	0.3746	0.3851	0.3835	0.4155
		8[1]	1.640	1.613	1.663	1.550	0.2547	0.3945	0.4011	0.3890	0.4174
		8[2]	1.647	1.660	1.683	1.520	0.2547	0.3928	0.3897	0.3844	0.4256
		9	1.580	1.607	1.640	1.557	0.2543	0.4088	0.4019	0.3939	0.4148
		10[1]	1.533	1.620	1.650	1.623	0.2550	0.4225	0.3998	0.3926	0.3991
		10[2]	1.627	1.663	1.697	1.517	0.2550	0.3981	0.3895	0.3817	0.4270
	Transverse[4]	11	2.207	2.173	2.203	1.900	0.2546	0.2930	0.2976	0.2936	0.3404
	Transverse[4]	12	2.287	2.260	2.180	2.070	0.2545	0.2827	0.2860	0.2965	0.3123
Flat Plate	Transverse[4]	13	2.500	--	--	--	0.2549	0.2590	--	--	--
		14	2.320	--	--	--	0.2549	0.2791	--	--	--
		15	2.200	--	--	--	0.2549	0.2943	--	--	--
		16	2.107	--	--	--	0.2549	0.3073	--	--	--
		17	2.380	--	--	--	0.2548	0.2719	--	--	--
		18	2.207	--	--	--	0.2550	0.2935	--	--	--
		19	2.120	--	--	--	0.2551	0.3056	--	--	--
		20	2.160	--	--	--	0.2552	0.3001	--	--	--
		21	2.207	--	--	--	0.2548	0.2933	--	--	--
		22	2.093	--	--	--	0.2551	0.3096	--	--	--
		23	2.060	--	--	--	0.2548	0.3142	--	--	--
		24	2.000	--	--	--	0.2550	0.3239	--	--	--
		25	2.067	--	--	--	0.2554	0.3131	--	--	--
		26	2.120	--	--	--	0.2550	0.3055	--	--	--
		27	2.060	2.060	2.100	2.063	0.2550	0.3144	0.3144	0.3084	0.3140
		28	2.113	2.117	2.123	2.070	0.2550	0.3065	0.3060	0.3051	0.3129
		29	2.140	2.113	2.153	2.110	0.2538	0.3012	0.3051	0.2994	0.3055
		30	2.067	2.103	2.200	2.080	0.2543	0.3125	0.3071	0.2936	0.3105
		31	2.133	2.087	2.217	2.153	0.2548	0.3034	0.3101	0.2919	0.3006
		32	2.040	2.055	2.133	2.100	0.2548	0.3173	0.3149	0.3034	0.3082
		P1	2.14	--	--	--	0.2540	0.3057	--	--	--
		P2	2.10	--	--	--	0.2537	0.3069	--	--	--
		P3	2.07	--	--	--	0.2540	0.3117	--	--	--
		P4	2.08	--	--	--	0.2537	0.3061	--	--	--
		P5	2.10	--	--	--	0.2540	0.3072	--	--	--
		P6	2.02	--	--	--	0.2540	0.3194	--	--	--

NOTE: *Average of 3 readings.
1 Measurement made 5/8" from center of specimen.
2 Measurement made 5/8" from center of specimen and 135° from item 1.
3 Parallel to direction of reinforcement.
4 Perpendicular to direction of reinforcement.

Table VIII. Summary of Longitudinal Wave-Velocities

Direction of Wave Propagation	Average Longitudinal Wave Velocity (cm/μsec)				Average of Four Frequencies
	0.5 MHz	1.0 MHz	2.25 MHz	5.0 MHz	
Longitudinal[1]	0.3996	0.3965	0.3870	0.4089	0.3980
Transverse[2]	0.3001	0.3051	0.2990	0.3131	0.3043

NOTES: [1] Parallel to direction of reinforcement.
[2] Perpendicular to direction of reinforcement.

Section IV

GAS-GUN TESTING

1. MOTIVATION

Eight of the specimens of quartz-phenolic were subjected to gas-gun launched flyer impact tests at Stanford Research Institute (SRI), under subcontract to MDAC-WD. These specimens were numbered 5, 7, 8, 9, 10, 29, 30, and 31. No data were obtained from the test on specimen 7. To emphasize what was stated in Section III: in fabricating and machining these specimens, the quartz fabric was oriented with plies either parallel to or perpendicular to the surfaces. Thus, specimens 5, 7, 8, 9, and 10 had quartz fibers running through their thickness dimension, while specimens 29, 30, and 31 had quartz fibers running in planes parallel to their surfaces. Specimens 5, 7, 8, 9, and 10 are commonly referred to as 90-degree shingle-angle, 0-degree bias-cut material, whereas specimens 29, 30, and 31 are called 0-degree shingle-angle, 0-degree bias-cut material. The testing of these two material orientations is described in this section. The data reduction is described in Section VII.

The purposes of the tests were:

- To determine whether the material exhibits anisotropy under low stress (5 to 10 Kbar) shock Hugoniot conditions.
- To identify whether the material exhibits work-hardening elastic-plastic behavior under low-stress shock-Hugoniot conditions, whether this is the most significant pulse-attenuating mechanism, and whether it is also an anisotropic mechanism.

Previous low and intermediate strain-rate testing at MDAC-WD has shown that quartz-phenolic is a work-hardening elastic-plastic material (Reference 12). It was suspected that this would be true under conditions of dynamic impact, such as during shock-Hugoniot and pulse-attenuation testing, if impact stresses were kept low enough. This elastic-plastic mechanism had previously been used at MDAC-WD to successfully explain thin-pulse attenuation in a carbon-phenolic (Reference 7). It was also felt that this dissipative mechanism may be more important than rate-effects for quartz-phenolic. Of course, elastic properties and acoustic-velocity testing show that the material is clearly anisotropic at low-stress levels.

To identify the above effects, four tests were first conducted (two Hugoniot and two attenuation, one of each at each shingle-angle), all at the same front-face impact-stress, between 5 and 10 Kbar. 5 Kbar was preferable,

Table IX. Hugoniot and Attenuation Data Obtained at SRI for the Quartz Phenolic

HUGONIOT SHOTS

MDAC-WD Specimen No.	Shingle Angle Orientation	Initial Density (g/cm^3)	Thickness (mm)	SRI Shot No.	Projectile Material	Projectile Velocity (mm/μsec)	Tilt Across 1/2" Gage (μsec)	Velocity of First Motion (mm/μsec)	Velocity of 1/2 Wave (mm/μsec)	Hugoniot State Estimated by SRI	
										Final Stress (kbar)	Particle Velocity (mm/μsec)
29	0°	1.67	6.32	13594	6061-T6 Al	0.128	0.047	3.31	2.87	4.8	0.099
9	90°	1.70	6.32	13603	6061-T6 Al	0.127	0.025	4.37	3.63	5.7	0.092
31	0°	1.67	6.28	13605	2024-T4 Al	0.272	0.031	5.50	3.33	11.5	0.204
5	90°	1.71	6.33	13606	2024-T4 Al	0.271	0.100	4.85	3.86	12.8	0.195
10	90°	1.70	6.31	13604	2024-T4 Al	0.413	0.017	5.00	4.05	20.2	0.292
7	90°	1.70	6.32	13593	6061-T6 Al	0.128	0.053	4.10	No Trace Obtained		

ATTENUATION SHOTS

MDAC-WD Specimen No.	Shingle Angle Orientation	Initial Density (g/cm^3)	Thickness (mm)	SRI Shot No.	Projectile Material	Projectile Velocity (mm/μsec)	Tilt Across 1/2" Gage (μsec)	Time of First Motion (μsec)	Time of 1/2 Wave (μsec)	Time of Crest Wave (μsec)	Time of Relief to Zero Stress (μsec)	Peak Stress (kbar)
8	90°	1.71	6.32	13592	Mylar	0.278	-0.05	1.61	1.90	2.06	2.40	1.28
30	0°	1.68	6.35	13595	Mylar	0.275	0.055	2.12	2.46	2.59	3.04	1.16

through 32 are the Hugoniot-type traces. Two Hugoniot traces were obtained for the zero-degree shingle-angle material (Figures 28 and 29). Three Hugoniot traces were obtained for the 90-degree shingle-angle material (Figures 30 through 32), although SRI was only contracted to get two. One of these three traces (shot 13606, Figure 31) is from a shot during which the flyer had marginally acceptable tilt. SRI elected to get the additional data at a higher impact pressure rather than repeat the marginally acceptable shot.

The Hugoniot shots were designed to produce impact pressures of about 5, 10, and (for the 90-degree material) 20 Kbar, using the aluminum projectiles indicated in Table IX. The impact conditions estimated by SRI to have been established behind the wave front (the Hugoniot State) are also listed in the table.

One pulse attenuation shot with a Mylar flyer plate was fired on each of the two orientations of quartz-phenolic. The flyer plate velocity was 0.28 mm/μsec in each case. The input stress at the Mylar-target interface was estimated by SRI to be 5.8 Kbar for the 90-degree shingle-angle material (Figure 33) and 5.3 Kbar for the 0-degree shingle-angle material (Figure 34).

As can be seen from the peak stress levels recorded at the target-quartz interface (Table IX), significant attenuation of the input stress level occurred during the passage of the shock wave through the quartz-phenolic.

Interpretation of the quartz-transducer traces and reduction of the gas-gun data will be considered in Section VII.

SECTION V
EXPLODING-FOIL TESTING

1. INTRODUCTION

This section describes the results of the plate-slap testing performed at the MDAC-WD exploding-foil facility. The plate-slap tests described in this Section and subsequent damage assessment described in Section VI, are part of the analysis cycle to determine the fracture threshold of the two-dimensional quartz-cloth-reinforced phenolic, zero-degree shingle-angle composites. The criterion expressing this threshold is derived from these data in Section VIII.

The specimens tested in this phase of the program were 1-1/4 by 1-1/4 by 1/4-inch thick, two-dimensional cloth-reinforced, zero-degree shingle-angle, quartz-phenolic composites. The specimens were impacted with 5-mil and 14.7-mil thick Mylar flyers. A detailed description of the test specimens is given in Section III. Specimens number 13 through 28 in Figure 12 were used for these tests.

2. PRETEST EXAMINATION

As previously indicated in Section III, all specimens were subjected to acoustic velocity measurements at selected frequencies, in the range 0.5 - 5.0 MHz. Photomicrographs and porosity and density measurements were made at selected locations of the flat plate and butter-bar configurations.

3. FRACTURE THRESHOLD TESTING AT THE MDAC-WD FACILITY

The purpose of the test program was to establish the incipient damage levels of a typical re-entry vehicle composite material subjected to a short-duration high-amplitude load environment. To this end, an exploding-foil apparatus was used to load the test specimens by plate-impact, and experimental data were obtained by high-speed frame and streak photography.

The following paragraphs contain a description of the MDAC-WD plate-slap facility, the instrumentation techniques, and the test results.

a. MDAC Exploding-Foil Facility

The basic circuit diagram of the MDAC-WD exploding foil apparatus is illustrated in Figure 35 with a foil connected across the capacitor bank. The switch is closed, and the capacitor bank is charged to the desired voltage (nominally 16 to 20 KeV). The capacitor bank consists of sixteen 12.5-mfd, 20-KeV capacitors. Each is connected to the common bus by a circular connector threaded on the capacitor terminal. A special tool enables the connectors to

be threaded on and off the bus, thus changing the bank configuration. At 20 KeV the combined energy of the capacitors is 40 Kilojoules. Charging current is provided by the high voltage power supplies. The power supplies used to charge the capacitor banks in the exploding-foil plate-slap facility are both rated at 1 KeV, and are current- and voltage-regulated. The current regulation feature allows a constant charging rate and provides short circuit protection. The voltage regulator allows the bank voltage to be preset to 1/2%. Both current and voltage regulation are obtained by controlling an SCR switching regulator (see Figure 36). When the capacitor bank is fully charged, the switch is opened to disconnect the power supply. The series circuit, which consists of capacitor bank foil and spark gap, is completed by an ionization of the air in the spark gap. Air ionization is initiated by a pulse from the trigger generator. A trigger electrode is situated between the capacitor bank electrodes. The trigger pulse is coupled to these electrodes through a step-up transformer. The breakdown of the spark gap initiates a discharge of the capacitor bank through the foil. The high amplitude current that flows in the foil causes the foil to explode.

The details of foil assembly design and fabrication may vary considerably and depend upon the nature of the work. Two types of foil assembly were used during this program, to achieve the desired flyer velocity spectrum (0.2 to 1.5 mm/μsec).

The first type, usually referred to as a single-plate assembly, is illustrated in Figure 37. When the foil explodes, a pressure pulse is generated that is substantially planar. The pressure pulse causes a Mylar projectile plate to tear out of the Mylar sheet and accelerate with very little tilt. After a free-run (about 0.60 inches for the present study) the projectile strikes the test specimen. The region between the projectile plate and the test specimen and the area completely surrounding the target and foil assembly were evacuated to a vacuum pressure of about 8×10^{-2} μHg before each shot to eliminate the complications of air cushion effects. Projectile plate velocities were varied by using different types of foil assembly and changing the voltage to which the capacitor bank was charged.

The other type of exploding-foil assembly that was used during this program is termed a double plate (Figure 38). The double-plate assembly is a combination of the single-plate flyer configuration and a moderator block in which a single-plate assembly is used to propel a flyer plate into the moderator material. The second flyer plate is greased onto the opposite surface of the moderator and is accelerated by momentum trapping over a free-run of 0.250 inches. The moderator material used in this study was Lucite.

Bank settings used to approximately achieve the desired impact velocities were determined by referring to calibration data for each of the specified foil assembly construction and firing conditions. The use of such calibration data permits one to obtain impact velocities within ±7% of those desired.

The target holder is comprised of a tool steel support (Figure 39), which applies a light compressive load to the sides of the target. The sides of the target are wrapped with one layer of a thin Teflon tape to prevent the target from binding in the holder upon impact.

The targets are caught after impact in a low-density (~2 lb/ft^3), open-cell commercial polystyrene foam. Open-cell construction is required to avoid the resistance incurred by impacting cells containing gas under atmospheric pressure. To prevent outgassing during evacuation and operation, the catcher is enclosed in a polethylene bag vented with a large valve. When the bell jar pressure is reduced to 1 μHg the valve is closed, sealing the catcher. Details of the catching apparatus are illustrated in Figures 40, 41, and 42.

A Beckman and Whittley Model 200 simultaneous streak and framing camera is used to record the motion of the flyer as it impacts the target. The camera is focused on the rear side of the flyer, which is backlighted with a 950 megalumen exploding foil light. The camera, with a 2 million frame-per-second capability, is operated at 800,000 frames per second, allowing use of a high-resolution positive/negative Polaroid film. Flyer planarity is evaluated from the framing pictures by comparing the orientation of the flyer boundary with the impacted target surface. Velocity measurements are not obtained from the framing pictures because the finite shutter speeds cause a blurring of the flyer image. A typical framing camera record of a Mylar flyer impacting a quartz-phenolic target is indicated in Figure 43. The flyer is moving from left to right in each frame. This blurred image precludes an accurate measurement of motion from one frame to the next. Consequently, the streak record is used to determine velocity. The technique consists of measuring the angle formed by the streak of the flyer and the horizontal streak formed by a stationary object in the field of view. With reference to Figure 44, which is a typical streak record velocity picture of a Mylar flyer impacting a quartz-phenolic target, in vacuum, the velocity is proportional to the tangent of this angle. Specifically it is related as

$$V = \frac{R}{M} \tan\theta \qquad (11)$$

where

R = the writing velocity on the film plane

M = the magnification factor between actual displacement and filmed displacement

θ = the angle formed by the flyer streak and a fixed object streak on the film

Figure 45 is a picture of the MDAC-WD plate-slap facility.

b. Test Results

All specimens tested were impacted with Mylar projectile plates approximately 1-inch square. The two projectile plate thicknesses used were nominally 5 mil and 14.7 mil. A total of 16 quartz-phenolic specimens were tested.

These 16 shots were used to establish the two points on the visual and microscopic thresholds of delamination of the zero-degree shingle-angle material. This provided sufficient data to design the proof-test configuration. Post-test acoustic velocity tests and rigorous microscopic examinations of the visually undamaged specimens indicated that these specimens were either actually damaged internally, or else had their microstructure altered in some way significant enough to change their acoustic-transmission properties.

As previously described, the MDAC-WD exploding-foil plate-slap facility uses a combined frame and streak camera record on every shot to determine the flyer velocity and planarity. However, four shots with Mylar impacting 32-mil 6061-T6 aluminum were performed, to establish an estimate of the degree of repeatability of projectile velocity. These four shots were performed as part of an exploding-foil velocity-calibration program currently in progress at MDAC-WD (Reference 14), and the data were provided to the contract at no additional cost.

Table X is a summary of the test and repeatability shots performed. Indicated in this table are the distance the flyer traverses prior to impacting the target (free-run), the flyer velocity, pre-test description of the specimen from the NDT characterization, and the post-test description of the specimens. The post-test microscopic examinations and results will be discussed in detail in Section VI.

Of the 16 test shots performed on quartz-phenolic, 5 did not yield a frame and/or streak record for the determination of the flyer velocity and simultaneity. To estimate a value for the projectile velocity on these shots and an indication of the flyer planarity, each of these shots was repeated with the same set-up conditions, but the target material used was 32-mil 6061-T6 aluminum. In addition, two shots on the quartz-phenolic were duplicated at each of two velocities.

Table X indicates that the difference in velocities between Shots No. 87 and No. 17, both of which were at identical conditions, is less than 5%. For Shots No. 18 and No. 91, the difference in flyer velocity at the same conditions is less than 7%; and for Shots No. 96 and 97, the difference is less than 7%.

The framing camera records of the shots on quartz-phenolic were examined, and each was reduced to a quantitative measure of simultaneity of impact. This was done by using an optical comparator to measure the position of the flyer relative to the target in the last framing picture prior to impact. The data indicate that the simultaneity of impact varied from 50 to 350 nanoseconds on all shots, over the flyer velocity range of 0.2 to 1.5 mm/μsec. The reader is referred to Reference 3 for a more complete discussion of reduction of framing camera records to a value of simultaneity of impact.

Table X. Summary of Photomicrographic Examination of Visually Undamaged Quartz-Phenolic Failure-Threshold Specimens

Shot or Specimen Number	Thickness mils	Flyer Characteristics			Material	Target Material	Comments	Post-test Evaluation	
		Velocity mm/μsec	Launch Assembly	Free Run mm				Macroscopic Inspection	Photomicrographs
13	5	0.966[1]	Single Plate	17	Mylar	Quartz Phenolic	No frame or streak record	No discernible damage ~4X	Discontinuities ~10X
87	5	0.955	Single Plate	17	Mylar	Aluminum	Same setup conditions as 13	(2)	(2)
17	5	0.966	Single Plate	17	Mylar	Quartz Phenolic	Same setup conditions as 13 & 87	No discernible damage ~4X	Discontinuities ~10X
18	5	1.11	Single Plate	17	Mylar	Quartz Phenolic		~30mm rear surface detached, spalled portion exhibits multiple delamination ~4X	(2)
89	5	1.18	Single Plate	17	Mylar	Aluminum	Same setup conditions as 18	(2)	(2)
15	5	0.98	Single Plate	17	Mylar	Quartz Phenolic		No discernible damage on back and front face, edge delamination ~4X	Two major discontinuities across width or specimen
19	5	0.98[1]	Single Plate	17	Mylar	Quartz Phenolic	No frame or streak record	No discernible damage on back, front, or edge of specimen ~4X	Discontinuities ~10X
25	5	0.77	Single Plate	17	Mylar	Quartz Phenolic		No discernible damage	No discernible damage ~10X
23	5	0.66	Single Plate	17	Mylar	Quartz Phenolic		No discernible damage	No discernible damage ~10X
24	5	0.61	Single Plate	17	Mylar	Quartz Phenolic		No discernible damage	No discernible damage ~10X
96	14.7	0.66	Moderator	6	Mylar	Aluminum	Calibration	(2)	(2)
97	14.7	0.62	Moderator	6	Mylar	Aluminum	Same setup conditions as 96	(2)	(2)
14	14.7	0.75	Moderator	6	Mylar	Quartz Phenolic	Spalled backface	~30mm rear surface detached, spalled portion exhibits multiple delaminations ~4X	(2)
21	14.7	0.41	Moderator	6	Mylar	Quartz Phenolic		No discernible damage ~4X	No discernible damage ~10X
20	14.7	0.38	Moderator	6	Mylar	Quartz Phenolic		No discernible damage ~4X	No discernible damage ~10X
26	14.7	0.59	Moderator	6	Mylar	Quartz Phenolic		Slight bulge in center of rear surface	Major discontinuity rear backface ~10X
22	14.7	0.57[1]	Moderator	6	Mylar	Quartz Phenolic	No frame or streak record. Velocity determined on the basis of Shot 26	Slight bulge in center of rear surface	Major discontinuity near backface ~10X
28	14.7		Moderator	6	Mylar	Quartz Phenolic	Arc over, shot data not applicable	No discernible damage	No discernible damage ~10X
27	14.7	0.39	Moderator	6	Mylar	Quartz Phenolic		No discernible damage	Multiple planes of delamination ~10X
16	14.7		Moderator	6	Mylar	Quartz Phenolic	Flyer disintegrated	No discernible damage	No discernible damage ~10X

[1] No frame or streak record.
[2] Not applicable.

BLANK PAGE

SECTION VI

EXAMINATION OF EXPLODING-FOIL TEST SPECIMENS

Following the impulsive-load failure testing in the exploding-foil facility at MDAC-WD described in the preceding section, the specimens were examined visually at the macroscopic level and photographed at about 4X magnification. They were subsequently sectioned and polished for microscopic examinations. Preliminary photomicrographs of some specimens were taken at 10X magnification. Subsequent microscopic examinations were conducted at magnifications up to 120X. These examinations were made in order to determine the visual and microscopic delamination thresholds of the specimens. These determinations are described in this section.

All of the visually undamaged specimens for which data were obtained were sectioned with a diamond-coated circular saw, polished, and then examined under a microscope. Photomicrographs were taken at selected locations of various quartz-phenolic specimens. The microscopic examinations were conducted to ascertain if the internal structure of the material was altered under the impulsive loading conditions of the plate-slap test. To qualitatively determine the degree of damage produced, several unimpacted specimens were also sectioned and photomicrographed (Figures 18 to 26). Table XI is a summary of the results of the post-test microscopic examinations of the visually undamaged specimens. Table X presented the visual observations. These visual and microscopic data are reduced to basic failure criteria for the zero-degree shingle-angle material, in Section VIII.

1. MACROSCOPIC AND PRELIMINARY MICROSCOPIC EXAMINATION OF SPECIMENS

For the 5- and 14.7-mil Mylar impactors, the visual damage thresholds are estimated to be about 0.98 mm/ μsec and 0.57 mm/ μsec, respectively. These values were deduced from the visual macroscopic post-test examination, macroscopic photographs, and preliminary post-test microscopy and photomicrographs. Photographs representative of the visual damage produced by impacting 5- and 14.7-mil Mylar against 0° shingle-angle quartz-phenolic, are illustrated in Figures 46 to 49. Figure 50 is an unpolished section through a specimen, exhibiting that delaminations discernable at an edge or as bulges of the back face do exist throughout the specimen, as was found in all cases. Each of the macroscopic photograph records of the specimen frontfaces (~4X) indicate where the flyer struck, and in some cases there is a slight impression. Figures 51 and 52 are representative of the condition of the target impact area. None of the specimens shows any other macroscopic evidence of frontface damage. The rear surfaces of specimens 13, 17, 19, 20, and 21 do not exhibit any macroscopic stress wave damage. Figure 53 is representative of the

Table XI. Summary of Post-Test Microscopic Examination of Quartz Phenolic Failure-Threshold Specimens (page 1 of 3)

Specimen No.	Flyer Thickness-mils	Flyer Velocity-mm/μsec	Magnification	Observation
51, 44, 46, 63	-	-	25, 75, 100X	Control - No evidence of resin and/or fiber cracking, or fiber/matrix delamination.
24	5	0.61	100X	Discontinuous cracks at fiber matrix interface in middle of specimen near backface.
23	5	0.66	100X	Continuous cracks through fiber bundles and at fiber matrix interface in middle of specimen near backface. Slight micro-cracking perpendicular to plane of reinforcement.
25	5	0.77	65X	Continuous cracks through fiber bundles and fiber matrix interface near backface. Micro-cracking perpendicular to plane of reinforcement, primarily in matrix.
13	5	0.966	30X	Distinct planes of delamination near backface extending over middle portion of specimen. Slight micro-cracking perpendicular to plane of reinforcement.

Table XI (page 2 of 3)

Specimen No.	Flyer Thickness-mils	Flyer Velocity-mm/μsec	Magnification	Observation
17	5	0.966	30, 100X	Distinct delamination plane across middle portion of specimen near rear face. Slight micro-cracking perpendicular to plane of reinforcement.
15	5	0.980	30X	Distinct delamination plane across width of specimen near rear face. Some evidence of uncoalesced cracks.
19	5	0.980	30, 100X	Distinct delamination planes across width of specimen near rear face. Heavy micro-cracking in matrix extending from the front face to back-face of the specimen.
20	14.7	0.38	30, 100X	Slight micro-cracking through resin and fiber bundles over middle portion of specimen near backface. Several uncoalesced cracks parallel to plane of reinforcement running through fiber bundles and fiber matrix interface.
27	14.7	0.39	33, 50, 120X	Heavy micro-cracking through matrix and several fiber bundles over middle portion of specimen near backface. Distinct coalesced cracks running through fiber bundles and fiber matrix interface.

Table XI (page 3 of 3)

Specimen No.	Flyer Thickness-mils	Flyer Velocity-mm/μsec	Magnification	Observation
21	14.7	0.41	30, 100X	Several disconnected cracks running through matrix and fiber/matrix interface. Cracks tend to line up along a preferred plane parallel to direction of reinforcement. Slight micro-cracking in resin perpendicular to direction of reinforcement.
22	14.7	0.57	30X	Distinct delamination plane over middle portion of specimen near backface. Micro-cracking perpendicular to direction of reinforcement in matrix and through fiber bundles.
28	14.7	-	30X	Slight micro-cracking perpendicular to direction of reinforcement through resin.
26	14.7	0.59	30X	Distinct plane of delamination parallel to direction of reinforcement over middle portion of specimen near backface. Connected cracks run through fiber bundles and fiber/matrix interface and resin.

condition of the backface of the aforementioned specimens. Specimens 18, 15, 14, 26, and 22 (Figures 46 to 50 and 54) do show macroscopic damage of the rear surface and edges of the target.

A 5-mil Mylar flyer impacted specimen 15 at 0.98 mm/μsec and resulted in macroscopic cracking (Figures 46 and 47). At higher velocities, the damage sustained was more severe (Figure 48); and at all other lower velocities tested, the damage was not macroscopically discernable. Preliminary microscopic examination of specimens 13, 19, and 17 at approximately 10X indicated the presence of discontinuities (Figures 55 and 56 are representative).

A 14.7-mil Mylar flyer impacted specimens 26 and 22 at 0.57 and 0.59 mm/sec, respectively, and produced a slight bulge in the rear surface. At higher velocities, damage was more severe (Figure 49); and at all other lower velocities tested, the damage was not macroscopically detectable. Preliminary microscopic examination of specimens 14, 21, 20, 26, 22, and 28 at 10X revealed the existence of major discontinuities near the back faces of specimens 22 and 26 (Table XI, Figures 46 and 57). Macroscopic inspection of these two specimens had revealed the presence of a slight bulge only over the center portion of the rear surface of each specimen.

2. HIGH MAGNIFICATION MICROSCOPIC EXAMINATION OF SPECIMENS

Microscopic examination at magnifications of 10X was employed on specimens 13, 14, 15, 17, 18, 19, 20, 21, 22, 26, and 28 as a preliminary technique to detect internal damage. Additional work at higher magnifications (30 to 120X) was conducted on these and the remaining specimens to further define the nonvisual failure modes of the zero-degree shingle-angle quartz-phenolic.

Post-test acoustic velocity measurements were made on the above-listed 11 specimens. Where velocities could be obtained, they were approximately one-third that of the velocity before plate-slap testing (Table XII). This decrease in sound velocity is evidence of an internal change in the specimen, even though there is little or no visual evidence of damage on the exterior surface. Preliminary microscopic examination of a section through the center of each of the 11 specimens in some cases revealed apparent delaminations, but not to the extent expected. The internal damage in the form of minute cracks in the resins or separations between the resin and the fiber reinforcement could conceivably have caused the high attenuation and reduction of acoustic velocities evident in the specimens. Microscopic examination at higher magnifications revealed these microcracks.

Following the examination of the first 11 specimens tested, the remaining 5 specimens (21, 23, 24, 25, and 27) were tested at lower velocities to determine 2 points on the microscopic delamination threshold. Specimens 23, 24, and 25 were impacted with a 5-mil Mylar flyer, whereas specimens 21 and 27 were impacted with a 14.7-mil Mylar flyer.

The velocities selected to achieve the microscopic delamination threshold were chosen in a trial-and-error fashion. The procedure was as follows: The flyer was propelled at a velocity arbitrarily chosen but lower than that of the flyers producing microscopic delamination during the series of 11 shots used to determine the 2 visual delamination values. The impacted target was subsequently sectioned, microscopically examined, and photomicrographed. If

Table XII. Sonic-Velocity Measurements Through 2D Quartz-Phenolic Specimens Before and After Plate-Slap Tests**

Specimen No.	Before Plate Slap Velocity (meters/sec)	After Plate Slap Velocity (meters/sec)
13	2589.0	*
15	2942.9	*
17	2719.3	*
19	3056.4	*
20	3056.4	1145.5
21	3001.0	1192.3
22	3095.8	1224.5
26	3131.1	*
28	3065.3	1141.2

*Velocity measurements could not be obtained due to the high attenuation (60 db) of the plate-slap specimens.
**Recording Frequency - 0.5 MHz

the examination revealed distinct planes of delamination at 30-120X, another shot was conducted at a lower velocity. If the micrograph revealed disconnected or noncoalesced microcracks parallel to the plane of reinforcement, then another shot was conducted at a slightly higher velocity until distinct planes of delamination could be observed at 30-120X. In this fashion, it was possible to bracket the microscopic delamination threshold using the additional 5 untested specimens and the previously tested 11 specimens.

Table XI is a summary of the observations that were recorded for each of the specimens sectioned and observed at magnification between 30 and 120X. Initially, a magnification range of 100-600X was utilized, but the higher magnifications tended to severely limit the resolution of the observation. To establish the validity of the observations recorded on Table XI, several control specimens were observed at these high magnifications. These control specimens were compared simultaneously to the impacted specimens to facilitate observation of perturbances in microstructure in the impacted specimens.

Figures 58 to 62 are representative photomicrographs of specimens 21-25 and 27 at a magnification of 30X-120X. Inspection of Figures 58 to 62 indicates that the microscopic threshold of delamination for the 5- and 14.7-mil

Mylar shots was approximately 0.60 and 0.39 mm/ sec, respectively, based on the arbitrary criterion of distinctly connected cracks parallel to the plane of reinforcement.

Figures 58 to 62 all show a pronounced evidence of microcracking perpendicular to the direction of reinforcement. These microcracks are usually very intense at the impact face and diminish in intensity and magnitude through the thickness of the specimen. In all cases, however, this crack density is most intense near the rear face and delaminated regions. In some cases, it is uniform throughout. These microcracks, which are not clearly evidenced in all the control specimens, may have resulted from damage to the specimens in the compressional mode of loading at impact. This would account for the orientation of the cracks perpendicular to the direction of reinforcement, and their decrease in intensity and magnitude from the impact face to the back face. On the other hand, because they often are most preponderant near the two faces of the specimens, the microcracks may have resulted from tensile stresses parallel to the faces of the specimens caused by late-time flexural motion of the plates. Such microcracks are seen in some of the control specimens (e.g., Figure 63), perhaps initially caused by thermal stresses during the cure and post-cure cycles. Because of this, it appears that the dynamic response mechanism causing them in the tested specimens is either causing the opening of existing cracks or nucleating such cracks at microscopically very small but similar cracks.

The density of the above-mentioned microcracks appears to increase monotonically with flyer velocity for each of the two flyer sizes.

The delamination-threshold data points identified in the above section (two visual and two microscopic) are used in Section VIII, with the constitutive model developed in Section VII, to determine a stress wave-propagation failure-criterion for the material in its zero-degree orientation.

BLANK PAGE

SECTION VII

DETERMINATION OF DYNAMIC STRESS-STRAIN CURVES FROM THE SRI GAS-GUN DATA

1. INTRODUCTION

The subcontract gas-gun testing at SRI to obtain constitutive data was discussed in Section IV and the data acquired presented there (Figures 28 to 34). After the SRI test data report (Reference 13) was received at MDAC-WD, the stress-time histories presented in the report for the two orientations of quartz-phenolic (0° and 90° shingle-angle) were reduced by MDAC-WD to a set of dynamic constitutive relations. These were assumed suitable for predicting subsequent wave propagation response in each direction tested, within the limits of applicability of the data. This section describes the theory used to reduce the data and the assumptions made in data reduction, and presents the reduced data. In Section VIII and IX, the constitutive relations developed in this section are applied in reduction of failure threshold data and prediction of the response of a proof-test configuration, respectively.

Although the material tested in this program is anisotropic, it is possible to overlook this fact in order to reduce these data for future use. This can be done by using the MDAC-WD versions of the PUFF codes (References 1 and 2) or other one-dimensional codes and/or techniques, because propagation has occurred along a material principal axis in each case (Reference 4 discusses this in more detail). The resulting physical parameters determined in each case would be those fitting a model established for an isotropic material. However, they need only be interpreted for the present as those values to use in the codes to reproduce the SRI data and subsequently to predict the results of 0° and 90° shingle-angle quartz-phenolic response to plate-impact for other cases of interest, within the range of applicability of the reduced data.

Data reduction was performed at MDAC-WD in an iterative fashion. The approach followed was somewhat similar to that indicated by Karnes (Reference 15) to have been used by Barker, Lundergan, and Herrmann (Reference 16), or that described by Oscarson and Graff (Reference 17). A similar trial-and-error approach was used in Reference 7 to get an engineering approximation to the constitutive properties of 90° shingle-angle carbon-phenolic.

The quartz-phenolic in each orientation was assumed to be a rate-independent elastic-plastic (work-hardening) material. It is recognized that using only two or three Hugoniot-type traces plus a single pulse-attenuation shot in each orientation does not provide enough data to firmly establish the parameters of such a model, or even its validity. However, the net dynamic stress-strain curve determined for monotonic loading under conditions of uniaxial-strain should be valid for subsequent determination of the response, caused by wave-propagation, of the rear surface material of a 0.25-inch plate of either material orientation.

The separate volumetric (hydrostatic) and deviatoric (work-hardening elastic-plastic) constitutive relations were subsequently estimated for each material

orientation from the acoustic velocity data and pulse-attenuation data, plus other data available in the literature (e.g., References 18 and 19) or obtained at MDAC-WD (Reference 12). These data adequately illustrate the effects of anisotropy of the quartz phenolic at the intermediate stress levels tested (10 Kbar is equivalent to about a 150,000 psi surface pressure loading). The effect of the obviously questionable validity or invalidity of the constitutive relations (and need for more data) in design use can be partially inferred from the relative success of the proof-testing phase of this program. However, it is the aspect of determining the deviatoric parts of each constitutive model, which in effect represents the determination of the dynamic unloading stress-strain curve (in uniaxial-strain) for the material, for which only representative quantities of plate-slap data have been obtained. This is, by intent, in accord with current plate-slap practices. By the same token, it should be recognized, for analogy, that unloading characteristics are not usually determined by investigators in even the simple, quasi-static, uniaxial-stress tension or compression tests conducted for most materials.

2. BASIC CONSIDERATIONS OF THE MECHANICS AND THERMODYNAMICS OF HIGH-AMPLITUDE STRESS-WAVE PROPAGATION

Reference 4 has pointed out the various material behavioral characteristics that must be accounted for in proper constitutive modeling of an anisotropic, heterogeneous, composite material, to be able to predict stress-wave propagation behavior or analyze wave-propagation data to acheive such constitutive models. References 20 through 23 present the basic mechanical and thermodynamical considerations also required, within the framework of continuum mechanics, to utilize such constitutive models. These references are all cited because they present the theory with varying degrees of sophistication from a mechanics viewpoint. In this subsection, we will review these basic relations of mechanics and thermodynamics which are pertinent to analysis of wave-propagation and reduction of plate-slap data. This is done for completeness in establishing the framework against which the technology as currently practiced must be measured. Thus, this subsection and portions of Section VIII supplement References 3 and 4 to provide a self-contained treatment of the fundamental theoretical and experimental aspects of plate-slap technology.

This subsection first presents the two sets of conservation relations appropriate respectively for continuously and discontinuously varying variables. These sets of relations form the basis for one-dimensional wave propagation analyses, but by themselves are each an incomplete set with which to solve problems. Each set is completed by introducing the constitutive relations for the material, plus adjunct phenomenological relations. These relations should be thermodynamically consistent, which introduces consideration of thermodynamic variables such as absolute temperatures and entropy. The difference between a thermodynamic equation of state and a general constitutive equation is then indicated. The constitutive models commonly used in wave propagation analyses are presented, and then their relation to shock-wave (Hugoniot) data is discussed.

a. The Conservation Relations

As indicated in the introductory paragraphs of this section, the quartz-phenolic study material has been assumed to exhibit only elastic-plastic behavior and has been modeled (for analysis purposes) as if it were a separate isotropic

material in each of its orientations (zero-degree and 90-degree shingle-angles). Furthermore, it has been assumed that the strains produced by the impact pressures are relatively small. This is easily corroborated by the results of the data reduction and appeared valid a priori because the impact pressures themselves are relatively low (20 Kbar ≈ 300,000 psi). This assumption permits easy use of the conservation equations written in Lagrangian coordinates. In addition, it is assumed that the body under consideration is a laterally semi-infinite plate, which may be taken to be in a state of only axial strain with null lateral strains during wave propagation through its thickness, which we call the "axial" direction. The following paragraphs present the basic equations of conservation of mass, momentum and energy. These are posed relative to a Lagrangian coordinate system and are presented in the simplified form which reflects the conditions that strains are small and that only unidirectional wave propagation in a laterally semi-infinite body is under consideration. (References 20 through 23 may be consulted for detailed derivations of the equations presented in these subsections). If the axial strain of any point in the body is designated as ϵ and lateral strains are null, it follows that, for small strains

$$\epsilon \equiv \epsilon(x, t) = \frac{\partial u}{\partial x} \tag{12}$$

where x is the generic Lagrangian coordinate of a point in the body and $u \equiv u(x, t)$ is the axial displacement at any time t of the point originally at x. All functions are considered independent of lateral coordinates because laterally uniform loading has been assumed. If $\rho_o(x)$ is the mass density of the body at all points having the axial coordinate x at time t=0, conservation of mass requires that the density $\rho(x, t)$ of the same mass element at time t is related to $\rho_o(x)$ as follows:

$$\rho(x, t) \; [1 + \epsilon(x, t)] = \rho_o(x) \tag{13}$$

The condensation of the material, $\mu(x, t)$, is related to density and strain as follows:

$$\mu = \frac{\rho}{\rho_o} - 1 = -\frac{\epsilon}{1 + \epsilon} \tag{14}$$

Since small strains have been assumed, equation (14) is approximated by the relation

$$\mu \doteq -\epsilon \tag{15}$$

It is seen that ϵ is positive in tension and μ is positive in compression.

The Lagrangian equations of conservation of momentum and energy can be written for this case of unidirectional small strain to yield

$$\frac{-\partial\sigma}{\partial x} + \rho_o F = \rho_o \frac{\partial^2 u}{\partial t^2} \tag{16}$$

$$\rho_o r - \sigma\frac{\partial\epsilon}{\partial t} - \frac{\partial q}{\partial x} = \rho_o \frac{\partial E}{\partial t} \tag{17}$$

In these equations, $F(x, t)$ is the body force per unit mass and $E(x, t)$ is the specific internal energy (energy density per unit mass), relative to the original body; $[-q(x, t)]$ is the axial heat flux per unit area into an element across a generic boundary $x=x$, while $\sigma(x, t)$ is the stress acting on this boundary, positive when compressive; r is the heat supply function per unit mass (e.g., the heat supply due to radiation).

Equations (12), (13), (16), and (17) suffice to define the conservation relations for the problem at hand if no discontinuities exist in the variables. If discontinuities exist across any surface in the body, it is necessary to write the "jump" conditions, which replace the above relationships, across the surface of discontinuity. Let the Lagrangian position of this surface be designated by $x = \lambda(t)$. The velocity of propagation of this surface through the material relative to the Lagrangian coordinates of the points will be called $U(t)$,

$$U = \frac{\partial\lambda}{\partial t} \tag{18}$$

Let the symbol Δf be used to designate the change in a function across this surface of discontinuity as it moves past a point $x = \lambda$. i.e.:

$$\Delta f = f\,(\text{AFTER}) - f\,(\text{BEFORE}) \tag{19}$$

The law of conservation of momentum then yields

$$\Delta\sigma = \rho_o U\Delta v \tag{20}$$

$v(x, t)$ is the velocity of each mass point,

$$v = \frac{\partial u}{\partial t} \tag{21}$$

Conservation of energy yields the relation

$$\Delta(\sigma v) + \Delta q = \rho_o U[\Delta(v^2/2) + \Delta E] \tag{22}$$

Conservation of mass yields an additional jump relation as an alternate form of Equation (13). This expresses the fact that due to the passage of a surface of discontinuity the mass of the element being observed does not change:

$$\Delta[\rho(1+\epsilon)] = 0 \tag{23}$$

Equations (12) and (21) combine to yield the following kinematic relation for continuous changes in variables:

$$\frac{\partial v}{\partial x} = \frac{\partial \epsilon}{\partial t} \tag{24}$$

As a counterpart during passage of a discontinuity, equation (13) is replaced by the kinematic jump condition

$$\Delta v = -U\Delta\epsilon \tag{25}$$

Equations (12) through (25) present the basic kinematic and conservation relations of mechanics and thermodynamics which are required to solve wave-propagation problems. However, by themselves they are incomplete. The subsequent sub-sections discuss the additional relations and principles which must be introduced to effect solutions.

b. Thermodynamics and the Constitutive Relations

To solve any problems using the relations stated above, additional relations are required. Among these are the constitutive equations of the material, which relate the mechanical variables (stresses and strains) to each other and to thermodynamic variables, such as the internal energy density. In addition, other thermodynamic variables describing the state of the material, such as the absolute temperature T (which is always ≥ 0) and specific entropy (entropy per unit mass) S, must be introduced. These are then related to the variables introduced in the above equations through the constitutive relations and other phenomenological relations (e. g., a law of heat conduction). This must be done so that the constitutive relations and adjunct phenomenological relations selected are consistent with the second law of thermodynamics. At the same time, wave-propagation phenomena and shock-wave data cannot be properly understood without considering these additional relations.

The second law of thermodynamics states that changes taking place within a system cannot destroy entropy: if the internal entropy increases due to a thermodynamic process, the process is called irreversible. If it does not change, the process is called reversible. This entropy production inequality takes the following form for the class of problems under consideration above:

$$\rho_o T \frac{\partial S}{\partial t} - \rho_o r + T \frac{\partial (q/T)}{\partial x} \geq 0 \tag{26}$$

From the above statement and equation (26), if desired, one can by definition consider the entropy to consist of two parts, that produced internally, S_i, and that added externally, S_e. Equation (26) states that $(\partial S_i/\partial t) \geq 0$ and, therefore, with $S = S_e + S_i$ it follows that the rate of external entropy addition is given by the relation

$$\rho_o T \frac{\partial S_e}{\partial t} = \rho_o r - T \frac{\partial (q/T)}{\partial x} \tag{27}$$

Equation (26) is used to restrict the forms of the various constitutive and phenomenological relations possible to be postulated for continua. For example, the following phenomenological relation between heat flux and temperature is the commonly known Fourier's law of heat conduction:

$$q = -k \frac{\partial T}{\partial x} \tag{28}$$

The requirement of positive rate of internal entropy production imposes the restriction that k, the thermal conductivity of the material, must be positive. This follows from equation (26) and the fact that if entropy changes occur only because heat is added to an element, the rate of change of total entropy is given by

$$\rho_o T \frac{\partial S}{\partial t} = \frac{-\partial q}{\partial x} + \rho_o r \tag{29}$$

At thermodynamic equilibrium, the internal energy density depends only upon the absolute temperature, T, and upon some aspects of the deformation measured by a set of N additional quantities called state deformation variables, which we designate by ϵ_α ($\alpha = 1, 2, 3, \ldots, N$). In addition, there can exist a set of M other deformation measures, d_β ($\beta = 1, 2, 3, \ldots, M$), which contribute effects to the energy balance during a thermodynamic process. These are called dissipative deformation variables. The net effect of changes of these variables is represented by the power term in the energy balance equation. That is, the negative of the power can be written

$$\sigma \frac{\partial \epsilon}{\partial t} = \sum_{\alpha=1}^{N} \sigma_\alpha \frac{\partial \epsilon_\alpha}{\partial t} + \sum_{\beta=1}^{M} s_\beta \frac{\partial d_\beta}{\partial t} \tag{30}$$

The multipliers σ_α and s_β in equation (30) are the generalized compressive forces corresponding to the deformation variables ϵ_α and d_β, respectively. The rates of change of the deformation variables are sometimes called generalized fluxes.

be considered to be equations of state, without errors being introduced into the analyses. However, this simplified thinking has to be recognized as being fundamentally in error. This fundamental lack of identification of dissipative deformation variables and separation of state functions from the other constitutive relations, as well as lack of understanding of the meaning of a thermodynamic equation of state, has lead to misnomers as well as mistakes. For example, identifying empirical fits to Hugoniot-state data as "The Hugoniot equation-of-state" is incorrect. More important, the poorly understood nomenclature has introduced confusion as well as errors into attempts to interpret data for attenuating shock-waves or attenuating and dispersing stress-wave pulses.

It is thus seen that the thermodynamic aspects of stress-wave processes must always be kept in mind while conducting wave-propagation analyses. This is important both during the establishment of constitutive models, and during the reduction of wave-propagation data to fit these models.

c. The Commonly Used Constitutive Relations

The previous subsections have presented the general mechanical and thermodynamic considerations pertinent to wave propagation analyses. In the following paragraphs, we present some specific constitutive relations. These are stated in the forms that they are commonly used in the computer codes employed in this study (References 1 and 2).

For the most part, high-amplitude stress-wave propagation analyses found in the literature have been based upon nonlinear elastic-plastic constitutive equations for isotropic materials. The axial stress σ has been considered to be composed of a mean pressure, p, and a stress deviator, s,

$$\sigma = p + s \tag{34}$$

The mean pressure is usually assumed to be a state function of the condensation, μ, and absolute temperature, T, chosen as state variables; $p = p(\mu, T)$. The stress deviator is usually considered to be given by the relations of ideal plasticity theory for a work-hardening isotropic material:

$$\frac{\partial s}{\partial t} = \frac{4}{3} G \frac{\partial \mu}{\partial t} \text{ if } |s| < \frac{2}{3} Y(\mu_p) \tag{35}$$

$$|s| = \frac{2}{3} Y(\mu_p) \text{ if } s \frac{\partial \mu_p}{\partial t} > 0 \tag{36}$$

In equations (35) and (36), G is the elastic shear modulus of the material and Y is the yield strength under conditions of uniaxial tension or compression. Y is considered to be positive and a work-hardening function of the plastic

strain measure, μ_p. Changes of this plastic strain measure are defined by the relation

$$\frac{\partial \mu_p}{\partial t} = \frac{1}{2G}\left[\frac{4}{3} G \frac{\partial \mu}{\partial t} - \frac{\partial s}{\partial t}\right] \tag{37}$$

If the material exhibits work-hardening and hysteresis without a significant Bauschinger effect, it is customary to consider Y to be a monotonic function of μ_p and define μ_p at any time t as follows:

$$\mu_p = \int_o^t \left|\frac{\partial \mu_p}{\partial t}\right| dt \tag{38}$$

The material is assumed to have not been strained plastically before time t = o.

It is noted that once yielding occurs, s cannot be expressed as a state function of μ, E, and μ_p. In the context of Section VI-1b, equation (30), μ_p is a dissipative deformation variable and s is a generalized force corresponding to this variable.

The forms of the expressions (state functions) usually used for the mean pressure p and the energy density E are those derived for fluids at high pressures (Reference 22). If the pressures are not extremely high these take the form

$$p(\mu, T) = p_o(\mu) + \rho\gamma(\mu)\, c_v T \tag{39}$$

$$E(\mu, T) = E_o(\mu) + c_v T \tag{40}$$

In the above relations, p_o and E_o are obviously the functional dependencies of p and E on the condensation at absolute zero (T=0). $\gamma(\mu)$ is called the Gruneisen coefficient, although it is a slowly varying function of condensation; c_v is the constant coefficient of heat capacity per unit mass (specific heat) at constant volume; ρ is related to μ by equation (14); and p_o and E_o are considered to be related by the following equation, which results from applying equation (33) to equations (39) and (40) at T=0 (for a fluid):

$$p_o = -\frac{dE_o}{dV} \tag{41}$$

where $V = 1/\rho$. For small strains (condensations), the product $\rho\gamma$ is essentially constant for a given material:

$$\rho\gamma(\mu) \doteq \rho_o \Gamma \tag{42}$$

where Γ is a constant.

Equation (39) can be combined into the form relating pressure directly to internal energy which is often used in computer codes like the PUFF code (References 1 and 2):

$$p(\mu, E) = p_o(\mu) + \rho\gamma(\mu)\left[E - E_o(\mu)\right] \tag{43}$$

It is seen that the mean pressure term of equation (34), p, is usually explicitly shown to be related to temperature or energy by equations (39) and (43), respectively, whereas the commonly used relations for the deviator term, s, do not offer any explicit forms for the dependence of the yield strength, Y, on T or E. Of course, empirical functional forms are available in the literature, but most developers and users of one-dimensional wave propagation codes do not even consider that the yield function is implicitly dependent upon temperature or energy, as well as on plastic strain. Equations (39) through (41) are thermodynamically consistent for fluids, and some attempts have been made to ensure the overall thermodynamic consistency of theories for solids (e.g., see References 20 and 21). The development of explicit dependencies of the various state functions on the state variables, based on fundamental atomic models, also has been attempted when other than fluid behavior has been considered, but those forms are not commonly utilized with wave propagation codes. Eyring's theory of absolute reaction rates for viscosity, plasticity, and diffusion (Reference 68) is an example of such models.

d. Shock Waves Produced by Plate Impacts

The above subsection introduces the commonly used form of the equation of state defining the mean pressure, p, as a state function in terms of the state variables μ and E. This relation, equation (43), is usually called the Mie-Grueneisen equation-of-state. The following paragraphs describe how data are obtained to develop explicit empirical forms for the generic functions p_o and E_o introduced in this equation.

High-speed impact of thick flyer plates on thick targets produces high-amplitude stress-wave fronts in the targets. If the amplitude is not extremely high, the front can be dispersive; it spreads out spatially as the wave propagates through the plate. On the other hand, if the peak stress is high enough, portions of the wave-front coalesce and propagate as shock-waves; there is a jump in variables across a moving surface of discontinuity, the shock-wave front. Whether the wave exhibits either dispersion or "shocking-up" of a front depends upon the peak stress amplitude and the constitutive relations of the material. This is discussed in detail in Reference 4.

The formation of shock-fronts takes a finite time and is accompanied by various rate-effects which alter the wave profile and change shock amplitudes (magnitudes of the jumps) as the shock-wave front propagates. For some materials, these rate-effects persist during the propagation, no matter how thick the target is, and no steady-state conditions are reached. In that case

the rate-effects must be accounted for in the constitutive relations of the material and analysis of the wave propagation. Usually, it is assumed that the rate-effects cease shortly after the wave is developed and steady-state conditions prevail thereafter.

The jump relations, equations (20), (22), (23), and (25), are the basic equations of the Rankine-Hugoniot theory of shocks in solids. It is assumed that steady-state conditions prevail, so that during the wave propagation the particles ahead of the shock-front are described by one set of state variables, constituting a specific state point, and the particles behind the front are at a second state point, independent of the spatial position of the front. The shocking of a mass particle is a thermodynamic process. It is assumed that particles pass through this process without any jump in heat flux. Thus, Δq is null in equation (22). If the subscript A is used on variables to denote their values Ahead of the shock-front and the subscript B to denote their values Behind the front, the jump equations can be combined to the following form:

$$(\sigma_B - \sigma_A) = \rho_o U(v_B - v_A) \tag{44}$$

$$(E_B - E_A) = \tfrac{1}{2}(\sigma_B + \sigma_A)(v_B - v_A)/(\rho_o U) \tag{45}$$

$$(\epsilon_B - \epsilon_A) = -(v_B - v_A)/U \tag{46}$$

$$\rho_B(1 + \epsilon_B) = \rho_A(1 + \epsilon_A) = \rho_o \tag{47}$$

The second relation in equation (47) is a restatement of equation (13). Similarly, for completeness, equation (14) gives the condensations ahead and behind the front in terms of the strains:

$$\mu_B = -\frac{\epsilon_B}{1 + \epsilon_B}, \quad \mu_A = -\frac{\epsilon_A}{1 + \epsilon_A} \tag{48}$$

It is seen that if the state is known ahead of the front, then conditions behind the front can be calculated when two additional relations or conditions are added to equations (44) to (47). One of these is a set of constitutive relations, such as in equations (34) to (43). The other conditions are the plate impact conditions (forcing function) producing the shock. Of course, for a wave profile exhibiting multiple shock-jumps, it is necessary to reapply equations (44) to (47) plus the constitutive relations across every jump, as well as to introduce the forcing conditions.

The Rankine-Hugoniot relations can be used with experimental data to construct the constitutive relations of the material. For example, if the shock velocity, U, and the particle velocity behind the shock, v_B, are measured experimentally and state conditions are known ahead of the shock, then equations (44) to (48) permit calculation of the stress, internal energy, strain, density, and condensation behind the shock. If the shock stress amplitudes are low enough so that no plastic yielding occurs in the material, then the constitutive relations discussed in the previous section can be written simply as

$$\sigma(\mu, E) = \frac{4}{3} G\mu + p_o(\mu) + \rho\gamma(\mu)\left[E - E_o(\mu)\right] \tag{49}$$

Assume the material is in an undisturbed state ahead of this shock-jump. Equation (49) must apply behind the jump. Instead of the subscript B, the subscript H is introduced for the calculated (or measured) quantities resulting from use of the Rankine-Hugoniot relations with these test data, which we call Hugoniot-type data. These data can be obtained for all values of μ up to the yield point (for this example) and the functions $\sigma_H(\mu)$ and $E_H(\mu)$ resulting from this shock-process data related using equation (49)

$$\sigma_H(\mu) \equiv \sigma_H\left[\mu, E_H(\mu)\right] = \frac{4}{3} G\mu + p_o(\mu) + p\gamma(\mu)\left[E_H(\mu) - E_o(\mu)\right] \tag{50}$$

Subtracting equation (50) from equation (49) gives the following relation for the stress states where yielding has not occurred:

$$\sigma(\mu, E) = \sigma_H(\mu) + \rho\gamma(\mu)\left[E - E_H(\mu)\right] \tag{51}$$

Thus, the Hugoniot states, represented by $\sigma_H(\mu)$ and $E_H(\mu)$, are used as reference states for the constitutive relation. Equation (51) can now be separated into volumetric and deviatoric components by subtracting out the deviator $s = (4/3)G\mu$. Note that, when this is done, the shear modulus G is implicitly assumed to be independent of the internal energy E. The resulting relation for p prior to yielding is

$$p(\mu, E) = \sigma_H(\mu) - \frac{4}{3} G\mu + \rho\gamma(\mu)\left[E - E_H(\mu)\right] \tag{52}$$

Suppose now it is assumed that the shock stress-amplitude is high enough to produce yielding. A two-fronted wave structure can result if a distinct yield point exists. If no distinct yield point exists, it is possible that a dispersive profile is produced, followed by a shock-jump. It is also possible

that the wave amplitude is high enough so that only a single step wave-front (shock-jump) is exhibited. All these possibilities can be considered and interpreted, using the jump-relations and constitutive model. The last case mentioned is the easiest to investigate. For monotonic loading, the yield stress $Y(\mu_p)$ can be considered a function of μ, for convenience, as a consequence of equations (36) and (37). However, for this monotonic shock loading producing a step wave-front it is also more convenient to consider the deviator s itself as a measure of plasticity. The relation analogous to Equation (52) for this problem is then achieved by repeating the above derivation, but with $s(\mu)$ replacing $(4/3)G\mu$, leading to

$$p(\mu, E) = \sigma_H(\mu) - s(\mu) + \rho\gamma(\mu)\left[E - E_H(\mu)\right] \tag{53}$$

The example with no yielding, leading to equation (52), is a subcase of equation (53). These results also infer that the yield function (or the stress deviator) is independent of E and is somehow obtained from other data.

Hugoniot test data can be used with waves which exhibit multiple jumps, as long as enough data are measured in each test. If two jumps exist, let the faster shock be designated with the index 1 and the second by the index 2. To determine conditions behind the first jump, it is again necessary to experimentally measure two variables behind this jump; e. g., U_1 and v_{B1}. These are measured ahead of the second jump. Equations (44) to (48) then permit calculation of the remaining state conditions behind the first jump, which becomes the conditions ahead of the second jump. If U_2 and v_{B2} are measured behind the second jump, these data plus the conditions calculated behind the first jump provide enough information to calculate the state conditions behind the second jump. The data (from either or both jumps) can then be used as reference state data to develop the constitutive relation for $p(\mu, E)$, in the same manner described previously. This again leads to equation (53) as the resulting relation.

The above procedure can be extended to more than two jumps. It is only necessary to experimentally measure two variables behind each jump and use equations (44) to (48) to calculate the remaining state conditions, which become the conditions ahead of the next jump. It should then be recognized easily that the number of jumps can be great and the magnitude of each jump can be quite small, (even infinitesimal) and equations (44) to (48) still apply. Thus, they apply in the limit to a continuously varying wave profile, such as a dispersive wave front, as long as each incremental jump propagates with its own steady-state velocity, U. This is precisely the assumption made in the von Karman rate-independent plastic-wave propagation model (Reference 26). For the incremental jumps, designate the difference of the value of any function, f, behind the front less the value ahead of the front as df. Equations (44) to (46) then may be written

$$d\sigma = \rho_o U dv \tag{54}$$

$$dE = \frac{1}{2}\sigma\, dv \tag{55}$$

$$d\epsilon = -(dv)/U \tag{56}$$

Equations (47) and (48) are most conveniently retained in the forms in which they are presented, which are given generically by equations (13) and (14). Equations (54) and (56) can be combined to yield the classical result

$$\frac{d\sigma}{d\epsilon} = -\rho_o U^2 \tag{57}$$

where the minus sign reflects the fact that σ is positive in compression and ϵ is positive in tension.

When the wave-front profile is considered dispersive and can be analyzed by equations (54) to (56), it is necessary to measure two variables continuously as functions of time and compute the remainder from these, using equations (54) to (56) and then equations (13) and (14). If the dispersive front is then followed by a jump in the wave-front profile, the conditions at the end of the continuously varying portion of the wave profile become the conditions ahead of the jump. Equations (44) to (48) are then used to determine the state behind the front, still requiring that two variables are measured behind the front. These data from continuous or partially continuous profiles then again can be identified as reference state data for the constitutive relation for $p(\mu, E)$, and equation (53) again applies.

3. DETERMINATION OF THE CONSTITUTIVE RELATIONS FROM THE GAS-GUN DATA

a. Determination of Hugoniot States by SRI

Hugoniot states were calculated graphically by SRI (Reference 13) by an impedance match technique, using the data presented in Section IV. This technique is based upon the boundary condition in plane flow that requires continuity of normal stress and particle velocity across the interface between the two media. In an experiment in which a projectile of known Hugoniot is impacted into an unknown target, measurements of the projectile velocity and the shock velocity in the target suffice to compute a Hugoniot point for the target. The technique is shown graphically in Figure 64. The results of the SRI analysis are shown in Table IX and Figure 65. The data show that the 90-degree shingle-angle quartz-phenolic is a higher shock impedance material below 25 kbar than the phenolic with the 0-degree shingle-angle orientation.

An underlying assumption of the analysis is that the shock-wave profile is in a steady state. Measuring the stress-time profiles through different

thicknesses of quartz-phenolic would resolve the question as to whether the shock wave in quartz-phenolic at these stress levels is a steady-state wave. However, such measurement was not possible under this study.

It is also assumed that the shock wave is plane with one-dimensional particle flow. However, in the case of the quartz-phenolic the wave may be slightly dimpled or corrugated over a dimension the width of the quartz-cloth laminae.

The projectile Hugoniot curve for 6061-T6 aluminum was obtained by SRI from data of Lundergan and Herrmann (Reference 27). The Hugoniot curve for 2024-T4 aluminum was obtained by SRI from the data of Fowles (Reference 28). The Mylar Hugoniot was calculated from a Mie-Gruneisen equation of state of the form (Reference 29).

$$\sigma = a\mu + b\mu^2 + \Gamma\rho_o E; \qquad \sigma \leq 16 \text{ kbar} \tag{58}$$

where

$a = 6.150 \times 10^{10}$ dynes/cm^2

$b = 3.657 \times 10^{10}$ dynes/cm^2

$\Gamma = 1.0$

$\rho_o = 1.39$ g/cm^3

and Equation (42) is assumed.

b. Reduction of the Hugoniot-type Gas-Gun Data at MDAC-WD

The gas-gun test data previously presented in Section IV (both Hugoniot and pulse attenuation) were reduced at MDAC-WD to constitutive relations for the material in both its orientations. In each case, a separate material was assumed and modeled as if it were isotropic. The theory presented in Section VII-1 was utilized. The PUFF code (References 1 and 2) was used in reducing the data from the pulse attenuation shots.

The Hugoniot data were reduced at MDAC-WD assuming that the Hugoniots of the aluminum projectiles used were bilinear. This assumption was based on the data presented in References 27 and 28. Continuity of stress and velocity were assumed as the boundary conditions and at first the only use made of the SRI quartz traces was to determine the arrival times of the waves. This was the same way that SRI used the traces. SRI assumed that a single step-wave (shock jump) was represented by the traces, and reduced the data accordingly. They used the arrival times of the stress at half the peak amplitude (amplitude of the first plateaus in Figures 28 to 32) to calculate the velocity of this shock. MDAC-WD also made this assumption

initially, but considered various different estimates of the arrival time of this shock. These were (1) the first arrival of the precursor seen in the traces (the "foot" seen in Figures 28 to 32), (2) the projection of the straight line portion of these traces to zero stress (removing the foot), and (3) an estimate of arrival time of the main wave in each trace.

These Hugoniot data are shown plotted as wave velocity versus particle velocity in Figure 66. Following the initial data reduction procedure, MDAC-WD reduced the data using a two-jump model, estimating the velocity and amplitude of the first wave based on the foot in each of Figures 28 to 32. This procedure did not significantly change the particle velocities and other Hugoniot variables calculated for the main wave from those based on the single-wave assumption. This was because the amplitude of the precursor wave chosen was relatively small (< 1 Kbar), based on examining the feet of the waves in Figures 28 to 32.

If a stress wave in any target material reaches the interface of that material with a quartz transducer, the interface stress differs from that in the incident wave. If the waves travel with constant propagation velocity in each material independent of stress amplitude, the ratio of the interface stress amplitude (and the stress wave excited in the quartz by this interface pressure) to the stress in the target material is a constant. (See Reference 4 for a discussion of this for elastic waves). This ratio is determined by requiring continuity of stress and particle velocity at the interface of the two materials. If the wave excited in the quartz is elastic, it will travel with constant velocity for all stress amplitudes < 25 Kbar. If a shock jump is propagating in the target material, the interaction at the interface can produce a second jump propagating back into the target material as a "reflected" shock wave. The ratio of the stress at the interface to the incident stress can be calculated easily if the velocity of the reflected wave is known, calculated, or assumed. It is common to assume that the reflected jump propagates with the velocity of the incident jump.

If subscripts Q and T are used for variables in the Quartz transducer and Target material, respectively, the relation between a jump in incident stress in the target, $\Delta\sigma_T$, and the jump in stress transmitted to the quartz transducer, $\Delta\sigma_Q$, for the cases described above (for elastic waves existing in the quartz) is

$$\Delta\sigma_T = \left[1 + \frac{\rho_{oT} U_T}{\rho_{oQ} U_Q}\right] \frac{\Delta\sigma_Q}{2} \qquad (59)$$

If a dispersive wave profile is incident on the quartz, the relation of incident to transmitted stresses can be calculated easily if it is assumed that (1) each increment of incident stress propagates at its own velocity, as given by equation (57); (2) each incremental jump in the reflected wave produced by the interaction at the interface propagates back into the target at a velocity essentially the same as the velocity of the incident increment; and (3) the reflected wave does not significantly alter the incident wave profile by interactions of the two waves as they "pass-through" each other before the

incident wave reaches the quartz. With these assumptions, each incident increment is related to the transmitted increment by a relation similar to equation (58). If time is introduced as a parameter, then $\sigma_Q(t)$ and $U_T(t)$ are measured functions of time and the time history of $\sigma_T(t)$ is

$$\sigma_T(t) = \int_o^{t1} \frac{2}{2} \left[1 + \frac{\rho_{oT} U_T(t)}{\rho_{oQ} U_Q} \right] \frac{d\sigma_Q(t)}{dt} \, dt \tag{60}$$

Equation (57) then permits calculation of the strain in the target, $\epsilon_T(t)$, corresponding to the stress $\sigma_T(t)$,

$$\epsilon_T(t) = -\int_o^t \left[\frac{1}{2\rho_{oT} U_T(t)^2} \right] \left[1 + \frac{\rho_{oT} U_T(t)}{\rho_{oQ} U_Q} \right] \frac{d\sigma_Q(t)}{dt} \, dt \tag{61}$$

The traces shown in Figures 28 to 32 were reduced to dynamic stress-strain curves using these relations [equations (60) and (61)]. The results are shown in Figures 67 to 71. In only one case was this data reduction process continued beyond the first crest in the trace. For the trace shown in Figure 29, the data reduction was carried out for the entire transducer reading time. The noise in the trace beyond the crest was smoothed out for purposes of integration. The result is seen in Figure 68.

c. Analysis of the Reduced Hugoniot Data

The Hugoniot data traces received from SRI exhibit various anomalies compared to elastic-plastic wave or shock-wave traces usually displayed for rate-independent metals. The most significant anomaly is that all the high-stress traces (Figures 29, 31, and 32) crest at stress amplitudes lower than predicted by the Rankine-Hugoniot jump relations by using the impact conditions and the shock velocity calculated from the arrival-time measurements from each trace. In addition, the ramping in each of these three traces after the plateaus at the crests is extreme and unusual. The precursor "foot" prior to the main wave in every trace is also subject to question.

The first two characteristics mentioned above have been observed by others conducting similar gas-gun testing of quartz-phenolics (Reference 30). At first glance, these three characteristics suggest that the material is rate-dependent. No gas-gun tests have been conducted to show conclusively that the material is not significantly rate-dependent. However, it is not expected that the material will exhibit significant rate-dependence if tested further. This conclusion is reached in part because the data obtained at MDAC-WD and elsewhere for similar quartz-phenolics at low and intermediate strain rates do not exhibit significant rate-dependence (References 12, 31-34). Furthermore, other investigators conducting gas-gun testing of quartz phenolics instrumented with quartz transducers have obtained consistent results, in zero-, 20- and 90-degree shingle-angle lay ups,

considering both shock velocity and stress at the crest of each trace (References 34 and 35). Moreover, other gas-gun tests of a 90-degree shingle-angle quartz-phenolic identical to the material studies under this program have been conducted by EG&G, inc., for MDAC-WD. Instead of using shunted transducers, which were employed by SRI, EG&G used the new unshunted wrap-around version, described in Reference 36. The test results agreed with SRI data, as far as wave arrival and shape prior to the crest are concerned. However, no premature cresting or subsequent ramping occurred, and the stress data were consistent with shock velocity data (Reference 37).

Considering these data discussed above, the conclusion is that the anomalies are not characteristics of rate-dependence. The premature cresting and subsequent ramping in three of the traces are caused by a breakdown of the shunted quartz-transducers (References 37 and 38), and does not occur for the wrap-around version of quartz-transducer (Reference 37).* The foot seen in all the traces must be explained by some mechanism other than rate-dependence. Its amplitude is too large and duration too long to attribute to a combination of nonsimultaneity of impact, air left in the gas-gun barrel (15 μHg is far from a perfect vacuum) and compressed by the projectile, and instrument lag. The explanation seems to be that this foot is characteristic of heterogeneous media and represents a slight geometric-dispersion effect (e.g., see Reference 4).

Figures 67 through 71, which are the dynamic stress-strain curves constructed from the Hugoniot data traces by application of equations (60) and (61), all have concave downward curvature. (The region above the crest in Figure 68 is not considered.) This would be expected for the dispersive traces obtained (Figures 30 through 34). However, in all but the two lowest velocity cases, the curves are very close to being bilinear. Even for the two lowest velocity shots, a bilinear approximation would not be far from the curves shown. Considering the assumptions used to derive equations (60) and (61), it was concluded that it was sufficient to use the constitutive model and shock data reduction techniques presented in Sections VII-1c and VII-1d, assuming that the traces 28 to 32 each represented a two-step wave structure: a shock-front with an elastic precursor. In this sense, Figures 67 through 71 can not be thought of as dynamic stress-strain curves, but instead define points on the elastic and Rayleigh lines of each wave, e.g., points on the two fronts.

d. Reduction and Analysis of the Pulse Attenuation Data

The pulse attenuation traces were used in combination with the Hugoniot traces discussed in Section V-2d to construct a constitutive model for each material. The procedure followed was to adjust the functional representations of p and s available in the PUFF code to be consistent with the Hugoniot

*At first, the cresting and ramping were thought to be some type of plastic dispersion effect, if they weren't rate effects. However, the statements of References 37 and 38, plus the unusual constitutive relations otherwise required, cause us to also reject that these anomalies are due to some unusual work-hardening plastic behavior.

state points and to match the pulse attenuation profile as well as possible. The model used incorporates the Mie-Gruneisen equation-of-state for p in the form

$$p = \left(C_\mu + D_\mu^2 + S_\mu^3 \right)\left(1 - \frac{\Gamma\mu}{2}\right) + \rho_o \Gamma E \tag{62}$$

where C, D, and S are empirical constants used to fit equation (62) to Hugoniot data. The deviator is linear when work-hardening plasticity is exhibited, and equations (35) and (36) apply. Thus, Y of equation (36) becomes in the specific instance

$$Y(\mu_p) = Y_o + C_1 \mu_y \tag{63}$$

where μ_y is a measure of plastic straining, used instead of μ_p,

$$\mu_y = \frac{3}{2} \int_y \left| d\mu \right| \tag{64}$$

The path of integration, y in equation (64), extends over the increments of μ when yielding is occurring.

It is seen that the linear work-hardening plasticity model chosen is also an isotropic work-hardening model; the yield surface expands uniformly whether deviatoric tension or compression is acting. This model exhibits hysteresis but not a Bauschinger effect. For example, loading such that the material experiences plastic yielding, with the deviatoric stress, s, first being compressive, and then unloading so that the deviatoric stress reverses its sense (i. e., goes tensile), produces a hysterisis loop in the plot of total stress, σ, versus condensation, μ. This is illustrated in more detail in Reference 4. This hysterisis loop represents the energy dissipation by plastic flow. It is produced during all cycles of loading and unloading when the deviatoric stress goes plastic on loading (i. e., satisfies equation (36)) and then reverses its sense upon loading (i. e., elastic unloading according to equation (35)).

Unloading can cause the deviatoric stress to again go plastic. For the isotropic work-hardening model, this occurs in accord with equation (36); the yield stress Y (μ_p) for the unloading part of a cycle has the same value that it obtained when loading ceased (say Y_1) -- it is a single valued function of μ_p. Also, if unloading ceased while the deviatoric stress was still elastic, and the material was reloaded until it went plastic again, the yield stress Y (μ_p) would assume the same value (Y_1) it would have had if the material had been unloaded until plasticity occurred. This is not the case for a material which exhibits a Bauschinger effect. For such a material,

the yield stress depends on the sense (i.e., tension or compression) of the deviatoric stress (or strain). If the yield stress on loading obtains a given value, say Y_1, yielding upon unloading would occur when the deviatoric stress reaches a different value, say Y_2. Usually, $Y_2 < Y_1$ prevails. Several plasticity theories which incorporate the Bauschinger effect, such as kinematic work-hardening models, have been developed by various investigators (e.g., see Reference 20).

It is possible to include nonlinear work hardening and the Bauschinger effect in the model existing in the MDAC-WD version of the PUFF code. Insufficient data for zero-degree or 90-degree shingle-angle quartz-phenolic materials were available (considering both MDAC-WD tests and the literature) to attempt use of this more sophisticated model. Such a PUFF-code model has been used by SRI for a well-characterized aluminum, and applied to problems of thin flyer impact with good agreement between prediction and experiment (Reference 39).

Starting with shear modulus and yield stress estimates based on uniaxial data available from MDAC-WD tests and the literature, and the acoustic velocities from this study, a trial-and-error procedure was followed to match the data and obtain the constants which fit equations (62) and (63). The Gruneisen constant Γ was calculated from data in the literature. The constitutive models for Mylar and the aluminums which were presented in Section VII-2a were used in the analyses. Table XIII lists the parameters used for the flyers and the best-fit parameters determined for the two target materials.

Table XIII. Constitutive Parameters for the Study Materials

Material	C (Kb)	D (Kb)	S (Kb)	Γ	ρ_o (g/cm^3)	G (Kb)	Y_o (Kb)	C_1 (Kb)
Mylar	71.3	131	200	0.448	1.39	0	0	0
6061-T6 Aluminum	760	1,293	816	2.130	2.70	205.7	2.53	20
2024-T4 Aluminum	778	1,326	838	2.190	2.77	353	3.00	8.13
Quartz	346	0	0	0.621	2.65	38.3	30	0
0° Quartz-Phenolic	95	740	3,700	0.110	1.67	38.3	0.40	10
90° Quartz-Phenolic	132.3	979	4,911	0.110	1.70	102.7	0.32	0

Figures 66, 72 and 73 show the results of the reduction of the Hugoniot data in the classical fashion. On all three plots, the Hugoniot state points for 20-degree shingle-angle quartz-phenolic from Reference 35 are also plotted for comparison. In Figure 73, the relation given in Reference 34 as a Hugoniot state relation for both the zero-degree and 90-degree materials studied in that work, is also plotted. All three figures clearly indicate the effect of the anisotropy of the material studied in this program. This effect also is apparent on comparing the original SRI traces for the two orientations of the material, Figures 28 to 34. Such differences, due to anisotropy, were not reported in Reference 34, although the effect was sought. It should be recognized that the material of that study is less anisotropic in other properties than that under current discussion, as evidenced by the acoustic velocities and other properties reported in References 40 and 41. The material of the present study is made of the same fabric as that material but has a higher resin content. It, therefore, naturally exhibits more anisotropy. The material of the MDAC-WD BORIS program, studied in Reference 35, has about the same density and porosity (and therefore resin content) as the material of this study, but was fabricated by tape wrapping using a bias cut tape of a different fabric weave. Thus, all three materials are inherently different in various aspects of their construction. Although all go by the name quartz-phenolic, their Hugoniot states also differ; however, the biggest difference in Hugoniots is exhibited by the two orientations of the single material of this study. This effect of anisotropy is most markedly shown by the plot of shock velocity versus particle velocity, Figure 66.

Figures 74 through 79 depict various aspects of the results of the PUFF-code simulation of the two pulse attenuation shots, Figures 33 and 34, using the best-fit properties listed in Table XIII for the two orientations of the study material. It is seen, by comparing the experimental and analytical traces shown in Figures 74 and 77, that the first-arrival times and peak stresses of the two test traces have been matched fairly well, but the profiles are significantly different. This is attributed to the isotropic and linear work-hardening models used in the analyses. These have also produced residual stress tails in the compressive pulses, most likely because Bauschinger effect parameters could not be determined for inclusion in the analyses. These tails are shown in the spatial plots of the pulses at the times the pulses just enter the quartz transducers (Figures 75 and 78).

The dispersive front of each pulse could have been matched much better by assuming a very low initial yield stress combined with a nonlinear work-hardening law which limits the maximum achievable value of the yield stress after a certain amount of work-hardening has occurred. This was not warranted under this study because only one pulse-profile in each material orientation was available for such matching, and would prove nothing conclusively.

The extent of attenuation and pulse dispersion resulting from the hydrodynamic-elastic-plastic modeling is seen by comparing the pulses produced at the front face by the Mylar impact, shown in Figures 76 and 79, to the pulses transmitted to the quartz, shown in Figures 74 and 77.

BLANK PAGE

Section VIII
DETERMINATION OF A FAILURE CRITERION

1. INTRODUCTION

The technology for prediction of failure due to stress-wave propagation, as presently employed by the aerospace technological community, normally assumes that one of several operating mechanisms can produce spallation of material caused by a reflected tensile pulse. The failure criteria are often cited in terms of critical tensile stress, critical particle velocity, or a combination of tensile impulse and peak tensile stress. Such criteria, although useful in practice, do not by themselves reflect how much material response characteristics - such as elastic-plastic behavior, work-hardening, strain-rate sensitivity, and anisotropy - influence stress-wave propagation and subsequent failure in homogeneous and composite materials. Similarly, it is unknown whether any of the one-variable, two-variable, or multi-variable failure criteria developed for monoconstituent materials apply to composite materials which exhibit a coupling of these material behavioral characteristics.

In developing a failure criterion for the zero-degree shingle-angle quartz-phenolic of this study, one of the first and most important objectives in this study has been the construction of an analytical model which is capable of accurately describing the stress-time history (both tensile and compressive) for stress-wave loading of materials. This is assumed to have been accomplished in Section VII. Once having an adequate capability to predict stress-time history, the second objective is to translate the history at failure data points into a failure criterion. This will be accomplished in this section.

Section VII and Reference 4 provide insight into the problem of wave propagation in materials which exhibit material strength effects, and how the response characteristics affect the variables in which failure criteria are expressed. Reference 4 indicates the role that basic material characteristics, such as anisotropy, elastic-plastic behavior, viscoelasticity, heterogeneity, rate-dependence, etc., play in the establishment of a constitutive model for the material's response to wave propagation. These have been accounted for in Section VII. Reference 4 differentiates between shock wave and dispersive stress-wave phenomena. The former occurs for a material which exhibits a stress/condensation diagram in which it is increasingly more difficult to increase the condensation with increase in stress. The latter occurs if the material through which the wave propagates has a stress/condensation diagram where the slope decreases with increased stress. The front of a wave traveling through the former material tends to shock-up, while in the latter case it spreads out. In this section, the assumption is made that an accurate stress-time history, for both compressive and tensile mode of propagation, exists for the zero-degree shingle angle quartz-phenolic. Therefore, this

section will be concerned only with the translation of this stress-time history, for those exploding-foil shots which produced damage, into a failure criterion which can be subsequently used to predict the failure of the material in other configurations, such as the proof-test configuration.

The remaining subsections contain a brief summary of existing dynamic fracture theories, a suggested failure theory which includes the stress-wave response variables of peak stress, impulse, pulse duration, and shape, and a description of how the exploding-foil data described in Section IV were reduced to these stress-wave loading parameters.

2. MATERIAL STRENGTH THEORIES FOR WAVE PROPAGATION

Two parameters which significantly affect material strength are time and temperature. The following paragraphs discuss some relevant theories concerning the influence of time of loading on material strength. Only passing reference will be made to associated temperature effects.

This section contains a summary of commonly used failure criteria for uniaxial strain, and suggests a failure theory which includes (as stress-wave response variables) peak tensile stress, tensile impulse, tensile pulse duration, and tensile pulse shape. The commonly used criteria discussed are:

a. Constant critical stress

b. Stress rate or stress gradient

c. Empirical algebraic relationships between stress and impulse or time

d. Rate process criteria

The various algebraic relationships for the above theories are summarized in Table XIV, and are briefly described below.

a. Critical Stress Failure Theory

In the distant past, the analysis of the breaking strength of solid bodies was based on the concept that a critical value of stress exists such that the material can sustain any loads less than this stress even if they remain on the body for an infinite period of time. This concept of material failure has been termed the Critical Stress Theory (i.e., a unique value of material strength), and has been experimentally refuted for many materials over various regimes of loading, and by several investigators. (See References 42 to 53.) Its survival over the years has been justified by several investigators in the area of dynamic fracture. They reasoned that it is, by far, the simplest dynamic fracture theory to employ and by conducting a set of simple experiments its validity can be readily ascertained for some materials.

Several procedures can be used to obtain this constant critical tensile stress value for the wave-propagation loading regime. One such method of specific interest is to impact a target material with a flyer plate of the same material, producing a reflected tensile pulse at the rear surface of the target material.

Table XIV. Summary of Dynamic Fracture Critieria

Theory	Functional Relationship	Comment
Critical Stress	$\sigma = \sigma_{cr}$	σ_{cr} = Dynamic tensile strength σ = Tensile stress
Stress Gradient	$\sigma = A + B\left(\frac{\partial\sigma}{\partial x}\right)^{1/2}$	A, B, α, β = Material and pulse shape constants
	$\sigma = \alpha + \beta\left(\frac{\partial\sigma}{\partial t}\right)^{1/2}$	σ = Tensile stress x, t = Spatial and time coordinates
Tuler-Butcher criterion and other empirical algebraic relationships between stress and impulse	(1) $(\sigma - \sigma_o)^{\lambda}\,\Delta t = K$ or $\int_o^t (\sigma - \sigma_o)^{\lambda}\,dt = K$	K, λ = Constants σ_o = Material strength constant Δt = Duration of tensile stress σ = Tensile stress
	(2) $I = \frac{K\sigma}{(\sigma - \sigma_o)^{\lambda}}$	I = Tensile impulse σ = Maximum (peak) tensile stress
	(3) $\sigma = \alpha I^{-B}$	λ, K, α, B = Constants
Rate Process Criteria	(1) $\sigma = A + B \log t$	σ = Maximum (peak) tensile stress t = Duration of tensile pulse
	(2) $\frac{I}{I_1} = \frac{\sigma}{\sigma_1} e^{-\sigma/\sigma_1}$	A, B, I_1, σ_1 = Material and pulse shape constants
	or $\sigma = \sigma_1 \ln (I_1/\sigma_1) - \sigma_1 \ln (I/\sigma)$	I = Tensile impulse

If the impactor and target dimensions are proportioned so that the duration of the tensile pulse at the spall plane is scaled according to a multiplication factor with the thickness of the impactor (Reference 54), various pulse durations at the same value of peak tensile stress can be produced in the target material. If the material does exhibit a constant critical tensile stress for wave propagation condition, the impactor velocity to produce spall will be constant when the impactor and target thicknesses are increased or decreased in the same ratio.

The work covered in Reference 55, as illustrated in Figure 80, indicates that a constant critical tensile stress exists for Lucite, and is approximately 1.0 Kbar at room temperature. Figure 80 indicates that this value is almost constant over pulse widths from 0.190 to 0.470 μsec, if an acoustic velocity of 0.27 cm/μsec is used to reduce the data of that figure. However, according to Reference 14, the tensile failure stress of 6061-T6 aluminum changes from about 6.5 Kbars to 31 Kbars over a range of pulse durations from about 0.500 to 0.060 μsec, respectively. These spall values were determined by impacting Mylar flyers against 6061-T6 aluminum targets. The work reported in References 56 and 57 shows a similar finding for 6061-T6 aluminum over a range of tensile pulse durations from 1.5 to 0.05 μsec. A similar observation has been recorded for I-400 Beryllium in Reference 58. Utilization of a constant critical stress failure criterion in wave propagation implies that the failure strength of the material is insensitive to the pulse shape, duration, and impulse. As reported in References 14, 56, and 57 for 6061-T6 aluminum, and in the work of Reference 58 for I-400 Be, strength is often related to peak stress, time duration of loading, impulse, and the pulse shape. Thus, it is often necessary to determine rate-dependent failure criteria.

b. Failure Theories in Which Critical Stress is Dependent Upon Stress Rate or Stress Gradient

Several authors, notably Breed, et al (Reference 59) and Whiteman (Reference 60) have proposed that failure caused by reflected tensile pulses during wave propagation initiated by impact of one flat plate on another, can be predicted by relating critical stress, σ, to stress rate, $(\partial\sigma/\partial t)$, or stress gradient, $(\partial\sigma/\partial x)$, by relations such as

$$\sigma = A + B(\partial\sigma/\partial x)^{1/2} \tag{65}$$

or

$$\sigma = \alpha + \beta(\partial\sigma/\partial t)^{1/2} \tag{66}$$

In equations (65) and (66), α, β, A and B are constants which reflect both the material and the pulse shape. The functional form of equation (66) is based on the work of Stroh (Reference 61) for dislocation motion. However, the use of equations (65) or (66) poses certain anomalous results, which raises caution as to their applicability.

Reference 62 limited consideration of Equation (67) to the case $\lambda = 1$. Instead of imposing this limitation, if the procedures of Reference 62 are again followed, but the general equation (67) for any λ is used, the resulting σ vs I criterion becomes (Reference 64)

$$I = K\sigma/(\sigma - \sigma_o)^{\lambda} \tag{70}$$

where

$$I = \sigma\Delta t \tag{71}$$

As in Reference 62, σ_o can be considered the static (or long pulse duration) strength of the material, but K cannot be identified in general with a limiting constant impulse value for short duration pulses. Employing the same reasoning as Reference 62, if Δt becomes small, it is expected that $\sigma/\sigma_o \gg 1$. Instead of the result found in Reference 62, equation (70) then is approximated by the general relation

$$I = K\sigma^{(1-\lambda)} \tag{72}$$

Equation (72) can also be written as

$$\sigma = \alpha I^{-\beta} \tag{73}$$

where α and β are two physical constants similar to K and λ. No attempt has been made to relate equations (70) or (73) to any criterion based on other physical parameters (e.g., stress gradients or stress rates).

d. Rate Process Oriented Failure Theories

Reference 65 discusses in detail supporting evidence for the use of rate process oriented failure theories. In this and the following subsections, the salient features of that evidence pertinent to this study, are summarized.

Several investigations, notably those cited in References 66, 67, and 68, have proposed a failure relationship for both homogeneous and composite materials of the form.

$$\sigma = c_1 + c_2 \log \dot{\epsilon} \tag{74}$$

or

$$\sigma = c_3 + c_4 \log t \tag{75}$$

where $\dot{\epsilon}$ is the strain rate and t is the duration of the applied load. The form of equation (75) has become known as Zhurkov's law, where c_3 and c_4 are constants dependent upon the temperature and composition of the material. Rewriting equation (75) in the form in which Zhurkov (Reference 66) presented it, the time to failure (t_c) is related to the failure strength (σ) as follows:

$$t_c = t_o \exp\left(\frac{U_o - \gamma\sigma}{KT}\right) \tag{76}$$

where

t_c = time to failure or durability under load

σ = flow stress

T = temperature, °K

U_o, t_o, γ = constants which define the strength properties of the substance

K = Boltzman constant

Equation (76) is based mainly on experimental evidence gathered by Zhurkov and his co-workers (see References 47 and 49) for both metallic and polymeric materials. Further credance of the Zhurkov relationship can be established, since the functional form of equation (76) is derivable from application of Eyring's theory for absolute reaction rates (Reference 69). An excellent example of this approach for polymeric materials can be found in the work of Bueche (Reference 70) which presents a phenomenological description of Eyring's rate process theory as applied to polymers. For the case of a constant load on a specimen, Bueche proposed that the time to failure (t_c) is related to the magnitude of the load (σ) as:

$$\sigma = 0.37\left(\frac{n}{\delta}\right)Q - 0.37\left(\frac{nKT}{\delta}\right)\log(t_c\omega) \tag{77}$$

δ = approximate distance the bond stretches before breaking

n = number of bonds per unit cross section

ω = segment oscillation frequency

Q = activation energy

ω can be physically interpreted as the number of times per second a segment of the molecular chain changes its energy.

In a later work (Reference 71) Bueche modified equation (77) to include chain relaxation. However, the linearity between failure stress and the logarithm of time to failure was still preserved. Following the procedures used by Bueche in Reference 70, the time to failure t_c in equation (77) can be made an explicit function of the activation energy and activation volume of the failure process involved, in the following form, similar to equation (76):

$$t_c = \text{Const. } \exp\left[\frac{Q}{KT} - \frac{V_o\sigma}{2KT}\right] \tag{78}$$

The activation volume, V_o, may be regarded as a measure of the volume of the activated segmental unit involved in the diffusion process. The activation energy, Q, represents the intermolecular energy barrier to diffusional movement.

Equations (70), (77), and (78) are all of the functional form:

$$t_c = Ae^{B\sigma} \quad \text{or} \quad \sigma = C + D \log t_c \tag{79}$$

and differ only algebraically in the value that they assign A, B, C and D. Each predicts a linear relationship between the failure stress and the logarithm of time to failure. Zhurkov's Law, equation (75), was proposed on the basis of experimental evidence. Comparing with equation (78), the constants in equation (75), U_o and γ, seem to be the activation energy and activation volume of the process.

Equations (74) to (78) have been applied primarily to predict failure of materials in the uniaxial stress loading conditions, at low to moderate rates of loading (i.e., $\dot{\epsilon} < 100 \text{ sec}^{-1}$). To extrapolate the use of equations (74) to (78) to the stress-wave loading regime (i.e., $\dot{\epsilon} \sim 1 \times 10^6 \text{ sec}^{-1}$, $t \sim 1 \times 10^{-6}$ sec)*, the form of these equations must be related to the stress-wave loading parameters; stress, impulse, time duration, and pulse shape.

The impulse in an arbitrary shaped tensile wave can be related to the duration of the tensile pulse load as

$$I = \kappa\sigma t \tag{80}$$

---

*Strain rates are a poor (and not clearly defined) loading parameter for the stress-wave loading regime, so pulse duration is included as an alternative parameter.

where κ is a pulse shape constant, I is the tensile impulse, σ the peak tensile stress of the pulse, and t the duration of the tensile pulse. Substituting equation (80) in equation (75), by algebraic manipulation, impulse can be related to failure stress in the following manner (Reference 64):

$$\sigma = \sigma_1 \log\left(\frac{I_1}{\sigma_1}\right) - \sigma_1 \log\left(\frac{I}{\sigma}\right) \tag{81}$$

where I_1 and σ_1 are constants for a given material and pulse shape. Rewriting equation (80) in exponential form one has:

$$\left(\frac{I}{I_1}\right) = \left(\frac{\sigma}{\sigma_1}\right) \exp\left[-\left(\frac{\sigma}{\sigma_1}\right)\right] \tag{82}$$

References 14 and 64 present a more rigorous derivation of equations (81) and (82). Reference 14 utilizes spall data for 6061-T6 aluminum over the range of pulse durations from 0.050 to 1.50 μsec. to demonstrate its validity.

e. Experimental Support for Time-Dependent Failure Theories at High Rates of Strains

For consistency we shall define the low to intermediate range of strain rate as $\dot{\epsilon} < 1,000\ \text{sec}^{-1}$, or a duration of loading of $t > 10^{-5}$ sec. Over this spectrum of loading there is experimental evidence to support several of the proposed time-dependent material strength relationships. However, most of the data are confined to the low rates of strain, $\dot{\epsilon} < 1\ \text{sec}^{-1}$, with only scant information at higher rates of loading up to and including those for wave propagation.

Figures 82 and 83 (redrawn from Reference 67) illustrate that a linear relationship exists between strength and log-time duration of loading over several decades in time. In particular, the data in Figure 83 indicate linearity between log-time and failure stress over a dozen decades of time for polystyrene, polymethyl methacrylate, and soda glass. The values of fracture stress given for $t > 10^3$ sec were obtained from creep tests. The values of fracture stress given for $10^{-2} < t < 10^3$ were obtained from constant strain-rate tests. The values indicated for $t \sim 10^{-5}$ sec were obtained from explosive loading tests (Reference 72). Similar evidence can be found for epoxy and phenolic polymers, as illustrated by the data in Figures 84 and 85 (Reference 73). The work of Reference 9 reveals a similar log-time strength relationship for a three-phase epoxy composite, i.e., particles, voids, and matrix (Figure 86).

The data of Figure 87 for aluminum annealed at 290°C, 420°C, and 550°C show a definite linear strength-log of time relationship in the range of $t < 10^4$ sec. The data presented in Figure 87 are from the work of Zhurkov (References 47 and 48) and it is from these that the linear strength-log of time relationship derives the name, Zhurkov's Law.

f. Applicability of Rate Process Oriented Theories

Extreme care must be taken in the application of Zhurkov's linear relation between strength and log of time. The discussions in preceding sections concerning Eyring's reaction-rate theory, as applied to failure, indicate that there is a definite physical basis for the meaning of the constant terms in the linear strength-log of time relationship; i.e., as applied to polymers, a measure of the activation energy and activation volume of the process. The activation energy represents the intermolecular energy barrier to diffusional or segmental movement, and the activation volume can be regarded as a measure of the volume of activated segmented unit involved in the diffusional process.

For metals, Zhurkov identifies the constant term U_o in equation (76) as the activation energy barrier at zero stress, which is of the same magnitude as the sublimation energy. The second constant term in equation (76), γ, has been identified by Zhurkov as a characteristic factor of the atomic structure of the material, which is approximately proportional to the square root of the grain dimension. Hence, such relationships, for both polymers and metals, could not be postulated as a general constitutive equation for material behavior, but rather should be confined to behavior at high-stress levels or at elevated temperature. Care should also be taken in attempting to employ the strength-log of time relationship for a polymeric material which is being tested through its glass-transition temperature. The molecular motion in the glassy state, below the glass-transition temperature, is greatly different from that above the transition temperature. There is experimental evidence for several polymeric materials that indicates that a strength-log of time linearity will not be preserved through the glass-transition temperature, and that the only way to determine the rate behavior of such a material is to employ a temperature-time shift.

As illustrated in this section, the most nearly complete information for most materials is for $\dot{\epsilon} < 10$ sec.$^{-1}$, and at room temperature. For several glassy polymers and metals, the data seem to indicate that strength and time duration of load application are intimately related, perhaps by a strength-log of time relationship. However, although there are some experimental data for material properties at higher rates of loading up to about $\dot{\epsilon} = 1,000$ sec^{-1}, there is only scant information for material failure in the stress-wave environment. In addition, it must be recognized that equations (74) to (78) are postulated for the condition of uniaxial stress, and it is uncertain how they relate to the complex triaxial stress state which exists during uniaxial strain-wave propagation.

3. REDUCTION AND ANALYSIS OF THE FAILURE DATA

a. Reduction of Exploding-Foil Data Using the MDAC-WD Version of PUFF

If flyer and target thicknesses, flyer and target constitutive relations, and flyer velocity producing damage are input into the MDAC-WD modified version of the PUFF V computer code, a wave propagation analysis can be conducted by PUFF to determine any of the basic variables in which one desires to express a failure criterion. At present, one MDAC-WD modified code calculates and stores peak tensile stress, tensile impulse, and tensile pulse

width as functions of time, at 30 selected points. These can be printed out in plot form or utilized in any failure criterion within the code which involves these three variables and permits the target material to spall. A more recently modified MDAC-WD version of PUFF, permits spall in any zone of the problem and then subsequent rejoining (secondary impact) and reseparation of the spalled parts, if they can occur. The former version of the code was used to reduce the failure threshold. The peak tensile stress, tensile impulse, and tensile pulse width as a function of time are printed out at selected points. The values when the main tensile pulse ceased at these points were plotted versus depth in the material, and fitted to various failure criteria.

The failure threshold data points analyzed included the two visual and two microscopic threshold values determined by testing under this study as presented in Sections V and VI. Another two points on each threshold were obtained by assuming that the long-duration-pulse failure conditions for the zero-degree shingle-angle material studied in Reference 40 applied to the material of the present study. The impact conditions analyzed are summarized in Table XV.

The tensile pulse width is the quantity which is least accurately determined from PUFF analysis. Most tensile pulses predicted by the code for the spall data developed a long, low-amplitude tail caused by the nature of the code and the constitutive relations used in the analysis. The stress levels in this tail are very low and therefore of questionable accuracy as far as the code is concerned, and contribute little to total impulse. However, the code will keep track of the tensile pulse duration and continue to add to tensile impulse as long as the stress in the pulse remains tensile. The code tends to overestimate the tensile pulse width based on this low-stress tail. For all practical purposes this low-stress tail is insignificant in magnitude and impulse and is not physically expected to exist often, nor significantly contribute toward producing the observed failure when it does exist. Thus, effective

Table XV. Assumed Impact Conditions Producing Failure Threshold Data Points

Flyer Material	Thicknesses		Threshold Velocities	
	Flyer mil	Target mil	Visual m/sec	Microscopic m/sec
Mylar	5	250	960	600
Mylar	14.7	250	560	390
Quartz-Phenolic, 0° Orientation	125	225	473	213
Quartz-Phenolic, 0° Orientation	60	125	473	213

pulse widths usually should be estimated based on pulse stress-history shape, neglecting any tail, rather than on the code output for pulse width.

Figures 88 through 95 are plots of the pertinent results output by the PUFF code for the eight cases listed in Table XV. Tables XVI and XVII show the mean values of the various parameters which were selected from this output to represent the failure parameters to use with the various failure conditions. They are also indicated on the figures. The ratio I/σ was chosen as a critical temporal measure.

The two-parameter (e. g., σ and I/σ) failure space appears to naturally fall into two regions. The rate process failure criterion, equations (80) or (81), was chosen as the criterion to use to fit the MDAC-WD data in one region. A constant stress criterion appeared appropriate to fit the data of Reference 40 in a second region. The other empirical relations could have been used to fit the data, but the authors favored this selection in light of its physical aspects. The resulting visual and microscopic criteria then are given by

$$\frac{I}{I_1} = \frac{\sigma}{\sigma_1} \exp\left(-\frac{\sigma}{\sigma_1}\right), \quad \frac{I}{\sigma} < \tau; \tag{83}$$

$$\sigma = \sigma_o, \quad \frac{I}{\sigma} \geq \tau.$$

Table XVI. Failure Parameters Selected as Representing Visual Threshold Points

Flyer Thickness* (mils)	Critical Tensile Pulse Parameters		
	Impulse, I (taps)**	Stress, σ (kilobars)	I/σ (μsec)
5	987	1.44	0.685
14.7	1700	3.45	0.492
60	950	1.05	0.906
125	1650	1.05	1.570

*See Table XV for flyer material and test configuration.
**1 tap = 1 dyne-sec/cm^2 = 1 bar-μsec

Table XVII. Failure Parameters Selected as Representing Microscopic Threshold Points

Flyer Thickness* (mils)	Critical Tensile Pulse Parameters		
	Impulse, I (taps)	Stress, σ (kilobars)	I/σ (μsec)
5	460	0.835	0.549
14.7	1080	2.51	0.429
60	515	0.55	0.938
125	900	0.55	1.64

*See Table XV for flyer material and test configuration.

where

	I_1, TAPS	σ_1, Kb	τ, μsec	σ_o, Kb
Visual:	5300	6.10	0.730	1.05
Microscopic:	4200	6.78	0.572	0.55

These results are plotted in Figures 96, 97 and 98 and were used for pretest analyses of the proof tests.

Examining Figures 97 and 98, it is seen that the time-dependent portion of each criterion produces a multi-valued threshold. This reflects a pulse-shape (history) effect. For a given impulse, the criterion essentially permits brief durations of the pulse peak to occur without failure at intermediate stress levels, but will indicate failure for long durations at a low-peak stress or short durations at a high stress. Extremely low stresses of any duration will not produce failure either. It is not physically unreasonable to expect this type of behavior.

The data points producing these multi-valued curves in this case lie to the left of the peaks of the curves. However, in Reference 14, the authors used the same criterion as above and, for the rate-dependent portion, curves were defined by points lying to the right of the peaks. Not enough data are presented for either material, to completely validate use of equations (83) in either case. We only can infer that, because such multivalued curves have been generated by data falling in one case to the left and in another case to the right of the respective crests, we have some support that such cresting will still be evidenced when sufficient data become available.

BLANK PAGE

Section IX

PROOF-TESTING

The major objective of this study was to evaluate the state of the art practices of plate-slap technology pertinent to characterization and design use of composite materials in re-entry vehicle applications. The previous sections of this report have described the characterization of the material with respect to the constitutive relations and failure criteria applicable for plate-slap environments. Once the material was characterized, it remained to apply this data to a design, simulating an application of similar data in re-entry vehicle design. The design then had to be plate-slap tested to ascertain its adequacy and thereafter evaluate the adequacy of the technology. This design and test portion of the study has been called the proof-test task. It is described and discussed in detail in this section.

1. DESIGN OF THE PROOF-TESTS

The proof-test configuration was designed to be significantly different than the failure threshold configuration, yet still be a configuration for which failure could be achieved in the MDAC-WD exploding-foil facility. The configuration chosen was nominally that of a 1/4-inch, zero-degree shingle-angle quartz-phenolic target, backed by a 3/4-inch 6061-T6 aluminum block and impacted by a 5-mil Mylar flyer. The aluminum back-up block (or anvil) was not in any way bonded to the quartz-phenolic target, but the interface of the two items was coated with vacuum grease to ensure adequate transmission to the aluminum of the compression pulse produced by the impact. The configuration is shown in Figure 99.

This configuration was designed to exhibit the following features during wave propagation:

(1) The initially thin compression pulse would first travel through the 1/4-inch quartz-phenolic. The pulse would then be partially transmitted to the anvil and partially reflected at the interface with the aluminum anvil (as another compression pulse), then travel back through the 1/4 inch of once-compressed material. When it again reflected off the impacted face, the compression pulse should be reflecting from a free (unloaded) boundary and, therefore, produce a tensile pulse. This tensile pulse would be the cause of any visual or microscopic delaminations that would be subsequently observed.

(2) The compression pulse transmitted to the anvil eventually reflects off its back face as a tensile wave. The nominally 3/4-inch (actually, 0.71-inch) aluminum anvil was chosen to be thick enough so that the interaction of the original compression pulse in the quartz-phenolic with the anvil would be completed before the tensile wave reflected from the free back face of the anvil reached the interface.

(3) The anvil would be thick enough that it would not spall, for conditions producing spall of the quartz-phenolic.

(4) The quartz-phenolic/aluminum interface was essentially a zero tensile strength connection. Thus, the reflected tensile wave in the aluminum arriving at the interface would not be transmitted to the quartz-phenolic and cause delamination. Instead, the aluminum would bounce off the back of the quartz-phenolic.

It was felt that this configuration was significantly different from those employed to get the basic failure and pulse attenuation data, and would thus provide a good proof-test. In addition, to provide more differences in the proof-test configuration, the targets were machined as nominally 1-1/2 by 1-1/2 inch squares, instead of the 1-1/4 by 1-1/4- inch size used previously. They were also tested without using the target-holder shown in Figure 39. Thus, their lateral boundaries had no edge constraints. The targets were simply rested on the exploding-foil assembly.

2. PRE-TEST ANALYSIS OF THE PROOF-TEST CONFIGURATION

The test configuration described above was modeled in the PUFF code using the properties listed in Table XIII. A range of impact velocities to use with the code was selected, based on estimates of the failure points. Both visual and microscopic thresholds of delamination were sought. It was therefore easier to use the option in the MDAC-WD PUFF code which incorporates the failure criterion and shows spalling and subsequent rejoining (if any) and reseparation (if any). The failure criteria developed in Section VIII were input to the code. The result predicted in each case (visual and microscopic) was that the first delamination would occur about 80 mils in from the front face at the following velocities:

- Visual delamination at between 2.1 and 2.2 mm/μsec
- Microscopic delamination at between 1.3 and 1.4 mm/μsec

3. PROOF-TESTING AT THE MDAC-WD EXPLODING-FOIL FACILITY

The proof-tests were conducted at the MDAC-WD exploding-foil facility in a manner similar to that used to obtain the basic failure data and described in Section V. Five-mil Mylar flyers impacted the proof-test target configurations (Figure 99). Simultaneous streak and frame photographs were taken, to determine impact velocity and non-simultaneity of impact. The specimens were examined visually at the facility.

A total of six shots were fired. The velocity range was varied to encompass the regime predicted to include no microscopic delamination through visual delamination. Table XVIII lists the impact velocities for the six shots and the visual condition of the specimens. The shots are listed in the order fired. It is seen that the predicted visual damage level was indeed a velocity at which visual damage was produced, even though a specimen (P5) was not damaged at an impact above this level. The observations listed in Table XVIII are discussed below.

at a higher level is characteristic of many plate-slap test results (e.g., references 6 and 14), and is attributed to the statistical variations of material strength, combined with the statistical variations of such flyer impact parameters as planarity and simultaneity. It is noted that the edge crack of specimen P4 was not easily discernable, unlike the distinct delaminations or bulging exhibited by the visually damaged failure threshold specimens.

There was the possibility that specimen P3 also exhibited a crack, on one edge. Visual examination of that specimen showed a very thin line, about 1/4-inch long, around the mid-plane, but this could just as easily have been a scratch.

In Figure 101, the edges of some of the specimens visually exhibit damage about one layer in from the front face. This is partially the effect of the Mylar flyer chewing-up the face along its edges, combined with the effects of post-test characterization prior to taking the photographs. A stripable vinyl coating was applied so that post-test acoustic velocities could be measured. When it was stripped off, the edge region outside the impact area was disturbed. This was not considered evidence of visual delamination, but rather was considered to be an edge effect. This is also seen in Figure 100.

4. PRE- AND POST-TEST CHARACTERIZATION OF SPECIMENS

The thicknesses and acoustic velocities of all the proof-test specimens were measured before and after testing. The acoustic velocities were measured as described in Section III. The above-mentioned stripable vinyl coating was employed to facilitate such measurements.

The results of this characterization are shown in Table XIX. Table XIX indicates that the least degradation of acoustic velocity was exhibited by the specimen impacted at the lowest velocity, but it did exhibit some (about 10%) degradation. There were no significant changes in thicknesses after testing.

Table XIX. Pre- and Post-Test Characteristics of the Proof-Test Specimens

Specimen No.	Impact Velocity mm/μsec	Thickness		Acoustic Velocity	
		Pre-Test mils	Post-Test mils	Pre-Test mm/μsec	Post-Test mm/μsec
P1	1.72	254	255	3.06	2.12
P2	1.47	254	255	3.07	1.66
P3	2.05	254	255	3.12	1.99
P4	2.20	254	255	3.06	1.82
P5	2.30	254	255	3.07	1.91
P6	1.07	254	255	3.19	2.62

An additional interesting result was obtained from the proof-testing. If the ratio of post-test to pre-test acoustic velocity for each specimen is plotted versus impact velocity, the resulting points shown in Figure 108 are obtained. If it is assumed that impact at any velocity will degrade the material, the ratio can only be unity for null impact velocity. If the point for specimen P2 is disregarded as being misrepresentative because of the high density of internal microcracking, the remaining points fall very close to or lie on the straight line shown in the figure. No explanation is offered for this linear relationship; it is simply presented as meriting future investigation. It would appear that if such a monotonic relation exists for other materials, the degradation of acoustic velocity might be a suitable non-destructive-test measure of degree of microscopic damage produced by stress-wave propagation.

Section X

CONCLUSIONS AND RECOMMENDATIONS

1. AN EVALUATION OF PLATE-SLAP TECHNOLOGY

The proof tests conducted in this study have shown that plate-slap technology as defined in this study works, as qualified in the following paragraphs.

The proof-tests were considered successful within engineering accuracy. A visual damage point in a delamination type of mode was predicted and achieved. Even though a specimen was tested above this threshold and did not clearly exhibit such damage, visually identifiable damage became apparent upon sectioning. Microscopic damage in the delamination mode was also achieved about where predicted. Microscopic damage was defined arbitrarily as connected delamination-type cracks. The proof tests established points above and below that arbitrary level.

Two other modes of damage were exhibited during this study: disconnected delaminations and microcracking. The later mode usually was exhibited in conjunction with any of the others, but its cause is unknown.

Consideration of the damage discussed above also indicated the following limitations: the internal damage that can only be observed visually upon sectioning of a specimen cannot always be identified without destructive testing, and the meaning of damage, in the light of adequate vehicle design, is not defined by current technology.

It is possible that the first limitation can be overcome by nondestructive test (NDT) techniques. The second is being studied by various investigators at this time.

The current practices limit the number of tests that can be conducted to characterize a material for preliminary design and evaluation purposes. This is usually caused by budget limitations, but could inadvertently lead to rejection of promising materials or to selection of the wrong materials for a re-entry-vehicle design. For example, it is obvious that the validity of the constitutive relations or failure criteria used have not been conclusively demonstrated. A poor choice of test conditions to obtain the data, or significantly erroneous data points, might have lead to a proof-test design that failed prematurely. This would have been very expensive if the data had been applied in preliminary design of a re-entry vehicle and then, following hours of design trade-off studies, the wrong material was chosen.

This error in choice might be caught by subsequent characterization testing before a vehicle is built, but current practices usually are to conduct such characterization while other expensive test structures are being fabricated. Sometimes such characterization is not conducted until these structures are in the process of being tested, at great expense.

Current practices cannot adequately account for the effects of anisotropy and heterogeneity inherent in composites. For example, Hugoniot and pulse-attenuation data can correctly be acquired at various shingle angles of laminated composites (e.g., reference 35). However, the entire tensor equation of state, and the constitutive relations for the associated dissipative variables, cannot be determined from such test data alone. Methodology to accomplish this has not yet been developed. Although this study has demonstrated the effects of anisotropy in the high-stress-amplitude wave-propagation regime, simple material orientations were chosen by intent, so that engineering constitutive models and failure criteria could be achieved. It is questionable whether similar thinking based upon isotropic models could have been successfully applied, if an oblique-shingle-angle cut had been the material orientation.

Rate effects may be exhibited in some quartz phenolics during wave propagation. It has been concluded that they do not exist for the study material.

Plate-slap technology is presently limited in respect to accounting for rate effects. However, various studies are currently in progress to experimentally determine models for such effects and include them in the computer codes used in analysis.

The low-magnitude precursors in the Hugoniot traces were tentatively attributed to wave dispersion caused by the heterogeneity of the quartz phenolic. Recently this problem has received much attention from the standpoint of linear elasticity. However, areas that still require development are the understanding and modeling of its effect under conditions of high-stress-amplitude wave propagation, and means to include it in associated one-dimensional computer analyses.

The test technique is severely limited because it does not entirely separate the stress-wave and structural-response regimes. For example, two causes of the microcracks that run normal to the lay-up planes have been suggested, one is a wave-propagation effect, while the other is a structural-damage mode.

The test technique is also limited because simultaneity of impact cannot be held within 10% of pulse duration, for thin pulses. In some cases, this limits the applicability of the data obtained.

The use of a technology based on flat-plate impacts has been evaluated, and thus one can only conclude that it is satisfactory in predicting the stress-wave response and stress-wave-induced failures of structurally strong, relatively thick, flat plates. However, the extension of the conclusion to curved geometries, such as relatively thin-walled re-entry-vehicle shells, is not implied.

In addition to evaluating the overall plate-slap technology, this study has produced various technical results, which are summarized in the following paragraphs.

a. The Nuances of Plate-Slap Testing

Current practices of plate-slap testing have been documented. The effects of thirteen aspects of this testing on the test results have been described. The extent to which the nuances of any specific aspect of the testing affects the resulting data depends on the purposes of the test. The plate-slap technologist has to consider carefully the available test techniques, test materials, and the future use of the test data before selecting a given technique, instrumentation, flyer material and thickness, target geometry and support conditions, and the remaining impact and postimpact conditions, discussed under this study.

b. The Mechanical Response of Composites to Stress-Pulse Loads

The current knowledge of unidirectional wave propagation in heterogeneous, anisotropic composite materials has also been documented. The effects of the phenomenological behavior of materials, and the assumptions of the current theories, as related to plate-slap environments, have been enumerated. The importance of recognizing and understanding all aspects of the material behavior, as well as nonequilibrium thermodynamics, while establishing material constitutive models and subsequently using these models in analyses has been indicated. The differences among the basic aspects of stress waves, and the means of reducing data for each type of wave effect have been demonstrated.

c. Failure Induced by Plate-Slap

Dynamic-failure theory applicable to wave-propagation environments induced by plate-slap has been summarized. It has been pointed out that this area of the technology is poorly understood, mainly because there is lack of sufficient wave-propagation data with which to definitely establish the validity of any candidate failure criterion.

d. Data Reduction

Practices of reducing plate-slap data, as well as means of using the results of the reduced data in design and analysis, have been documented. The procedures followed have indicated how data reduction must reflect an understanding of the test techniques, material response, and the basic mechanics and thermodynamics of wave propagation, to properly interpret and use the raw data for future purposes.

e. Effects of Anisotropy of Composites

It has been analytically demonstrated, by using low-stress-amplitude elastic-wave theory, that the anisotropy of composite materials can significantly influence the measurement of parameters of wave propagation induced by plate-slap. The constitutive models used for analysis of high-amplitude stress-wave propagation along two principal axes of the material differ significantly from each other. This anisotropic effect was experimentally

displayed by the stress-wave profiles obtained as Hugoniot data and thin-pulse attenuation data, as well as by the parameters for the aforementioned constitutive models resulting from reduction of these data.

f. Material Variations

Comparison to data in the literature showed that the Hugoniots for various quartz phenolics differing in construction or proportions of constituents from the study material differ considerably from the Hugoniots of this study. Therefore, each quartz-phenolic material must be considered by itself as a different material and characterized as such. Also, wave-propagation data obtained for only one orientation of an anisotropic material do not provide enough information for complete characterization of the material. However, if only propagation along a material principal axis is of concern, isotropic models can be used for analytical expediency, as long as it is recognized that the parameters for such models do not necessarily have the same physical meaning that they bear for an isotropic material.

g. Failure Criteria

A failure criterion for one orientation of the study material has been developed. This criterion is an empirical model based in part on rate-process theory. The engineering form used reflects the peak stress, total impulse, and shape of the tensile pulse producing the damage. This rate-dependent criterion tentatively is only applicable for pulses of short equivalent duration; 0.5 to 1.0 μsec or less. For pulses of longer equivalent duration, it has been suggested that a rate-independent constant-stress criterion is applicable.

h. Validation of the Predicted Behavior of a Design

The constitutive model and failure criterion developed for one orientation of the study material have been used in an analysis of damage induced by wave propagation. Those impact velocities of a Mylar flyer plate required to produce varying degrees of plate-slap damage of a proof-test configuration were predicted. The predictions agreed with the experimental results of plate-slap tests, within the engineering accuracy usually required for preliminary design.

2. RECOMMENDATIONS

a. Testing for Engineering Data

Characterization models for use in preliminary design should be based on more test data points than used in this study. It is suggested that at least four of each type of test point (Hugoniot, attenuation, and thin-pulse failure) should be obtained. For the zero-degree shingle-angle orientation, if any data points had been significantly in error, predictions of the behavior of the proof-test configuration could have been erroneous.

The success of the proof test has not necessarily established the validity of either the constitutive model or the failure model. Without more basic data, there is no means to identify possible errors in either of the models.

It has only been demonstrated that the entire plate-slap technology, which consists of the design-analysis loop starting with testing and ending with prediction, is adequate for engineering purposes of preliminary design. Although this study has endeavored to reflect all the independent aspects of the technology in the acquisition, interpretation, and use of the data obtained, the uncertainty about the models developed has to be kept in mind when they are considered independently.

To minimize the possibility that errors exist, the quantities of data indicated previously should be obtained. This should improve the accuracy of analytical predictions and also help ensure that application of the overall technology will always yield correct results.

b. Testing to Establish Failure Threshold Data Points

To satisfactorily determine a failure threshold data point for preliminary design data, it is suggested that 12 to 15 specimens be used. The current practice of using six to eight specimens is minimally adequate, in order to locate microscopic and visual damage levels approximately. However, the current quantity is not sufficient to achieve a good definition of each threshold point and indicate the statistical variation to be expected as a result of natural variations of material properties and impact conditions. These statistics result in the phenomenon evidenced during the proof tests; one specimen failed visually at the predicted level, another specimen (impacted at a higher velocity) did not display visual failure, and a specimen impacted at a lower velocity displayed what might have been visual failure.

Therefore, there must be enough specimens provided to check the statistics of the failure level once it has been identified. This is no different than required in establishing a failure strength for a material by a simple tensile test.

c. Complete Constitutive Characterization

A correct general formulation of the constitutive models for composite materials is needed for wave-propagation analyses. To predict wave propagation along material principal axes, isotropic models were sufficient for the purposes of this study, but they do not reflect the true anisotropy of the material. Investigations of wave-propagation in directions other than a principal axis, are required. The anisotropy of composite materials is evidenced during the response of these materials to high-magnitude, impulsively applied, long- and short-duration dynamic loads. Pulse-attenuation attributable to material plasticity has been observed. In addition, shock-dispersion and other anomalous features are evidenced by quartz-transducer measurements. It is thus necessary to study in detail the response of these heterogeneous, anisotropic, composites and to determine the appropriate constitutive equations with which to predict this response. As an initial study, a combined experimental and analytical program involving a laminate, such as the material of this study, is suggested. Constitutive data should be obtained by Hugoniot and thin-pulse testing of various shingle-angle cuts of the material. Various specimen thicknesses should be used to investigate rate effects. Analysis should be made of this data and previously obtained data, plus low and intermediate strain rate data, to develop the constitutive equations.

d. Development of Failure Criteria

A failure criterion to predict delamination of the zero-degree shingle-angle orientation of the study material has been proposed. The criterion is physically based upon rate-process theory, but its general applicability has not yet been verified. It is recommended that extensive exploding-foil plate-slap failure data be obtained for this laminated material in various shingle-angle orientations, and also for other composite materials. As many pulse parameters as possible should be varied in these tests. The failure data should be studied in detail and used to investigate the validity of the criterion.

e. Additional Studies

The following list of additional possible research studies suggests itself as a result of this study:

(1) An Experimental and Analytical Study of the Effects of Boundary and Catcher Conditions on the Observed Response of Composite-Material Targets Subjected to Plate-Slap Testing. How much do boundary and catcher conditions enhance damage by producing structural response or combined response insteady of only stress-wave response? Can the different modes of damage be identified? Can the structural damage be eliminated?

(2) Development of Time and Temperature Dependent Failure Criteria for Composite Materials Subjected to Plate-Slap Type Loading Environments. How does the temperature of the target change its failure threshold? How are these thresholds related to low and intermediate strain-rate data at various temperatures?

(3) Effects of Target Temperature on Constitutive Relations of Composite Materials Obtained by Hugoniot-Type Plate-Slap Testing. For those composite materials for which a tensor equation of state exists, how does the initial temperature of the target influence the constitutive relations obtained from plate-slap data?

(4) Development of Experimental Techniques for Measuring Stress-Wave Response of Composite Materials. Can standard optical techniques be applied to obtain meaningful data from plate-slap testing of composite materials? Can new techniques, such as combining holography with Moire' fringe techniques, be developed to measure response?

(5) Development of Cumulative Damage Failure Criteria for Materials Subjected to Multiple Stress-Pulse Loadings. If any material (homogeneous and isotropic or heterogeneous and anisotropic) is plate-slap tested below its incipient failure threshold, what is the threshold upon subsequent plate-slap testing? What are the relationships among pulse parameters and number of pulse applications producing failure?

(6) Effects of Specimen Geometry Upon Failure Thresholds Produced by Plate-Slap Testing. If curved plates or rings of homogeneous, isotropic materials or heterogeneous, anisotropic (composite) materials are subjected to plate-slap testing for stress-wave response, does the curvature of the specimen influence the thresholds of failure compared to thresholds for flat plate specimens?

(7) Size as a Factor in the Dynamic Fracture Strength of Brittle Materials. How does specimen size influence the dynamic fracture of nominally brittle materials subjected to plate-slap stress wave loading conditions?

(8) Non-Destructive Test (NDT) Measurements of Plate-Slap Damage. Can NDT techniques be used to identify the extent and nature of plate-slap induced damage? Are there any fundamental relations between NDT parameters and wave propagation damage levels?

BLANK PAGE

REFERENCES

1. R. N. Brodie and J. E. Hormuth, The PUFF-66 and P PUFF-66 Computer Programs, AFWL-TR-66-48, Air Force Weapons Laboratory, Kirtland Air Force Base, New Mexico, May 1966.

2. L. E. Bothell and C. E. Archuleta, PUFF V - EP Code, Report No. KN-703-67-101(R), Parts I and II, Kaman Nuclear, Colorado Springs, Colorado, December 1967 (SRD).

3. L. J. Cohen and H. M. Berkowitz, The Nuances of Plate-Slap Testing of Composite Materials, Part II of Final Report: A Study of Plate-Slap Technology, AFML-TR - 69-106, Part II, Air Force Materials Laboratory, Wright-Patterson Air Force Base, Ohio, 15 May 1969.

4. H. M. Berkowitz, The Mechanical Response of Composite Materials to Stress-Pulse Loading. Part III of Final Report: A Study of Plate-Slap Technology, AFML-TR-69-106, Part III, Air Force Materials Laboratory, Wright-Patterson Air Force Base, Ohio, 15 May 1969.

5. R. K. Penny and F. A. Leckie, "The Mechanics of Tensile Testing," Int. J. Mech. Sci., Vol. 10, pp. 265-273, 1968.

6. J. C. Peck, Stress-Wave Response of Geometrically Attenuating Materials with High-Modulus Reinforcements (U), AFWL-TR-68-42, Air Force Weapons Laboratory, Kirtland Air Force Base, New Mexico, November 1968.

7. H. M. Berkowitz and G. A. Gurtman, Measurement of Pulse Propagation in Unidirectionally Reinforced Composites (U), SAMSO TR-68-265, Vol. IV, Space and Missile Systems Organization, Norton Air Force Base, California, September 1968 (SRD/Gp-1).

8. H. M. Berkowitz and L. J. Cohen, A Critical Evaluation of Plate-Slap Technology: Six-Month Technical Management Report for the Period 15 April 1968 Through October 1968, Inclusive. Vol. I, Program Synopsis and Experimental Results, DAC 62443, MDAC-WD, Santa Monica, California, October 1968.

9. L. J. Cohen and O. Ishai, "The Elastic Properties of Three-Phase Composites," J. Composite Materials, Vol. 1, No. 4, p. 390, 1968.

10. J. P. Stevens and Co., Inc., Properties Bulletin-Astroquartz, No. 310-7, Jan. 1966.

11. L. J. Cohen, Modulus and Strength of Multi-Phase Phenolic Composites, Internal Memorandum A-830-BBGO-203, MDAC-WD, Santa Monica, California, 1968.

12. L. J. Cohen, Mechanical Hysteresis and Strain-Rate Effect in 2-D Quartz-Phenolic Composites, Internal Memorandum No. A-830-BBGO-623, MDAC-WD, Santa Monica, California, August 1968.

13. J. J. Dick, Hugoniot States and Pulse Attenuation in a Quartz-Phenolic, Subcontract Report, Stanford Research Institute, Menlo Park, California, September, 1968.

14. L. J. Cohen and H. M. Berkowitz, Time-Dependent Fracture Criteria for 6061-T6 Aluminum Under Stress-Wave Loading in Uniaxial-Strain, Douglas Paper 10191, MDAC-WD, Santa Monica, California (in preparation).

15. C. H. Karnes, The Plate Impact Configuration for Determining Mechanical Properties at High Strain Rates, in Mechanical Behavior of Materials Under Dynamic Loads, Springor-Vorlag, New York, U. S. Lindholm, Ed., Inc., 1968 (pp 270-293).

16. L. M. Barker, C. D. Lundergan and W. Herrmann, Dynamic Response of Aluminum, J. Appl. Phys., Vol. 35, No. 4, April 1964.

17. J. H. Oscarson and K. F. Graff, Spall Fracture and Dynamic Response of Materials, BAT-197A-4-3, Battelle Memorial Institute, Columbus, Ohio, March 1968.

18. C. J. Maiden and S. J. Green, Interim Report on Response of Materials and Structures to Suddenly Applied Stress Loads (Phase I), DASA-1716, Defense Atomic Support Agency, Advance Research Projects Agency, Department of Defense, October 1965.

19. M. C. Atkins, et al., Radiation Damage Study (RADS), Final Report, Vol. V, Materials Data Handbook (U), BSD TR 66-372, Vol. V, Ballistic Systems Division, Norton Air Force Base, California, September 1966 (SRD).

20. Y. C. Fung, Foundations of Solid Mechanics, Prentice-Hall, Inc., Englewood Cliffs, New Jersey, 1965.

21. B. A. Boley and J. H. Weiner, Theory of Thermal Stresses, John Wiley and Sons, Inc., New York, New York, 1966.

22. N. Cristescu, Dynamic Plasticity, John Wiley and Sons, Inc , New York, New York, 1967.

23. A. E. Green and P. M. Naghdi, A General Theory of an Elastic-Plastic Continuum, Arch. Rational Mech. Anal., Vol. 18, pp. 251-281, 1965.

24. H. A. Bethe, On the Theory of Shock Waves for an Arbitrary Equation of State, OSRD No. 545, National Defense Research Committee, Office of Scientific Research and Development, May 4, 1942.

25. M. H. Rice, R. G. McQueen, and J. M. Walsh, Compression of Solids by Strong Shock-Waves, Solid-State Physics, Vol. 6, pp. 1-63, F. Seitz and D. Turnbull, Eds., Academic Press, Inc., New York, 1958.

26. T. von Karman and P. Duwez, The Propagation of Plastic Deformations in Solids, J. Appl. Phys., Vol. 21, pp. 987-994, October 1950.

27. C. D. Lundergan and W. Hermann, Equation-of-State of 6061-T6 Aluminum at Low Pressures, J. Appl. Phys., Vol. 31, p. 2016, July 1963.

28. G. R. Fowles, Shock-Wave Compression of Hardened and Annealed 2024 Aluminum, J. Appl. Phys., Vol. 32, p. 1475, August 1961.

29. Report D2-9516, The Boeing Company, Aerospace Division, Seattle, Washington.

30. Larry Lee, Sandia Laboratories, Albuquerque, New Mexico. Personal Communication.

31. D. L. McLellan and T. N. Eichenberger, Constitutive Equation Development (COED) SAMSO-TR-68-320, Space and Missile Systems Organization, Norton Air Force Base, California, July 1968.

32. S. G. Babcock and R. D. Perkins, Material Response Studies (MARS I). Volume II - High Strain-Rate Response of Three Heat-Shield Materials at Elevated Temperatures, SAMSO-TR-68-71, Vol. II, Space and Missile Systems Organization, Norton Air Force Base, California, January 1968.

33. A. Kumar, R. D. Perkins, F. L. Schierloch and D. L. Holt, Material Response Studies (MARS I), Volume V - Dynamic Behavior of Polymers and Composites, SAMSO TR-68-71, Vol. V, Space and Missile Systems Organization, Norton Air Force Base, California, January 1968.

34. W. M. Isbell, N. Froula and F. H. Shipman, Shock-Wave Propagation and Equation-of-State Measurements of Quartz-Phenolic, BSD-TR-67-25, Ballistic Systems Division, Norton Air Force Base, California, February 1967.

35. J. A. Charest and B. D. Jenrette, Hugoniot Equations-of-State of Tape Wrapped Two-Dimensional Quartz-Phenolic, Technical Report No. S-448-R, EG&G, Inc., Goleta, California, February 1969.

36. G. A. Jones, The Shorted Guard-Ring Quartz Gage, SC-RR-67-568, Sandia Laboratories, Albuquerque, New Mexico, August 1967.

37. J. A. Charest, EG&G, Inc., Goleta, California. Personal Communication.

38. J. J. Dick, Stanford Research Institute, Menlo Park, California. Personal Communication.

39. Lynn Seaman, Stanford Research Institute, Menlo Park, California. Personal Communication.

40. R. L. Warnica and J. A. Charest, Spallation Thresholds of Quartz-Phenolic, BSD-TR-67-24, Ballistic Systems Division, Norton Air Force Base, California, February 1967.

41. S. J. Green, S. G. Babcock, and R. D. Perkins, Response of Several Re-entry Vehicle Materials to Impulsive Loads, BSD-TR-67-23, Ballistic Systems Division, Norton Air Force Base, California, February 1967.

42. J. L. Clathart and F. W. Preston, The Fatigue Modulus of Glass, J. Appl. Phys., Vol. 17, p. 189, 1946.

43. N. W. Taylor, Mechanism of Fracture of Glass and Similar Brittle Solids, J. Appl. Phys., Vol. 18, p. 943, 1947.

44. A. J. Holland and W. E. S. Truner, Effect of Sustained Loading or Breading Strength of Sheet Glass, J. Soc, Glass Technol., Vol. 24, p. 47, 1940.

45. J. Glucklich and L. J. Cohen, Strain Energy and Size Effects in a Brittle Material, ASTM, Materials Research and Standards, October 1968.

46. O. Ishai, Delayed Yielding of Epoxy Resin Under Tension, Compression, and Flexure, Part I: Behavior Under Constant Strain Rate; Part II: Behavior Under Constant Stress, J. of Applied Polymer Science, Vol. II, 1967 (Part I: p. 963, Part II: p. 2303).

47. S. N. Zhurkov and T. P. Sanforova, Relation Between Strength and Creep of Metals and Alloys, Soviet Physicis - Technical Physicis, 3, 1958, p. 1586.

48. S. N. Zhurkov and T. P. Sanforova, Study of the Time-Temperature Dependence of Mechanical Strength, Soviet Physicis - Solid State, 1960, p. 933.

49. C. A. Hazel, The Effect of Strain Rate on the Tensile Properties of Thermoplastics: Part 3, Stress and Time and Maximum Yield, Report No. 2/R/61, AD 267-492, Ministry of Aviation, Explosives Research and Development Establishment, Watham Abbey, Essex, 1961.

50. F. M. Klinger, Tensile Properties of Some Aircraft Materials at Various Rates of Loadings, Proc. ASTM, Vol. 50, p. 1035, 1950.

51. H. Kolsky and Y. Y. Shi, Fractures Produced by Stress Pulses in Glass-Like Solids. Proc. of the Physical Soc., Vol. 72, pt. 3, No. 465, p. 447, London 1958.

52. The Modulus and Yield Stress of Glassy PMMA at Strain Rates up to 10^3 Inch/Inch/Second, MARS TASK 5 Progress Report, USAF, Space and Missiles Systems Organization, Norton Air Force Base, California, July 1967.

53. S. G. Babcock, A. Kumar, S. J. Green, Response of Materials to Suddenly Applied Stress Loads, Part I: High-Strain Rate Properties of Eleven Re-Entry Vehicle Materials at Elevated Temperature, AFFDL-TR-67-35, Part 1, Air Force Flight Dynamics Laboratory, Wright-Patterson Air Force Base, Ohio, April 1967.

54. W. Herrmann, Basic Response Phenomenology and Analytical Techniques, Unclassified Paper in: Proceedings of the X-Ray Effects Conference. Vol. I, Material Response (Unclassified Title), DASA Report 2007, Defense Atomic Support Agency, November 1967 (SRD).

55. D. R. Keller and D. M. Young, A Method for Determining Spallation Criteria in Solids, AFSWC-TRD-61-102, Air Force Special Weapons Center, Kirtland Air Force Base, New Mexico, November 1961.

56. J. R. Penning, D. M. Young and J. H. Prindle, Negative Equation of State and Spall Criteria, RTD-TDR-63-3039, Air Force Weapons Laboratory, Kirtland Air Force Base, New Mexico, September 1963.

57. B. M. Butcher, L. M. Barker, D. E. Munson and C. D. Lundergan, "Influence of Stress History on Time-Dependent Spall in Metals," AIAA Journal, Vol. 2, No. 6, p. 977, 1964.

58. J. A. Charest and R. L. Warnica, Spallation Thresholds of I-400 Beryllium. G. M. Defense Research Laboratories, Santa Barbara, California, TR-66-34, July 1966.

59. B. R. Breed, C. L. Mader, and D. Venable, Technique for the Determination of Dynamic-Tensile-Strength Characteristics, J. Appl. Phys., 38, p. 3271, 1967.

60. P. Whiteman, Report No. UNDEX 445, Atomic Weapons Research Establishment, 1962.

61. A. N. Stroh, A Theory of the Fracture of Metals, Advances in Physics, Vol. 6, pp. 418-465, October 1967.

62. J. C. Peck, H. M. Berkowitz, and L. J. Cohen, The Relationship of the Critical Stress Versus Impulse Theory of Spall Fracture to Stress-Gradient or Stress-Rate Theories, Douglas Paper 5318, MDAC-WD Santa Monica, California, September 1968. (To be published in the Int. J. Fracture Mechanics.)

63. F. R. Tuler and B. M. Butcher, A Criterion for the Time-Dependence of Dynamic Fracture. (To be published in the Int. J. Fracture Mechanics.)

64. H. M. Berkowitz, Failure Criteria for Short Duration Stress-Wave Pulse Loads, Internal Memorandum No. A-830-BBGO-798, MDAC-WD, Santa Monica, California, October, 1968.

65. L. J. Cohen, Fundamental Considerations of Dynamic Fracture Caused by Wave Propagation Through Plates, DAC 62274, MDAC-WD, Santa Monica, California, June 1968.

66. Z. N. Zhurkov and B. N. Narzullaev, J. Tech. Phys. (USSR), Vol. 23, p. 1677, 1953.

67. C. C. Hsiao, Time-Dependent Fracture, Tech. Report 18, AEC Contract AT (11-1) 532, September 1962.

68. L. J. Cohen and O. Ishai, Delayed Yielding of Three-Phase Epoxy Composites, Meeting Preprint 711, ASCE Annual Meeting and National Meeting of Structural Engineering, September 30 - October 4, 1960, Pittsburgh, Pa. (to be published).

69. H. Eyring, "Viscosity, Plasticity and Diffusion as Examples of Absolute Reaction Rates," J. Chem. Phys., Vol. 4, p. 283, 1936.

70. F. Bueche, Physical Properties of Polymers, Interscience Publishers, New York, p. 251, 1962.

71. F. Bueche, "Tensile Strength of Plastics: Effects of Flaws and Chain Relaxation," J. Appl. Phys., Vol. 29, p. 1231, 1958.

72. H. Kolsky, "Fracture Produced by Stress Waves," In Fracture, edited by B. L. Averbauch, D. K. Felbeck, G. T. Hahn and D. A. Thomas, p. 281, John Wiley and Sons, New York, New York, 1959.

73. L. J. Cohen, Rate-Dependent Yielding of a Three-Phase Composite Material, Internal Memorandum A-830-BBGO-60, 1968, MDAC-WD, Santa Monica, California.

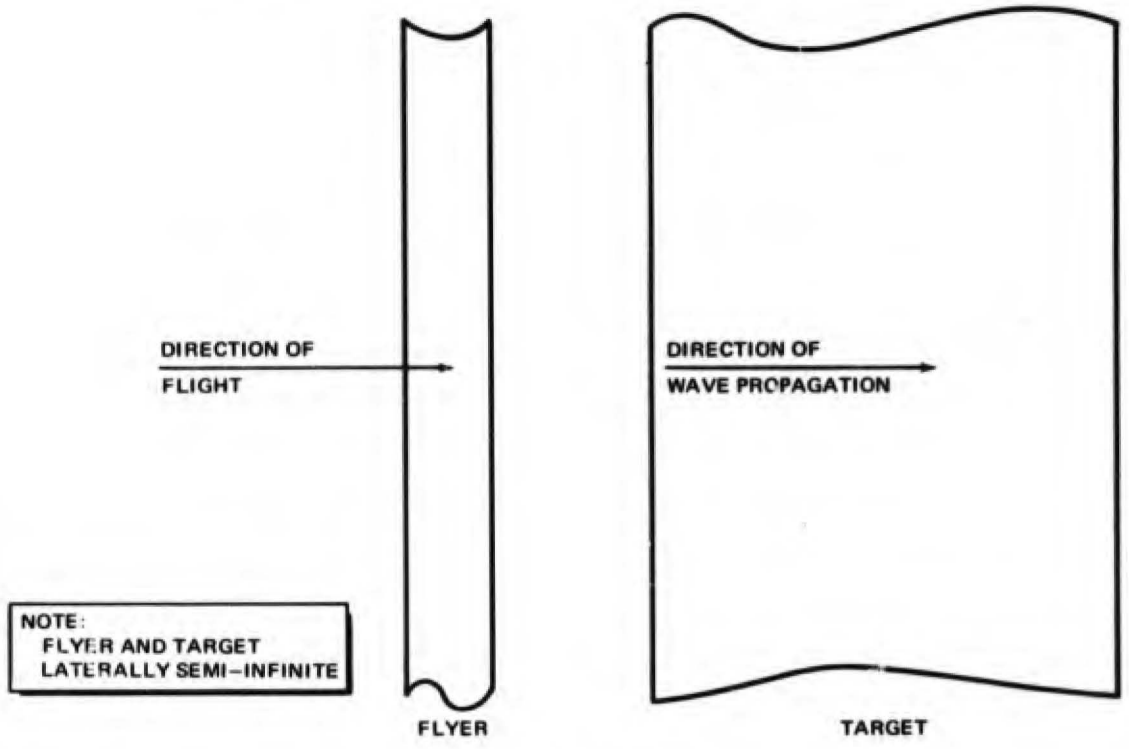

Figure 1. Idealization of Plate-Impact Configuration

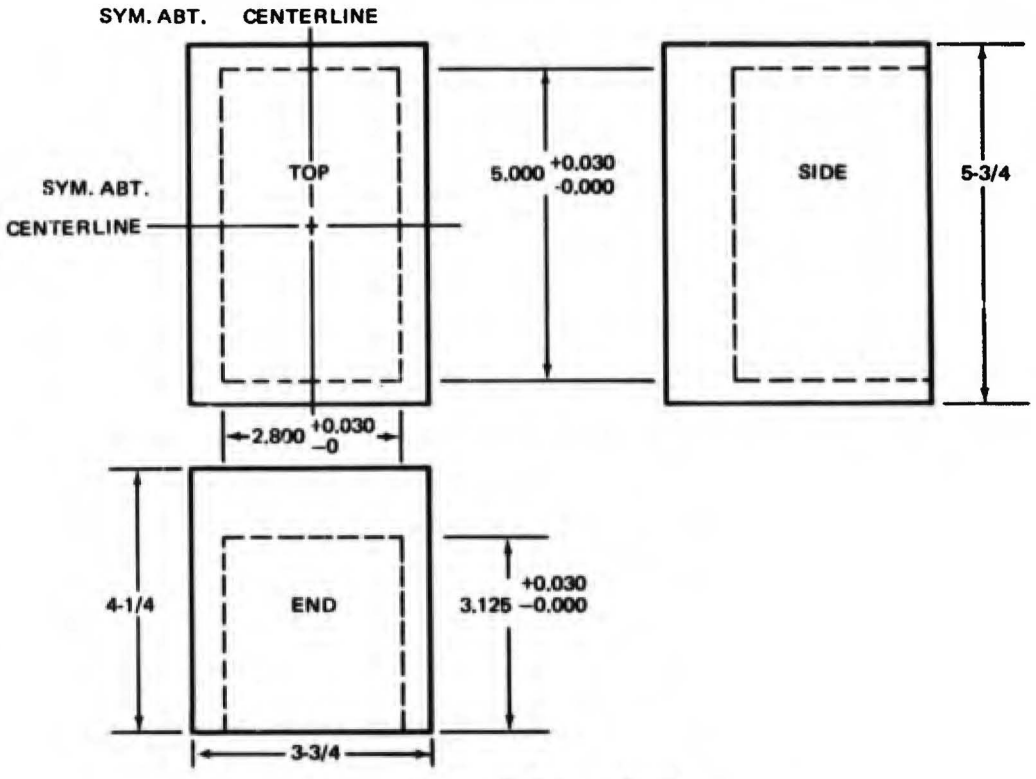

Figure 2. Trim of Block

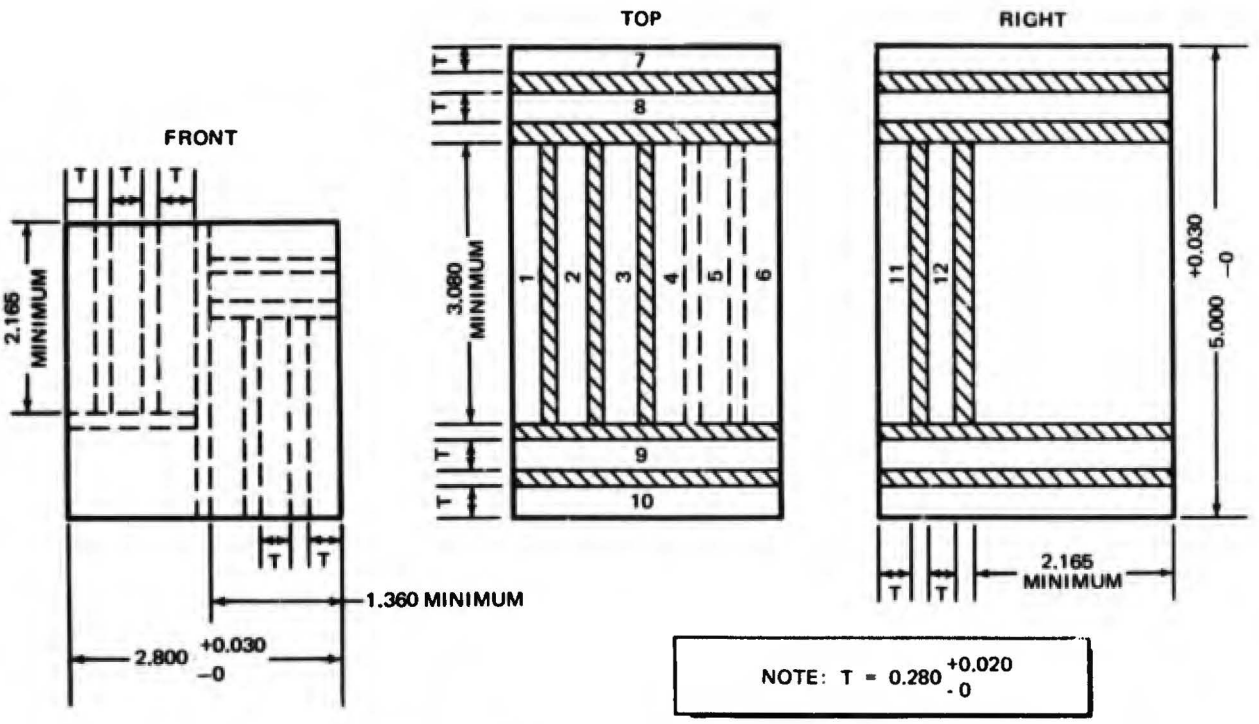

Figure 3. Blanks from Block Remaining After Trim

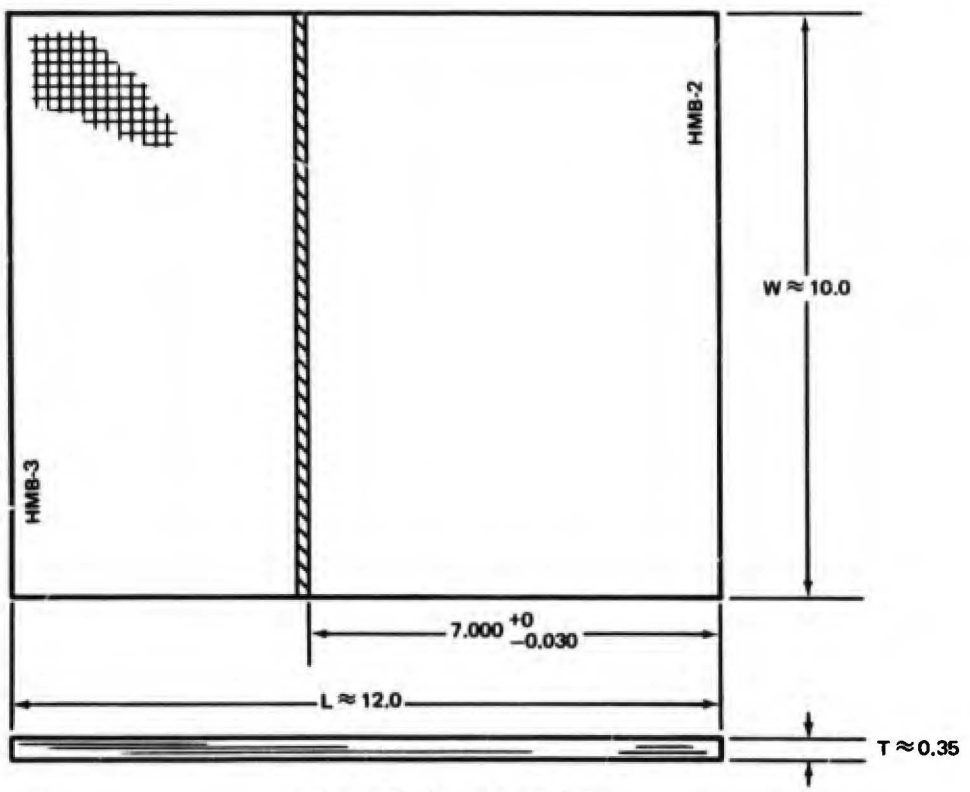

Figure 4. Blanks from Panel

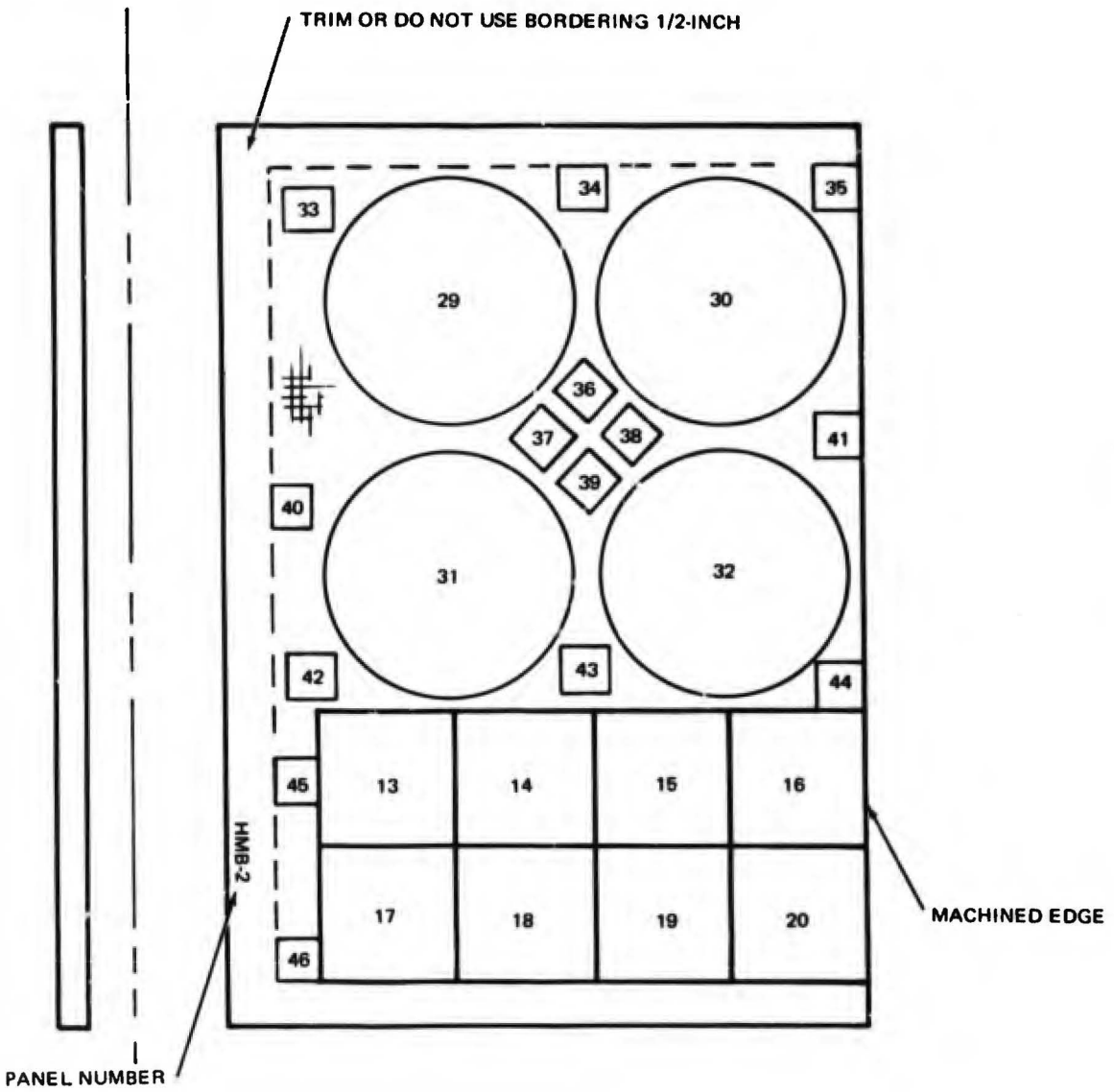

Figure 5. Specimens from Panel HMB-2

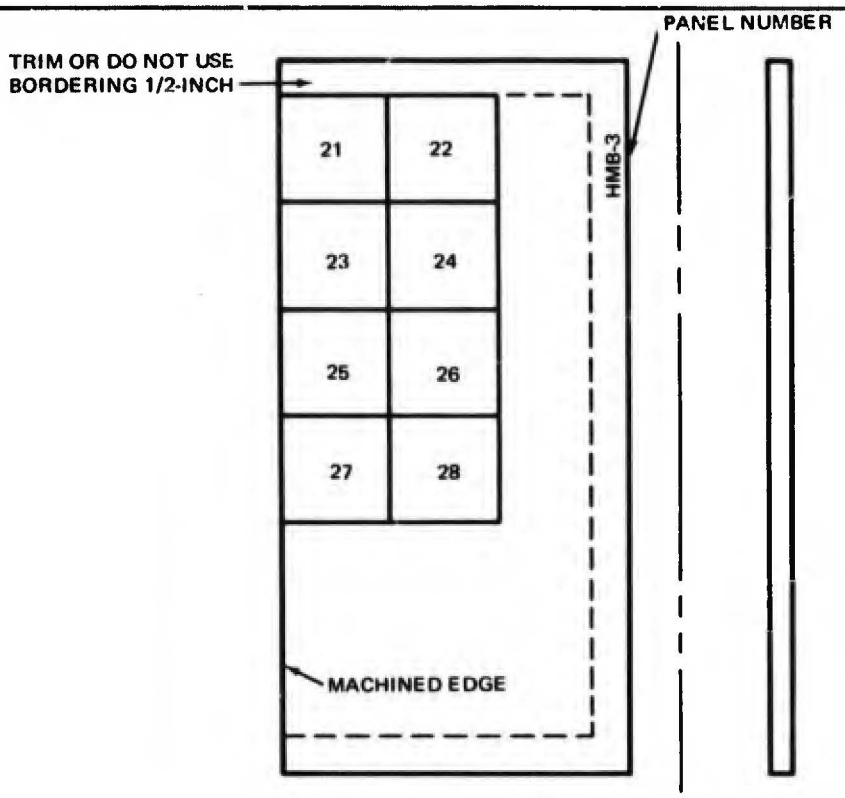

Figure 6. Specimens from Panel HMB-3

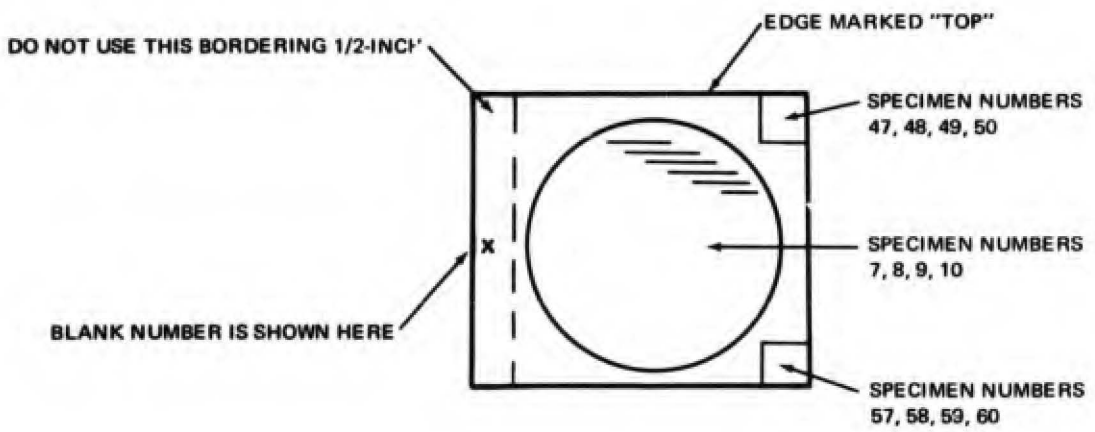

NOTE: LAST DIGIT IN SPECIMEN NUMBER CORRESPONDS TO LAST DIGIT OF NUMBER ON BLANK

Figure 7. Specimens from Blanks 7, 8, 9, 10

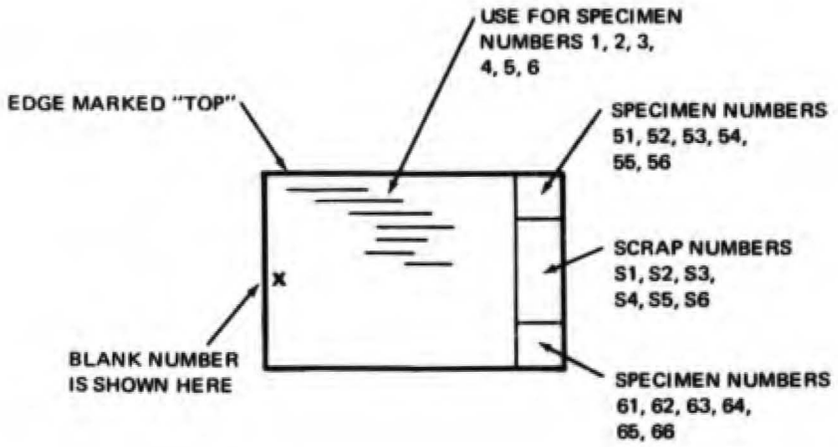

NOTE: LAST DIGIT IN SPECIMEN NUMBER CORRESPONDS TO NUMBER ON BLANK

Figure 8. Specimens from Blanks 1, 2, 3, 4, 5, 6

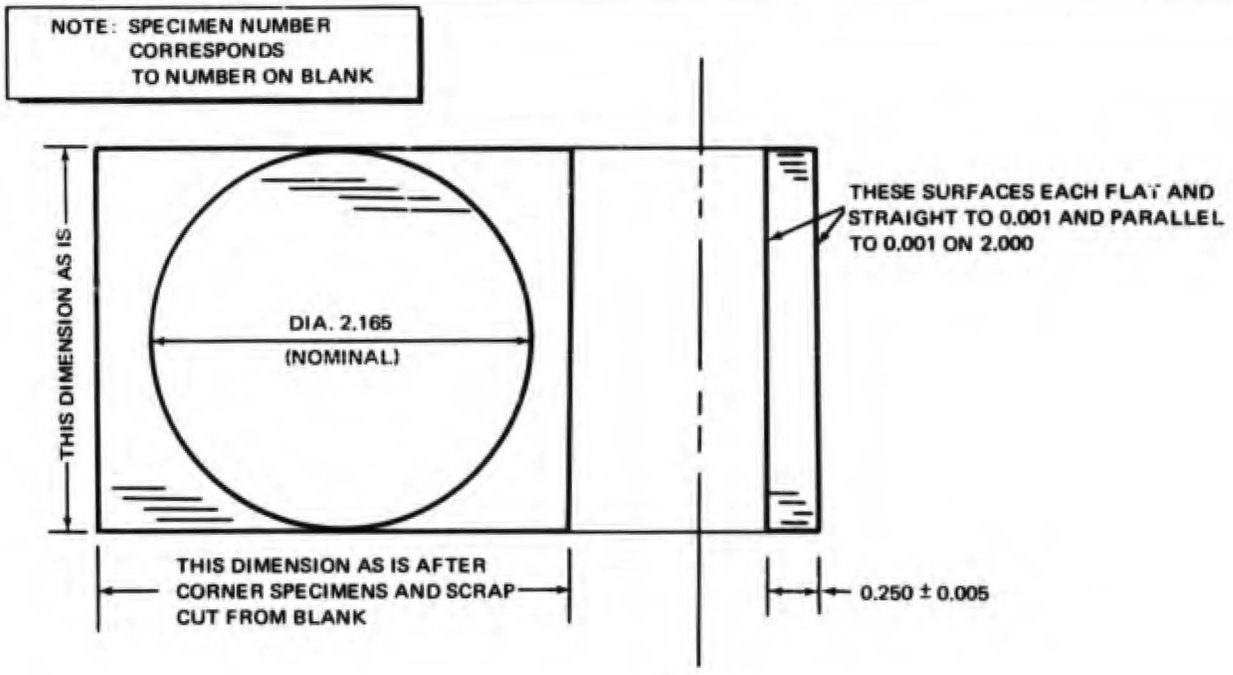

Figure 9. Dimensions of Specimens 1, 2, 3, 4, 5, 6

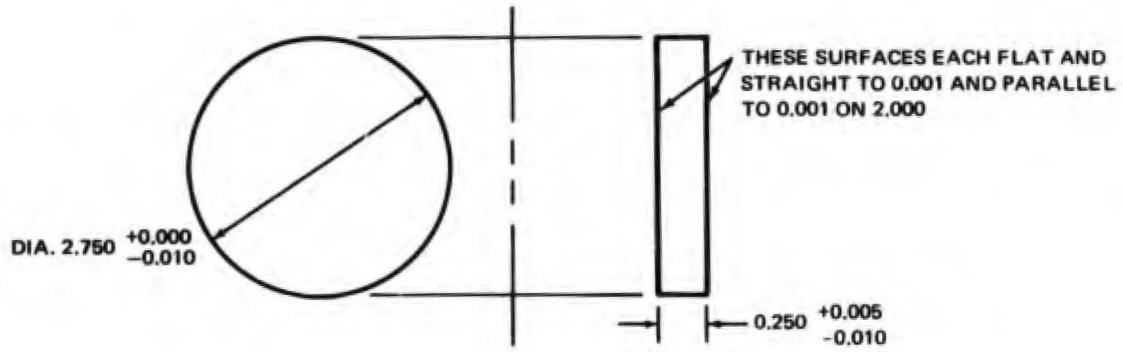

NOTE: MACHINE BOTH SURFACES
FOR SPECIMENS 29, 30, 31, 32
TO REMOVE EXCESS RESIN LAYER

Figure 10. Dimensions of Specimens 7, 8, 9, 10, 29, 30, 31, 32

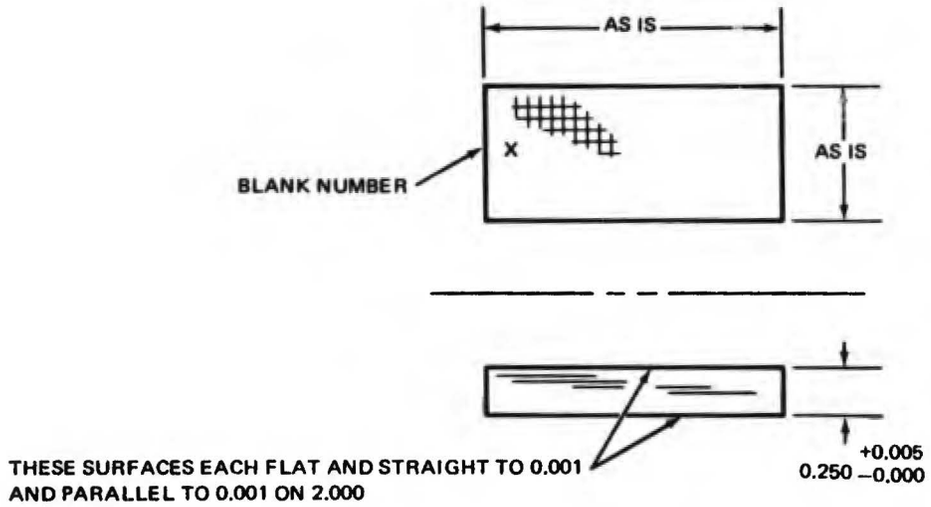

Figure 11. Dimensions of Specimens 11 and 12 (from Blanks 11 and 12)

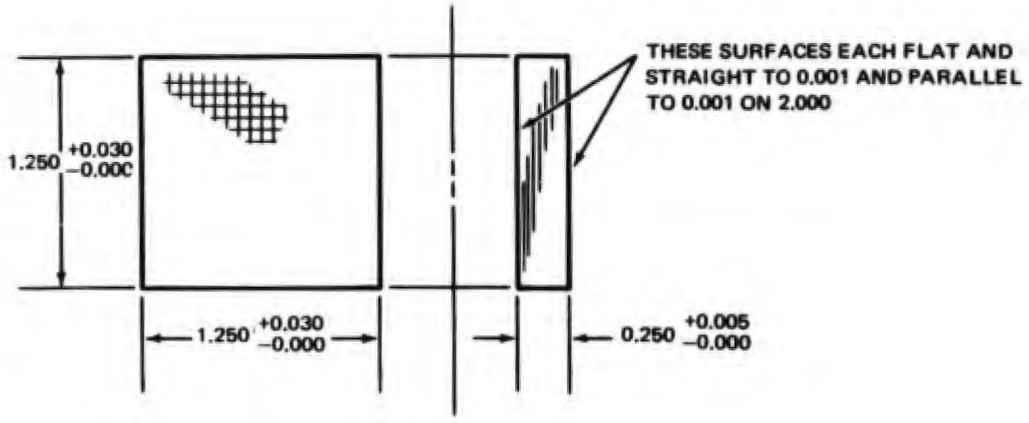

NOTE: MACHINE BOTH SURFACES TO REMOVE EXCESS RESIN LAYER

Figure 12. Dimensions of Specimens 13 Through 28

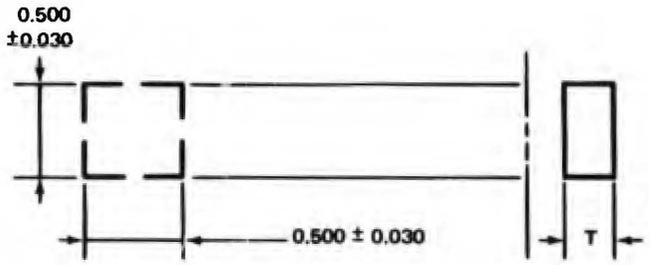

NOTES: (a) SPECIMENS 33 THROUGH 46; T = 0.250 +0.050 −0.000 (MACHINE BOTH SURFACES)

(b) SPECIMENS 47 THROUGH 66; T = AS IS

Figure 13. Dimensions of Specimens 33 Through 66

NOTE: ALL DIMENSIONS IN INCHES
NOT TO SCALE
(SCALE APPROX.)

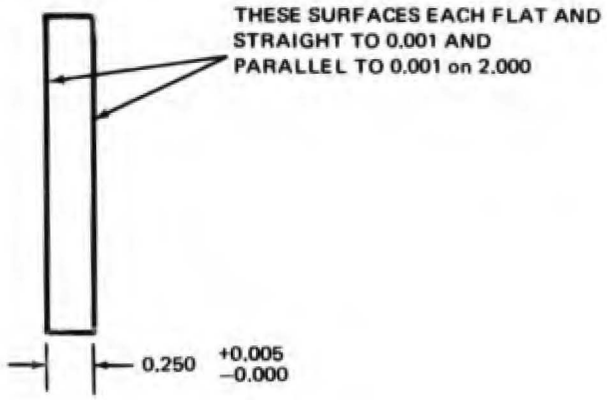

Figure 14. Thickness Machining of Surfaces of Quartz-Phenolic Blanks for Specimen P1 – P6

NOTE: ALL DIMENSIONS IN INCHES

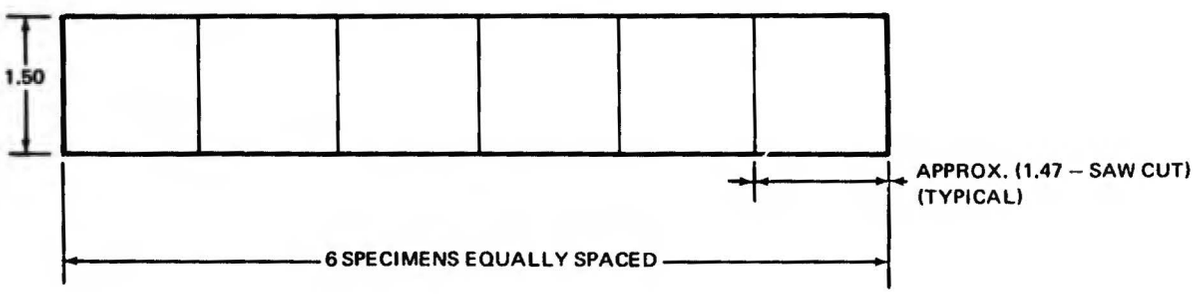

Figure 15. Cutting of Quartz-Phenolic Specimens P1 Through P6 from Machined Blank

NOTE: ALL DIMENSIONS IN INCHES

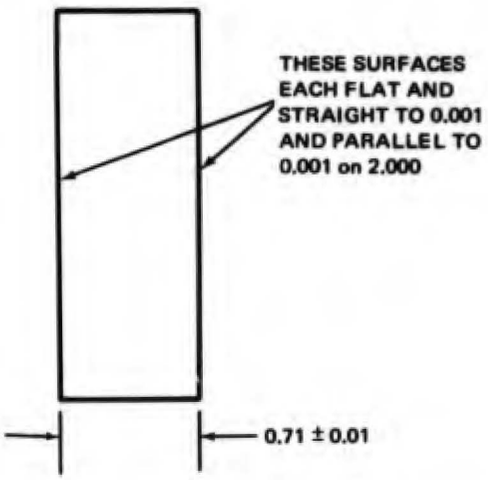

Figure 16. Thickness Machining of Surfaces of 6061-T6 Aluminum Blank

NOTE: ALL DIMESIONS IN INCHES

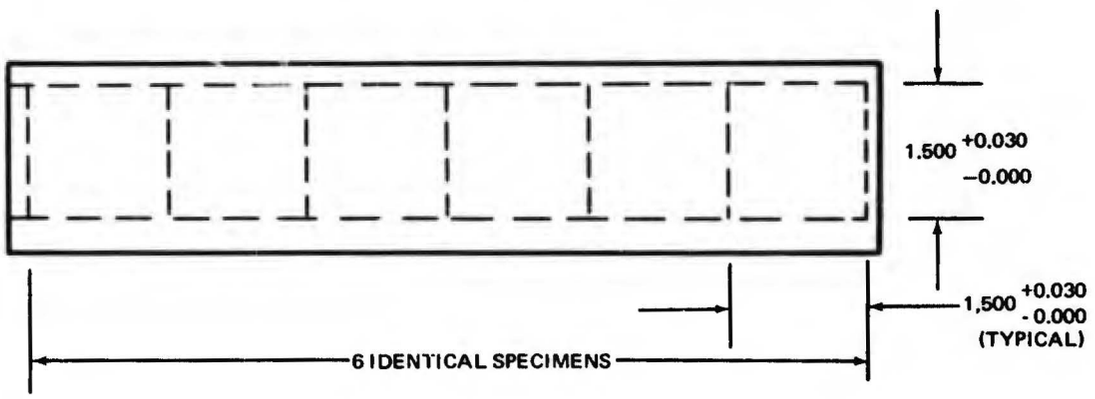

Figure 17. Cutting of Aluminum Back Up Blocks from Machined Blank

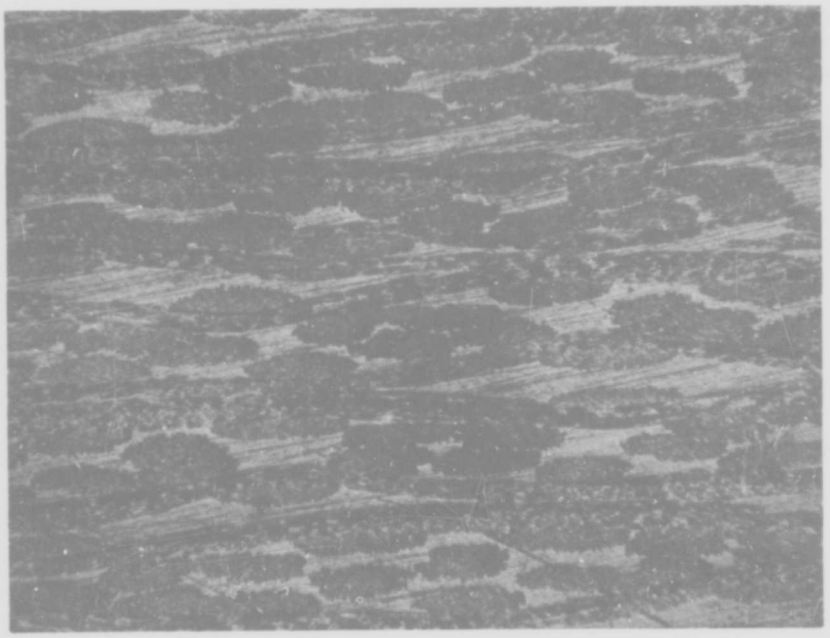

Figure 18. Specimen No. 44 Parallel to Direction of Reinforcement – 25X

Figure 19. Specimen No. 46 Parallel to Direction of Reinforcement – 25X

Figure 20. Specimen No. 51 Perpendicular to Direction of Reinforcement – 25X

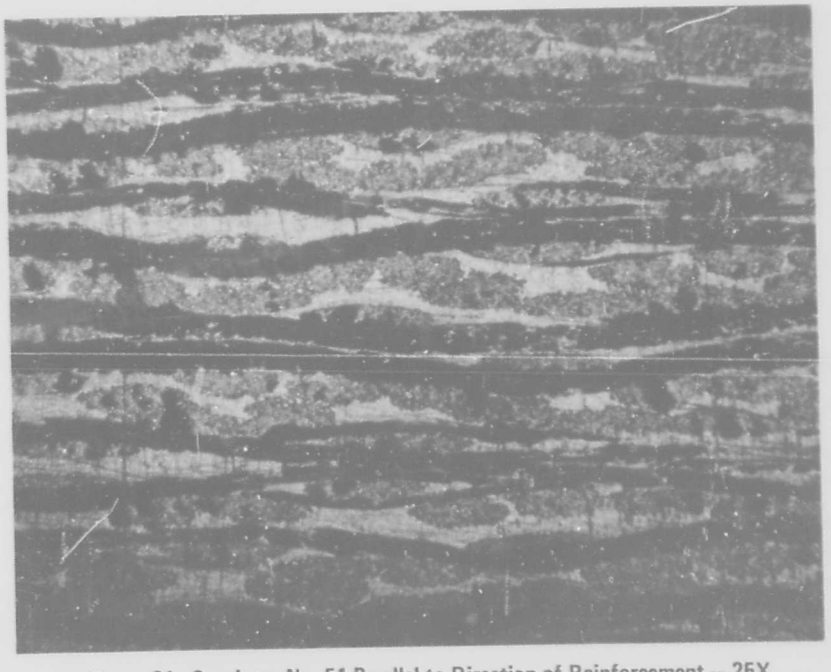

Figure 21. Specimen No. 51 Parallel to Direction of Reinforcement – 25X

NOT REPRODUCIBLE

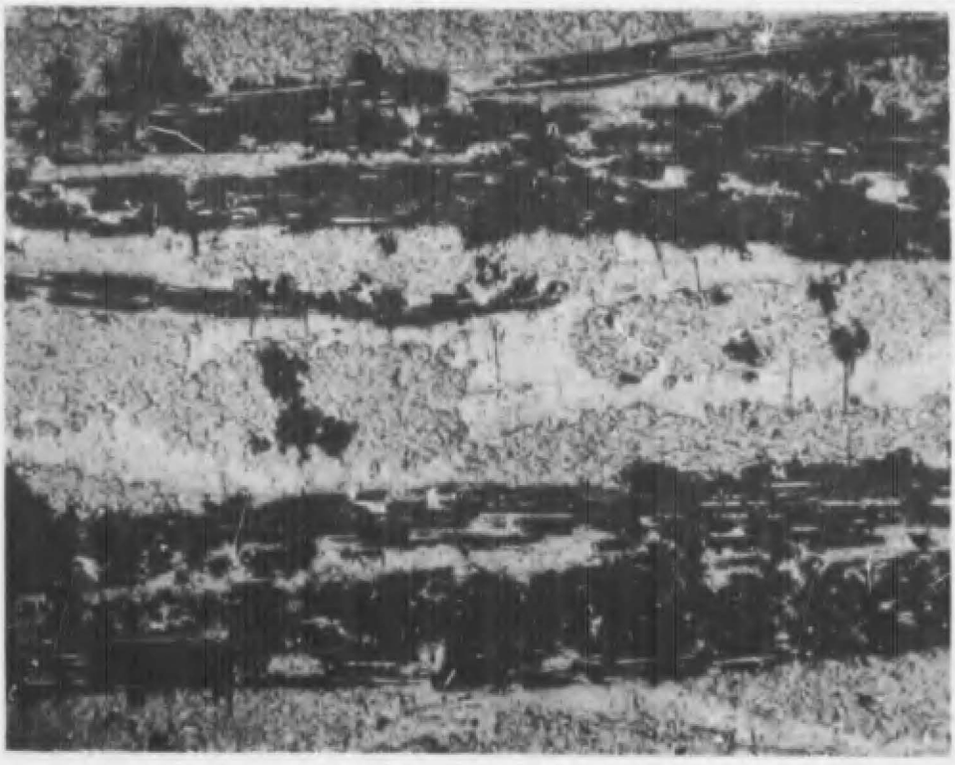

Figure 22. Specimen No. 51 Parallel to Direction of Reinforcement – 75X

Figure 23. Specimen No. 63 Perpendicular to Direction of Reinforcement – 6X

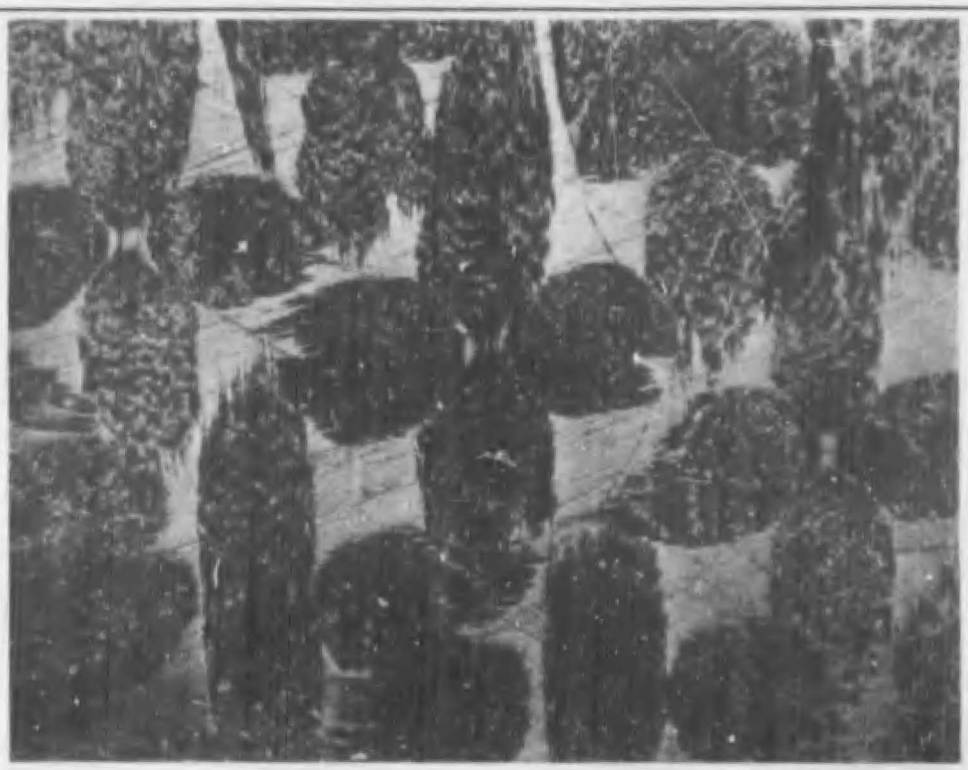

Figure 24. Specimen No. 63 Perpendicular to Direction of Reinforcement – 25X

Figure 25. Specimen No. 63 Parallel to Direction of Reinforcement – 6X

NOT REPRODUCIBLE

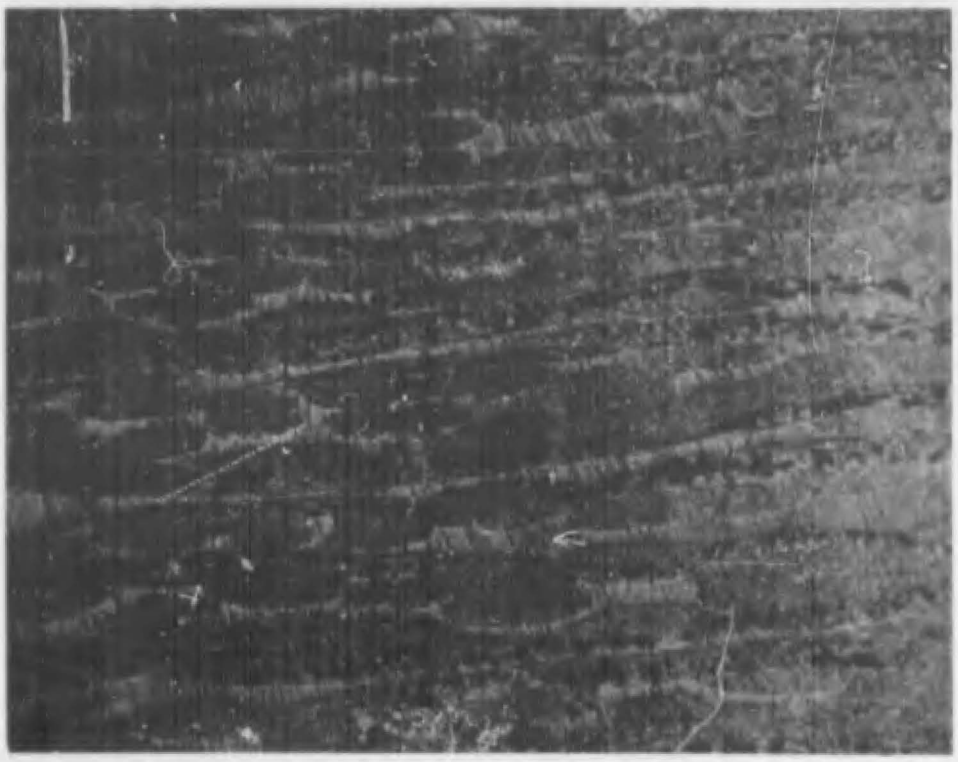

Figure 26. Specimen No. 63 Parallel to Direction of Reinforcement – 25X

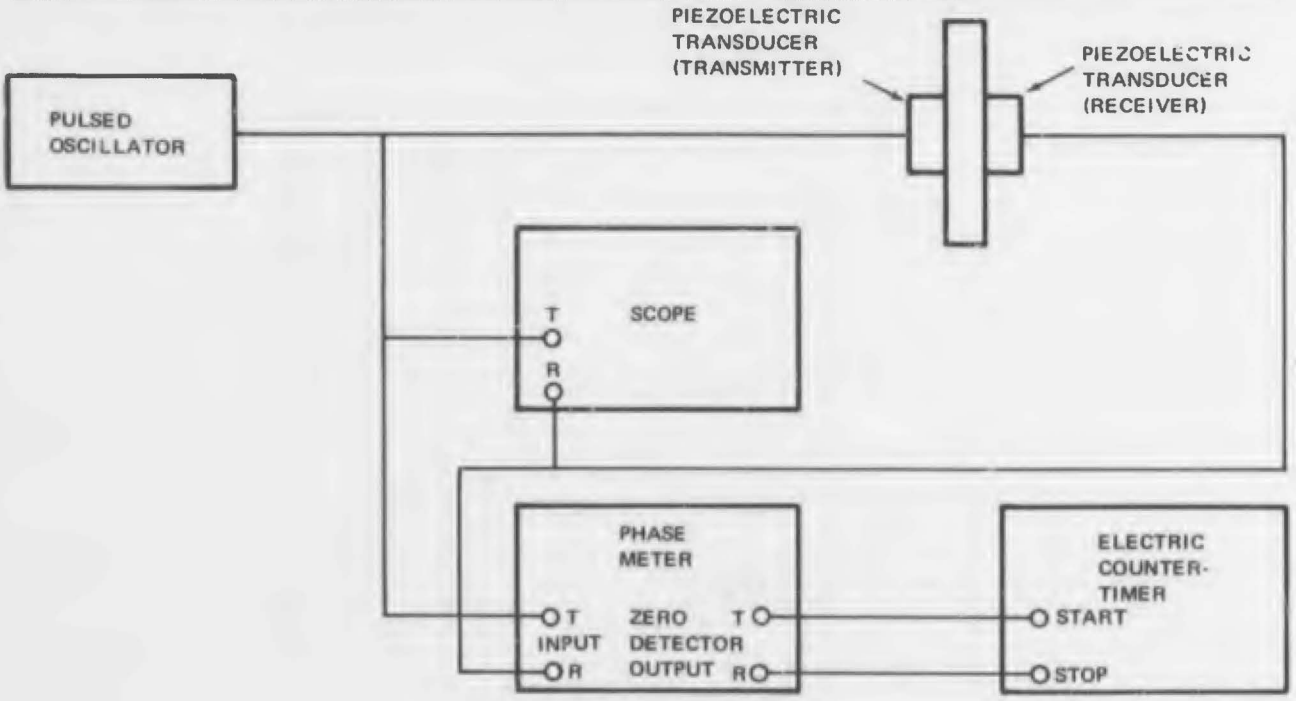

Figure 27. Test Setup for Measurement of Sinusoidal Wave Velocity in Materials

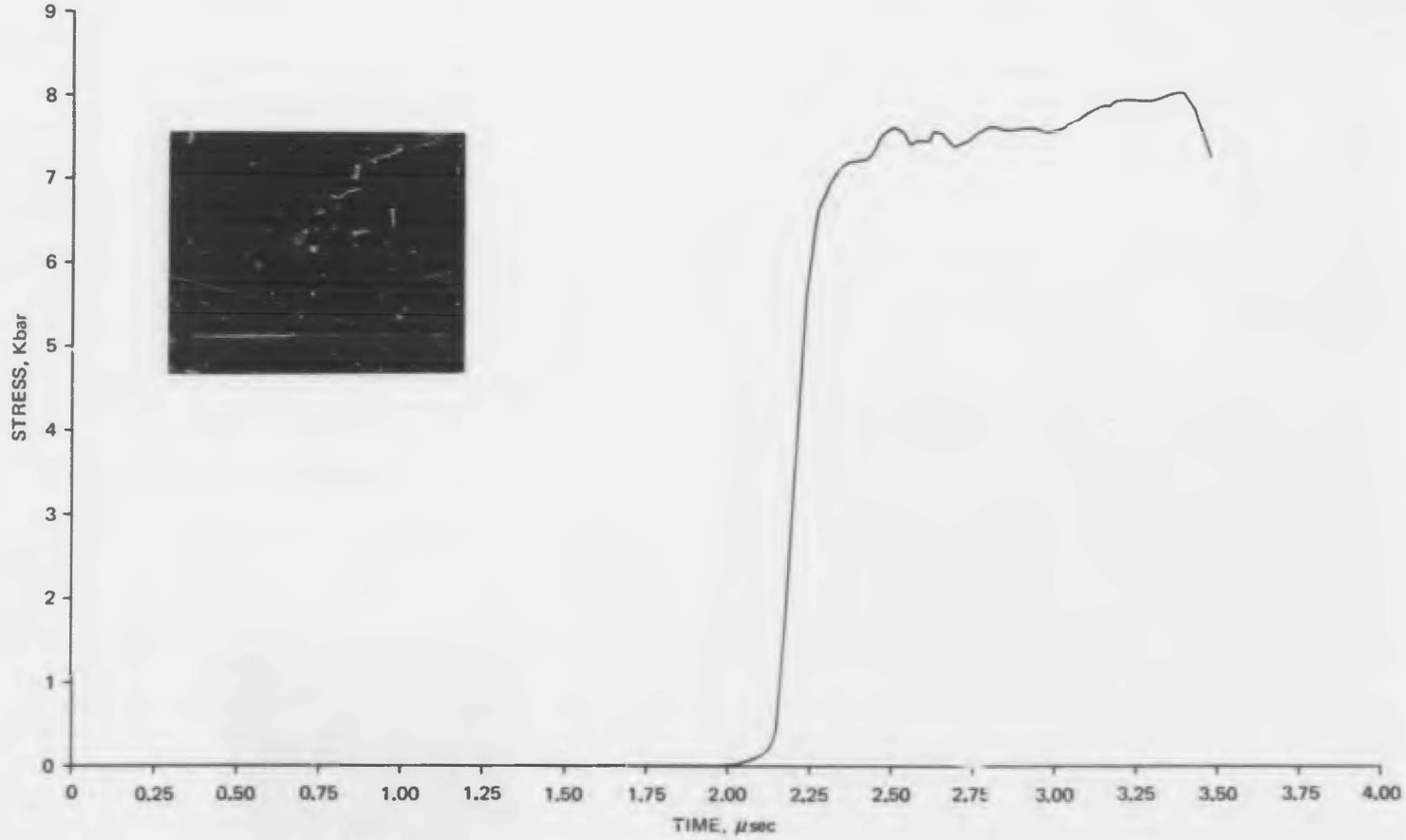

Figure 28. Stress-Time Profile, Shot 13594: Hugoniot Shot on Zero-Degree Quartz-Phenolic

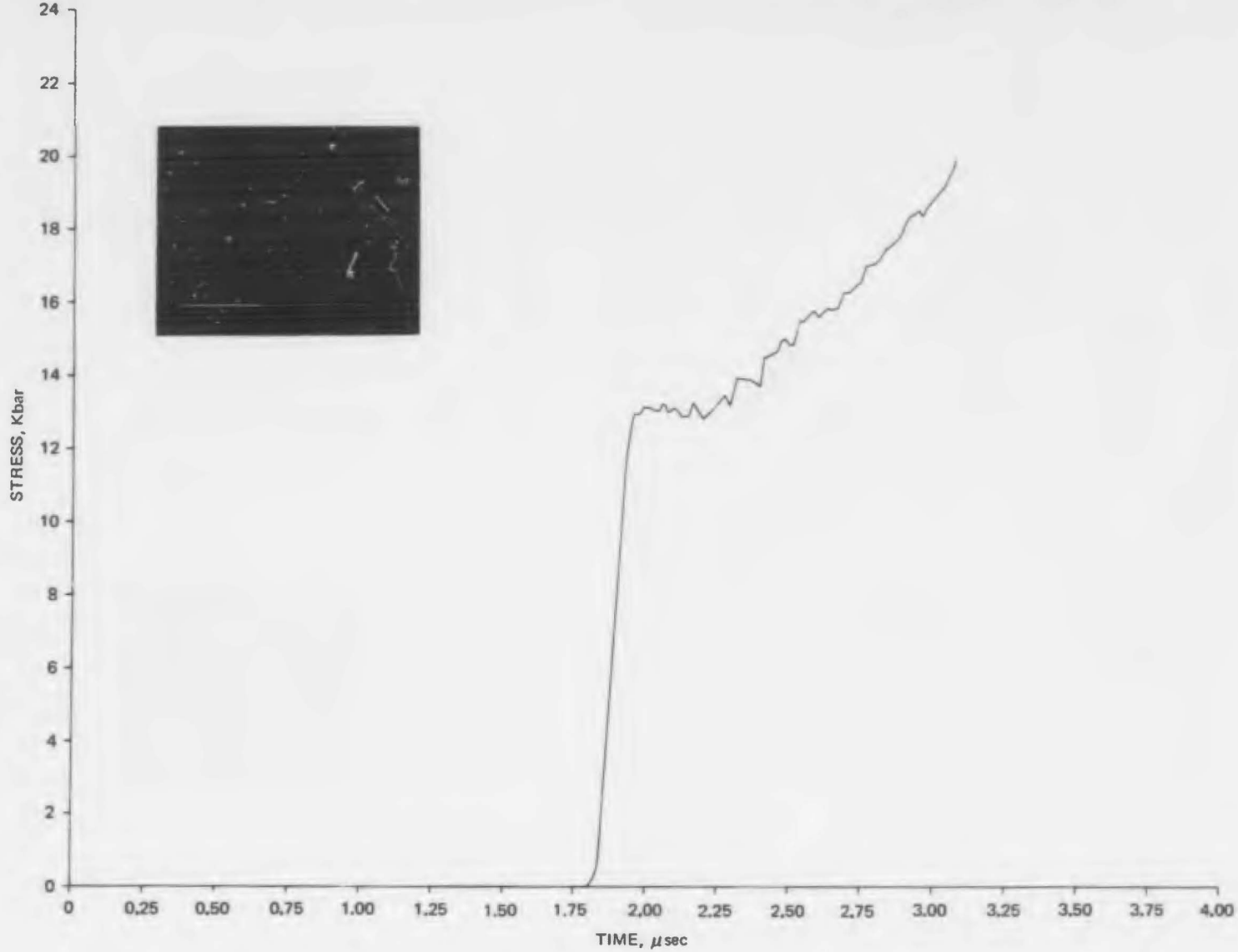

Figure 29. Stress-Time Profile, Shot 13605: Hugoniot Shot on Zero-Degree Quartz-Phenolic

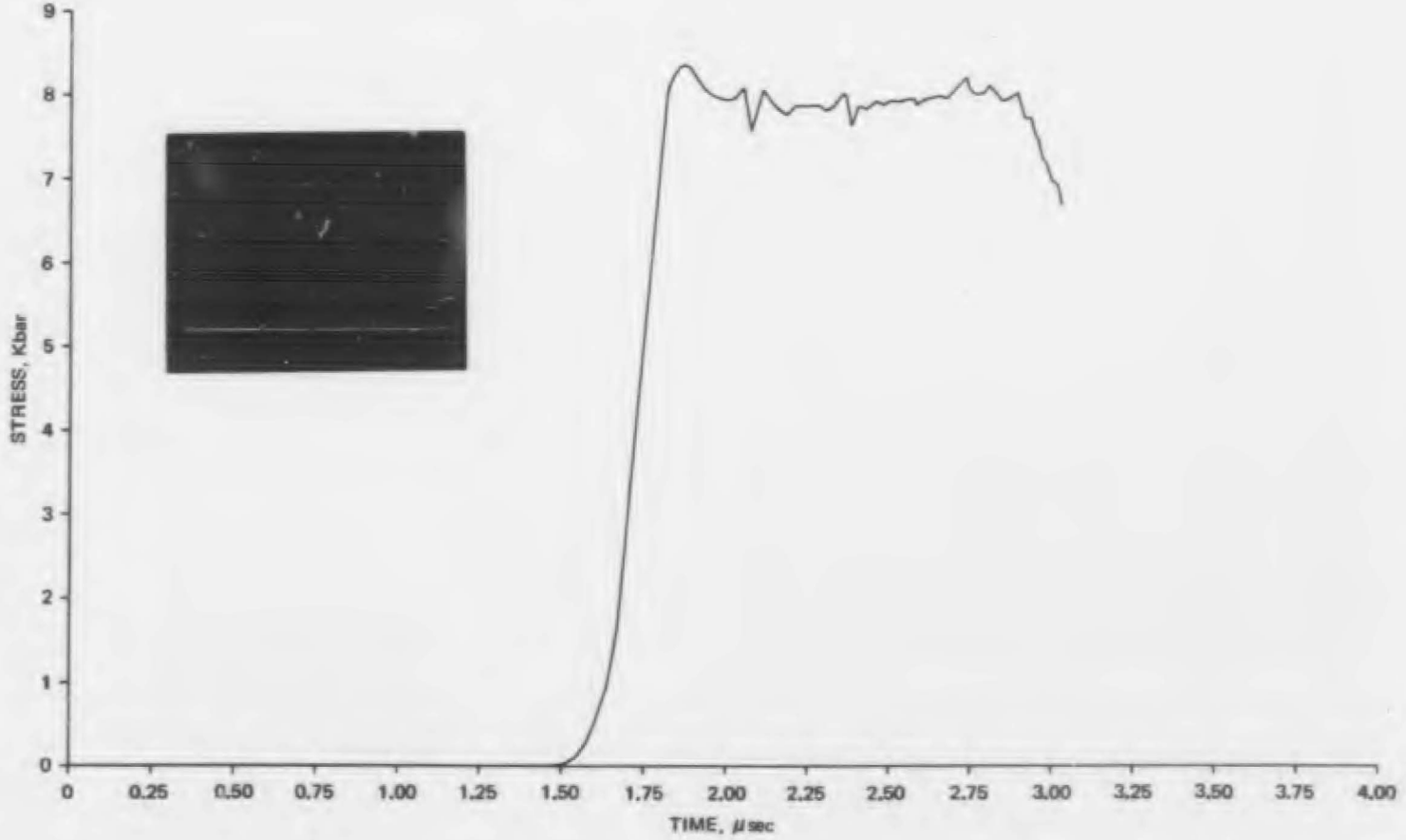

Figure 30. Stress-Time Profile, Shot 13603: Hugoniot Shot on 90-Degree Quartz-Phenolic

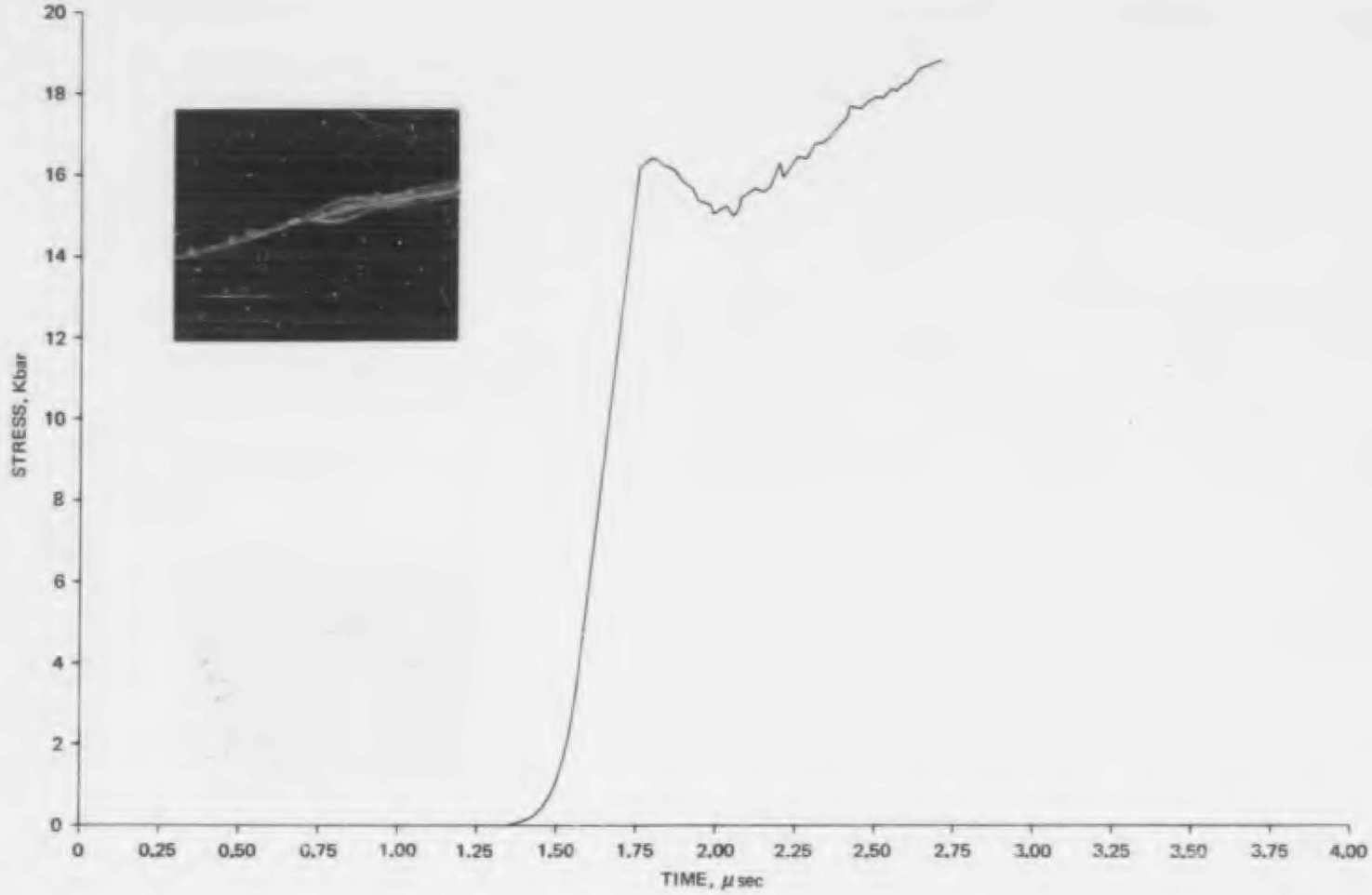

Figure 31. Stress-Time Profile, Shot 13606: Hugoniot Shot on 90-Degree Quartz-Phenolic

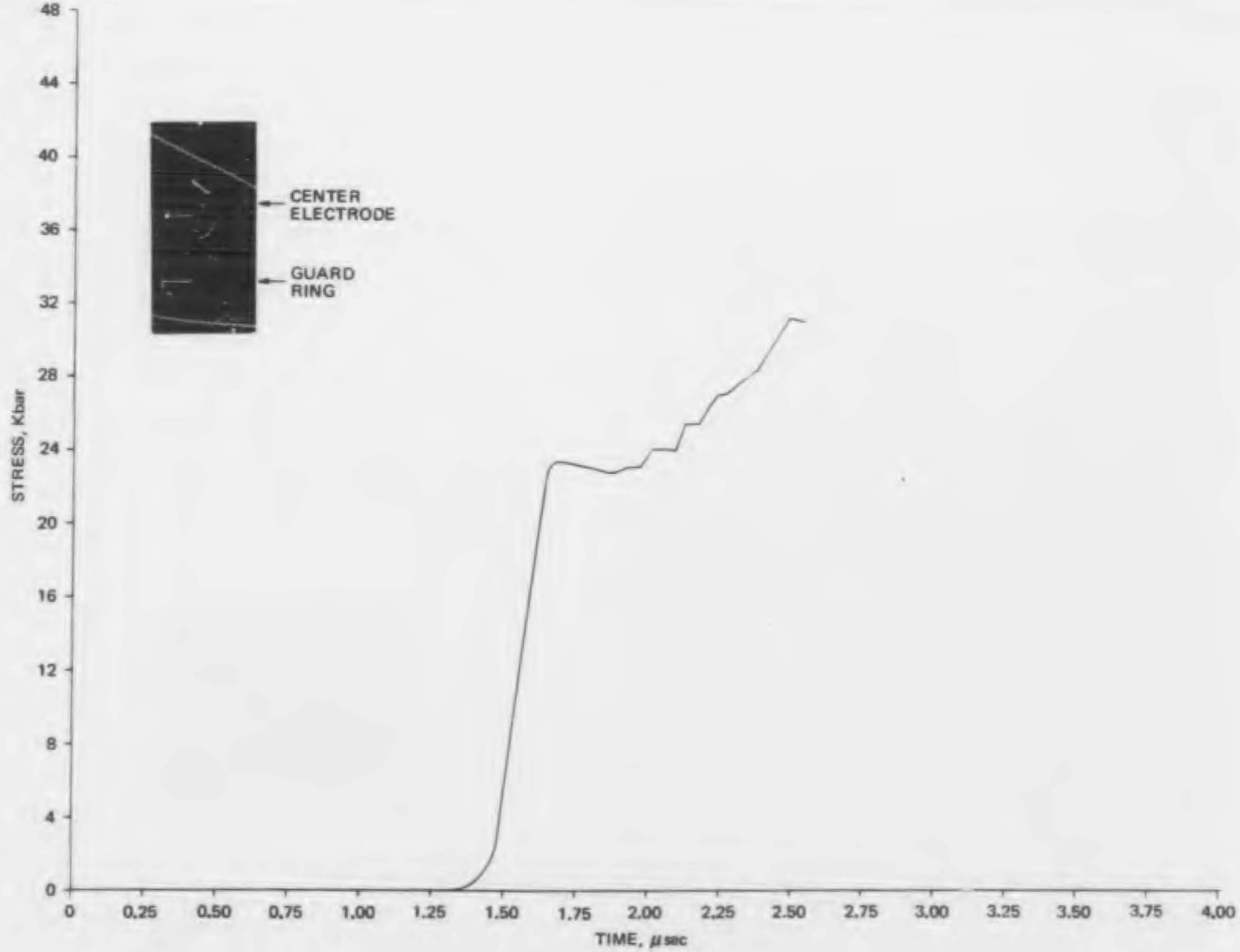

Figure 32. Stress-Time Profile, Shot 13604: Hugoniot Shot on 90-Degree Quartz-Phenolic

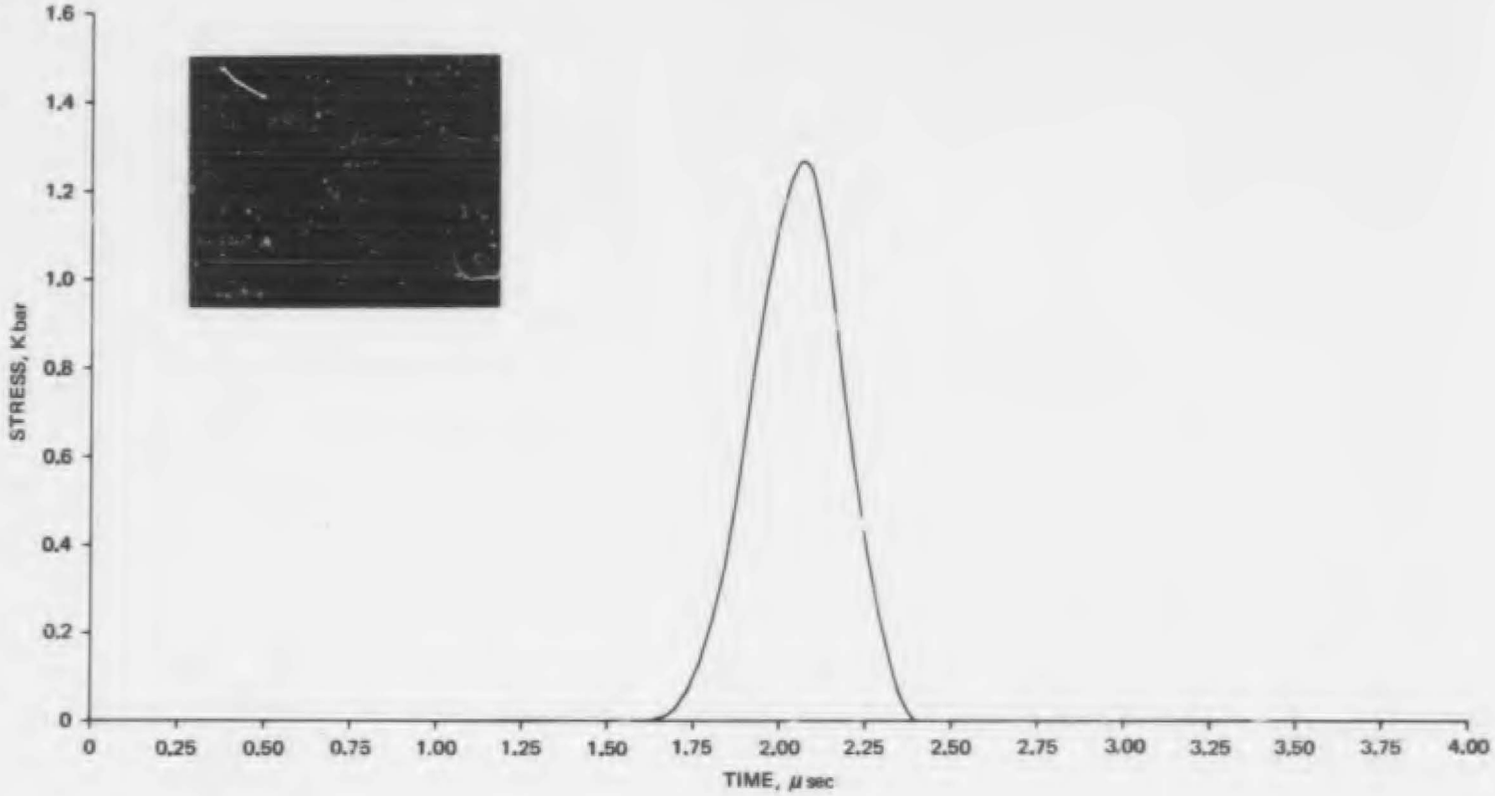

Figure 33. Stress-Time Profile, Shot 13592: Attenuation Shot on 90-Degree Quartz-Phenolic

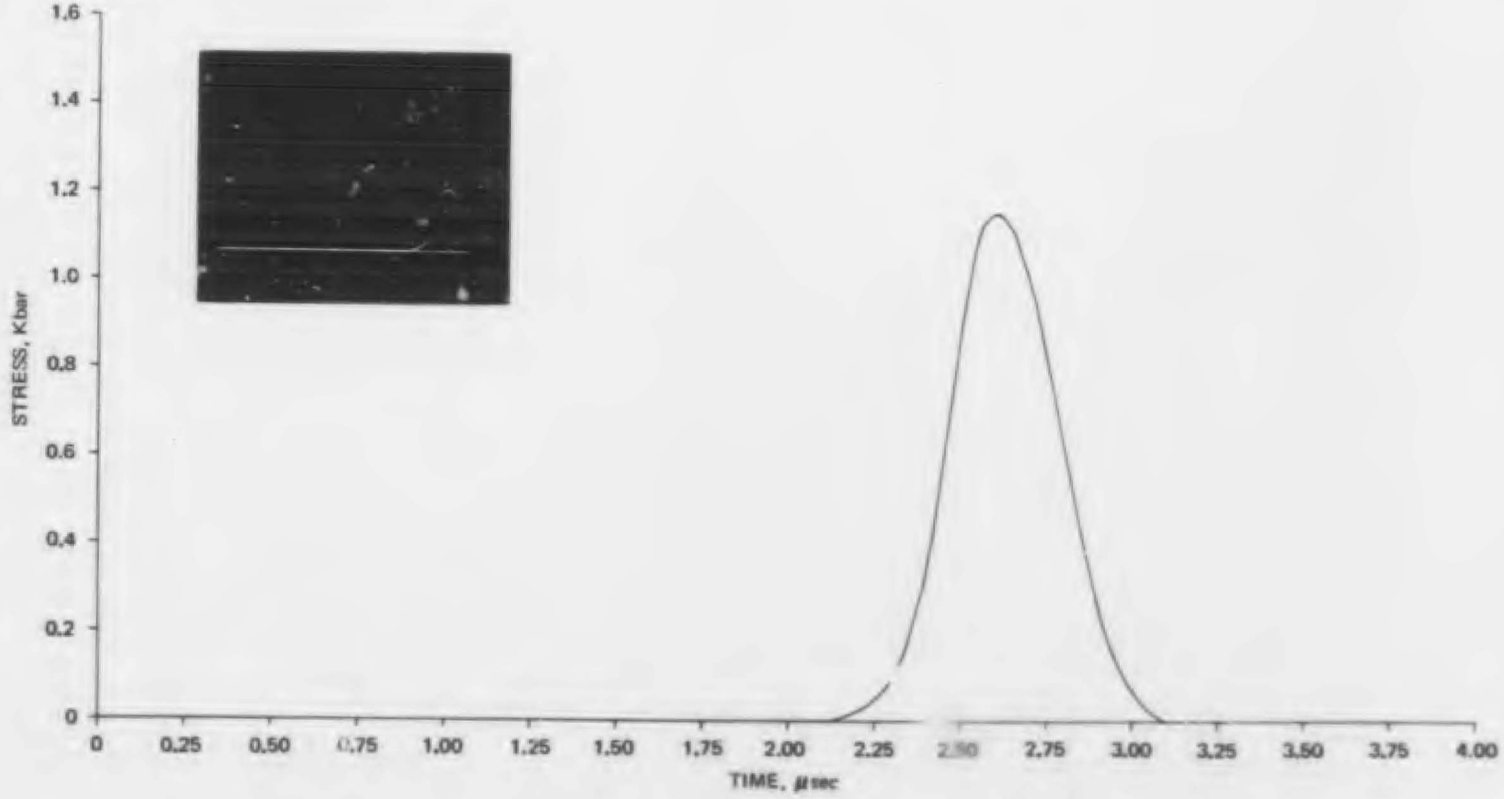

Figure 34. Stress-Time Profile, Shot 13595: Attenuation Shot on Zero-Degree Quartz-Phenolic

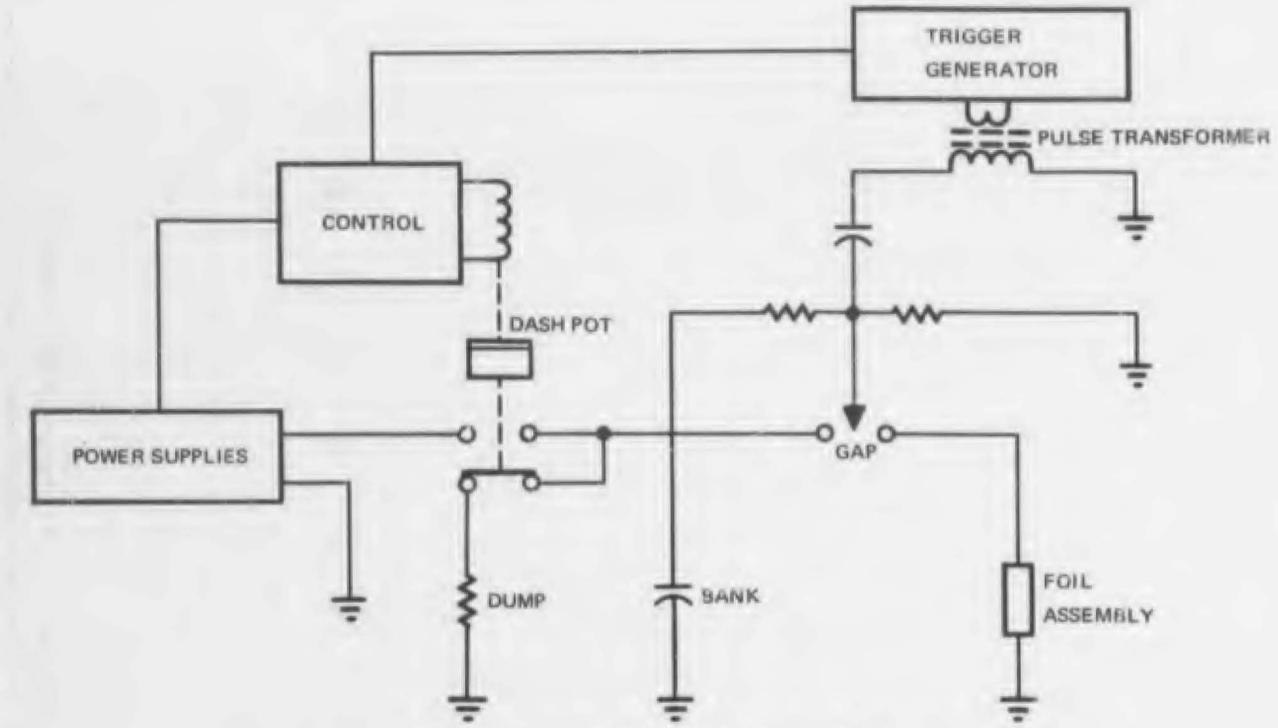

Figure 35. Schematic of MDAC-WD Exploding-Foil Facility

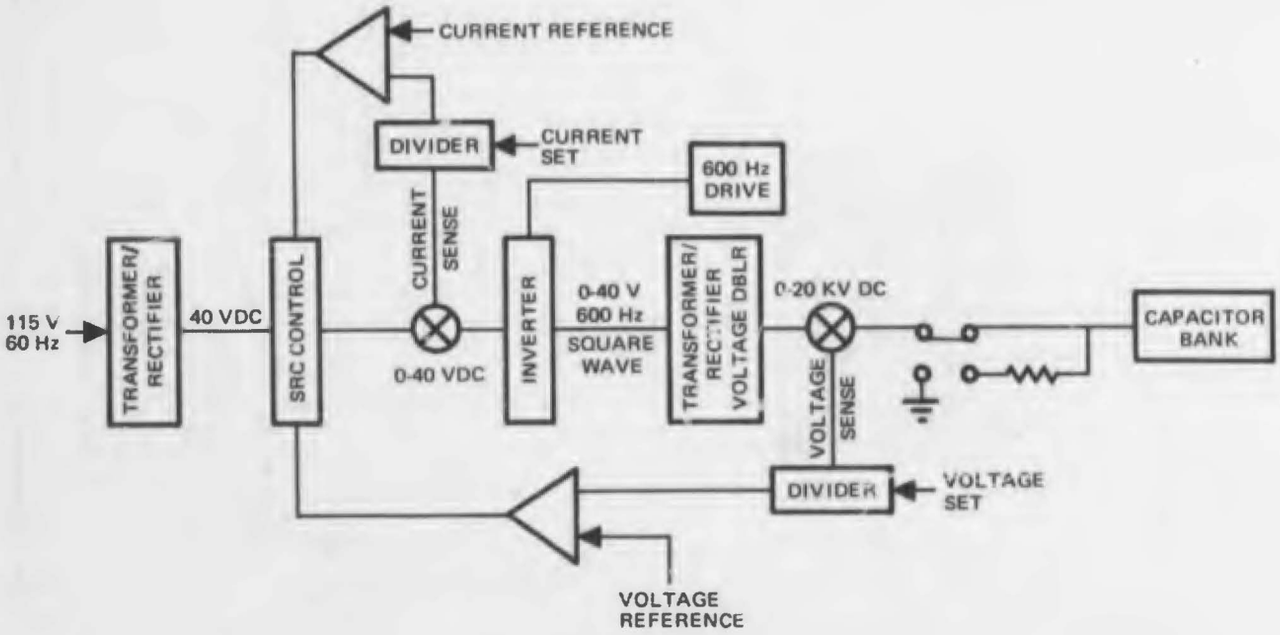

Figure 36. Schematic of MDAC-WD Exploding-Foil Facility Power Supply

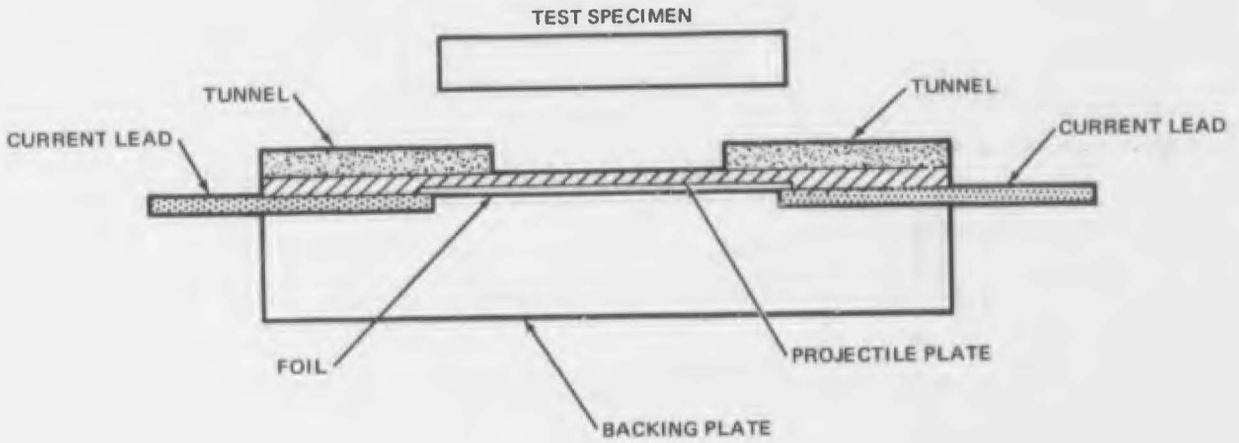

Figure 37. Single-Plate Exploding-Foil Assembly

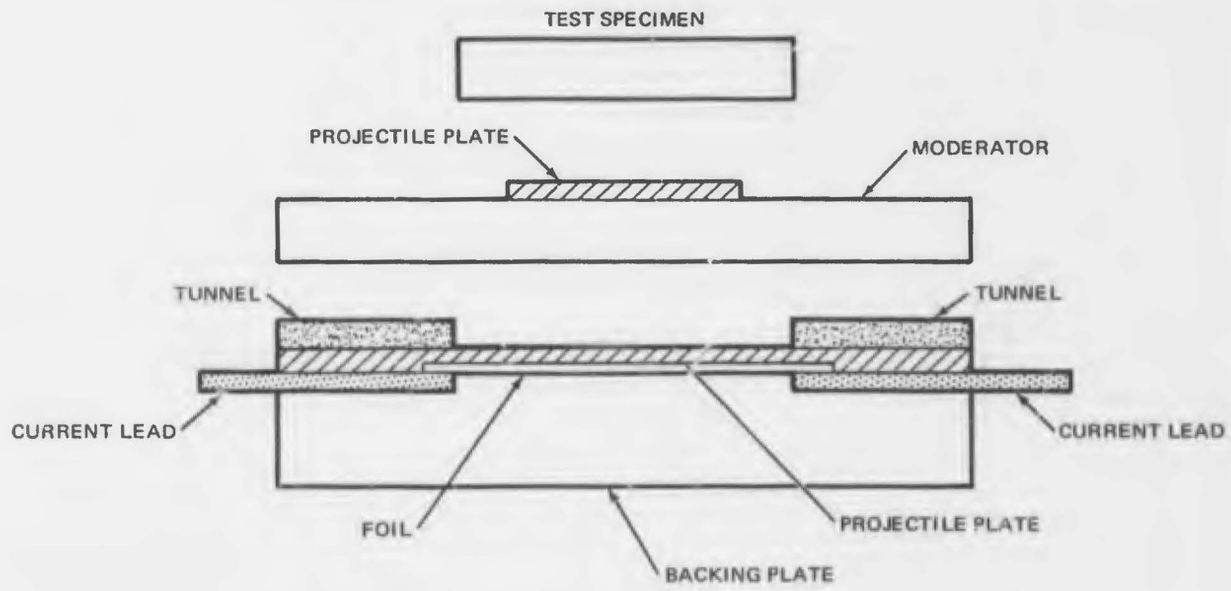

Figure 38. Double-Plate Exploding-Foil Assembly

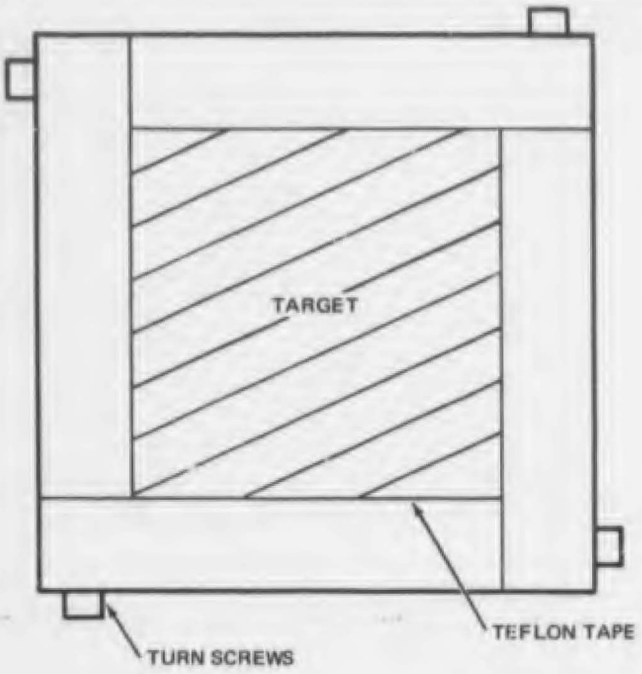

Figure 39. Exploding-Foil Target Holder

Figure 40. Target Catcher

Figure 41. Exploded View of Target Catcher

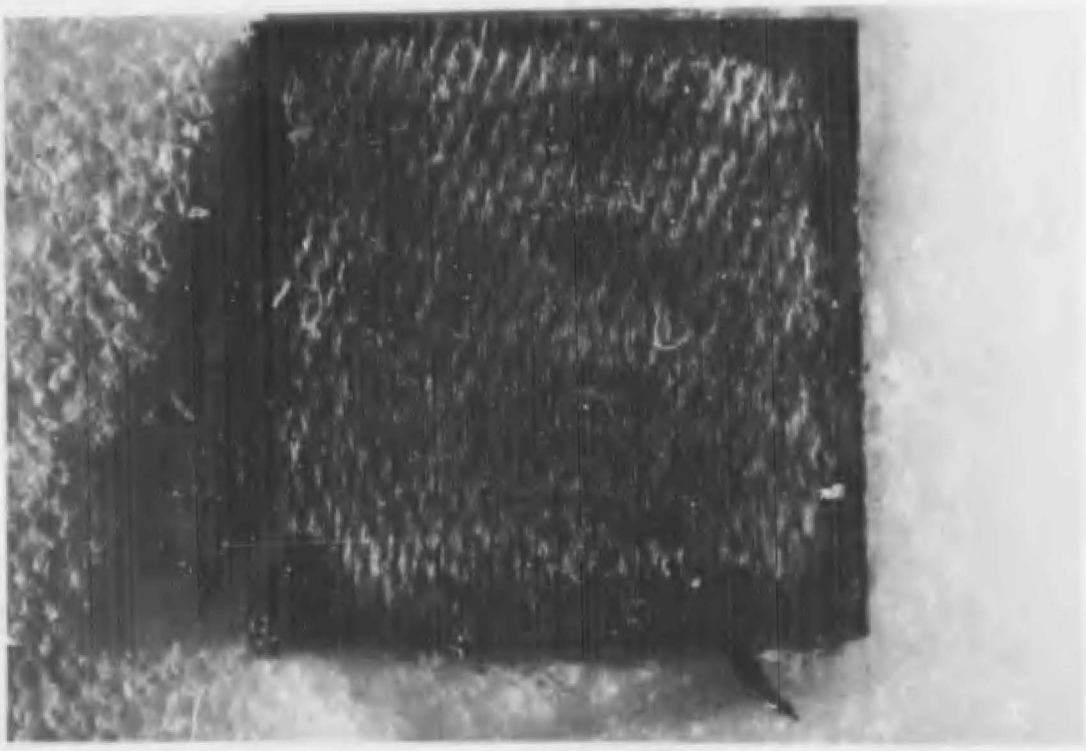

Figure 42. Indentation of Quartz-Phenolic Target Against Foam Catcher

NOT REPRODUCIBLE

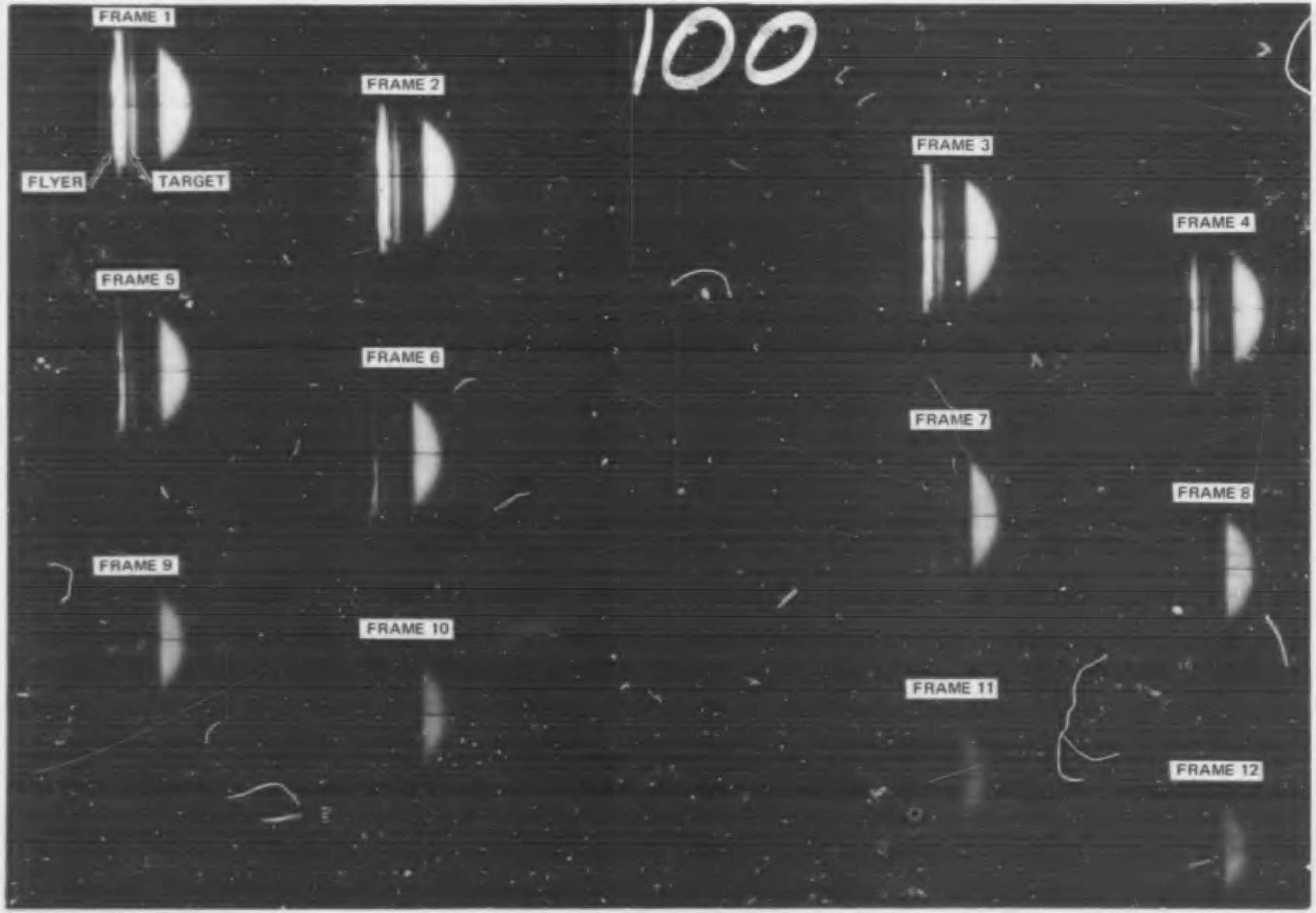

Figure 43. Framing Camera Record of Flyer Target Impact

NOT REPRODUCIBLE

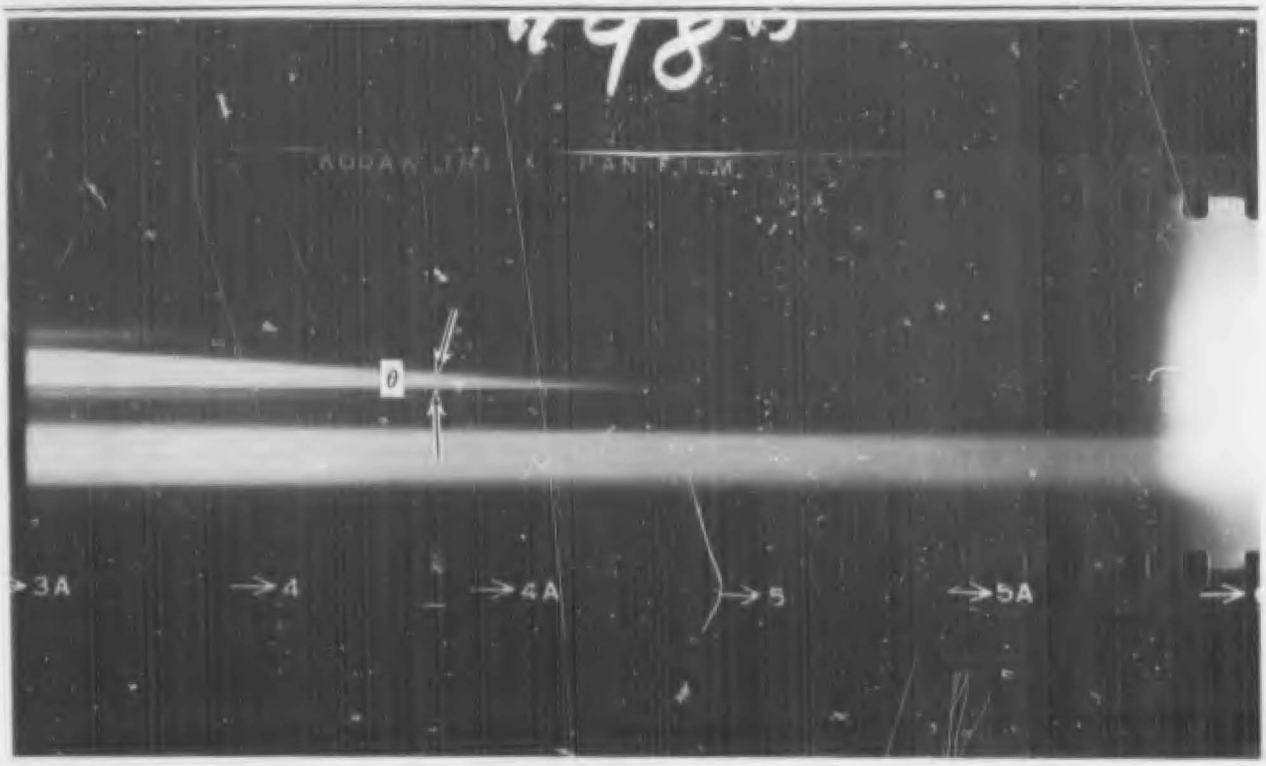

Figure 44. Streak Camera Record for Determination of Flyer Velocity

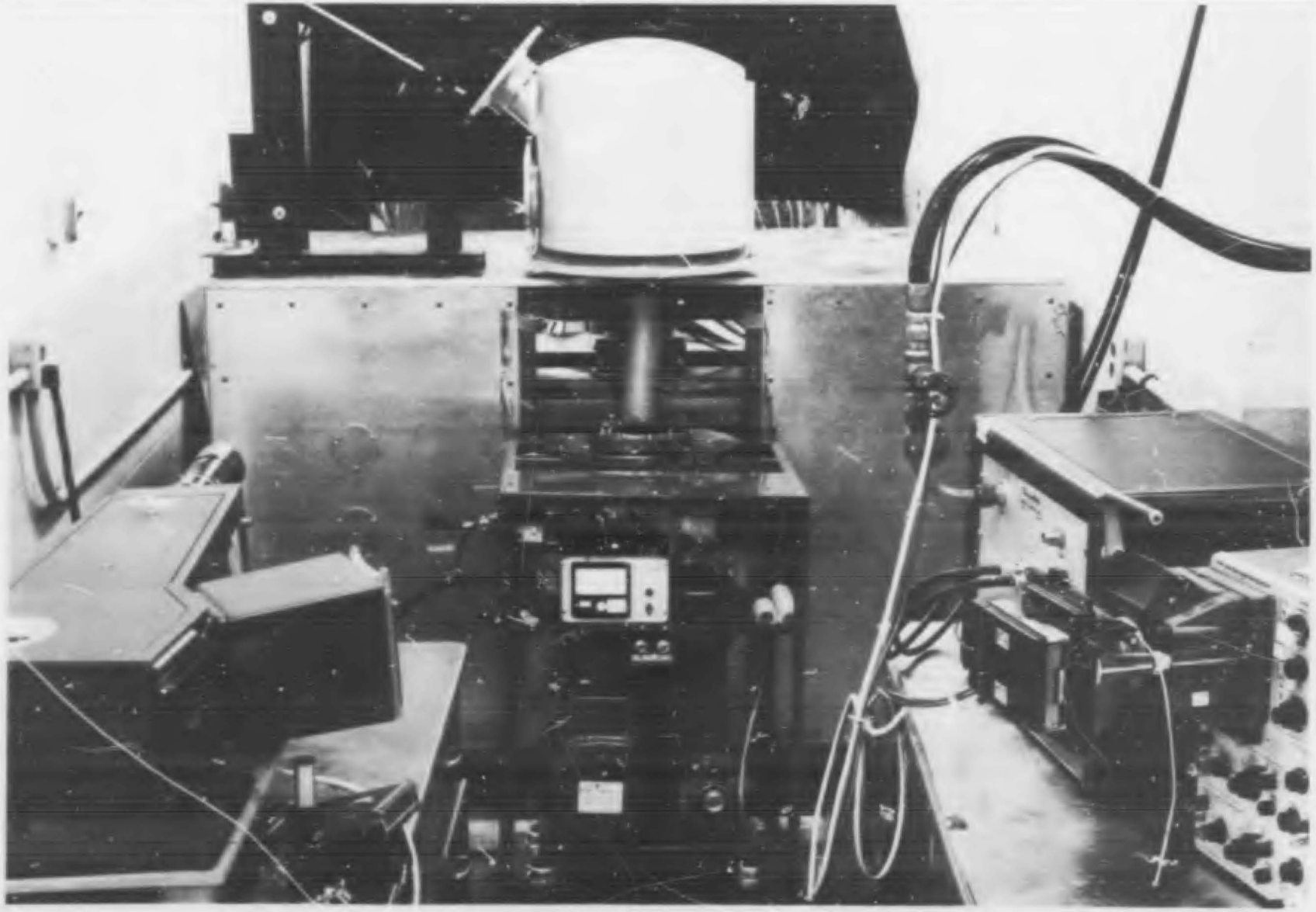

Figure 45. MDAC-WD Exploding-Foil Facility

NOT REPRODUCIBLE

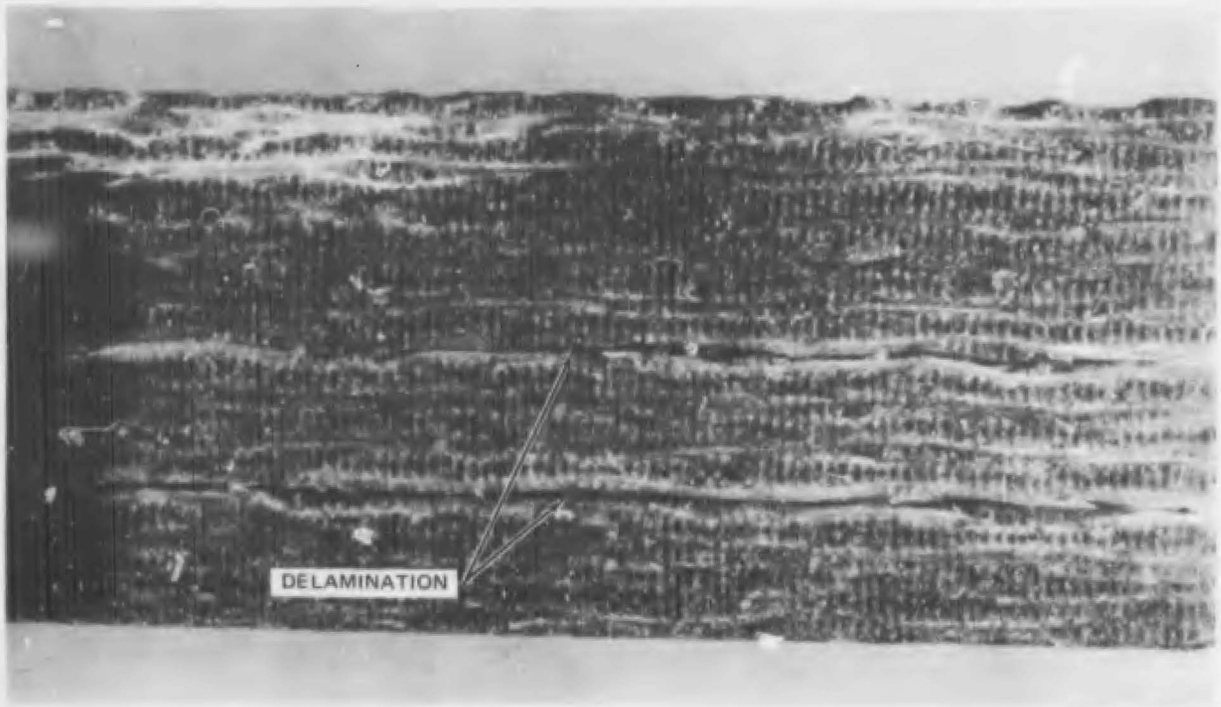

Figure 46. Post-Test Damage Produced by 5-Mil Flyer Impacting at 0.98 mm/μsec. Specimen No. 15, Edge

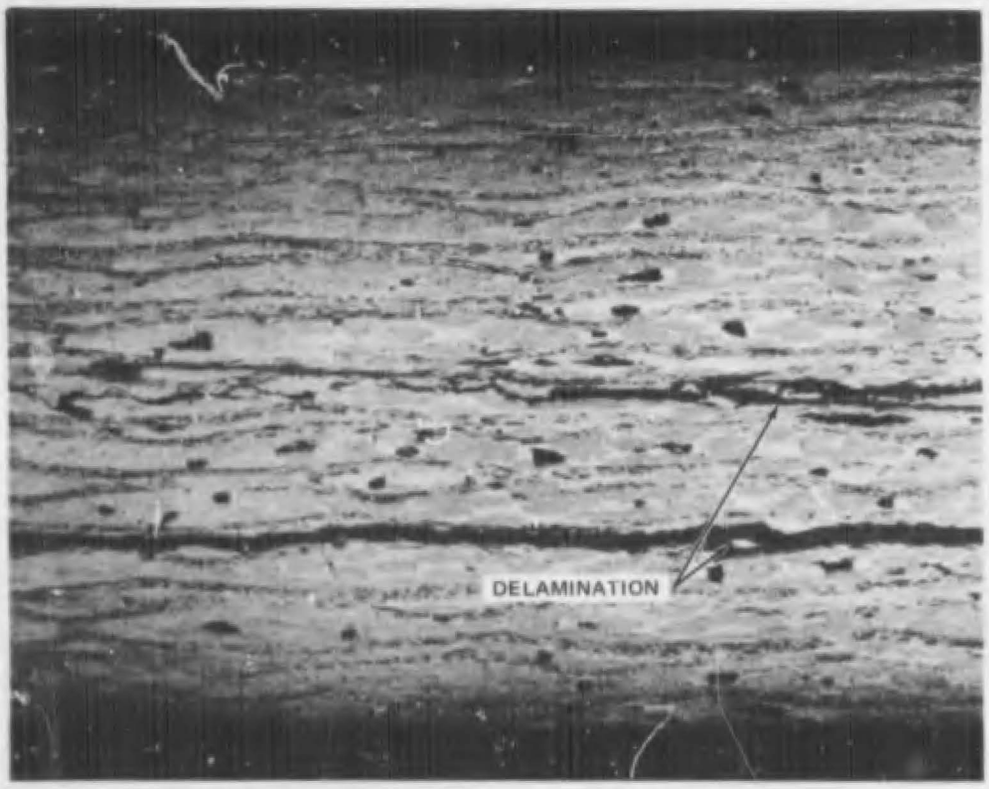

Figure 47. Post-Test Internal Damage Produced by 5-mil Flyer Impacting at 0.98 mm/μsec. Specimen No. 15 – 10X

NOT REPRODUCIBLE

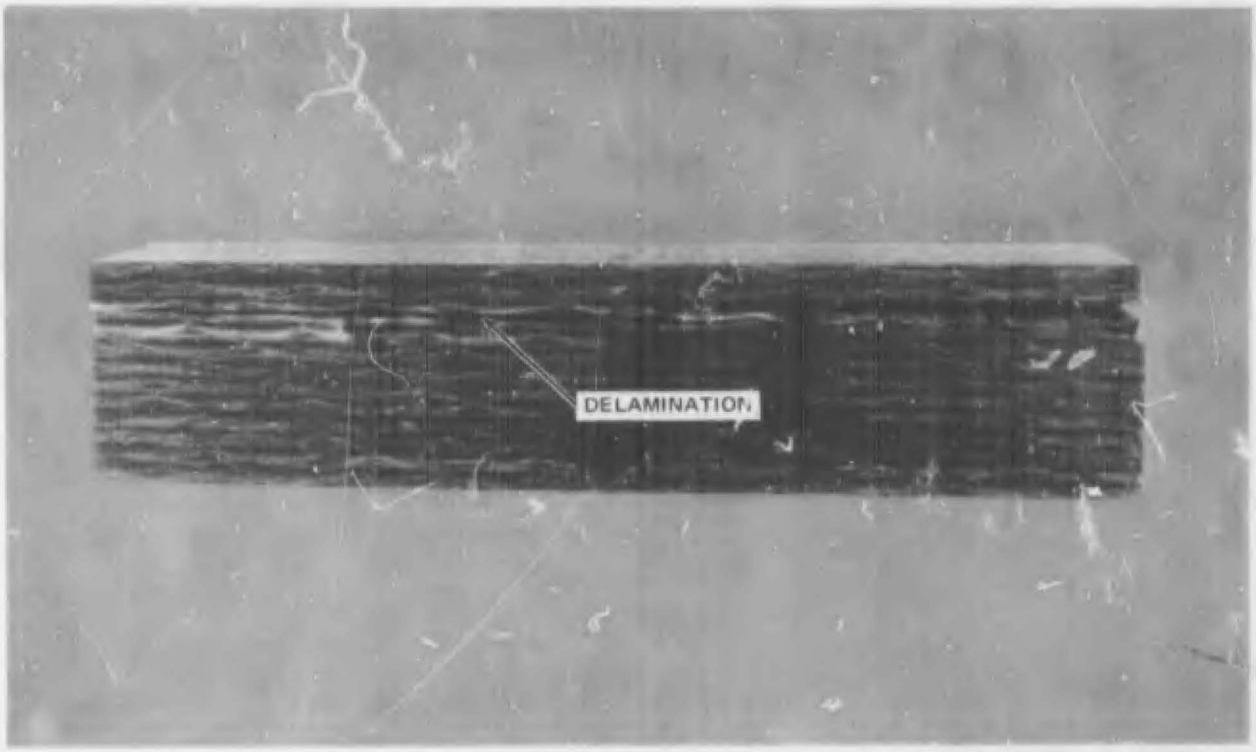

Figure 48. Post-Test Damage Produced by 5-Mil Flyer Impacting at 1.11 mm/μsec. Specimen No. 18

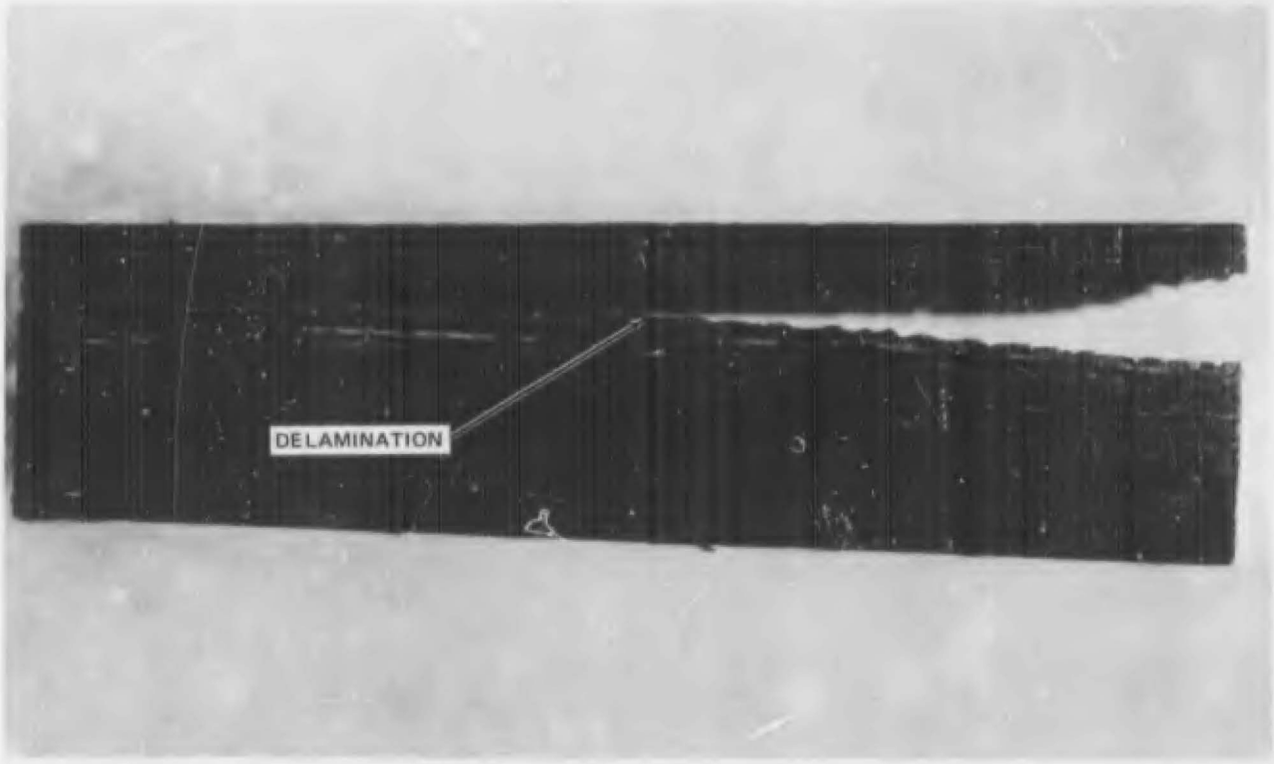

Figure 49. Post-Test Damage Produced by 14.7-Mil Flyer Impacting at 0.75 mm/μsec. Specimen No. 14, Edge – 4X

NOT REPRODUCIBLE

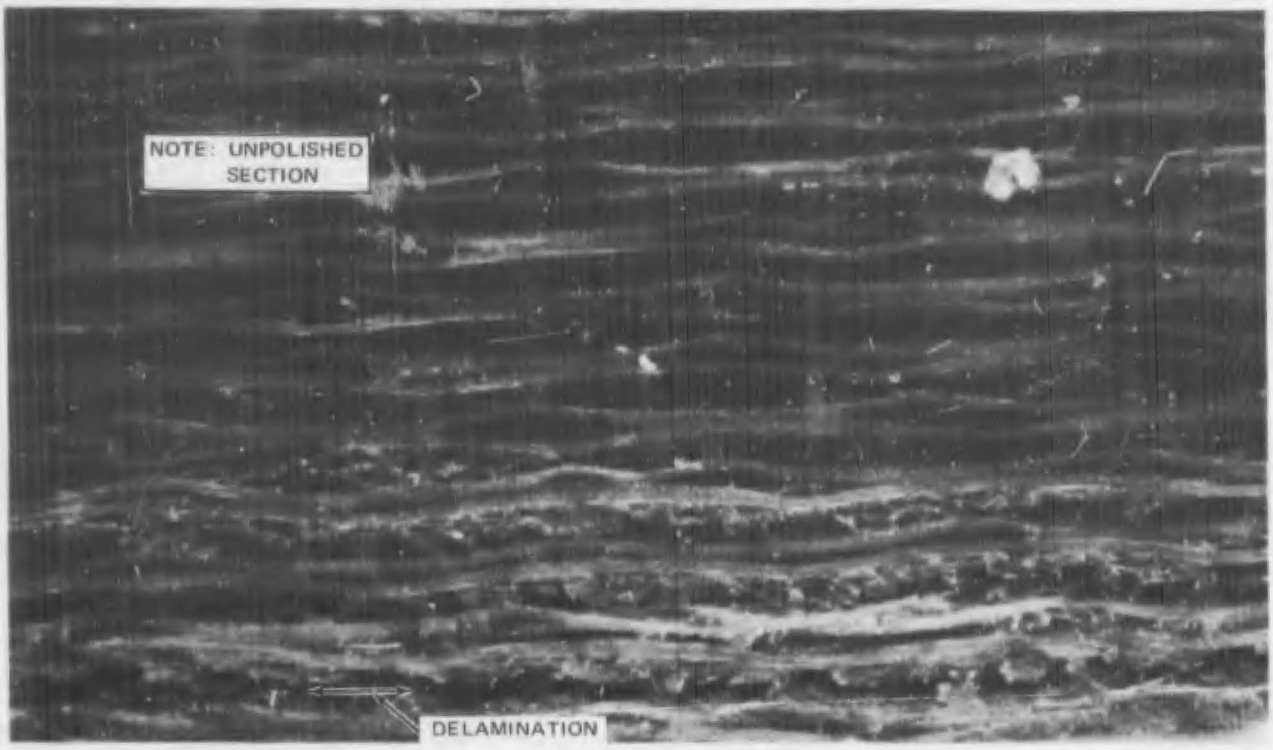

Figure 50. Post-Test Damage Produced by 14.7-Mil Flyer Impacting at 0.59 mm/μsec Specimen No. 26

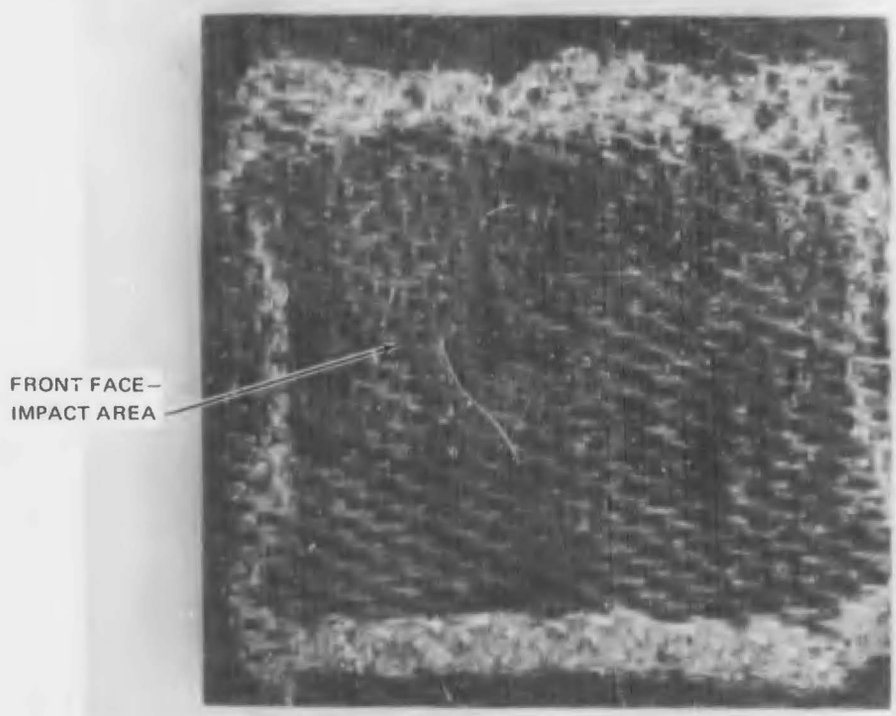

Figure 51. Post-Test Inspection of Condition Produced by 5-Mil Flyer Impacting at 1.11 mm/μsec. Specimen No. 18, Front Face – 4X

NOT REPRODUCIBLE

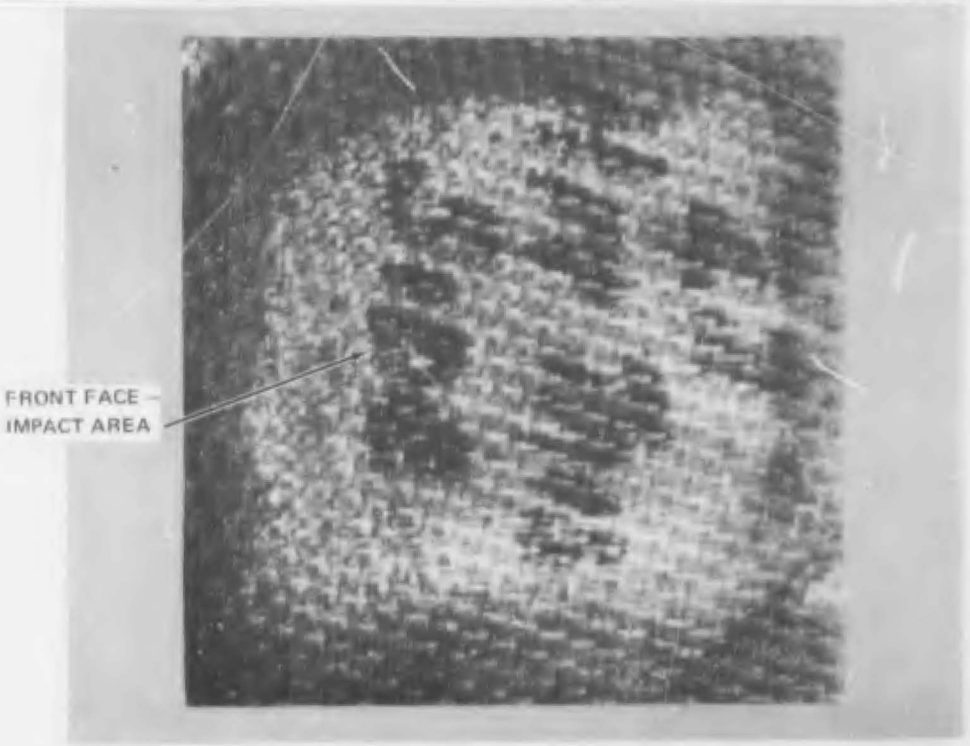

Figure 52. Post-Test Inspection of Condition Produced by 14.7-Mil Flyer Impacting at 0.57 mm/μsec. Specimen No. 22, Front Face – 4X

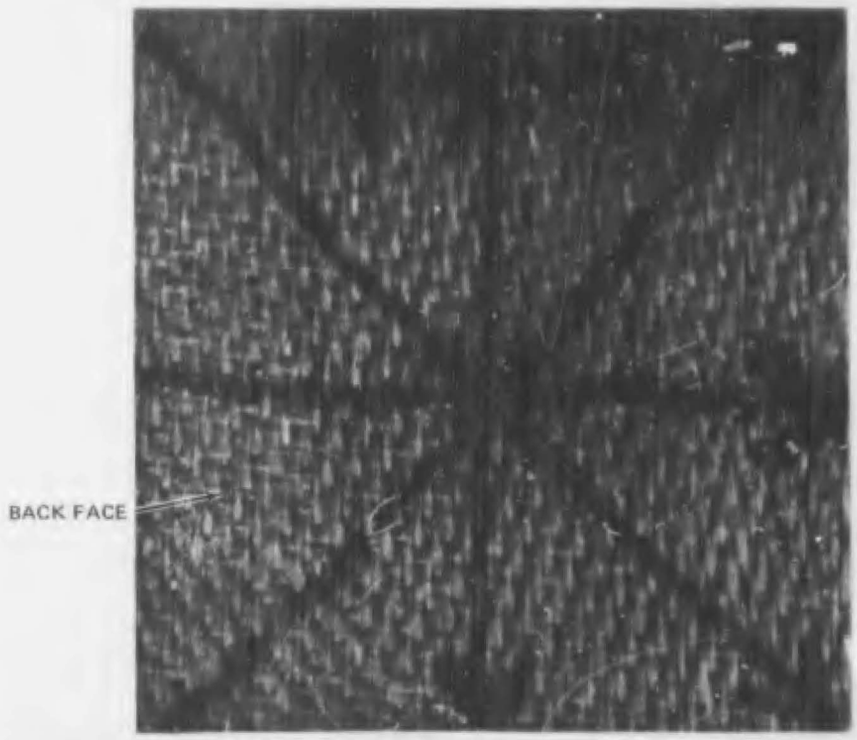

Figure 53. Post-Test Inspection of Condition Produced by 5-Mil Flyer Impacting at 0.?8 mm/μsec. Specimen No. 19, Back Face – 4X.

NOT REPRODUCIBLE

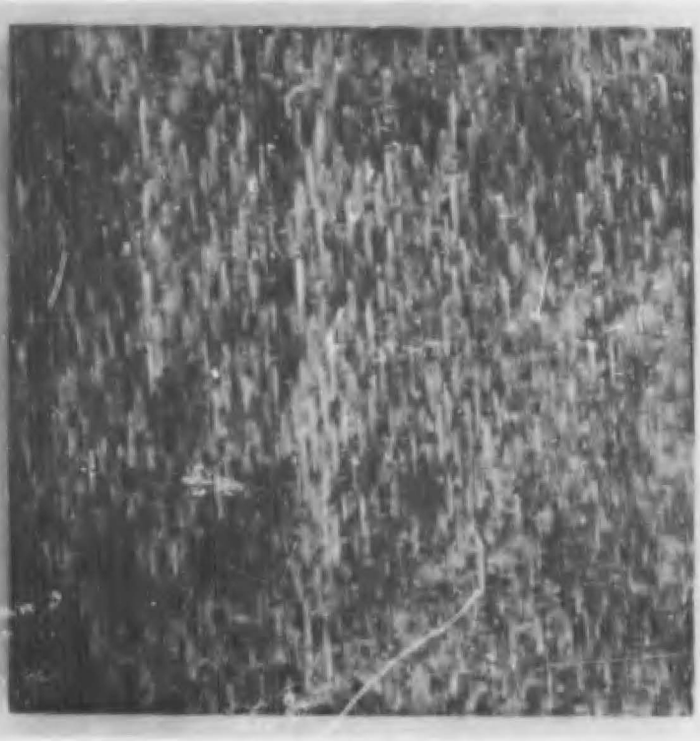

Figure 54. Post-Test Damage Produced by 5-Mil Flyer Impacting at 1.11 mm/μsec. Specimen No. 18, Delaminated Plane–4X

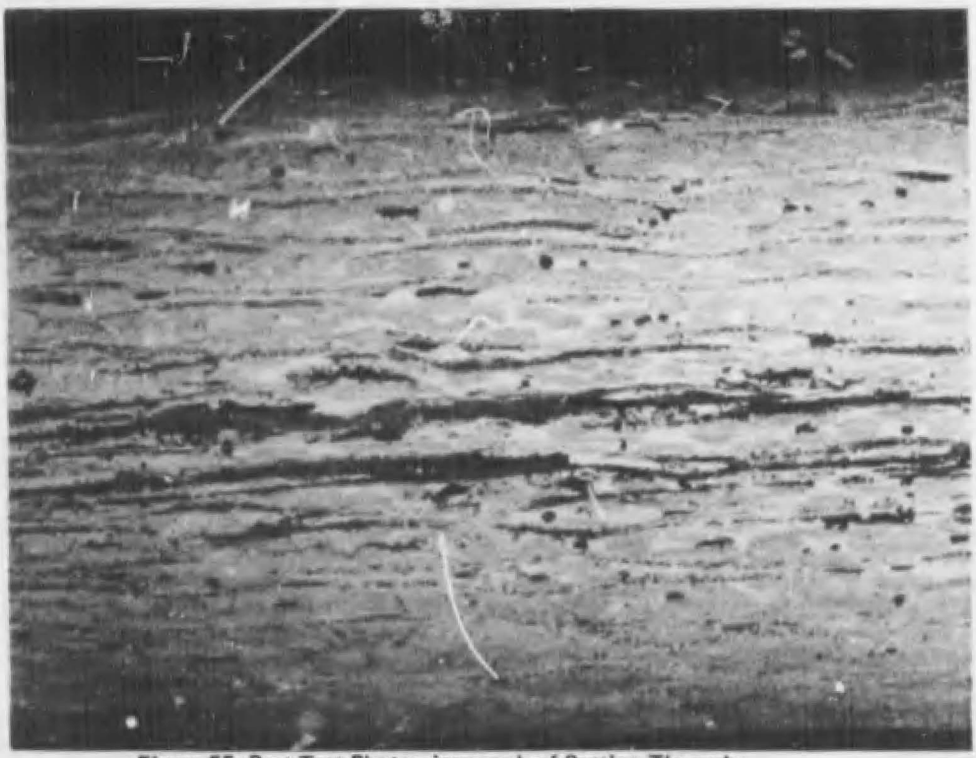

Figure 55. Post-Test Photomicrograph of Section Through Specimen No. 13-10X (5-Mil Flyer at 0.966 mm/μsec.)

NOT REPRODUCIBLE

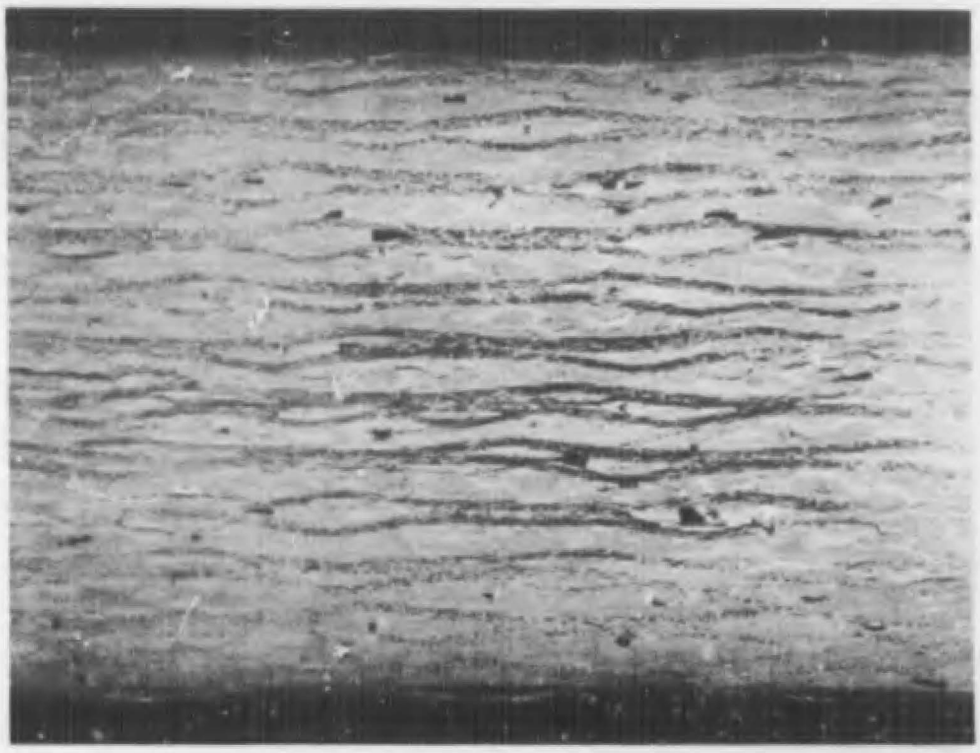

Figure 56. Post-Test Photomicrograph of Section Through Specimen No. 19-10X. (5-Mil Flyer at 0.98 mm/μsec)

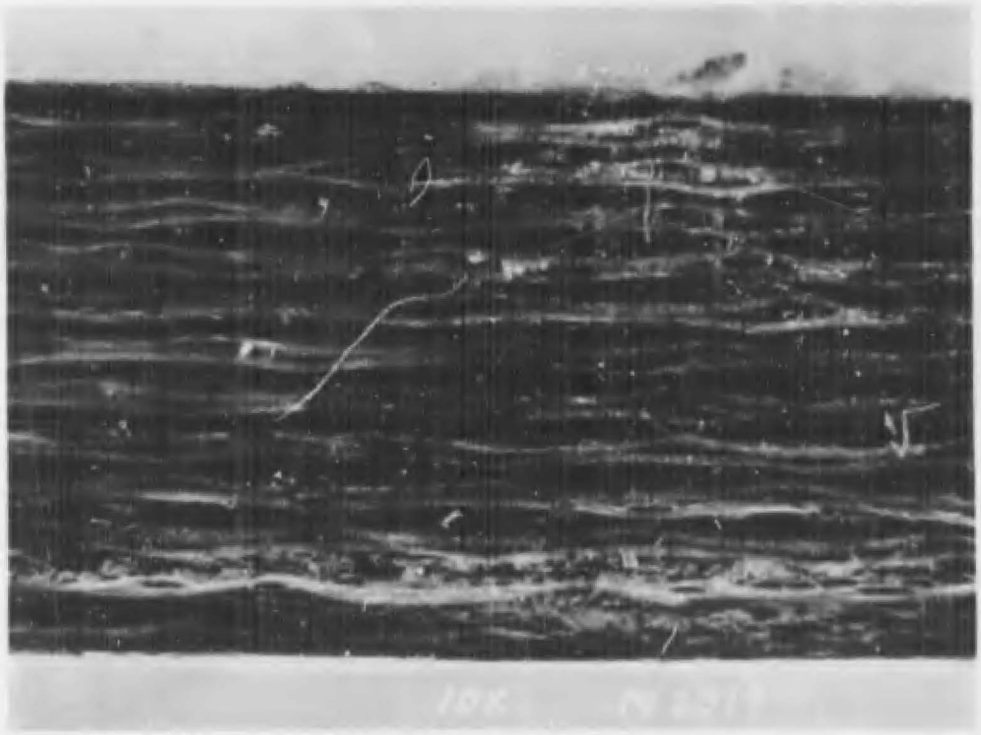

Figure 57. Post-Test Photomicrograph Specimen No. 22-10X Unpolished Section

NOT REPRODUCIBLE

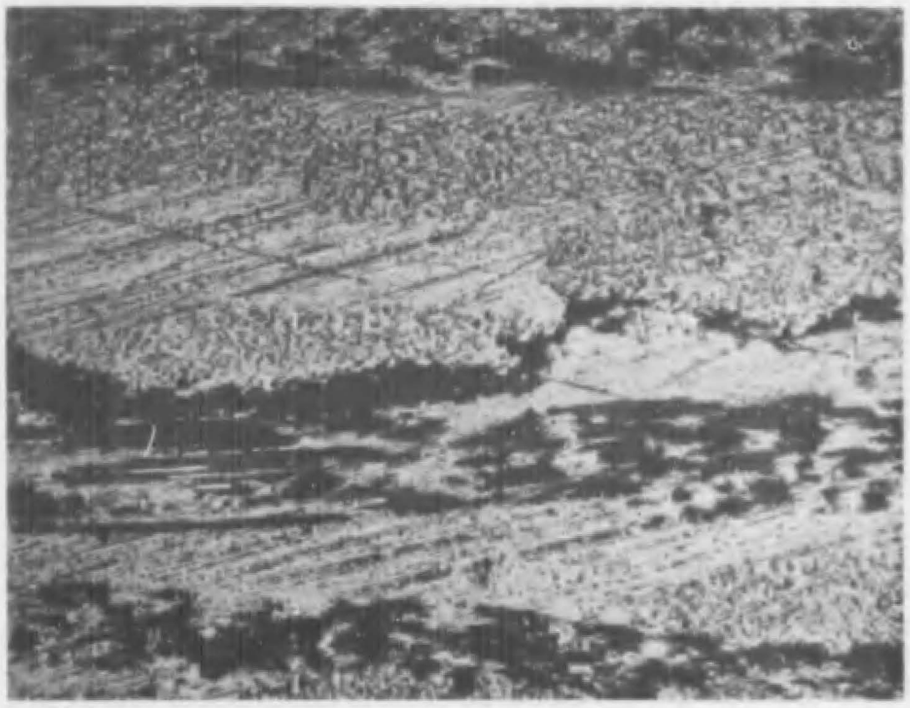

Figure 58. Specimen No. 24, Impacted at 0.61 mm/μsec. with 5-Mil Flyer, 100X Magnification

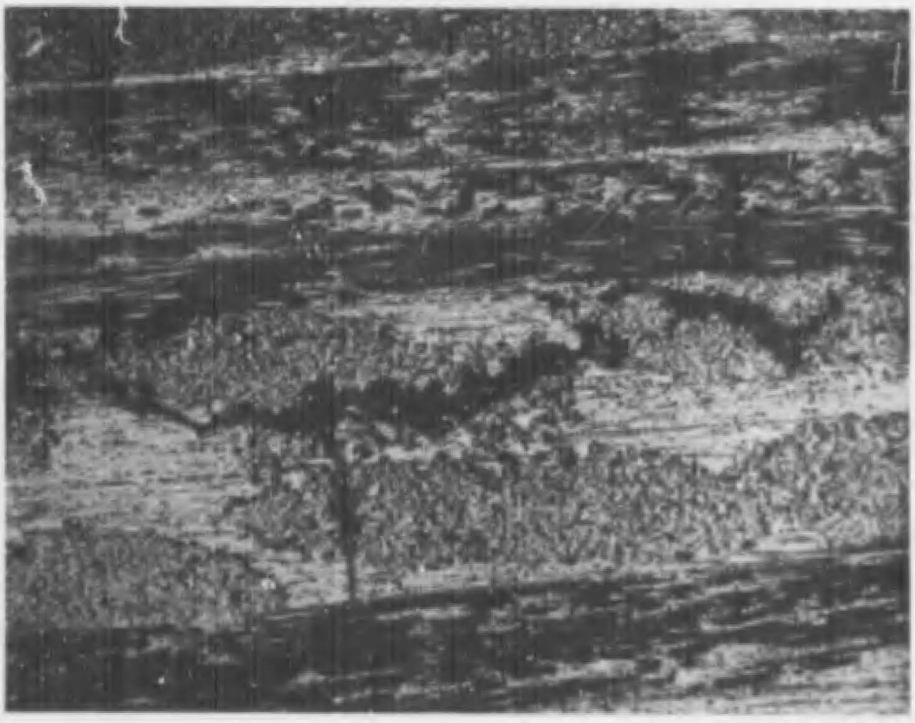

Figure 59. Specimen No. 23, Impacted at 0.66 mm/μsec. with 5-Mil Flyer, 100X Magnification

NOT REPRODUCIBLE

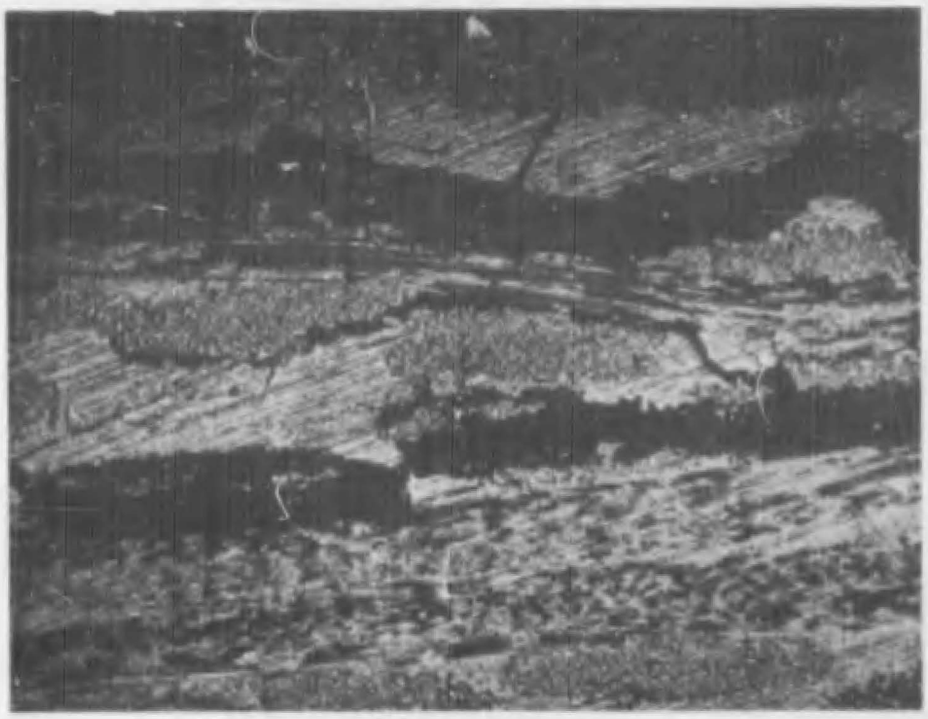

Figure 60. Specimen No. 25, Impacted at 0.77 mm/μsec. with 5-Mil Flyer, 65X Magnification

Figure 61. Specimen No. 27, Impacted at 0.39 mm/μsec.with 14.7-Mil Flyer, 50X Magnfiication

NOT REPRODUCIBLE

Figure 62. Specimen No. 21, Impacted at 0.41 mm/μsec. with 14.7-Mil Flyer, 30X Magnification

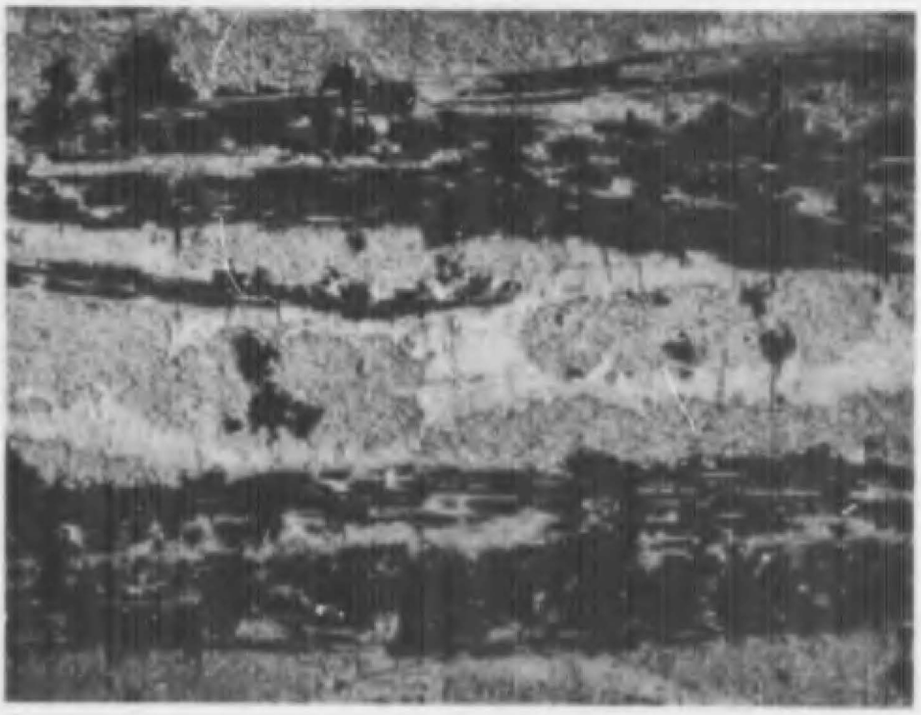

Figure 63. Control Specimen at 75X Magnification, Showing Microcracks

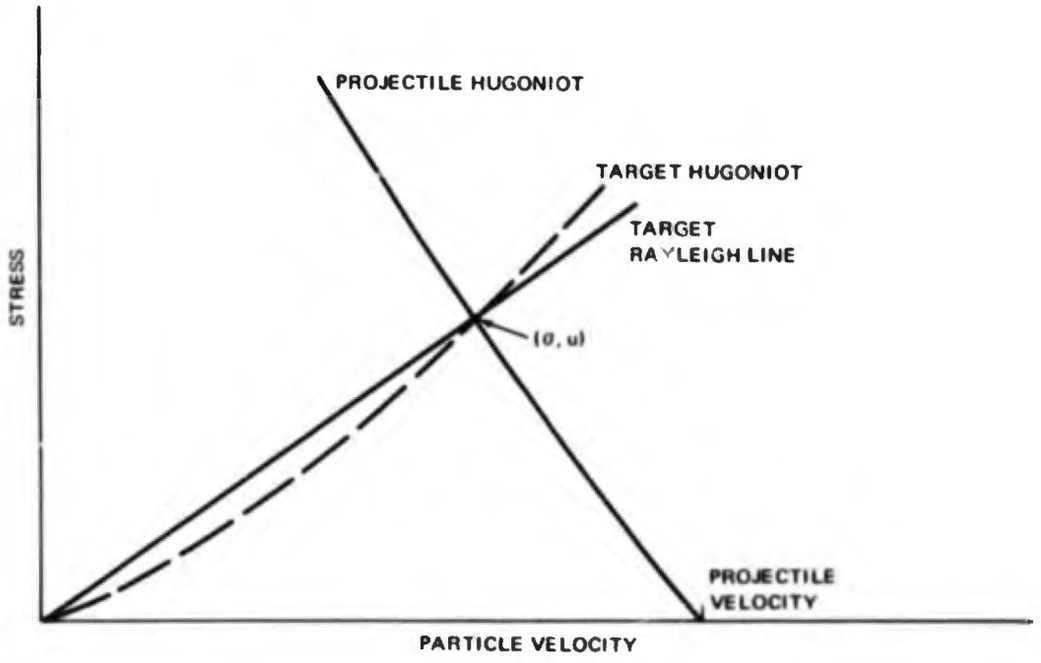

Figure 64. Hugoniot Impedance Match Solution

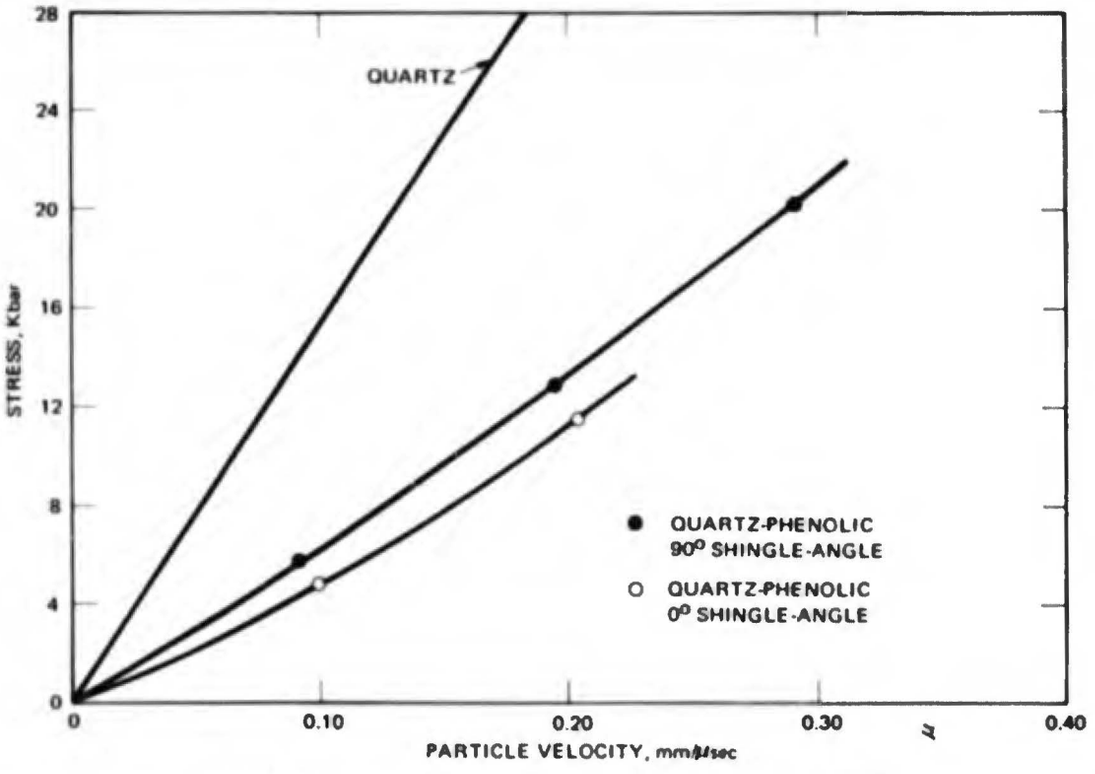

Figure 65. Quartz-Phenolic Hugoniot Curves Calculated by SRI

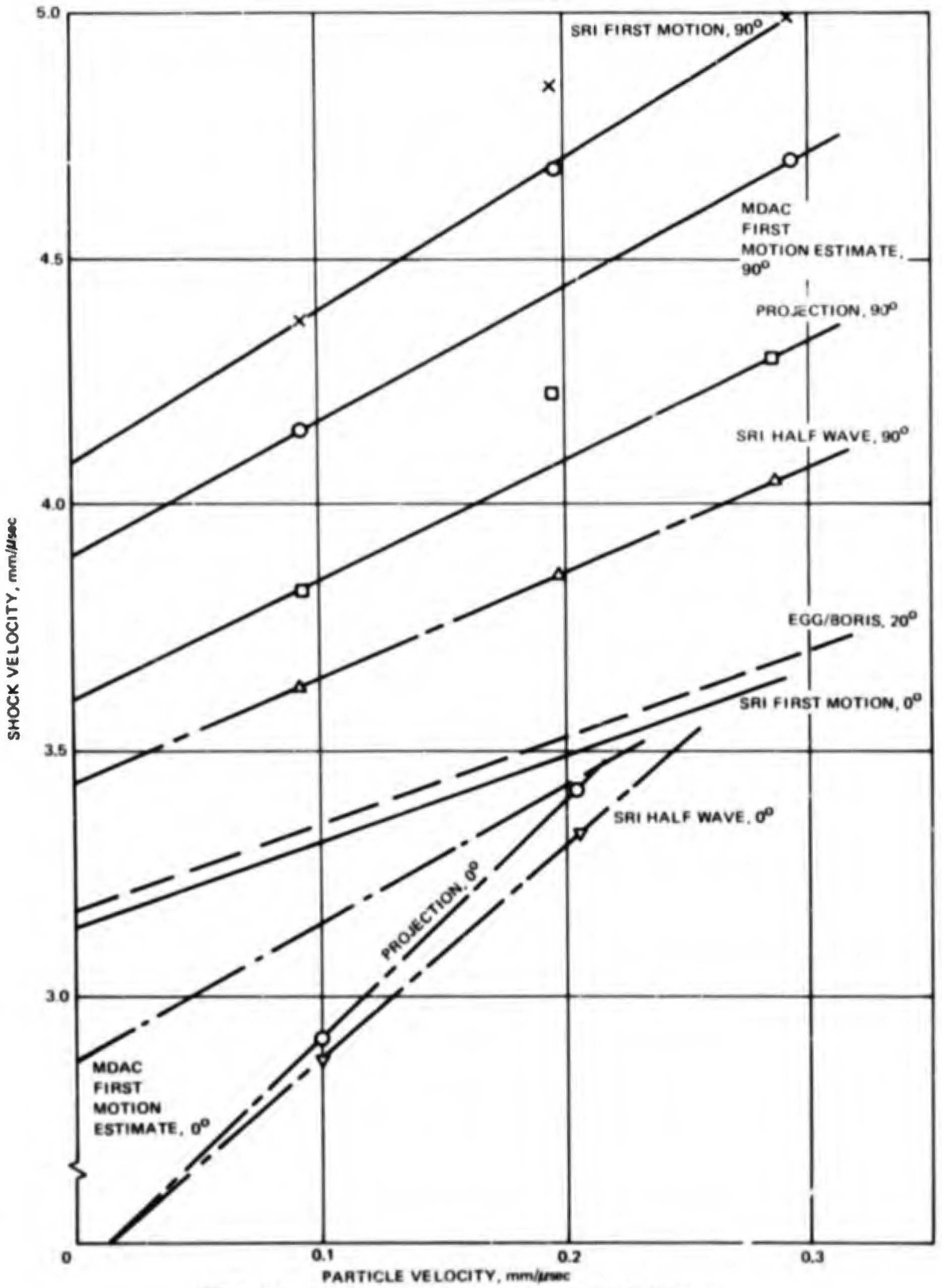

Figure 66. Hugonoit Shock Velocity Versus Particle Velocity

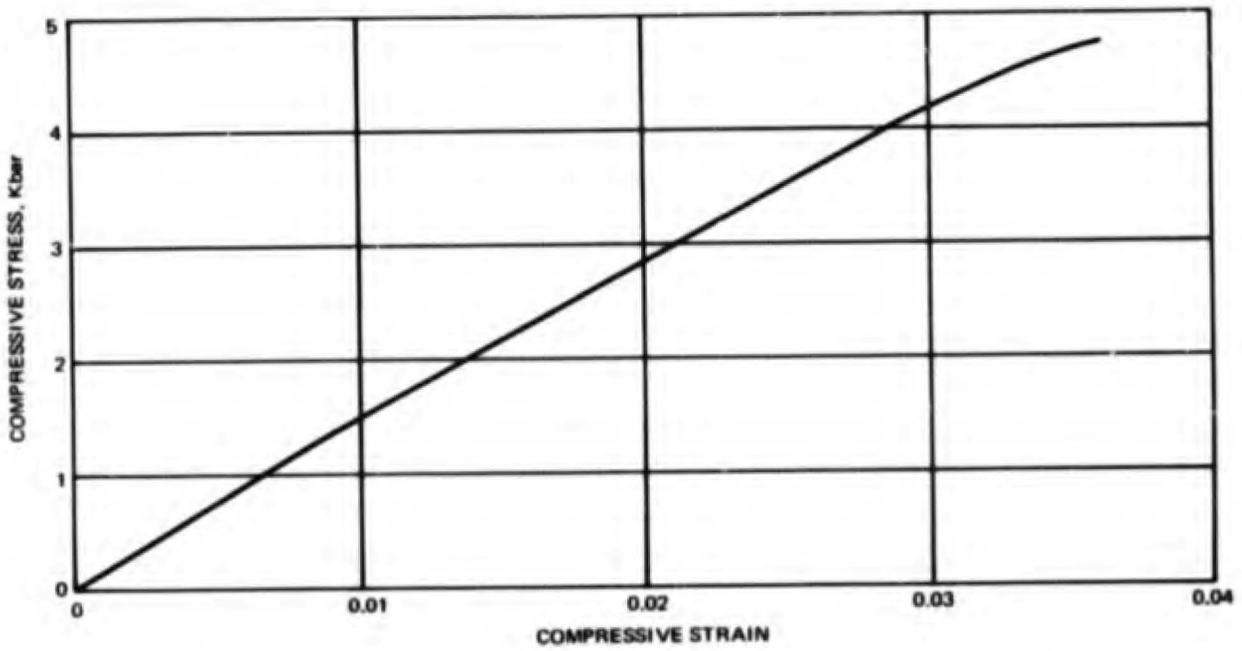

Figure 67. Dynamic Stress-Strain Curve from Low-Velocity Shot (No. 13594), Zero-Degree Orientation

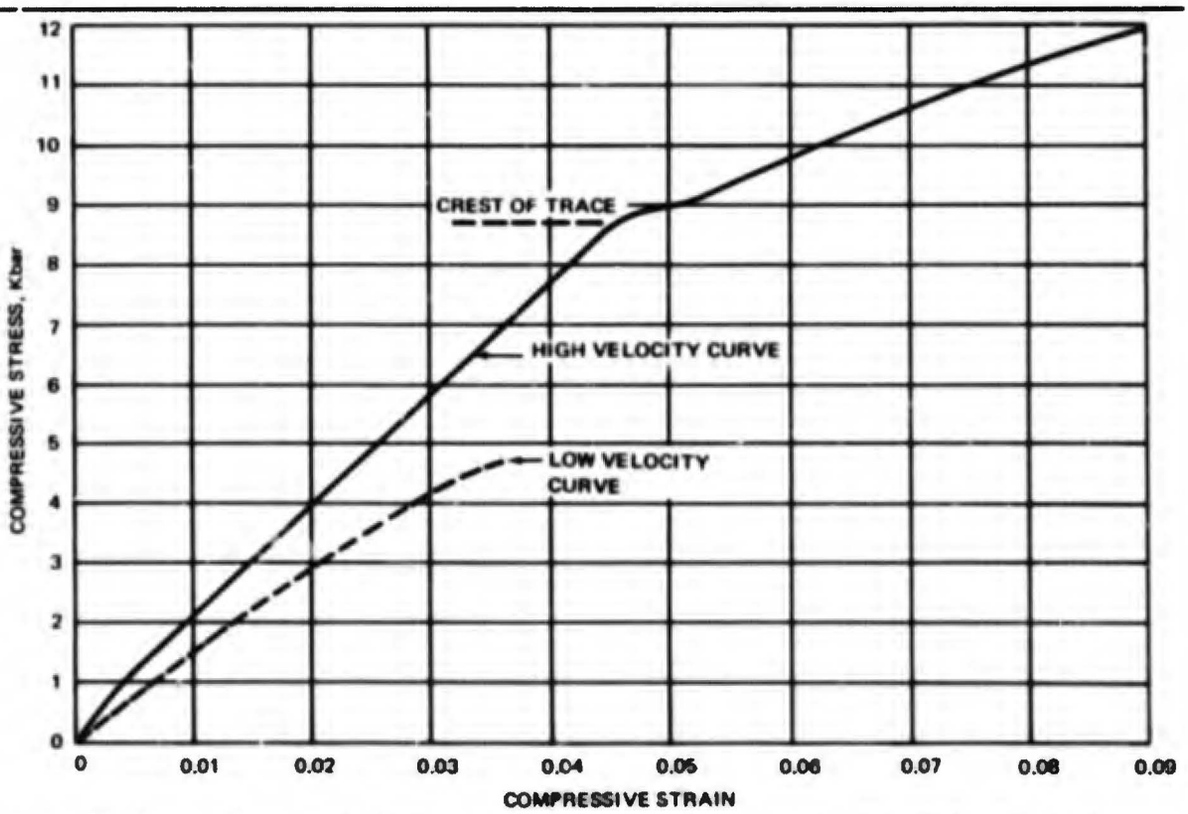

Figure 68. Dynamic Stress-Strain Curve from High-Velocity Shot (No. 13605), Zero-Degree Orientation

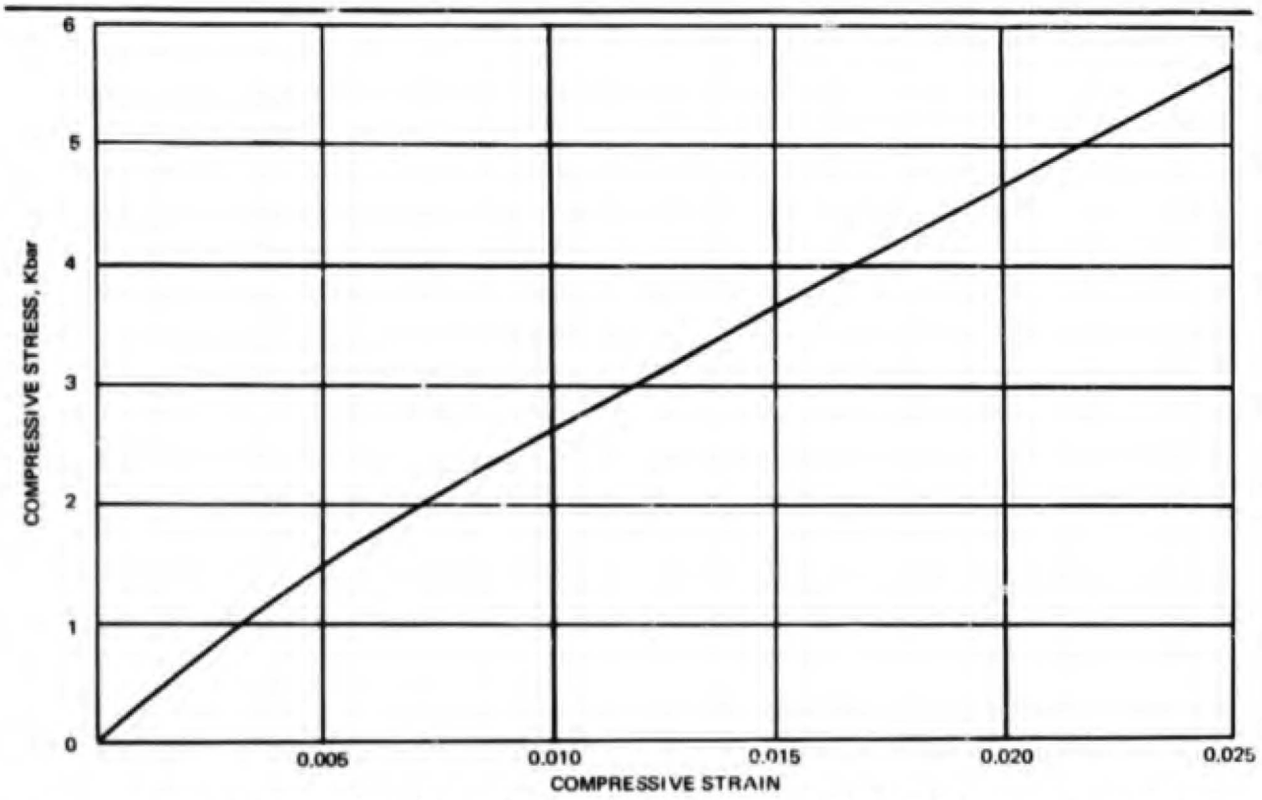

Figure 69. Dynamic Stress-Strain Curve From Low-Velocity Shot (No. 13603), 90-Degree Orientation

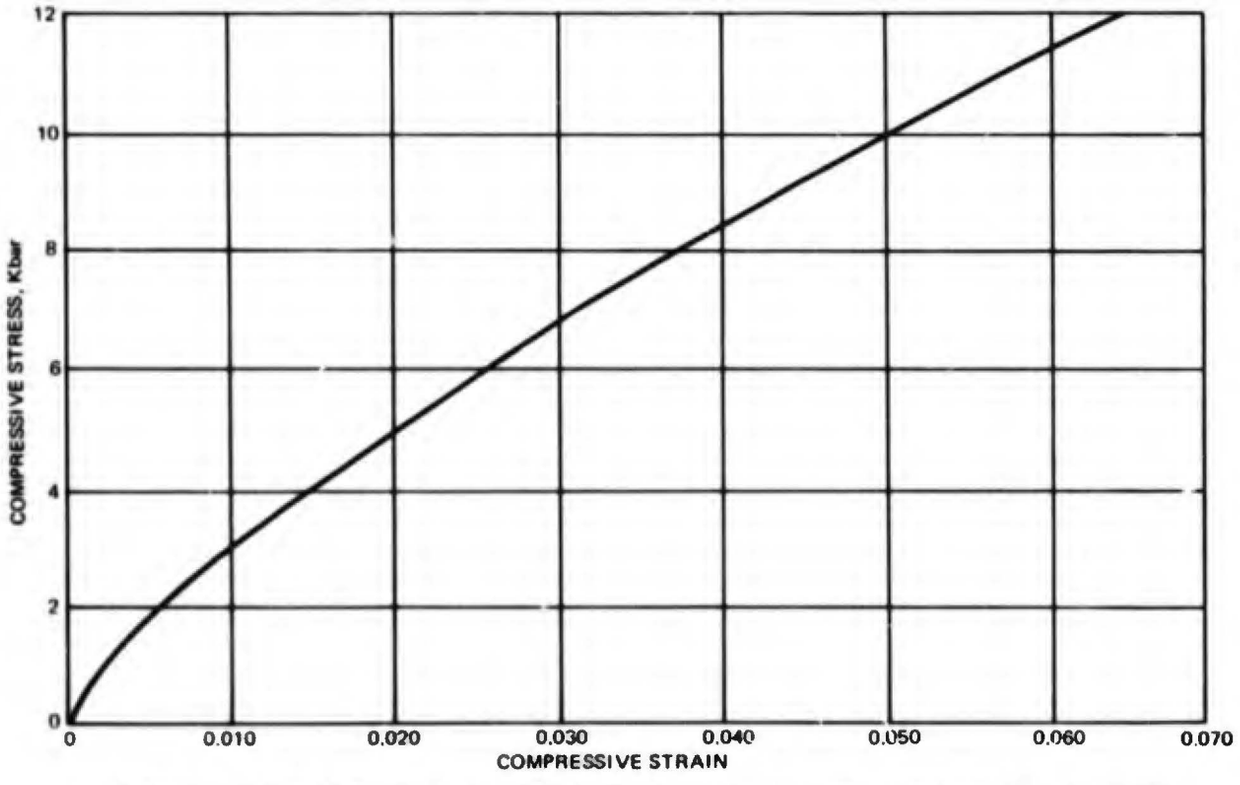

Figure 70. Dynamic Stress-Strain Curve from Intermediate Velocity Shot (No. 13606), 90-Degree Orientation

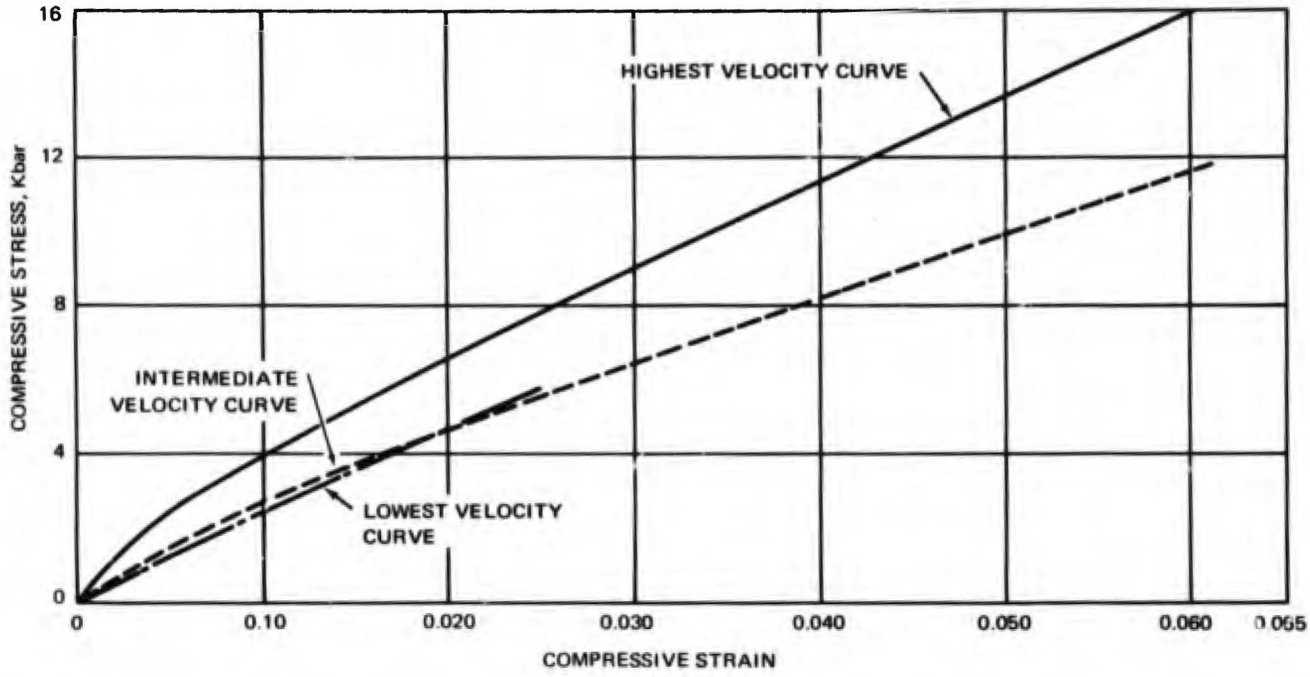

Figure 71. Dynamic Stress-Strain Curve from Highest Velocity Shot (No. 13604), 90-Degree Orientation

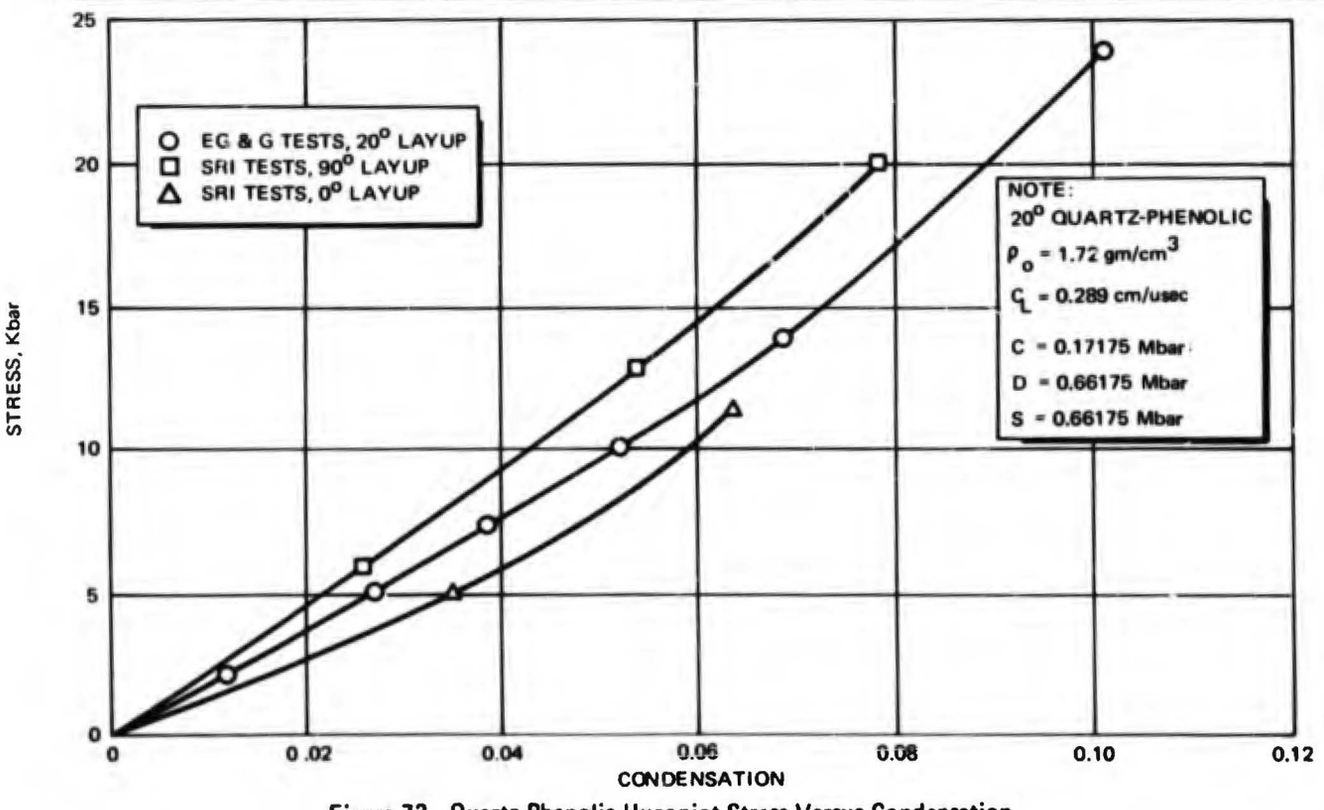

Figure 72. Quartz-Phenolic Hugoniot Stress Versus Condensation

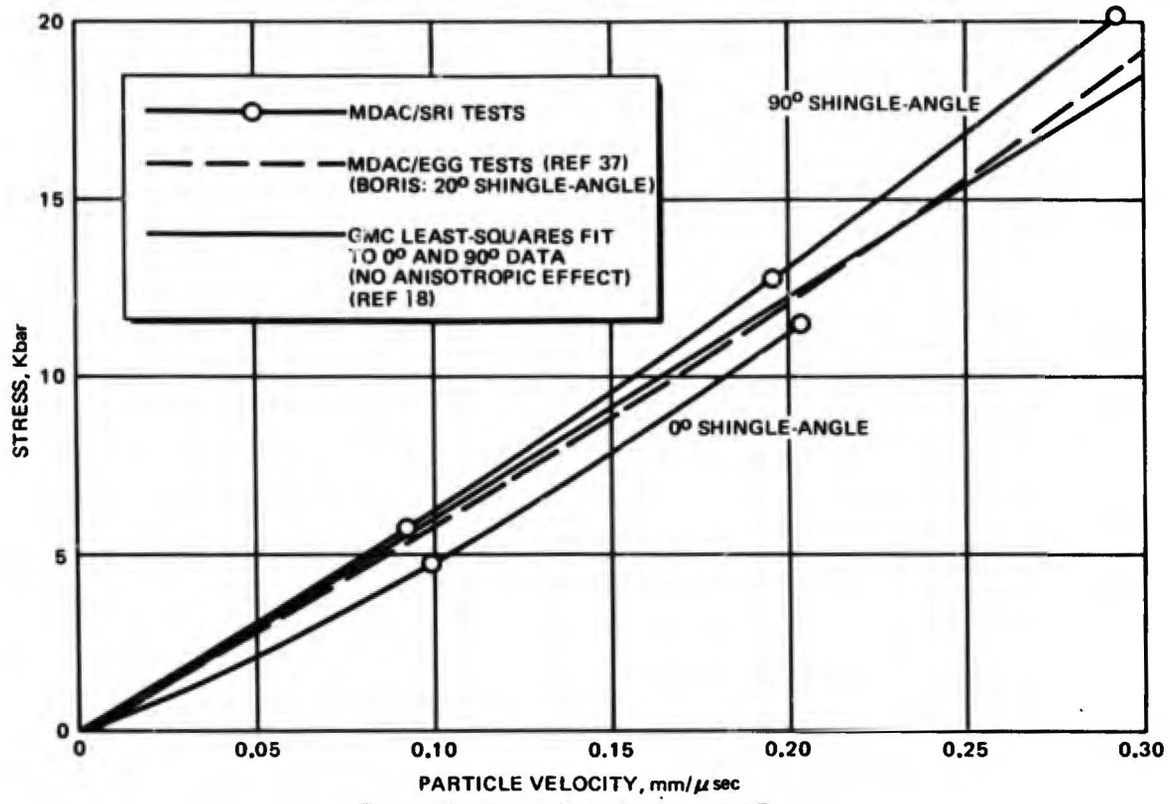

Figure 73. Quartz-Phenolic Hugoniot Data

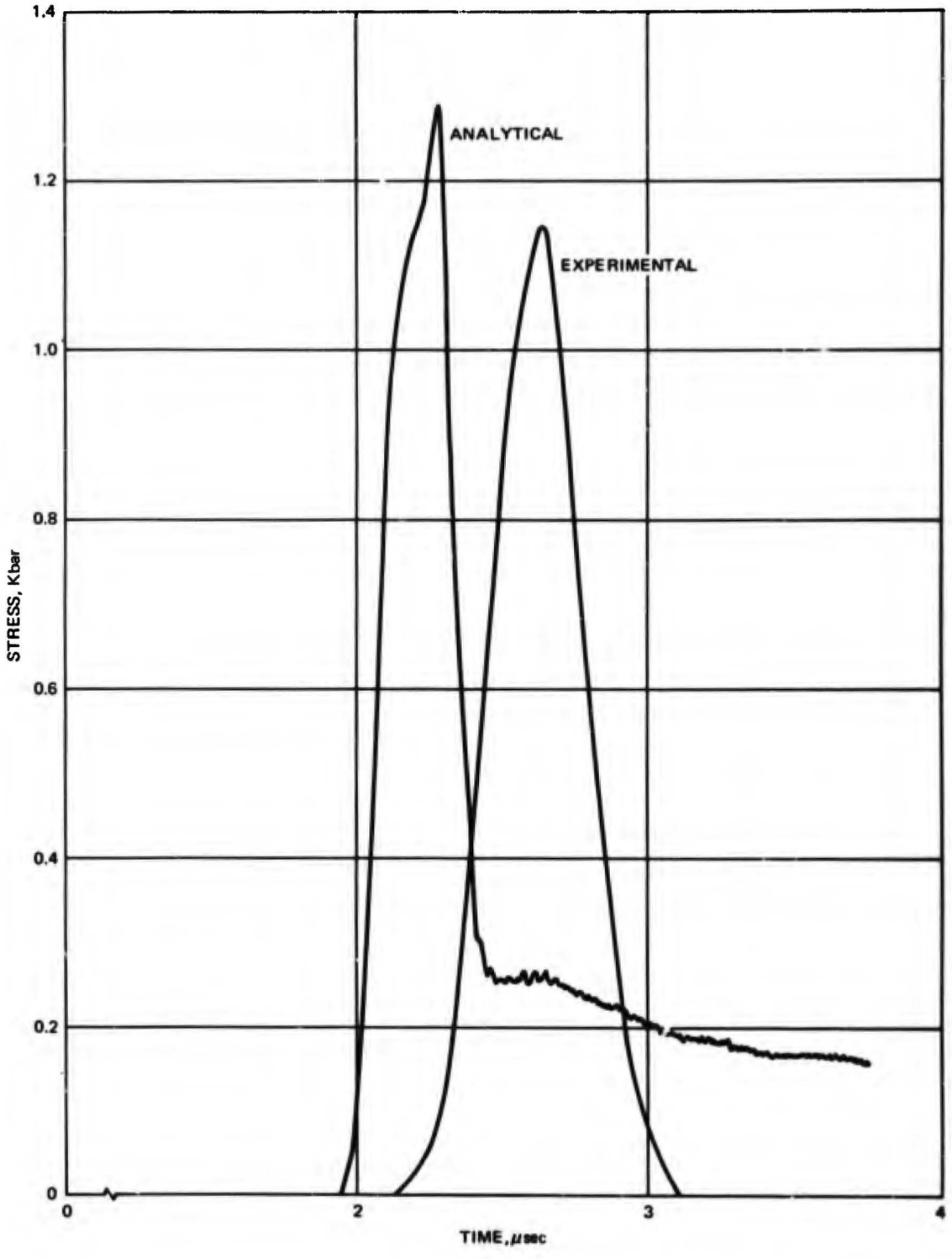

Figure 74. History of Stress at Quartz-Phenolic/Quartz Interface, Attenuation Shot, Zero-Degree Orientation

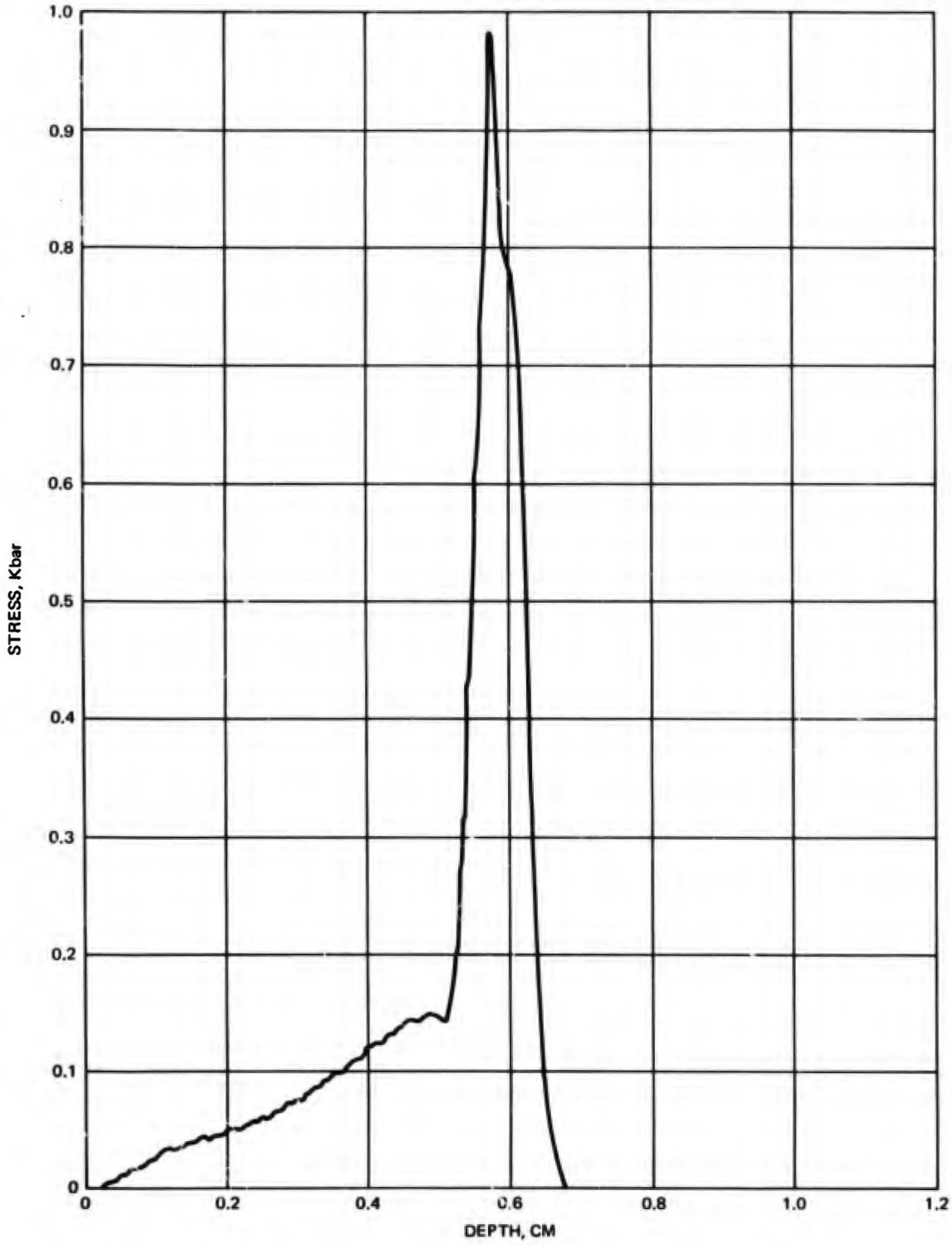

Figure 75. Stress Profile at 2.0003 μsec, Attenuation Shot, Zero-Degree Orientation

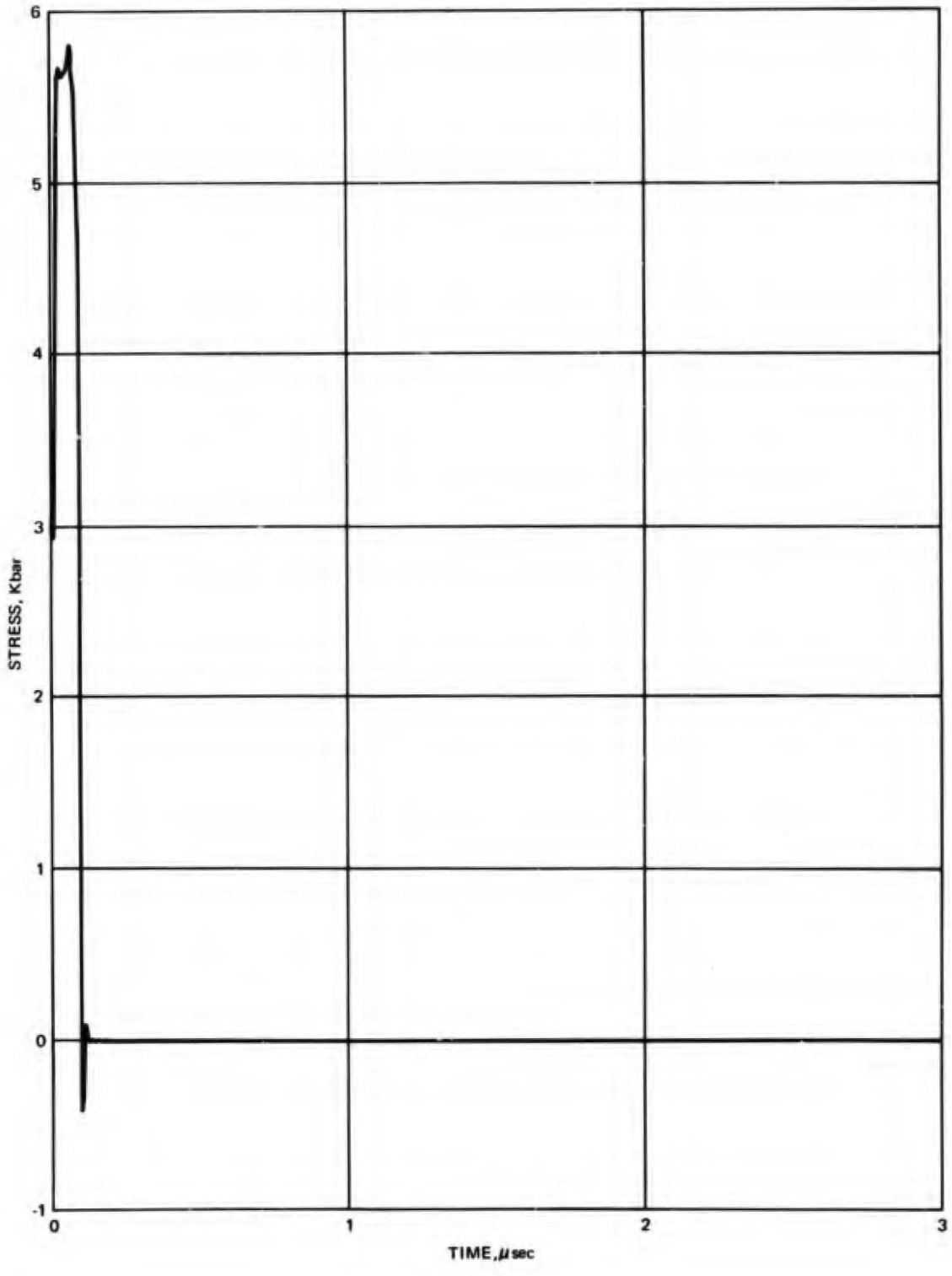

Figure 76. History of Stress at Mylar/Quartz-Phenolic Interface, Attenuation Shot, Zero-Degree Orientation

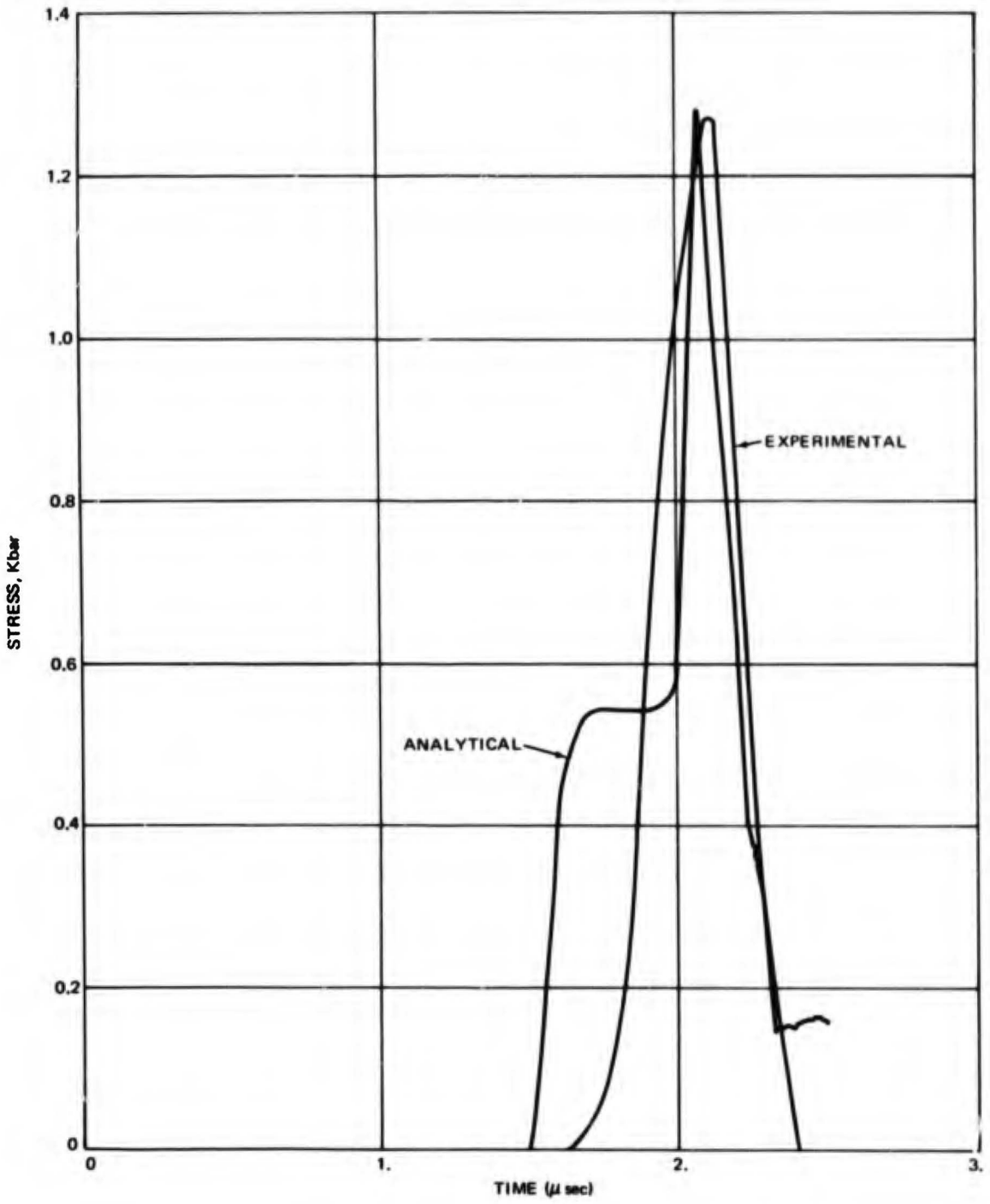

Figure 77. History of Stress at Quartz-Phenolic/Quartz Interface, Attenuation Shot, 90-Degree Orientation

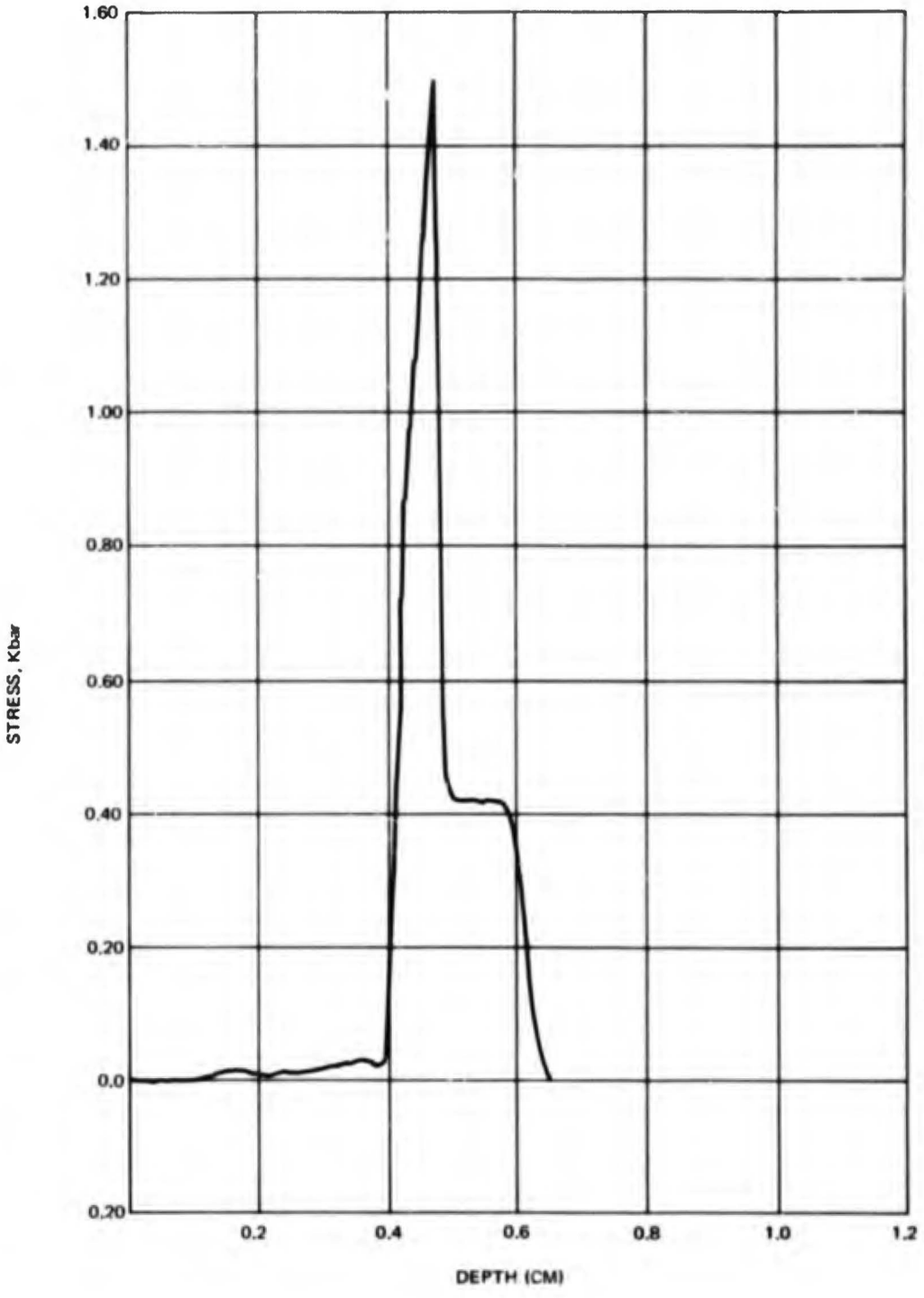

Figure 78. Stress Profile at 1.5007 μsec; Attenuation Shot, 90-Degree Orientation

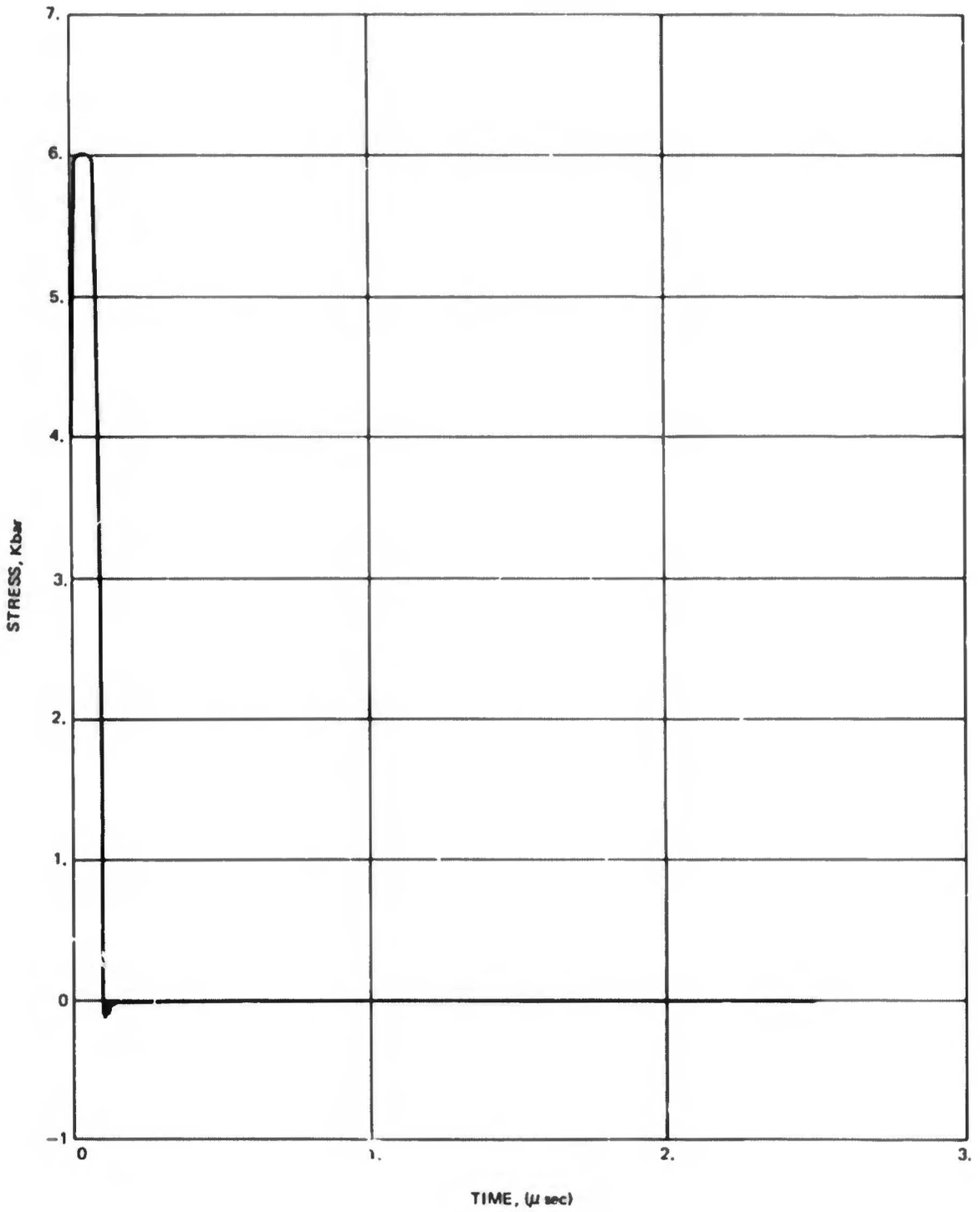

Figure 79. History of Stress at Mylar/Quartz-Phenolic Interface, Attenuation Shot, 90-Degree Orientation

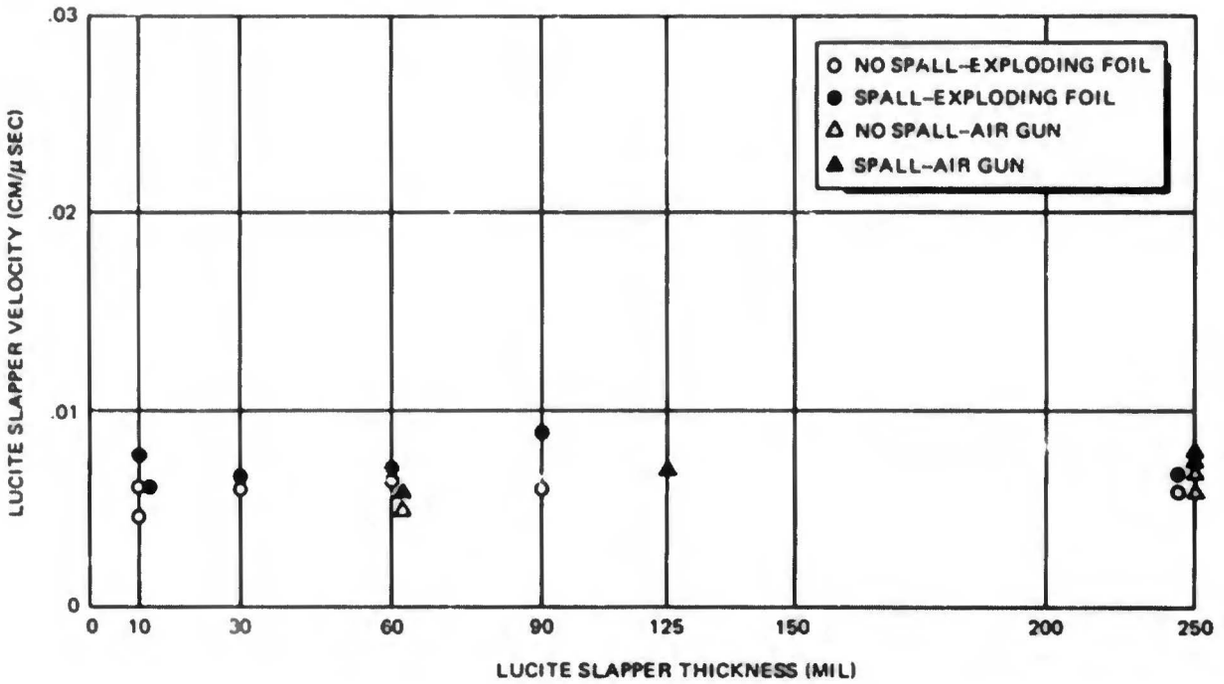

Figure 80. Spall Data for Lucite. Like-on-Like Impact. Slapper to Target Thickness Ratio = 1:4

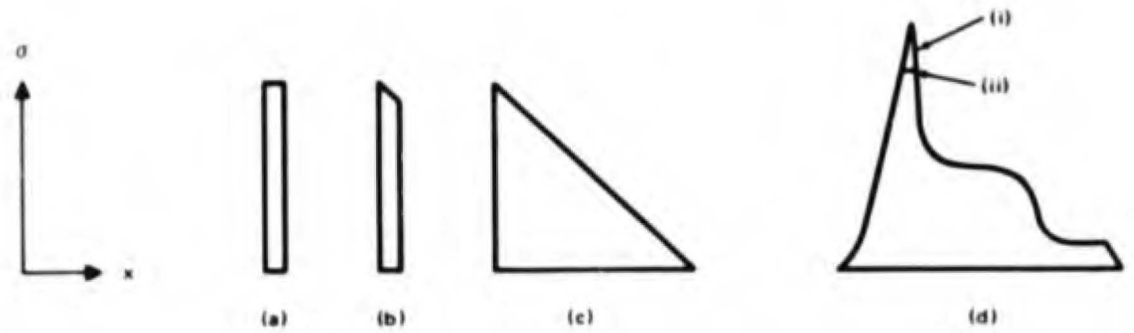

Figure 81. Stress Wave Pulse Shapes

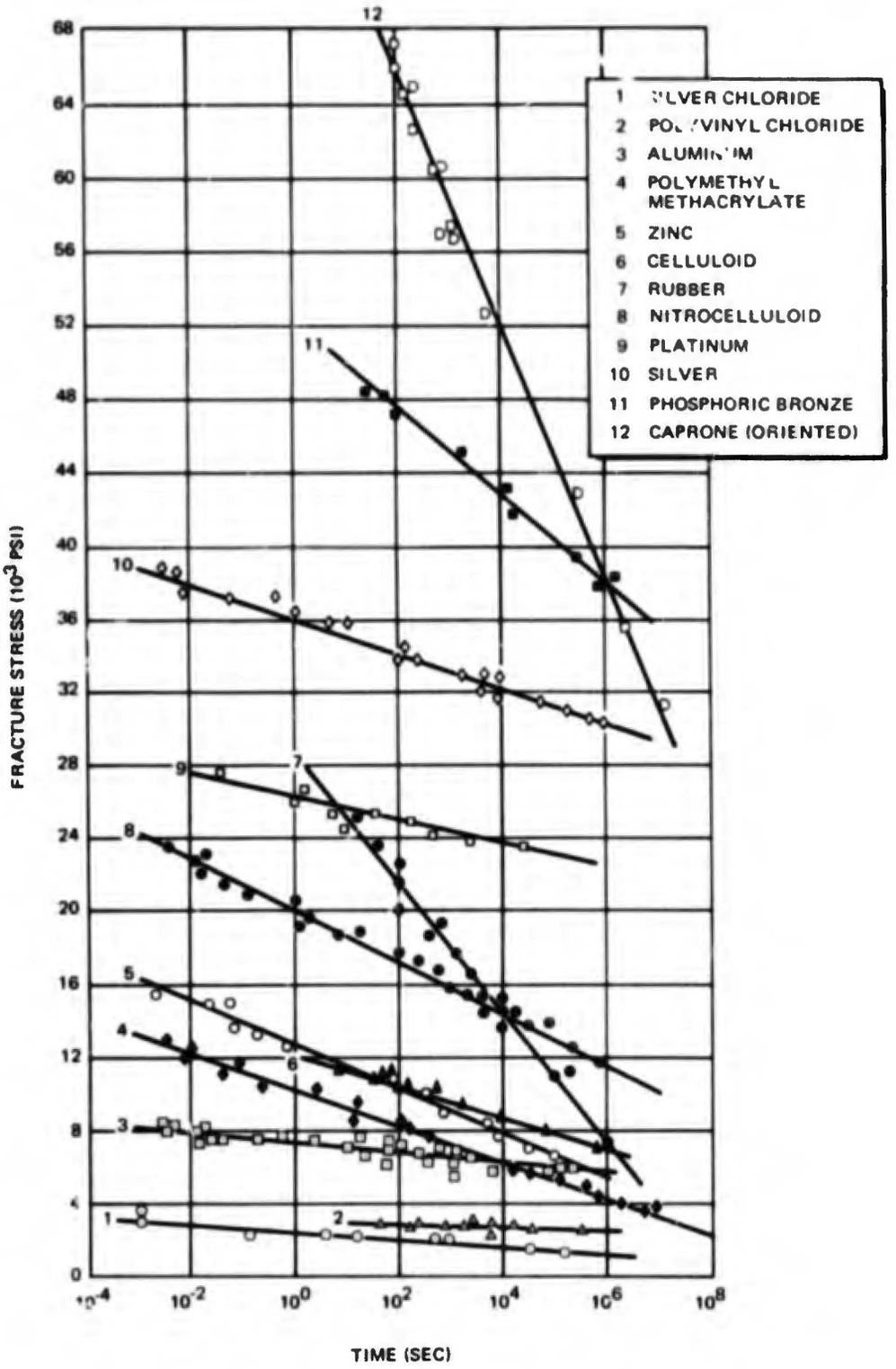

Figure 82. Time-Dependent Strength of Solids

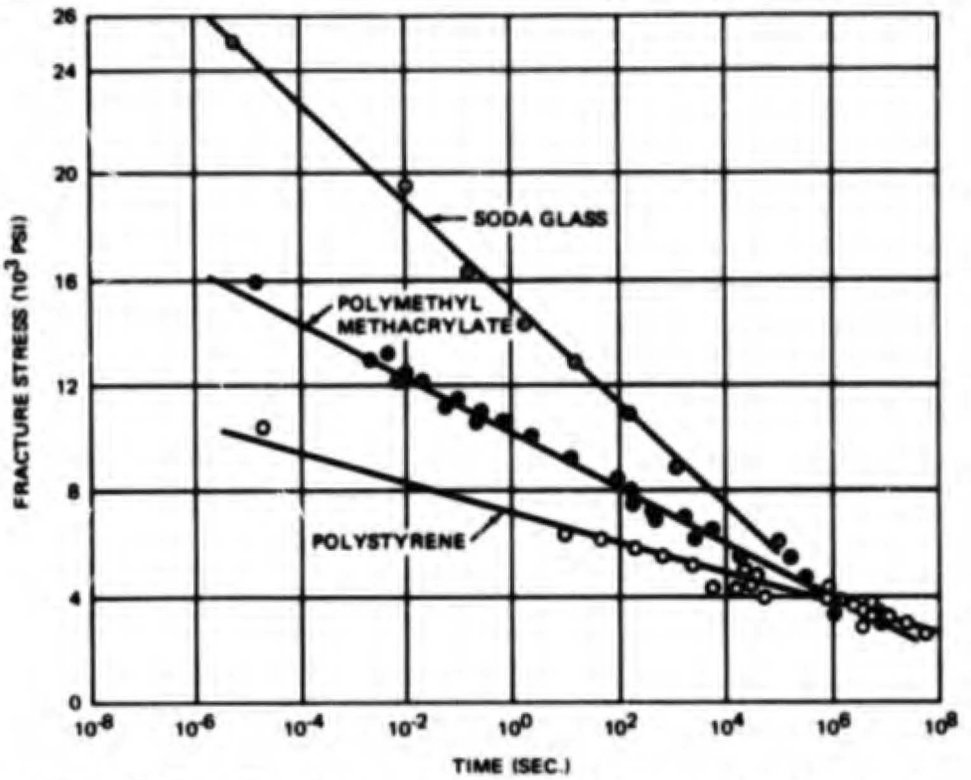

Figure 83. Time-Dependent Fracture Stress of Several Materials at Room Temperature

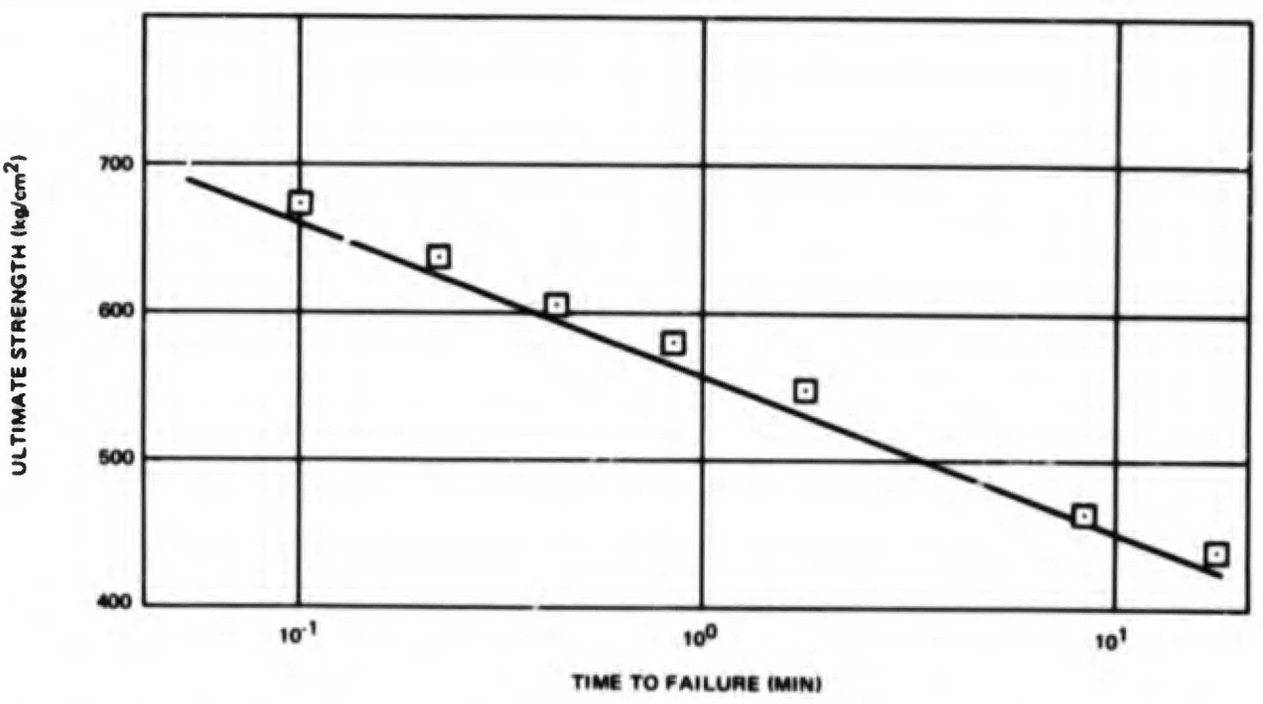

Figure 84. Time-Dependent Failure of Epoxy Resin-Constant Strain Rate (Epon 815/Versamide 140 (1:1 Mix))

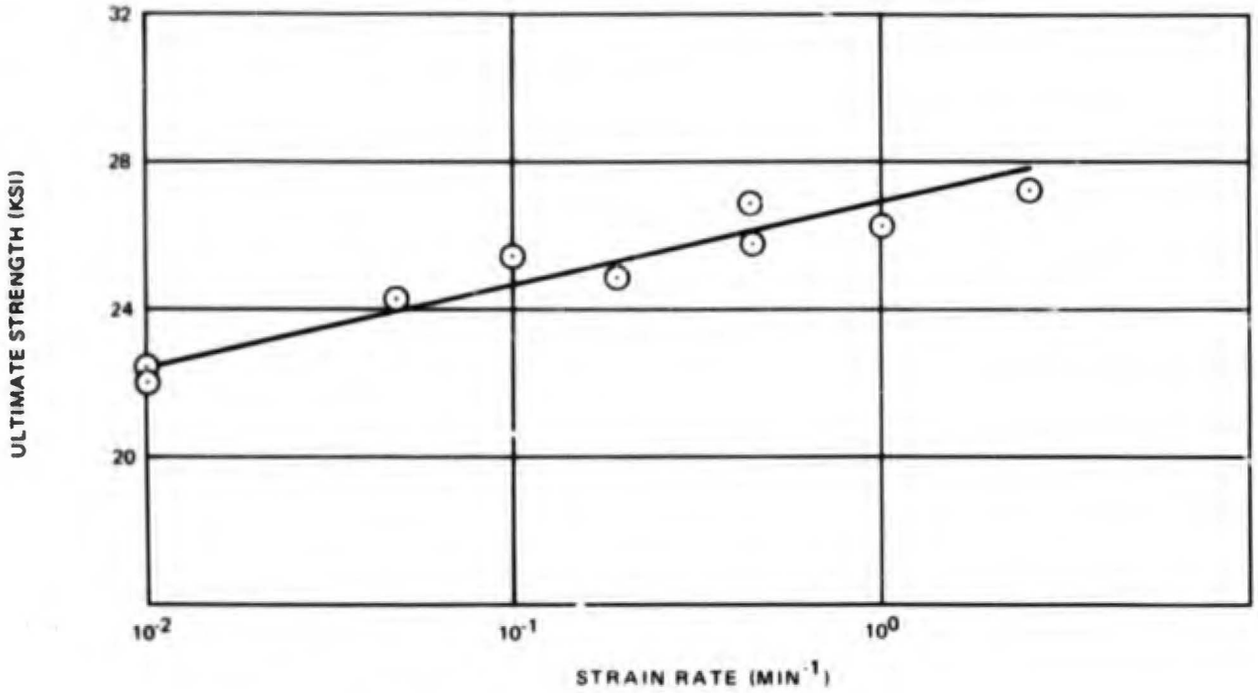

Figure 85. Stress vs Strain Rate – SC1008 Phenolic

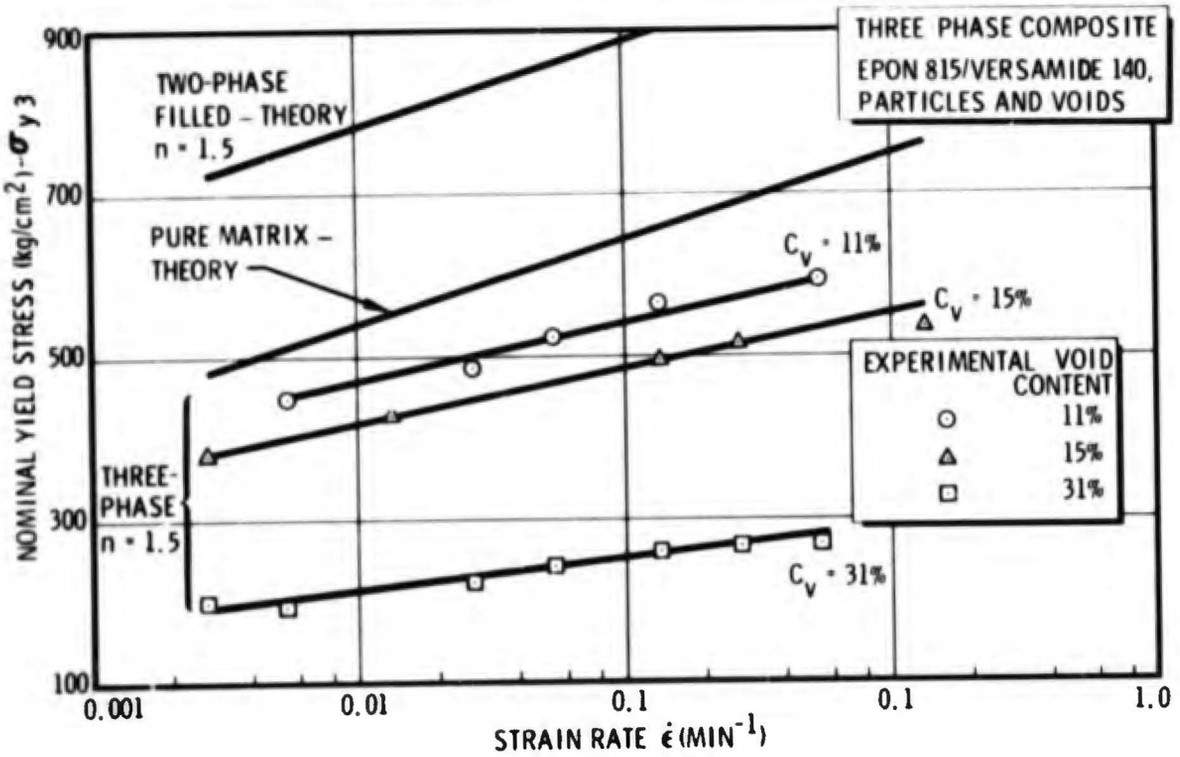

Figure 86. Yield Stress of 3-Phase Composite vs Strain Rate

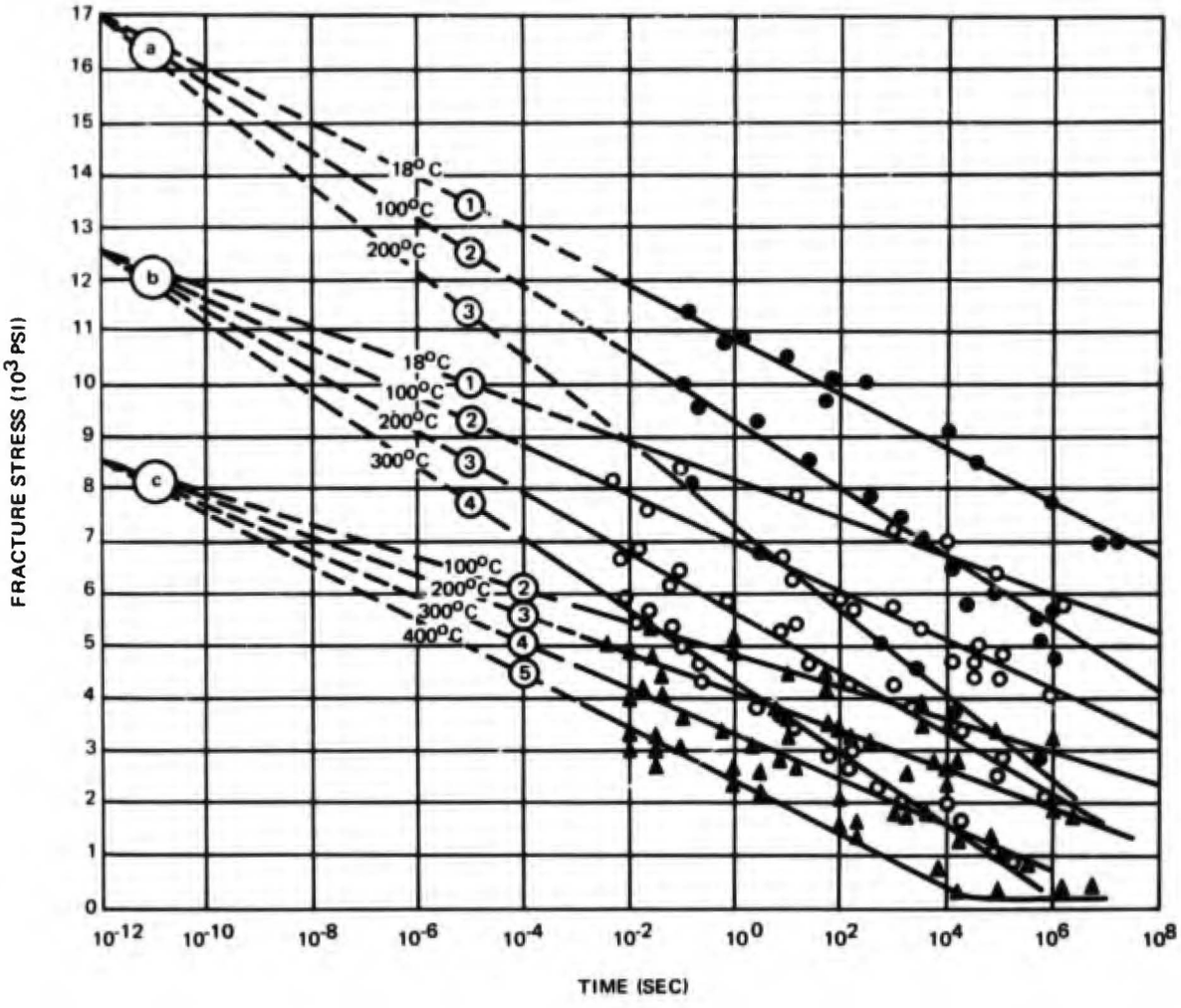

Figure 87. Time-Dependent Fracture Strength of Aluminum Annealed at: a) 290°C; b) 420°C; c) 550°C

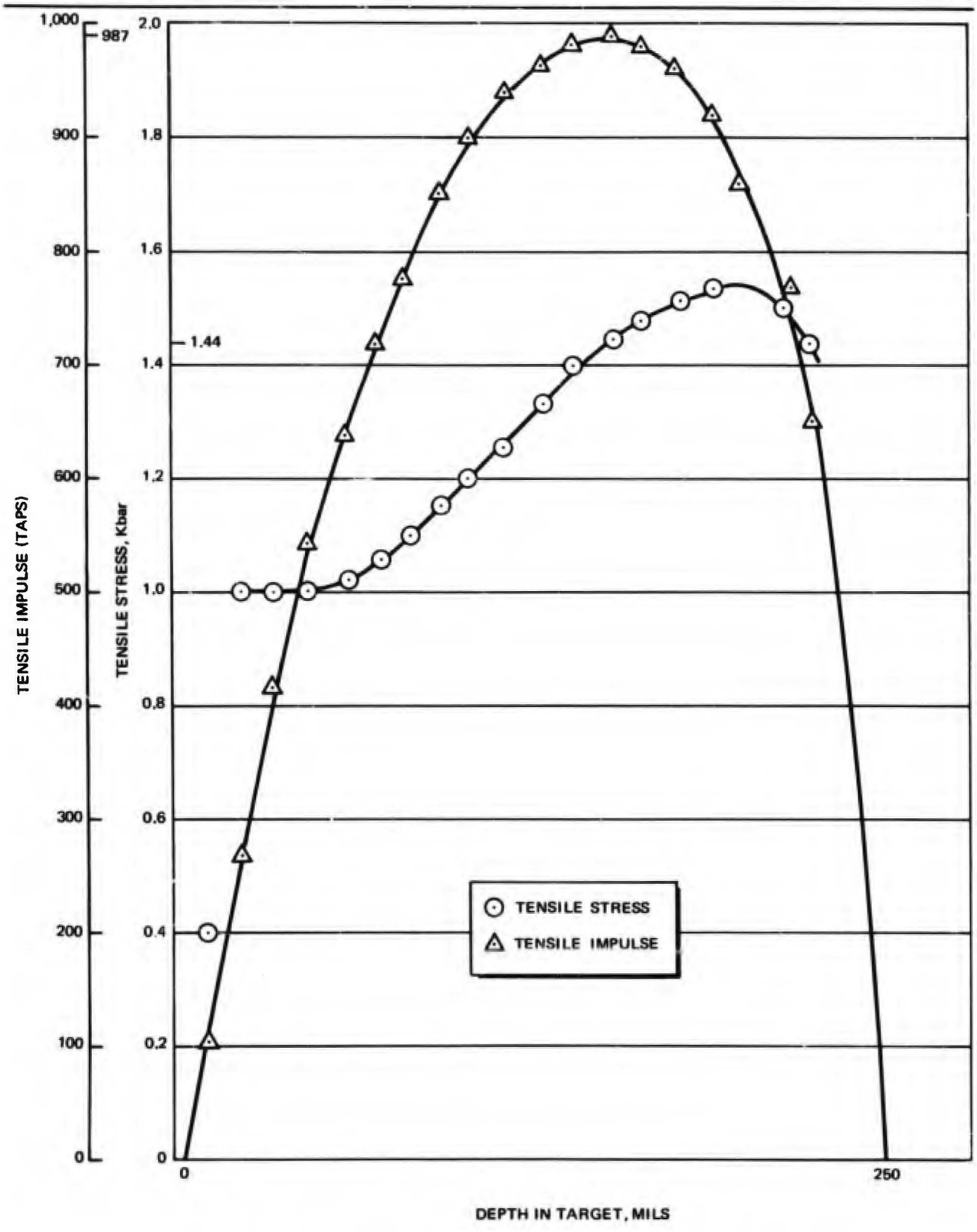

Figure 88. 5-Mil Mylar Impactor on 250-Mil Quartz-Phenolic Target at 0.960 mm/μ sec

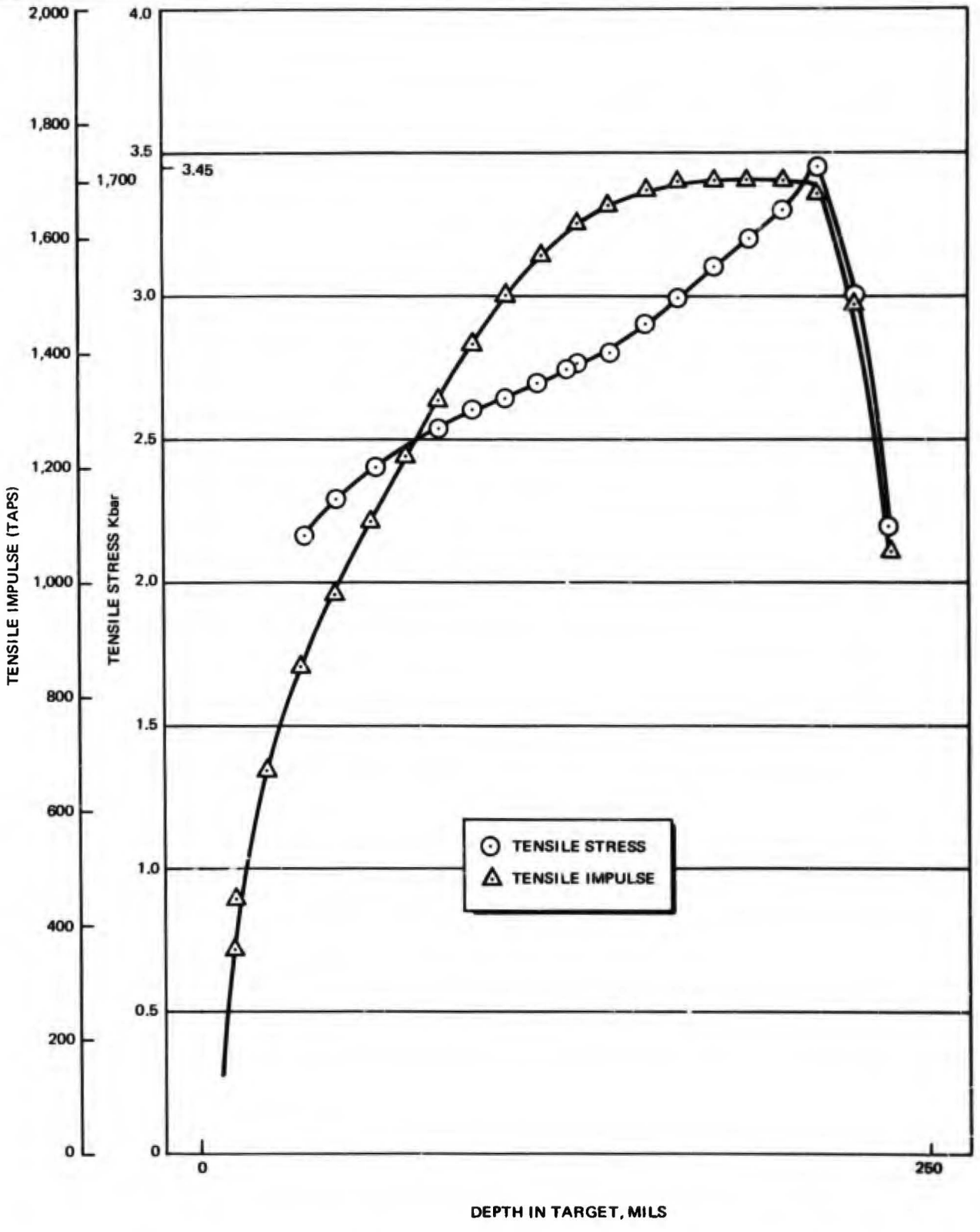

Figure 89. 14.7-Mil Mylar Impactor on 250-Mil Quartz-Phenolic Target at 0.56 mm/μsec

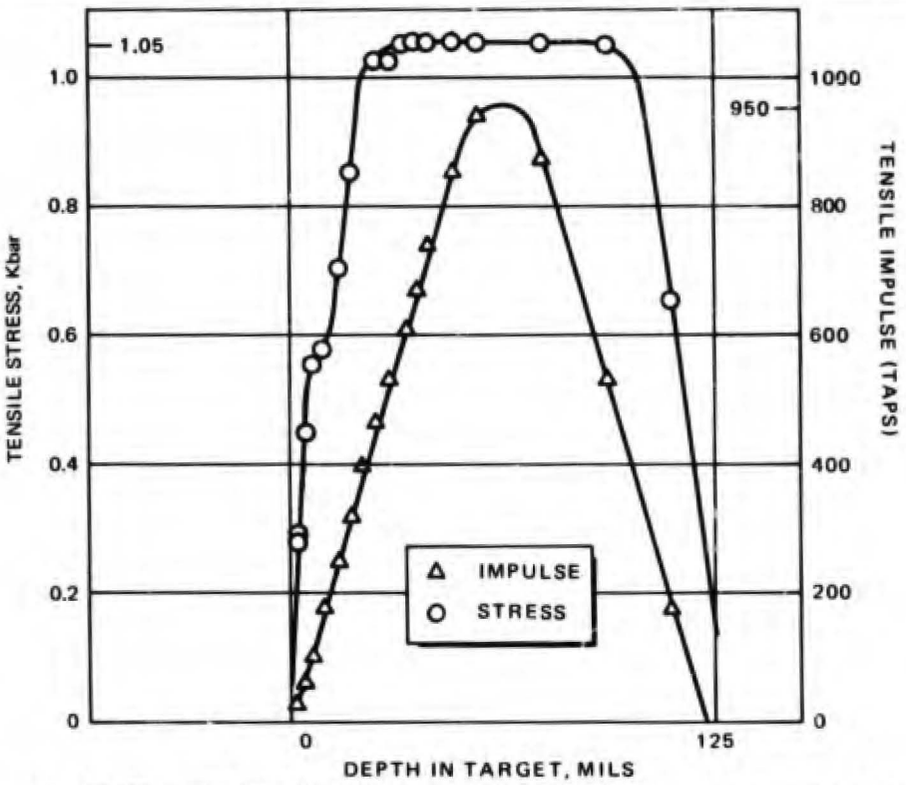

Figure 90. 60-Mil Quartz-Phenolic Impactor on 125-Mil Quartz-Phenolic Target at 0.473 mm/μsec.

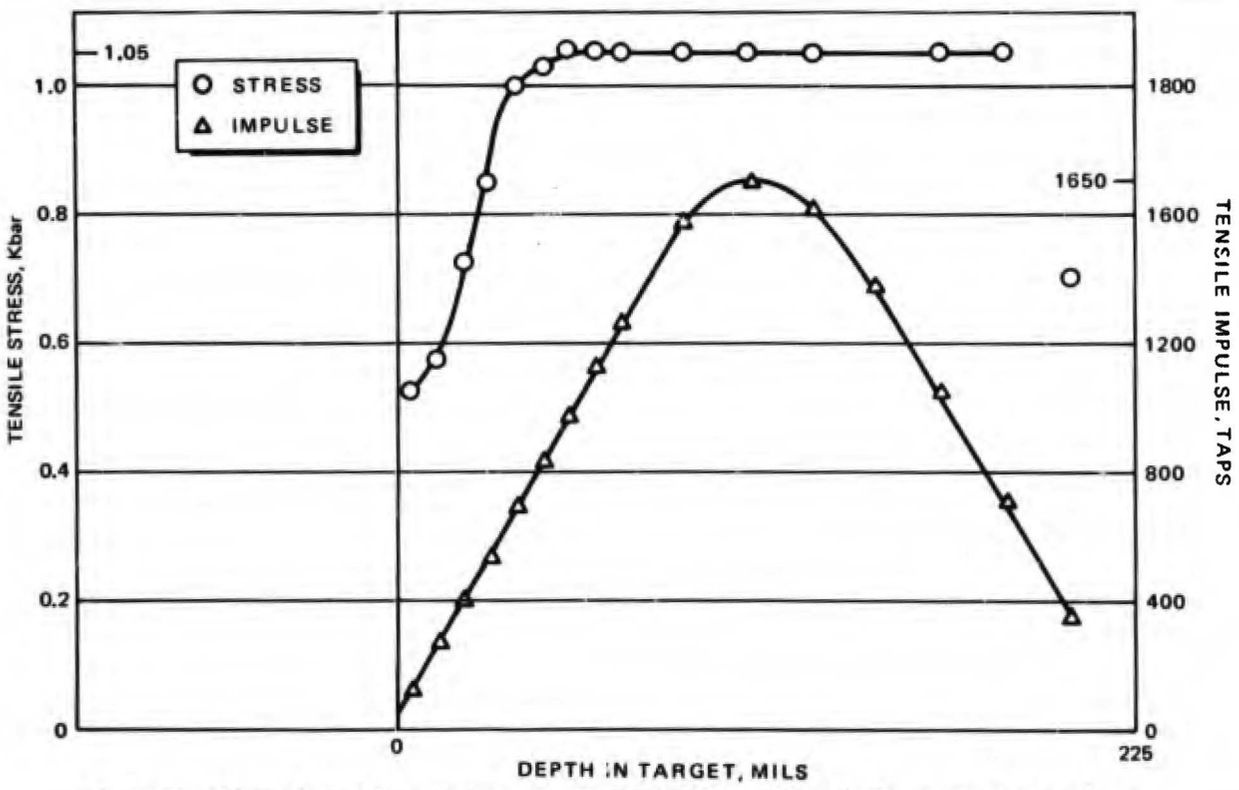

Figure 91. 125-Mil Quartz-Phenolic Impactor On 225-Mil Quartz-Phenolic Target At 0.473 mm/μsec

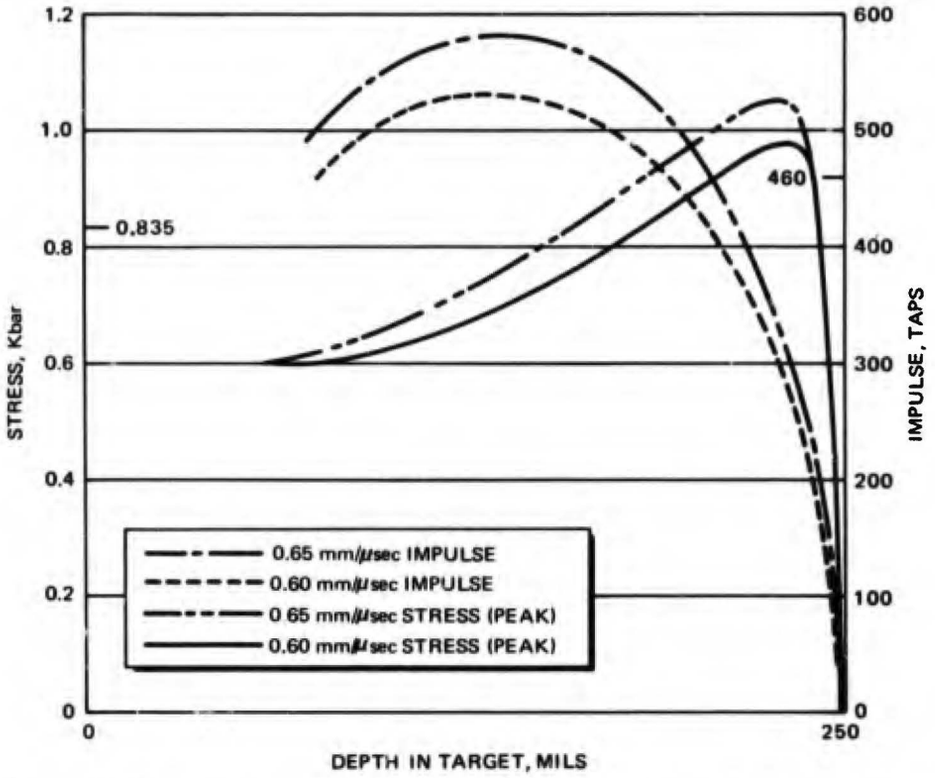

Figure 92. 5-Mil Mylar Impactor on 250-Mil Quartz-Phenolic Target at 0.600 and 0.650 mm/μsec.

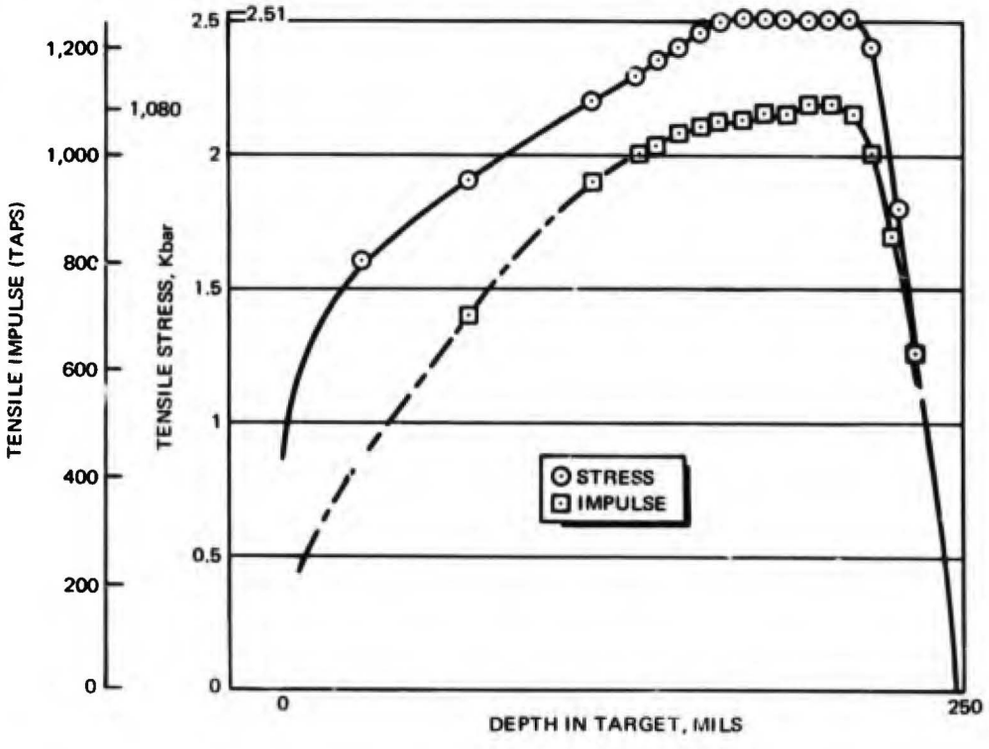

Figure 93. 14.7-Mil Mylar Impactor on 250-Mil Quartz-Phenolic Target at 0.390 mm/μsec.

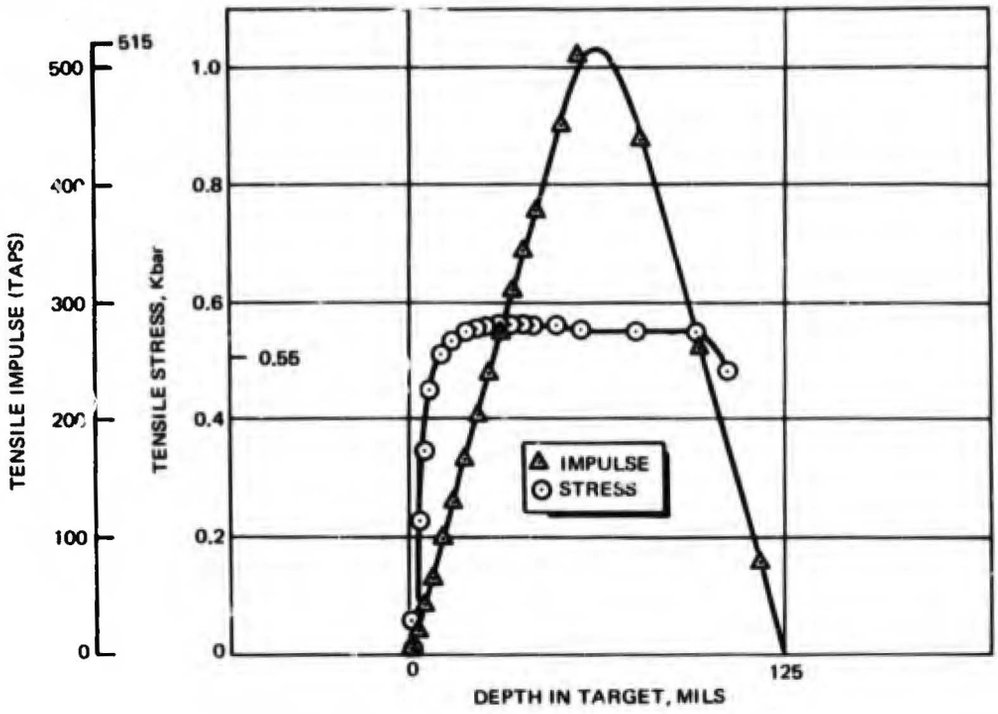

Figure 94. 60-Mil Quartz-Phenolic Impactor on 125-Mil Quartz-Phenolic Target at 0.213 mm/μsec.

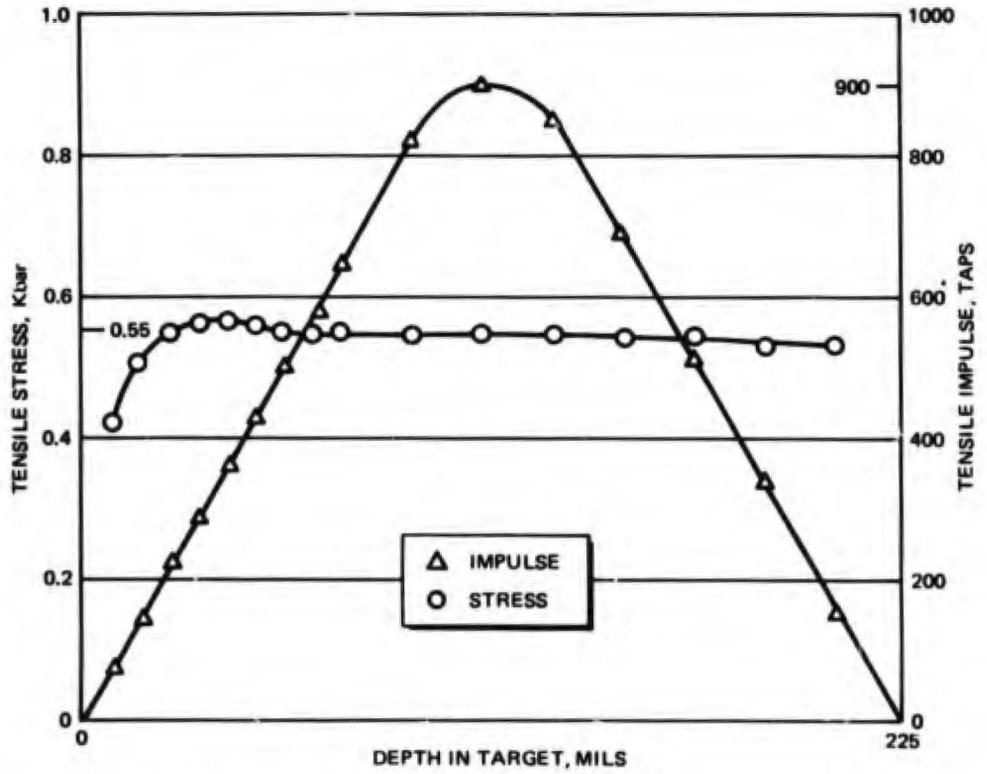

Figure 95. 125-Mil Quartz-Phenolic Impactor on 225-Mil Quartz-Phenolic Target at 0.213 mm/μsec.

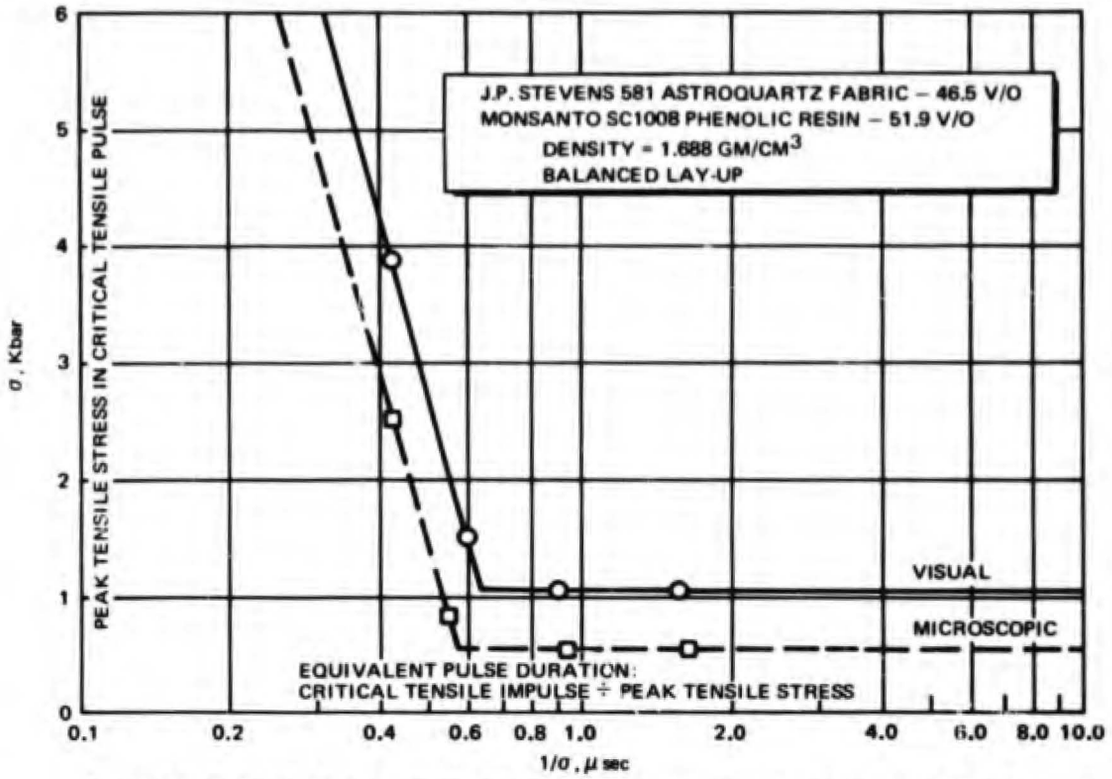

Figure 96. Estimated Delamination Thresholds Zero-Degree Shingle-Angle Quartz-Phenolic

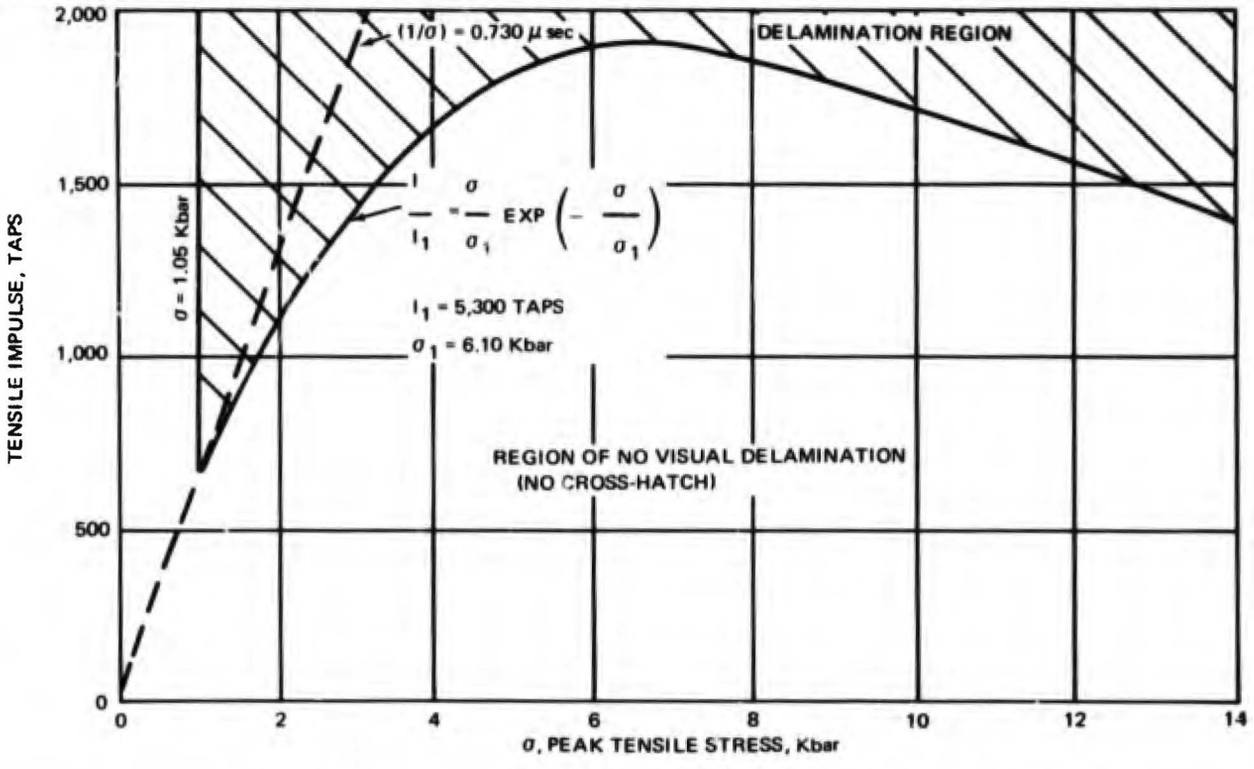

Figure 97. Visual Delamination Threshold Zero-Degree Shingle-Angle Quartz-Phenolic

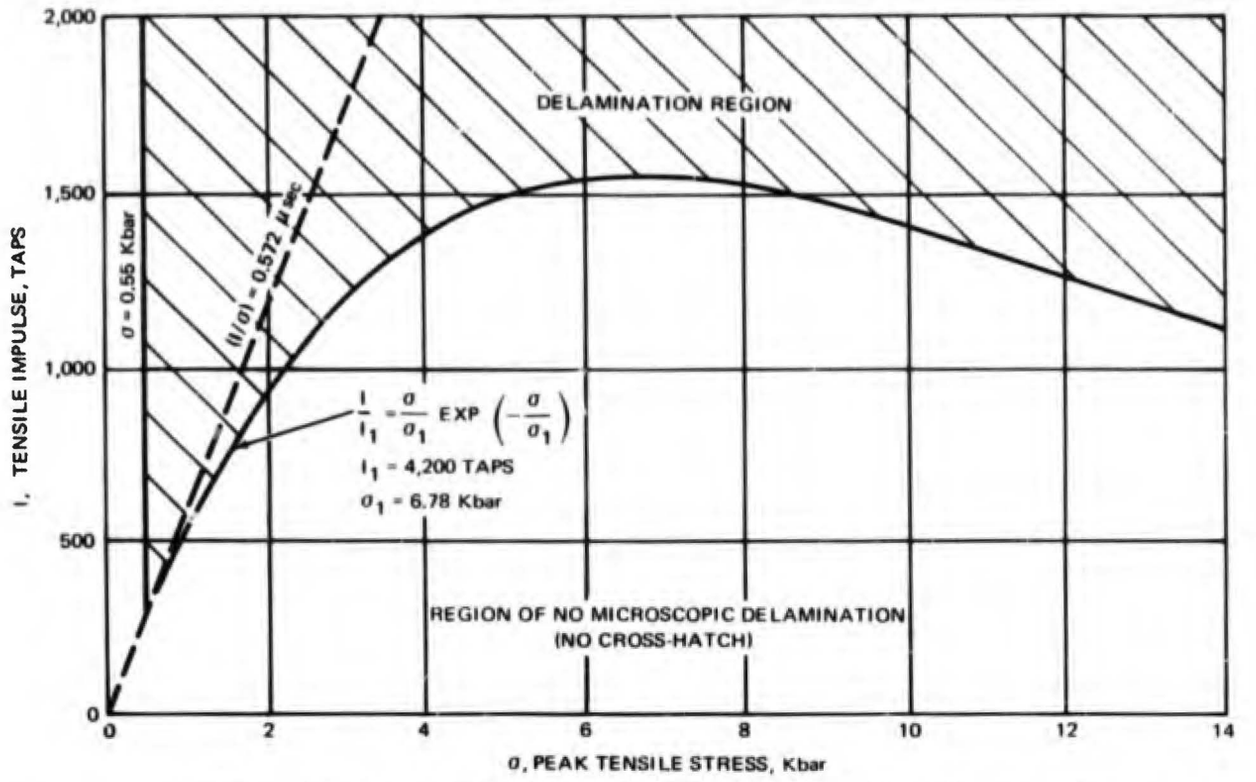

Figure 98. Microscopic Delamination Threshold Zero-Degree Shingle-Angle Quartz-Phenolic

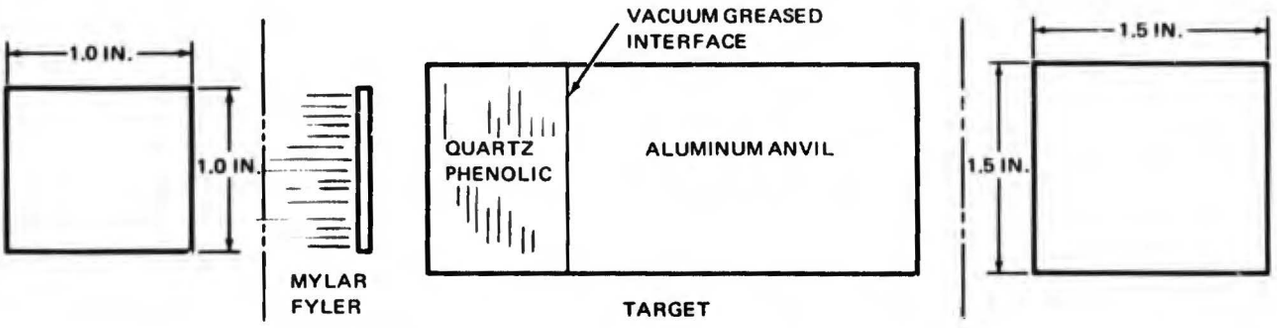

5-MIL MYLAR FLYER IMPACTING 250-MIL OF
ZERO-DEGREE SHINGLE-ANGLE QUARTZ-PHENOLIC
BACKED BY ABOUT 710-MIL OF 6061-T6 ALUMINUM

Figure 99. Proof-Test Configuration

NOT REPRODUCIBLE

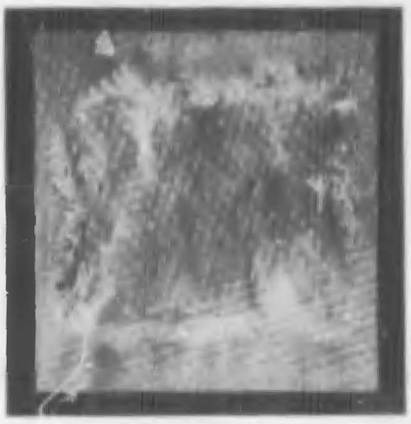

1.72 mm/μsec
P1

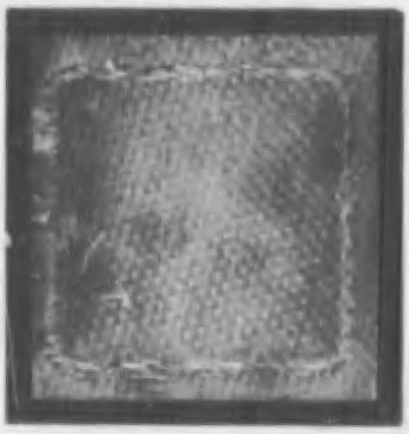

2.20 mm/μsec
P4

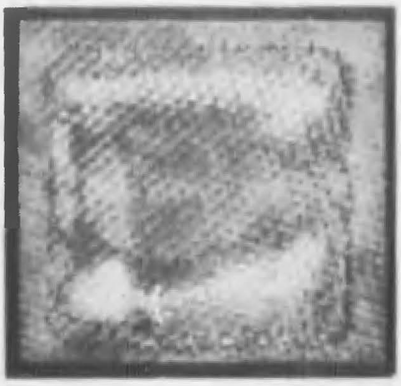

1.47 mm/μsec
P2

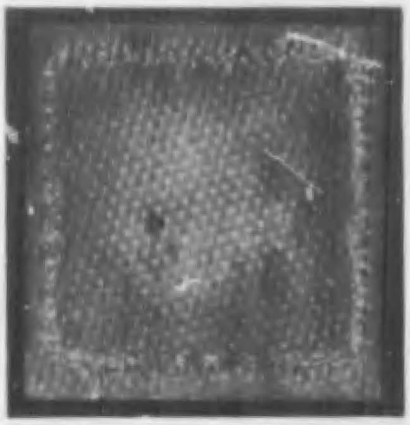

2.30 mm/μsec
P5

2.05 mm/μsec
P3

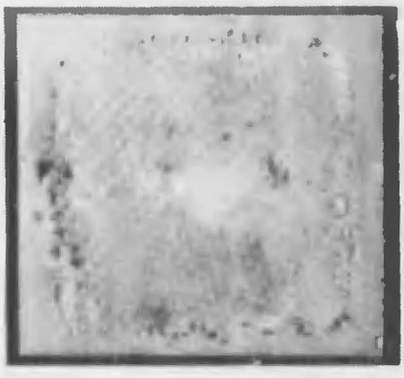

1.07 mm/μsec
P6

Figure 100. Post-Test Photographs (2X) of the Front Faces of the Specimens

NOT REPRODUCIBLE

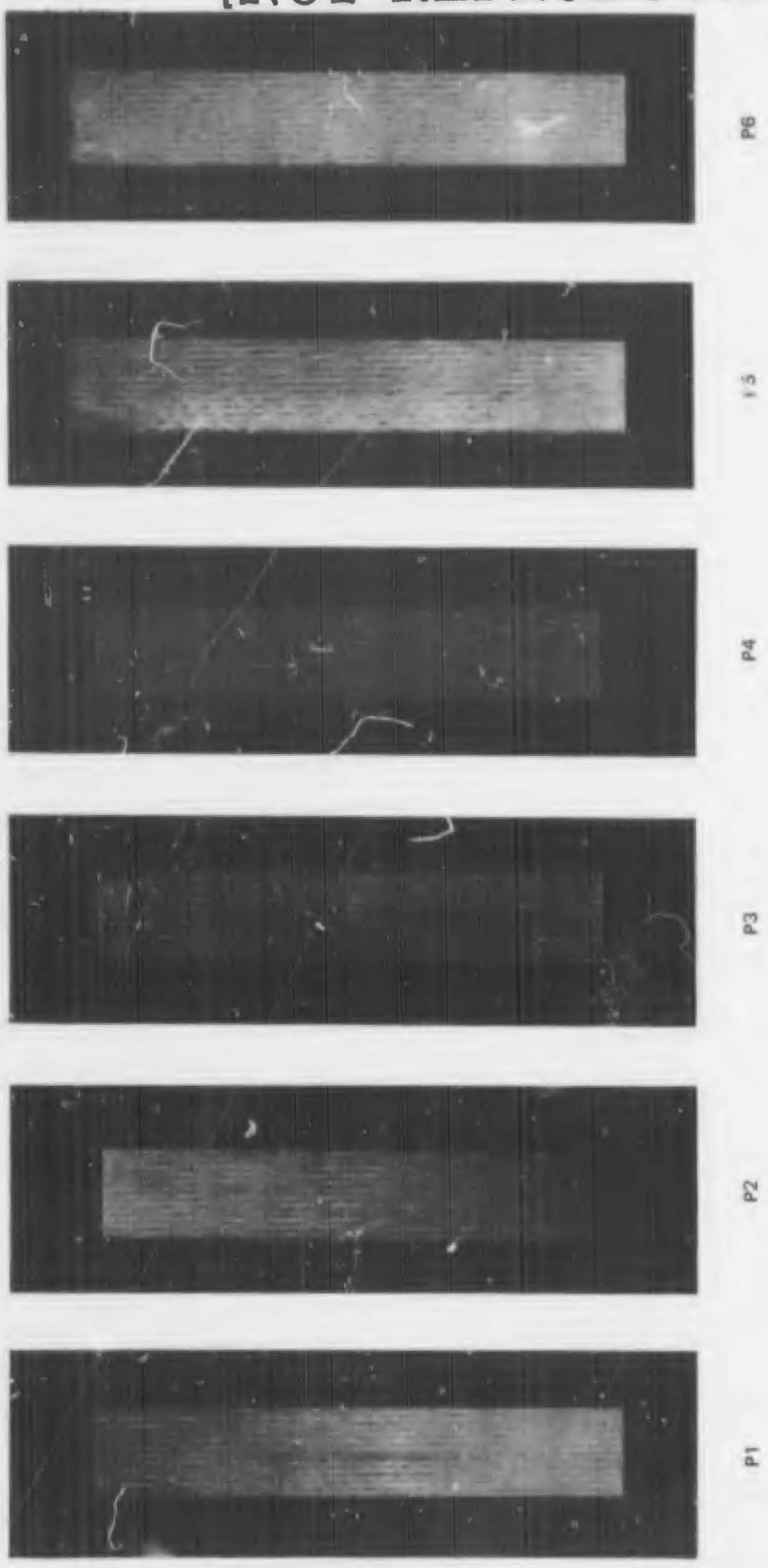

Figure 101. Post – Test Photographs (2X) of The Edges of the Specimens

VISUALLY DAMAGED SPECIMEN
AT 80X, SHOWING DELAMINATION
(2.20 mm/μsec)

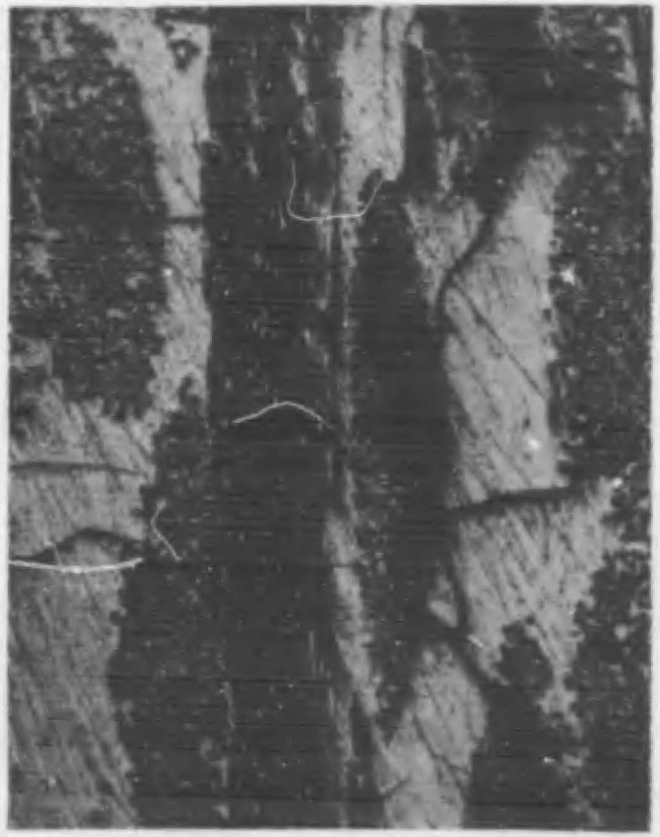

MICROSCOPICALLY DAMAGED
SPECIMEN AT 100X, SHOWING
MEANDERING DELAMINATION AND
MICROCRACKS (1.72 mm/μsec

Figure 102. Delamination of Visually Damaged Specimen Contrasted to Microscopically Damaged Specimen

NOT REPRODUCIBLE

NOT REPRODUCIBLE

2.05 mm/μsec

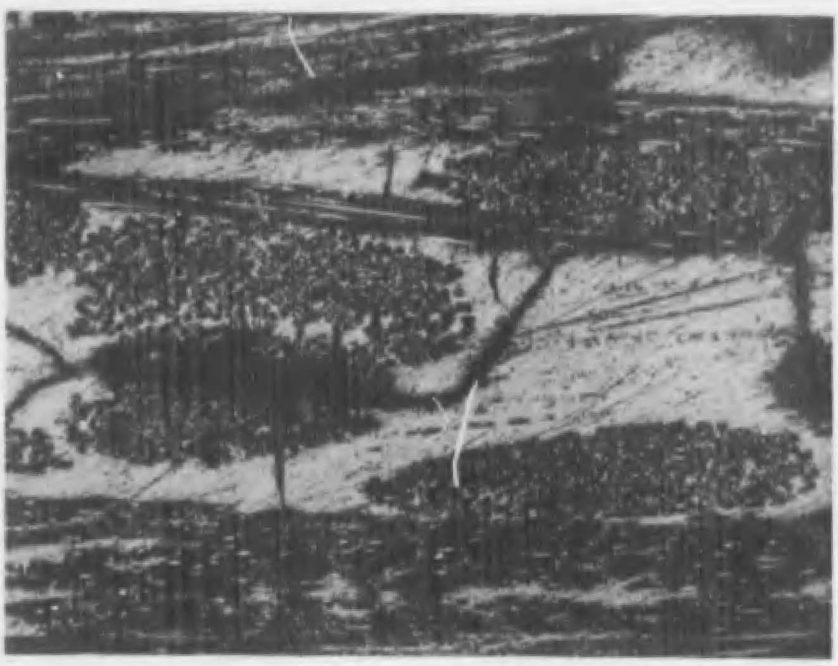

1.47 mm/μsec

Figure 103. Microscopically Damaged Specimens Showing Meandering Delaminations/Microcracks at 100X

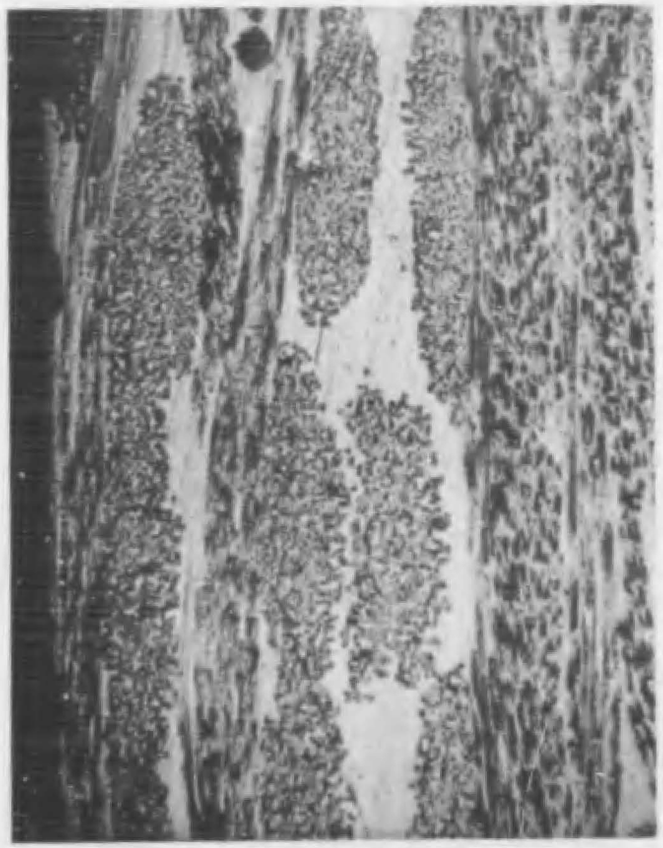

1.07 mm/μsec
NO DELAMINATION

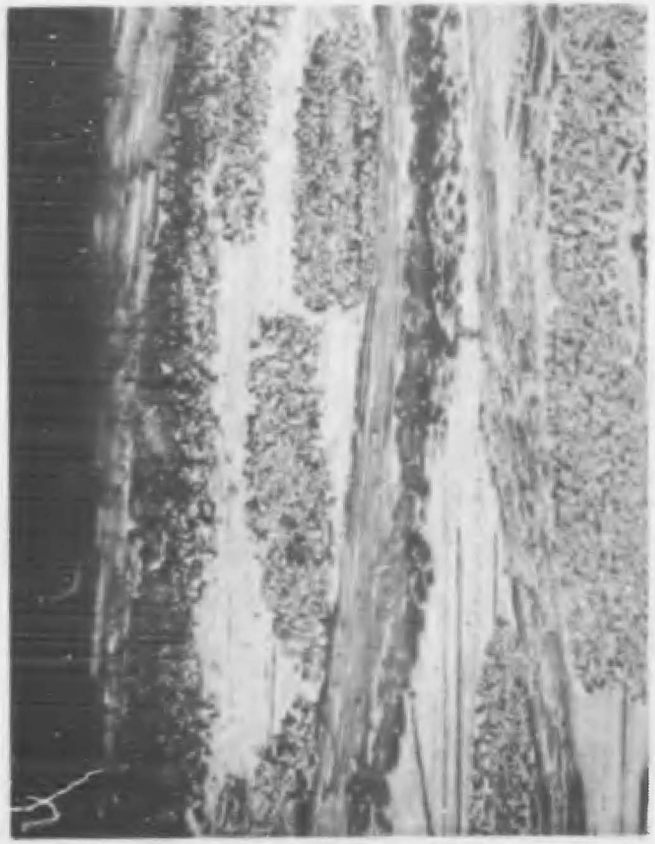

2.30 mm/μsec
CONTINUOUS DELAMINATION

Figure 104. Contrast of Front Face Microscopic Delamination at High- and Low-Velocity Impacts (100X Magnification)

NOT REPRODUCIBLE

NOT REPRODUCIBLE

Figure 105. Contrast of Condition of Mid-Plane Regions of Specimens at High- and Low-Velocity Impacts (100X Magnification)

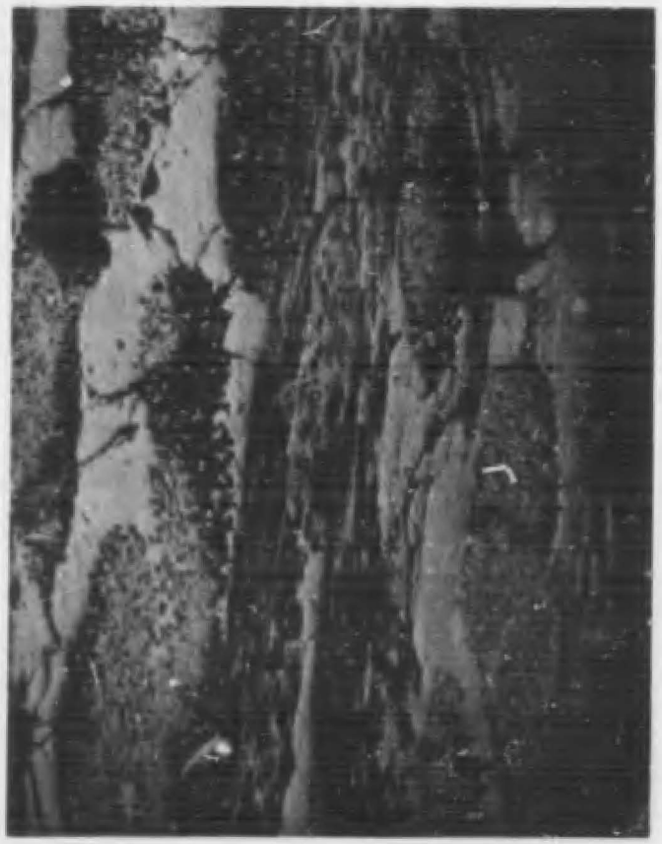

1.07 mm/μ sec

2.30 mm/μ sec
(NOTE DELAMINATION)

NOT REPRODUCIBLE

Figure 106. Contrast of Condition of Specimens Near Rear Face Following High- and Low-Velocity Impacts (100X Magnification)

NOT REPRODUCIBLE

Figure 107. Dense Microcracking Exhibited by Specimen P2 at 65X Magnification

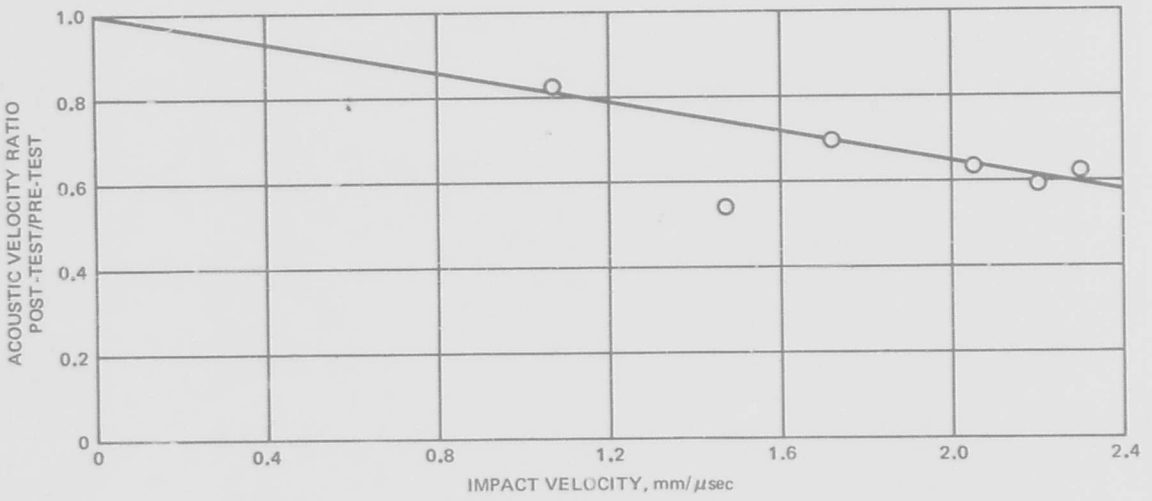

Figure 108. Acoustic Velocity Degradation Versus Impact Velocity

Unclassified

Security Classification

DOCUMENT CONTROL DATA - R & D

(Security classification of title, body of abstract and indexing annotation must be entered when the overall report is classified)

1. ORIGINATING ACTIVITY *(Corporate author)*
McDonnell Douglas Astronautics Company - Western Division, Santa Monica, California

2a. REPORT SECURITY CLASSIFICATION
Unclassified

2b. GROUP
N/A

3. REPORT TITLE
Final Report, A Study of Plate-Slap Technology
Part I--A Critical Evaluation of Plate-Slap Technology

4. DESCRIPTIVE NOTES *(Type of report and inclusive dates)*
Final Report: 15 April 1968 - 15 May 1969

5. AUTHOR(S) *(First name, middle initial, last name)*
Harvey M. Berkowitz
Leslie J. Cohen

6. REPORT DATE
June 1969

7a. TOTAL NO. OF PAGES
186

7b. NO. OF REFS
73

8a. CONTRACT OR GRANT NO.
F33615-68-C-1414

b. PROJECT NO.
7351

c. TASK NO.

d. 735106

9a. ORIGINATOR'S REPORT NUMBER(S)
DAC-63180

9b. OTHER REPORT NO(S) *(Any other numbers that may be assigned this report)*
AFML-TR-69-106, Part I

10. DISTRIBUTION STATEMENT This document is subject to special expert controls and each transmittal to foreign governments or foreign nationals may be made only with prior approval of the Metals and Ceramics Division (MAM), Air Force Materials Laboratory, Wright-Patterson Air Force Base, Ohio 45433

11. SUPPLEMENTARY NOTES
N/A

12. SPONSORING MILITARY ACTIVITY
Metals and Ceramics Division
Air Force Materials Laboratory
Wright-Patterson AFB, Ohio

13. ABSTRACT

This report presents the motivation, philosophy, technical approach, and results of the part of "A Study of Plate-Slap Technology" entitled "A Critical Evaluation of Plate-Slap Technology." Under this study, state of the art practices of plate-slap technology pertinent to characterization and design use of anisotropic composite-materials for re-entry vehicle thermal-protection systems, have been documented and evaluated. The program plan, results, and conclusions are summarized herein. Basic characterization data, high stress-amplitude constitutive data obtained by gas-gun testing, and short load-duration failure data obtained by exploding-foil testing are all presented for the study material, a quartz-cloth reinforced-phenolic. Methods of data reduction are described. The results of the proof-testing conducted to provide a check on the validity of the design use of the data are presented, and the overall technology is evaluated. In addition, the other two volumes making up this final report are summarized. These are "The Nuances of Plate-Slap Testing of Composite Materials," (Part II) and "The Mechanical Response of Composite Materials to Stress-Pulse Loading" (Part III).

This abstract is subject to special export controls and each transmittal to foreign governments or foreign nationals may be made only with prior approval of the Metals and Ceramics Division (MAM), Air Force Materials Laboratory, Wright-Patterson Air Force Base, Ohio 45433.

DD FORM 1 NOV 68 1473

Unclassified

Security Classification

14. KEY WORDS	LINK A		LINK B		LINK C	
	ROLE	WT	ROLE	WT	ROLE	WT
Anisotropic materials						
Composite Materials						
Dynamic fracture						
Exploding-foil testing						
Gas-gun testing						
Quartz-phenolic						
Plate-slap technology						
Re-entry thermal-protection system						
Shock waves						
Stress waves						
Equation of state						
Constitutive equations						
Hugoniot data						
Wave propagation						
Spallation						
Delamination						